

**OCTADENTATE CHELATORS FOR ZIRCONIUM- AND OTHER  
METAL-BASED RADIOPHARMACEUTICALS**

by

Christian Buchwalder

B.Sc., University of Zurich, Switzerland, 2011

M.Sc., University of Zurich, Switzerland, 2013

A THESIS SUBMITTED IN PARTIAL FULFILLMENT OF  
THE REQUIREMENTS FOR THE DEGREE OF

DOCTOR OF PHILOSOPHY

in

THE FACULTY OF GRADUATE AND POSTDOCTORAL STUDIES  
(Pharmaceutical Sciences)

THE UNIVERSITY OF BRITISH COLUMBIA  
(Vancouver)

December 2018

© Christian Buchwalder, 2018

## Committee Page

The following individuals certify that they have read, and recommend to the Faculty of Graduate and Postdoctoral Studies for acceptance, the dissertation entitled:

Octadentate Chelators for Zirconium- and Other Metal-Based Radiopharmaceuticals

---

submitted by Christian Buchwalder in partial fulfillment of the requirements for

the degree of Doctor of Philosophy

in Pharmaceutical Sciences

### **Examining Committee:**

Prof. Urs Häfeli, Pharmaceutical Sciences

---

Supervisor

Prof. Paul Schaffer, TRIUMF

---

Supervisory Committee Member

Prof. Chris Orvig, Chemistry

---

Supervisory Committee Member

Prof. W. Russell Algar, Chemistry

---

University Examiner

Prof. Adam Frankel, Pharmaceutical Sciences

---

University Examiner

### **Additional Supervisory Committee Members:**

Prof. David Grierson, Pharmaceutical Sciences

---

Supervisory Committee Member

Prof. Daniel Renouf, BC Cancer Agency

---

Supervisory Committee Member

## Abstract

Metal-based radiopharmaceuticals are critical in nuclear medicine for non-invasive diagnosis and treatment of serious diseases such as cancer. To be successfully deployed in such radioactive drugs, radiometal ions need to be stably sequestered by a suitable chelating agent. This work investigates a new class of octadentate chelating agents containing four 3-hydroxy-4-pyridinone (3,4-HOPO) entities with a focus on the development of new zirconium(IV) chelates. The diagnostic radionuclide zirconium-89 ( $^{89}\text{Zr}$ ,  $t_{1/2}$  78.41 h,  $I_{\beta^+}$  22.7%,  $E_{\beta^+ \text{ mean}}$  395.5 keV) is of particular interest for antibody-targeted positron emission tomography (immunoPET). The developed tetrakis(3,4-HOPO) chelator is capable of quantitatively sequestering  $^{89}\text{Zr}$  within 10 min at ambient temperature. The resultant  $\text{Zr}^{\text{IV}}$  complex was found to be of exceptional thermodynamic stability ( $\log \beta$  50.3), showed a favourable pharmacokinetic profile *in vivo*, and exceeded the current standard Zr-chelator in direct *in vitro* stability tests. The tetrapodal chelator was derivatized in a multi-step synthesis for covalent attachment to targeting vectors or other carriers. The conjugation and  $^{89}\text{Zr}$ -radiolabeling of the bifunctional chelator (BFC) was subsequently optimized and investigated in detail with two monoclonal antibodies, a model protein, and with polymeric nanoparticles. The long-term *in vivo* stability of the  $^{89}\text{Zr}$ -radiochelate was assessed in a novel way over six days by utilizing long-circulating hyperbranched polyglycerol (HPG) nanoparticles. The radiochelate-nanocarrier conjugates were examined over six days by non-invasive positron emission tomography (PET) and in a biodistribution study. Although *in vitro* exams demonstrated extended plasma stability, these data revealed a physiologic susceptibility of the tetrakis(HOPO) complex attributed to kinetic lability. In addition to investigations with  $\text{Zr}^{\text{IV}}$ , the new ligand system was briefly explored with

$\text{Fe}^{\text{III}}$ ,  $\text{Ga}^{\text{III}}$ ,  $\text{Y}^{\text{III}}$ ,  $\text{Sm}^{\text{III}}$ ,  $\text{Gd}^{\text{III}}$ ,  $\text{Tb}^{\text{III}}$ ,  $\text{Lu}^{\text{III}}$ , and  $\text{Bi}^{\text{III}}$  and indicated to be a promising chelator for iron(III), gallium(III), yttrium(III), and lanthanide ion coordination.

## Lay Summary

Radiolabeled drugs are routinely used to detect, monitor, and treat a number of serious diseases such as cancer. To develop more sensitive and specific radiopharmaceuticals, researchers are exploring different isotopes and attach them to new targeting molecules that bind to diseased cells. As some of the current attachment methods are plagued by limited stability, we synthesized and explored here for the first time a new class of binding molecules to attach a diagnostic isotope of zirconium to different targeting molecules. We investigated the chemistry of these radioactive constructs in detail and tested how they can be coupled to different carriers. The stability of those complexes was further examined over several days in the blood stream. The findings of this work are expected to advance nuclear medicine and help develop better diagnostic positron emission tomography imaging agents and new targeted radioactive therapies.

## Preface

The presented work was conducted at the Faculty of Pharmaceutical Sciences at the University of British Columbia with the exception of animal studies that were performed at the UBC Centre for Comparative Medicine (Chapter 3) or at the BC Cancer Research Centre (Chapter 4). All animal studies were performed in accordance with the University of British Columbia's Animal Care Committee (ACC) under the approved protocols A12-0172 and A16-0104. I, C. Buchwalder, was the lead investigator for the projects described herein and conducted this work with the following contributions by others:

Sections of Chapter 1 were written by myself for a published work and are reproduced in part with permission from The Royal Society of Chemistry (C. Buchwalder, C. Rodríguez-Rodríguez, P. Schaffer, S. K. Karagiozov, K. Saatchi and U. O. Häfeli, *Dalton Trans.*, **2017**, *46*, 9654-9663).

In Chapter 2, K. Saatchi conceived an initial tetrakis(hydroxypyrrone) chelator design, which I adapted for the intended bifunctional derivative. K. Saatchi and S. K. Karagiozov produced a starting material, compound **2.3**. The synthetic route pursued was devised by myself and R. Gealageas. I conceptualized, executed, analyzed, and interpreted all syntheses and experiments and discussed findings with U. O. Häfeli and K. Saatchi.

Chapter 3 is, in part, an adaptation of published work reproduced with permission from The Royal Society of Chemistry (C. Buchwalder, C. Rodríguez-Rodríguez, P. Schaffer, S. K. Karagiozov, K. Saatchi and U. O. Häfeli, *Dalton Trans.*, **2017**, *46*, 9654-9663). I conceptualized and wrote most of the manuscript with editorial help from C. Rodríguez-Rodríguez, P. Schaffer, and U. O. Häfeli. K. Saatchi suggested the initial ligand design, was involved in the study design, and harvested organs for the biodistribution study. K. Saatchi and S. K. Karagiozov produced a starting material, compound **3.1**. C. Rodríguez-Rodríguez performed the

computational study, operated the PET scanner, and wrote the corresponding experimental section. P. Schaffer was involved in the design of radiochemical experiments and provided access to  $^{89}\text{Zr}$ . U. O. Häfeli was the supervisory investigator and provided support and guidance. I selected the metal ion  $\text{Zr}^{\text{IV}}$  and designed, conducted, evaluated, and interpreted all syntheses and experiments. I discussed findings with U. O. Häfeli, C. Rodríguez-Rodríguez, P. Schaffer, and K. Saatchi.

The thermodynamic solution studies in Chapter 3 are unpublished and will be reported together with results from Chapter 4. M. G. Jaraquemada-Peláez and I conducted all experiments, analyzed and interpreted the results, and wrote the corresponding sections together (sub-chapters 3.2.3 and 3.4.4).

In Chapter 4, I designed and synthesized the bifunctional chelator with some suggestions from K. Saatchi. Polymeric nanoparticles were produced by K. Saatchi. S. K. Karagiozov produced a starting material, compound **4.6**. J. Rousseau and H. Merkens were involved with *in vivo* studies, together with staff at the BC Cancer Research Centre. J. Rousseau and I analyzed the *in vivo* results together. U. O. Häfeli was the supervisory investigator and provided support and guidance in the study design and execution. I designed and conducted all other experiments including syntheses, characterizations, radiolabelings, and analyses. I evaluated and interpreted all data and discussed results with U. O. Häfeli, P. Schaffer, K. Saatchi, J. Rousseau, C. Rodríguez-Rodríguez, and T. V. Esposito. A manuscript reporting these findings is in preparation.

All experiments in Chapter 5 were designed, conducted, and interpreted by myself.

# Table of Contents

Abstract.....	iii
Lay Summary .....	v
Preface.....	vi
Table of Contents .....	viii
List of Tables.....	xv
List of Figures .....	xvi
List of Schemes .....	xx
List of Abbreviations .....	xxi
Acknowledgements .....	xxvii
Dedication .....	xxix
<b>Chapter 1: Introduction .....</b>	<b>1</b>
1.1 Radiopharmaceuticals for Diagnostic Imaging .....	1
1.2 Radiopharmaceuticals for Therapy .....	6
1.3 Design of Metal-based Radiopharmaceuticals .....	11
1.4 Hydroxypyridinones and Hydroxypyrones as Metal Binding Units.....	17
1.5 Zirconium-89 for PET Imaging .....	18
1.6 Reported Zirconium-89 Chelates.....	20
1.7 Dissertation Overview and Research Objectives.....	24
<b>Chapter 2: Efforts Towards an Octadentate Hydroxypyrene-Based Ligand System.....</b>	<b>25</b>
2.1 Introduction .....	25
2.2 Results and Discussion.....	25

2.2.1	Synthesis and Characterization .....	25
2.2.2	Ester Bond Instability .....	27
2.3	Conclusions.....	31
2.4	Experimental.....	32
2.4.1	Materials and Methods .....	32
2.4.2	Syntheses .....	33
2.4.2.1	<i>N</i> -(9-Fluorenylmethoxycarbonyl)iminodiacetic acid (2.2) .....	33
2.4.2.2	Bis((3-(benzyloxy)-6-methyl-4-oxo-4 <i>H</i> -pyran-2-yl)methyl) 2,2' <i>N</i> -(9-fluorenyl methoxycarbonyl)iminodiacetate (2.4) .....	34
2.4.2.3	Bis((3-(benzyloxy)-6-methyl-4-oxo-4 <i>H</i> -pyran-2-yl)methyl) 2,2'-iminodiacetate (2.5).....	35
2.4.3	Decomposition Study.....	36
<b>Chapter 3: The Octadentate Tetrakis(3-Hydroxy-4-Pyridinone) Chelator THPN for Zirconium(IV) Complexation .....</b>		<b>37</b>
3.1	Introduction .....	37
3.2	Results and Discussion.....	38
3.2.1	Synthesis and Characterization of THPN and Zr-THPN .....	38
3.2.2	Computational Studies .....	40
3.2.3	Thermodynamic Solution Studies.....	43
3.2.3.1	THPN Ligand Protonation Constants .....	43
3.2.3.2	Complex Formation Equilibria with Fe <sup>3+</sup> and Zr <sup>4+</sup> .....	45
3.2.4	Radiolabeling of THPN with <sup>89</sup> Zr <sup>IV</sup> .....	51
3.2.5	Concentration Dependence of Radiolabeling.....	52

3.2.6	Distribution Coefficients.....	54
3.2.7	In Vitro Stability Experiments .....	54
3.2.7.1	Transchelation Competition Study .....	55
3.2.7.2	EDTA Challenge .....	57
3.2.7.3	Serum Stability Study .....	58
3.2.8	<i>In Vivo</i> Behaviour.....	58
3.3	Conclusions.....	60
3.4	Experimental.....	61
3.4.1	Materials and Methods .....	61
3.4.2	Syntheses .....	63
3.4.2.1	2,2',2'',2'''-((Propane-1,3-diyl)bis(azanetriyl))tetrakis( <i>N</i> -((1,6-dimethyl-3-(phenylmethoxy)-4-oxo-1,4-dihydropyridin-2-yl)methyl)acetamide) (3.2) .....	63
3.4.2.2	2,2',2'',2'''-((Propane-1,3-diyl)bis(azanetriyl))tetrakis( <i>N</i> -((1,6-dimethyl-3-hydroxy-4-oxo-1,4-dihydropyridin-2-yl)methyl)acetamide) (THPN).....	64
3.4.2.3	Zr-THPN Complex .....	65
3.4.3	Computational Studies .....	65
3.4.4	Thermodynamic Solution Studies.....	66
3.4.4.1	Materials and Methods.....	66
3.4.4.2	THPN Ligand Protonation Constants .....	67
3.4.4.3	Metal Complex Formation Constants .....	68
3.4.5	Concentration Dependence of <sup>89</sup> Zr-Radiolabeling .....	69
3.4.6	Human Serum Stability .....	69
3.4.7	Distribution Coefficients.....	69
3.4.8	Transchelation Competition Study .....	70

3.4.9	EDTA Competition Study.....	71
3.4.10	<i>In Vivo</i> Study of <sup>89</sup> Zr Complexes.....	71
3.4.11	PET/CT Imaging .....	72
<b>Chapter 4: Bifunctionalization of THPN and Study of <sup>89</sup>Zr-THPN Conjugates.....</b>		<b>73</b>
4.1	Introduction .....	73
4.2	Results and Discussion.....	74
4.2.1	Synthesis of Bifunctional THPN.....	74
4.2.2	<sup>89</sup> Zr-Trastuzumab Radioimmunoconjugates .....	80
4.2.2.1	<sup>89</sup> Zr-Labeling of Trastuzumab by Postlabeling .....	82
4.2.2.2	<sup>89</sup> Zr-Labeling of Trastuzumab by Prelabeling.....	86
4.2.2.3	<i>In Vitro</i> Plasma Stability Study .....	88
4.2.3	<sup>89</sup> Zr-Anti-PD-L1 Radioimmunoconjugates .....	89
4.2.4	<sup>89</sup> Zr-Mouse Serum Albumin (MSA) Radioconjugates.....	93
4.2.5	<sup>89</sup> Zr-Hyperbranched Polyglycerol (HPG) Radioconjugates .....	95
4.2.5.1	Chelator Conjugation and Radiolabeling .....	95
4.2.5.2	<i>In Vitro</i> Plasma Stability of <sup>89</sup> Zr-HPG Conjugates .....	97
4.2.5.3	<i>In Vivo</i> Stability of <sup>89</sup> Zr-HPG Conjugates .....	98
4.3	Conclusions.....	103
4.4	Experimental.....	105
4.4.1	Materials and Methods .....	105
4.4.2	Syntheses .....	108
4.4.2.1	Diethyl-2-(4-nitrobenzyl)malonate (4.1).....	108
4.4.2.2	2-(4-Nitrobenzyl)propanediamide (4.2).....	109

4.4.2.3	1,3-Diamino-2-(4-nitrobenzyl)propane dihydrochloride (4.3).....	110
4.4.2.4	Tetra- <i>tert</i> -butyl 2,2',2'',2'''-((2-(4-nitrobenzyl)propane-1,3-diyl)bis(azanetriyl))-tetraacetate (4.4) .....	111
4.4.2.5	2,2',2'',2'''-(2-(4-Nitrobenzyl)propane-1,3-diyl-bis(azanetriyl))-tetraacetic acid (4.5).....	111
4.4.2.6	2,2',2'',2'''-((2-(4-Nitrobenzyl)propane-1,3-diyl)bis(azanetriyl))tetrakis( <i>N</i> -((1,6-dimethyl-3-(phenylmethoxy)-4-oxo-1,4-dihydropyridin-2-yl)methyl)acetamide) (4.7) .....	112
4.4.2.7	2,2',2'',2'''-((2-(4-Nitrobenzyl)propane-1,3-diyl)bis(azanetriyl))tetrakis( <i>N</i> -((1,6-dimethyl-3-hydroxy-4-oxo-1,4-dihydropyridin-2-yl)methyl)acetamide) (4.8).....	113
4.4.2.8	2,2',2'',2'''-((2-(4-Aminobenzyl)propane-1,3-diyl)bis(azanetriyl))tetrakis( <i>N</i> -((1,6-dimethyl-3-hydroxy-4-oxo-1,4-dihydropyridin-2-yl)methyl)acetamide) (4.9).....	114
4.4.2.9	2,2',2'',2'''-((2-(4-Isothiocyanatobenzyl)propane-1,3-diyl)bis(azanetriyl))tetrakis( <i>N</i> -((1,6-dimethyl-3-hydroxy-4-oxo-1,4-dihydropyridin-2-yl)methyl)acetamide) ( <i>p</i> -SCN-Bn-THPN, 4.10).....	115
4.4.2.10	2,2',2'',2'''-((2-(4-(3-(2-(2-(2-(2-(4-(6-methyl-1,2,4,5-tetrazin-3-yl)phenoxy)ethoxy)ethoxy)ethoxy)ethylthioureido)benzyl)propane-1,3-diyl)bis(azanetriyl))-tetrakis( <i>N</i> -((1,6-dimethyl-3-hydroxy-4-oxo-1,4-dihydropyridin-2-yl)methyl)-acetamide) (Tz-THPN, 4.12) .....	116
4.4.3	<sup>89</sup> Zr-Trastuzumab Radioimmunoconjugates .....	117
4.4.3.1	Postlabeling Strategy .....	117
4.4.3.2	Prelabeling Strategy .....	118

4.4.3.3	<i>In Vitro</i> Plasma Stability Study .....	119
4.4.3.4	<i>Trans</i> -Cyclooctene (TCO) Modification of Trastuzumab .....	120
4.4.3.5	Determination of Number of Reactive TCO Groups per mAb.....	121
4.4.3.6	Radiolabeling by Tetrazine/ <i>Trans</i> -Cyclooctene Click Chemistry.....	121
4.4.4	<sup>89</sup> Zr-Anti-PD-L1 Radioimmunoconjugates .....	123
4.4.4.1	THPN-Modification of anti-PD-L1 mAb .....	123
4.4.4.2	<sup>89</sup> Zr-Labeling of THPN-anti-PD-L1 immunoconjugate.....	123
4.4.5	<sup>89</sup> Zr-Mouse Serum Albumin (MSA) Radioconjugates.....	124
4.4.5.1	THPN-Modification of MSA.....	124
4.4.5.2	<sup>89</sup> Zr-Radiolabeling of THPN-MSA.....	124
4.4.6	<sup>89</sup> Zr-HPG Radioconjugates .....	125
4.4.6.1	Chelator Conjugation to HPG-Nanoparticles .....	125
4.4.6.2	<sup>89</sup> Zr-Radiolabeling of HPG-Chelator Conjugates.....	126
4.4.6.3	<i>In Vitro</i> Plasma Stability of <sup>89</sup> Zr-HPG Conjugates .....	126
4.4.6.4	<i>In Vivo</i> Study of <sup>89</sup> Zr-HPG Conjugates .....	127
<b>Chapter 5: THPN with Other Medically Relevant Metal Ions.....</b>		<b>129</b>
5.1	Introduction .....	129
5.2	Results and Discussion.....	129
5.3	Conclusions.....	132
5.4	Experimental.....	133
5.4.1	Materials and Methods .....	133
5.4.2	Syntheses .....	133
<b>Chapter 6: Conclusions and Outlook.....</b>		<b>136</b>

References .....	140
Appendices .....	157
Appendix A: Data for Zr-THPN and <sup>89</sup> Zr-Labeling.....	157
Appendix B: PET/CT Images from <i>In Vivo</i> Study of <sup>89</sup> Zr-Chelates.....	160
Appendix C: Spectra Pertaining to Thermodynamic Solution Studies .....	161
Appendix D: Inverse Electron Demand Diels-Alder Conjugation Conjugations .....	163

## List of Tables

Table 1.1. Properties of radionuclides used for nuclear imaging by SPECT or PET, respectively.....	4
Table 1.2. Properties of selected radionuclides appropriate for radionuclide therapy.....	8
Table 3.1. Comparison of Zr–O bond lengths for different Zr-complexes. <sup>a</sup> .....	42
Table 3.2. O–Zr–O bond angles for DFT-optimized Zr-THPN structure calculated with different DFT basis sets.....	42
Table 3.3. Protonation constants of THPN. <sup>a</sup> .....	43
Table 3.4. Stability constants for the complexes formed by THPN with Fe <sup>3+</sup> and Zr <sup>4+</sup> ions, respectively at 25 °C, I = 0.16 M NaCl.....	49
Table 3.5. Comparison of pM values for Zr <sup>IV</sup> -complexes with THPN or literature chelators.....	51
Table 3.6. Distribution coefficients log <i>D</i> <sub>7.4</sub> measured for <sup>89</sup> Zr-complexes. <sup>a</sup> .....	54
Table 3.7. EDTA challenge. <sup>a</sup> .....	58
Table 3.8. Biodistribution of <sup>89</sup> Zr-THPN and <sup>89</sup> Zr-DFO after 24 h post injection. <sup>a</sup> .....	59
Table 4.1. Plasma stability of <sup>89</sup> Zr-chelate-trastuzumab radioimmunoconjugates. <sup>a</sup> .....	89
Table 4.2. <i>In vitro</i> plasma stability of <sup>89</sup> Zr-chelate-HPG radioconjugates. <sup>a</sup> .....	97
Table 4.3. Acute biodistribution data for <sup>89</sup> Zr-HPG conjugates with values expressed as %ID/g. <sup>a</sup> .....	102

## List of Figures

Figure 1.1. Working principle of SPECT, which relies on spatial detection of $\gamma$ photons that pass a collimator. ....	2
Figure 1.2. Working principle of PET, which relies on coincidence detection of annihilation photons. ....	3
Figure 1.3. A selection of diagnostic imaging agents clinically used for PET or SPECT. ....	5
Figure 1.4. Comparison of ionization effects to DNA and linear energy transfer between a) $\beta^-$ emission, b) Auger electron emission, and c) $\alpha$ emission. ....	7
Figure 1.5. A selection of therapeutic radiopharmaceuticals. ....	9
Figure 1.6. A clinical example demonstrating the huge potential of radiopharmaceuticals for therapy and diagnostic treatment monitoring. ....	10
Figure 1.7. A large number of elements possess useful radioisotopes for applications in nuclear medicine. ....	11
Figure 1.8. Schematic overview of the components of metal-based radiopharmaceuticals using a bifunctional chelate approach. ....	12
Figure 1.9. Gold-standard chelators and their bifunctional isothiocyanate derivatives that are commonly used with a range of radiometal nuclides. ....	14
Figure 1.10. A selection of conjugation strategies commonly used for the attachment of chelates (dark-green) to targeting vectors (red) ....	15
Figure 1.11. Chemical structures of selected bidentate binding units. ....	16
Figure 1.12. Chemical structures of the two hydroxypyrones maltol and ethylmaltol, which are approved food additives, and of the 3,4-HOPO deferiprone, which is an approved medication for iron chelation therapy. ....	17

Figure 1.13. Three forms of hydroxypyridinones in their neutral and zwitterionic aromatic resonance forms.....	18
Figure 1.14. A simplified nuclear decay scheme for $^{89}\text{Zr}$ .....	19
Figure 1.15. A selection of reported $\text{Zr}^{\text{IV}}$ -chelators.....	22
Figure 2.1. Retrosynthetic analysis of the intended tetrakis(hydroxypyrrone) chelator <i>p</i> -SCN-Bn-THPO reveals the building blocks from which the chelator may be assembled. ....	26
Figure 2.2. HPLC analysis over 4 days showed decomposition of compound 2.5.....	29
Figure 3.1. DFT-optimized Zr-THPN complex structures in top-down (left) and side views (right).....	41
Figure 3.2. a-c) Representative spectra of the UV-potentiometric titration of an $8.47 \times 10^{-5}$ M solution of THPN at different pH (at 25 °C, 0.16 M NaCl, <i>l</i> = 0.2 cm); d) Speciation plot for the THPN ligand .....	45
Figure 3.3. Representative spectra of the UV-Vis titrations of the $\text{Fe}^{\text{III}}$ -THPN system at increasing pH values.....	47
Figure 3.4. Metal-metal competition spectra of the $\text{Fe}^{\text{III}}$ -THPN system with increasing equivalents of $\text{Zr}^{4+}$ . ....	48
Figure 3.5. Speciation plots for a) $\text{Fe}^{\text{III}}$ -THPN complexes and b) $\text{Zr}^{\text{IV}}$ -THPN complexes calculated with stability constants from Table 3.4.....	50
Figure 3.6. UV-HPLC trace of non-radioactive Zr-THPN (top) compared with radio-HPLC trace of $^{89}\text{Zr}$ -THPN (bottom in blue).....	52
Figure 3.7. Radiochemical yield (RCY) of $^{89}\text{Zr}$ -radiolabeling over time with THPN (left) or DFO ligand (right) at different ligand concentrations .....	53

Figure 3.8. ITLC chromatograms of A) $^{89}\text{Zr}$ -THPN complex alone; B) $^{89}\text{Zr}$ -DFO complex alone; C) transchelation challenge of $^{89}\text{Zr}$ -THPN incubated with different amounts of DFO over time; D) transchelation challenge of $^{89}\text{Zr}$ -DFO incubated with different amounts of THPN over time .....	56
Figure 4.1. Retrosynthetic analysis of the intended bifunctional THPN derivative <i>p</i> -SCN-Bn-THPN reveals the building blocks from which the bifunctional chelator may be assembled. ....	74
Figure 4.2. Possible side products and by-products that can form during the amide coupling reaction between compounds 4.5 and 4.6 in addition to the desired product 4.7.....	78
Figure 4.3. Two strategies can be pursued for the conjugation and radiolabeling of a bifunctional chelator. ....	81
Figure 4.4. (Radio-)SE-HPLC chromatograms of a) THPN-, b) DFO-, and c) DFO*-modified trastuzumab before (top) and after $^{89}\text{Zr}$ -radiolabeling by postlabeling (centre and bottom).....	83
Figure 4.5. Radio-SE-HPLC chromatograms of $^{89}\text{Zr}$ -THPN-trastuzumab using improved postlabeling conditions showed less aggregates on a small scale (left), but when repeated with more $^{89}\text{Zr}$ , aggregate formation was again more pronounced (right).....	85
Figure 4.6. Analyses of $^{89}\text{Zr}$ -THPN-trastuzumab produced by a prelabeling approach (A) by radio-SE-HPLC and (B) by gel electrophoresis. ....	87
Figure 4.7. (Radio-)SE-HPLC chromatograms of a) unmodified anti-PD-L1 mAb, b) THPN-modified anti-PD-L1 mAb, and c & d) $^{89}\text{Zr}$ -THPN-anti-PD-L1. ....	90
Figure 4.8. (Radio-)SE-HPLC chromatograms of a) unmodified anti-PD-L1 mAb, b) THPN-modified anti-PD-L1 mAb, c & d) $^{89}\text{Zr}$ -THPN-anti-PD-L1.....	91

Figure 4.9. Analyses of anti-PD-L1 antibodies by SDS-PAGE.....	92
Figure 4.10. (Radio-)SE-HPLC chromatograms of unmodified MSA, THPN-modified MSA, and radiolabeled <sup>89</sup> Zr-THPN-MSA. ....	94
Figure 4.11. Analysis by SDS-PAGE (12%) of a) unmodified MSA (66 kDa), b) THPN- modified MSA, c & d) radiolabeled <sup>89</sup> Zr-THPN-MSA .....	95
Figure 4.12. (Radio-)SE-HPLC chromatograms of a) unconjugated HPG-NH <sub>2</sub> , b) HPG- chelator conjugates, and c) radiolabeled <sup>89</sup> Zr-chelate-HPGs show no difference upon conjugation and radiolabeling.....	96
Figure 4.13. Bone uptake of <sup>89</sup> Zr for the three radioconjugates measured in biodistribution studies after 1, 3, or 6 days post-injection. ....	99
Figure 4.14. Schematic representation comparing thermodynamic and kinetic effects governing the stability of a radiometal complex <i>in vivo</i> , with the dissociation rate constant <i>k</i> <sub>off</sub> being a critical factor.....	100
Figure 4.15. Maximum intensity projections of PET (left) and fused PET/CT images (right) over six days of three mice injected i.v. with either <sup>89</sup> Zr-THPN-HPG (top), <sup>89</sup> Zr- DFO-HPG (centre), or <sup>89</sup> Zr-DFO*-HPG (bottom).....	101
Figure 6.1. Suggested structures for a bi-macrocyclic cage (left) or “clam-shell” like derivative (right) of THPN.....	138
Figure 6.2. DFT-optimized structures of Zr-chelates with the proposed bi-macrocyclic cage- (left) or “clam-shell”-like chelator (right).....	138

## List of Schemes

Scheme 2.1. Synthetic route towards the intended tetrakis(hydroxypyrrone) chelator <i>p</i> -SCN-Bn-THPO. ....	26
Scheme 2.2. The two degradation products 2.3 and 2.6 formed by transesterification of intermediate 2.5. ....	28
Scheme 2.3. Proposed mechanism of ester degradation by transesterification with methanol yielding the observed fragments 2.3 and 2.6. ....	30
Scheme 3.1. Two-step synthesis of the tetrakis(3,4-HOPO) ligand THPN. ....	39
Scheme 4.1. Nine-step synthesis of the bifunctional ligand <i>p</i> -SCN-Bn-THPN, 4.10. ....	75
Scheme 4.2. Alkylation of diethyl malonate greatly depends on reaction conditions leading to addition of either one or two equivalents of nitrobenzyl. ....	76
Scheme 4.3. Modification of trastuzumab with the three chelators <i>p</i> -SCN-Bn-THPN, <i>p</i> -SCN-Phe-DFO, and <i>p</i> -SCN-Phe-DFO*. ....	82

## List of Abbreviations

~	Approximate
$\alpha$	Alpha
Å	Ångström, $10^{-10}$ m
$\beta$	Cumulative stability constant
$\beta^+$	Positron, beta plus
$\beta^-$	Beta minus
$\gamma$	Gamma ray
$\delta$	Chemical shift (NMR)
$\epsilon_\lambda$	Extinction coefficient at wavelength $\lambda$
$\lambda$	Wavelength
$\mu$	Micro ( $10^{-6}$ )
$\nu_{\max}$	Wavenumber of maximal absorption peak (IR)
$\Omega$	Ohm
AcOH	Acetic acid
AE	Auger electron
ATR	Attenuated total reflectance
avg.	Average
BC	British Columbia
Bn	Benzyl
Bq	Becquerel
br	Broadened
c	Centi ( $10^{-2}$ )
°C	Degree Celsius

calcd.	Calculated
Ci	Curie
CT	Computed Tomography
d	Day(s), doublet (NMR), diameter (DLS)
Da	Dalton
DCC	<i>N,N'</i> -Dicyclohexylcarbodiimide
DCM	Dichloromethane
DFO	Desferrioxamine B, deferoxamine
DFO*	DFO-star, <i>N</i> <sup>1</sup> -[5-(Acetylhydroxyamino)pentyl]- <i>N</i> <sup>26</sup> -(5-aminopentyl)- <i>N</i> <sup>26,5,16</sup> -trihydroxy-4,12,15,23-tetraoxo-5,11,16,22-tetraazahexacosanediamide
DFT	Density functional theory
DLS	Dynamic light scattering
DMF	<i>N,N</i> -Dimethylformamide
DMSO	Dimethyl sulfoxide
DOTA	1,4,7,10-Tetraazacyclododecane-1,4,7,10-tetraacetic acid
DTPA	Diethylenetriaminepentaacetic acid
$E_{\beta^+ \text{ max}}$	Maximal positron energy
$E_{\beta^+ \text{ mean}}$	Mean positron energy
EC	Electron capture
EDTA	Ethylenediaminetetraacetic acid
EDTMP	Ethylenediaminetetramethylenephosphonate, lexicidronam
EMA	European Medicines Agency
eq.	Equivalent
ESI	Electrospray ionization

EtOAc	Ethyl acetate
eV	Electronvolt
FA	Formic acid
FDA	U.S. Food and Drug Administration
Fmoc	9-Fluorenylmethyloxycarbonyl
FT-IR	Fourier-transform infrared spectroscopy
h	Hour(s)
HBED-CC	<i>N,N'</i> -Bis[2-hydroxy-5-(carboxyethyl)-benzyl]ethylenediamine- <i>N,N'</i> -diacetic acid
HEPES	4-(2-Hydroxyethyl)-1-piperazineethanesulfonic acid
HER2	Human epidermal growth factor receptor 2
HOBt	1-Hydroxybenzotriazole
HOPO	Hydroxypyridinone
HPG	Hyperbranched polyglycerol
HPLC	High-performance liquid chromatography
HR	High-resolution
Hz	Hertz
<i>I</i>	Ionic strength
<i>I</i> <sub>β<sup>+</sup></sub>	Positron abundance
<i>I</i> <sub>γ</sub>	Gamma emission intensity
ID	Injected dose
IEDDA	Inverse electron demand Diels-Alder
IgG	Immunoglobulin G
ITLC	Instant thin-layer chromatography

IR	Infrared
IT	Isomeric transition
IUPAC	International Union of Pure and Applied Chemistry
i.v.	Intravenous
<i>J</i>	Coupling constant (NMR)
k	Kilo ( $10^3$ )
K	Kelvin
L	Ligand
l	Path length (UV-Vis)
LC	Liquid chromatography
LET	Linear energy transfer
Ln	Lanthanide
m	Metre(s), milli ( $10^{-3}$ ), or multiplet (NMR)
M	Molarity, metal, or mega ( $10^6$ )
mAb	Monoclonal antibody
MALDI	Matrix-assisted laser desorption/ionization
MeCN	Acetonitrile
MeOH	Methanol
MIP	Maximum intensity projection
MS	Mass spectrometry
MSA	Mouse serum albumin
MW	Microwave
<i>m/z</i>	Mass-to-charge ratio (MS)
n	Nano ( $10^{-9}$ )

N	Normality
NHS	<i>N</i> -Hydroxysuccinimide
NMR	Nuclear magnetic resonance
NMWL	Nominal molecular weight limit
NSG	NOD. <i>Cg-Prkdc<sup>scid</sup>Il2rg<sup>tm1Wjl</sup>/SzJ</i>
<i>o</i>	<i>ortho</i>
<i>p</i>	<i>para</i> or probability value
p	Pico (10 <sup>-12</sup> )
PAGE	Polyacrylamide gel electrophoresis
PBS	Phosphate-buffered saline
Pd/C	Palladium on carbon
PDI	Polydispersity index
PDTA	1,3-Propanediamine- <i>N,N,N',N'</i> -tetraacetic acid
PEG	Polyethylene glycol
PET	Positron emission tomography
pH	- log [H <sub>3</sub> O <sup>+</sup> ]
Phe	Phenylene
p.i.	Post-injection
pM	- log[M <sup>n+</sup> ] <sub>free</sub> at pH 7.4 with [M <sup>n+</sup> ] = 1 μM and [L <sup>x-</sup> ] = 10 μM
ppm	Parts per million
PSMA	Prostate-specific membrane antigen
$R_{\beta^+ \text{ mean}}$	Mean positron range
RCP	Radiochemical purity
RCY	Radiochemical yield

$R_f$	Retention factor (TLC)
RP	Reversed phase
RT	Room temperature
s	Second(s), singlet (NMR)
SD	Standard deviation
SDS	Sodium dodecyl sulfate
SE	Size-exclusion
SEC	Size-exclusion chromatography
SPECT	Single-photon emission computed tomography
t	Triplet (NMR)
$t_{1/2}$	Half-life
TCO	<i>trans</i> -Cyclooctene
<i>tert</i>	Tertiary
TFA	Trifluoroacetic acid
THF	Tetrahydrofuran
THPN	2,2',2'',2'''-((Propane-1,3-diyl)bis(azanetriyl))tetrakis( <i>N</i> -((1,6-dimethyl-3-hydroxy-4-oxo-1,4-dihydropyridin-2-yl)methyl)acetamide)
TLC	Thin-layer chromatography
TOF	Time of flight
$t_R$	Retention time
Tz	1,2,4,5-Tetrazine
UBC	University of British Columbia
UV-Vis	Ultraviolet-visible

## Acknowledgements

I am extremely grateful to many people who were instrumental in bringing this work to fruition and who encouraged and supported me throughout this journey. To my supervisor Dr. Urs Häfeli, thank you for all your help and guidance, for giving me the freedom to pursue this project, and for always being available for discussions. My sincerest gratitude also to my committee members, Drs. Paul Schaffer, Chris Orvig, David Grierson, Daniel Renouf, and Brian Cairns (chair). Thank you for all your input, time, and guidance. Paul, I appreciated our many meetings that inspired and truly motivated me when I needed it most. Thank you for the thought-provoking discussions looking over raw data with me and for suggesting many plan Bs. Special thanks also to Dr. Orvig for facilitating the collaboration to investigate the solution stabilities.

To Dr. Cristina Rodríguez-Rodríguez, a big thank-you for all your help in this project, many *cafecitos*, your encouragement, and for believing in me. *Muchas gracias* also to Dr. María de Guadalupe “Lupe” Jaraquemada-Peláez for all your help and hard work with the solution studies—even after it turned out to be a tad more complicated than we had thought. To Dr. Kathy Saatchi, thank you for your help and input, and for suggesting this ligand system. Thank you Dr. Julie Rousseau, Helen Merkens, Dr. François Bénard, and the other members of the Bénard lab for your help with the smooth *in vivo* study. To Dr. Veronika Schmitt, Tullio V. Esposito, Marta Bergamo, Jenna Neufeld-Peters, Zeynab Nosrati, Lennart Bohrmann, and all other members of the Häfeli lab, thank you for helpful discussions and your help in the lab. I also acknowledge Nick Zacchia and TRIUMF’s TR13 team for producing  $^{89}\text{Zr}$ , Dr. Stoyan K. Karagiozov for starting materials, Dr. Ronan Gealageas for helpful discussions on retrosyntheses, Dr. Caterina Ramogida for help with my first  $^{89}\text{Zr}$ - and  $^{225}\text{Ac}$ -labeling experiments, and members of the Orvig lab for help with semi-prep. HPLC-purification.

I would also like to thank Drs. Roger Alberto, Felix H. Zelder, and Jochen Müller for everything you taught me about chemistry, for instilling your fascination and passion for science in me, and for encouraging me to pursue this journey.

I acknowledge financial support from the NSERC IsoSiM program as well as from UBC and generous donors through a Four-Year Doctoral Fellowship, a Mitchell-Dwivedi graduate award, a John H. McNeill scholarship, and symposium and travel awards. Computational resources are acknowledged from WestGrid and Compute Canada.

On a personal note, I would like to thank all the great friends I was fortunate to make here in Vancouver, many of whom have meanwhile moved on to conquer the world: Veronika, Jacob, and Jonathon, all of whom I was delighted to share this Ph.D. journey with, along with Shambhavi, Irene, Natalie, Meagan, Cristina, Ronan, Alice, and Bharat. Thank you all so much for helping make rough times bearable and most times phenomenal. I am also truly grateful to my friends back home, Tobi, Chäbe, Mario, Thierry, Maurice, Laura, Päsge, Dieter, Simon, Felix, and Majorie. Many thanks for your visits, *Frösspäcklis*, and ultimately, for making me feel as though it had only been a few months apart. Finally, I must express my deepest gratitude to my dear Tiffany and to my parents for all their support and love. Tiffany, thank you for your encouragement and for always being there to cheer me up. I am tremendously grateful for our love, friendship, and adventures. And to my dear parents, thank you for encouraging me to pursue my dreams and for being extremely supportive, kind, and loving throughout my life and in particular this journey. This thesis is for you and for my dear grandparents.

*Meiner Familie*

*A ma famille*

*To my family*

# Chapter 1: Introduction

The concept of using radioactivity to study biological processes or to treat disease emerged shortly after the discovery of radioactivity itself.<sup>1-3</sup> Nuclear medicine has since become an integral part in the research and clinical management of many diseases, such as cancer or cardiovascular disease. Radiopharmaceuticals are radioactive compounds that are administered to patients for the diagnosis or treatment of disease.<sup>4</sup> The radiation is emitted from inside the patient's body and is used either diagnostically for molecular imaging, therapeutically for treatment, or in a combination of the two, then referred to as a theranostic application.

## 1.1 Radiopharmaceuticals for Diagnostic Imaging

Diagnostic radiopharmaceuticals are based on radionuclides that emit penetrating radiation in the form of gamma rays ( $\gamma$ ) or annihilation photons from positron decay ( $\beta^+$ ). This radiation is then detected outside the patient by an appropriate detector. Detection of  $\gamma$  photons is achieved with gamma cameras either by planar radioscintigraphy or by the more sophisticated three-dimensional single-photon emission computed tomography (SPECT). SPECT uses a collimator and an array of detectors to register incident gamma photons of specific energies. From these data, a three-dimensional volume rendering of the radiation distribution is then reconstructed (Figure 1.1).

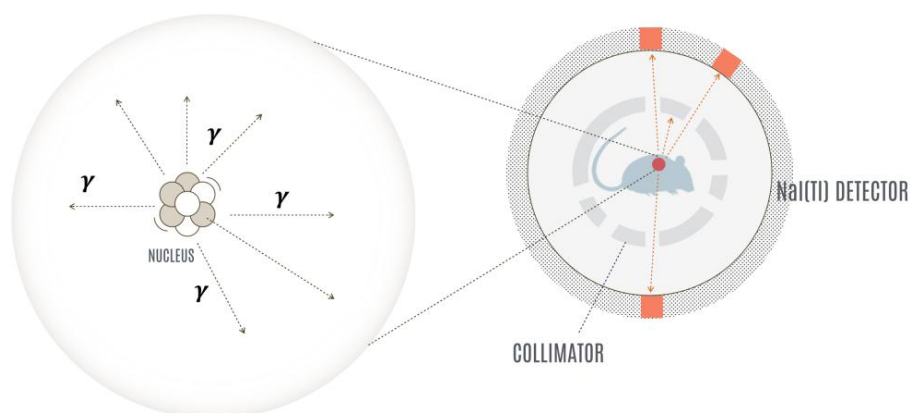


**Figure 1.1.** Working principle of SPECT, which relies on spatial detection of  $\gamma$  photons that pass a collimator. Reproduced with permission, © 2018 Dr. Cristina Rodríguez-Rodríguez.

In contrast, emission from  $\beta^+$  decay is typically detected employing positron emission tomography (PET). PET relies on the detection of annihilation photons that are the result of a  $\beta^+$  decay. Radionuclides that undergo  $\beta^+$  decay emit a positron and a neutrino. The positron (a positively charged electron) travels a short distance losing almost all of its energy, before it combines with an atomic electron from the medium in an annihilation event. In this process, two  $\gamma$  photons of 511 keV energy each are generated and emitted in opposite directions.<sup>5</sup> PET scanners use coincidence detection of these two annihilation photons by a circular array of gamma detectors. The two impinging photons allow the calculation of a line of response along which the annihilation event must have taken place. By intersecting many such lines and taking attenuation and scatter factors into account, a computer can then back calculate the origin of the decay event and thus, generate a three-dimensional volume rendering of the radiation distribution in the patient (Figure 1.2).

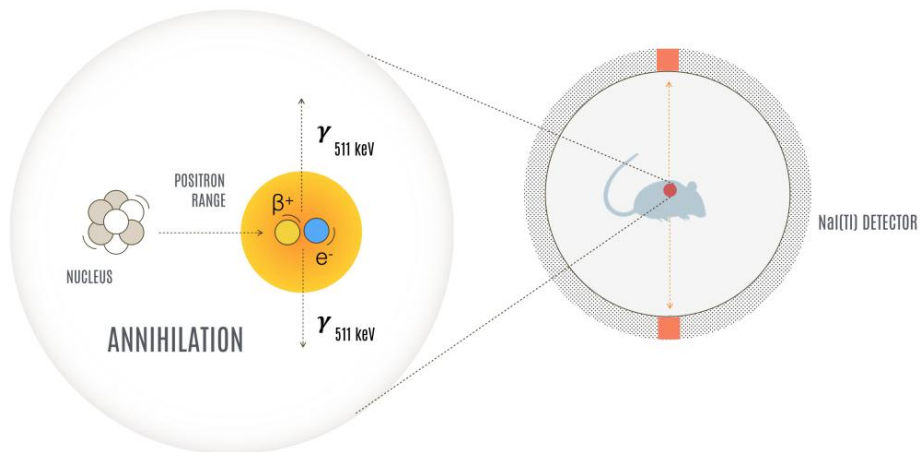


**Figure 1.2.** Working principle of PET, which relies on coincidence detection of annihilation photons. Adapted with permission, © 2018 Dr. Cristina Rodríguez-Rodríguez.

The positron energy dictates how far the  $\beta^+$  travels before it annihilates and hence directly affects the PET image resolution.<sup>6</sup> Low-energy positron emitters (*e.g.*,  $^{18}\text{F}$ ,  $E_{\beta^+ \text{ mean}} = 249.8 \text{ keV}$  (96.7%),  $R_{\beta^+ \text{ mean}} = 0.6 \text{ mm}$  in water)<sup>7, 8</sup> have lower positron range ( $R_{\beta^+}$ ) and therefore provide PET images of higher resolution than higher energetic positron emitters (*e.g.*,  $^{82}\text{Rb}$ ,  $E_{\beta^+ 1 \text{ mean}} = 1167.6 \text{ keV}$  (13.1%),  $R_{\beta^+ 1 \text{ mean}} = 5.0 \text{ mm}$  in water;  $E_{\beta^+ 2 \text{ mean}} = 1534.6 \text{ keV}$  (81.8%),  $R_{\beta^+ 2 \text{ mean}} = 7.1 \text{ mm}$  in water).<sup>7, 8</sup> In contrast to SPECT, PET uses coincident detection and therefore does not require a collimator. This results in an increased sensitivity of PET over SPECT and has secured PET recent popularity. Still, SPECT remains a powerful technique and both imaging modalities are routinely used in clinical practice.

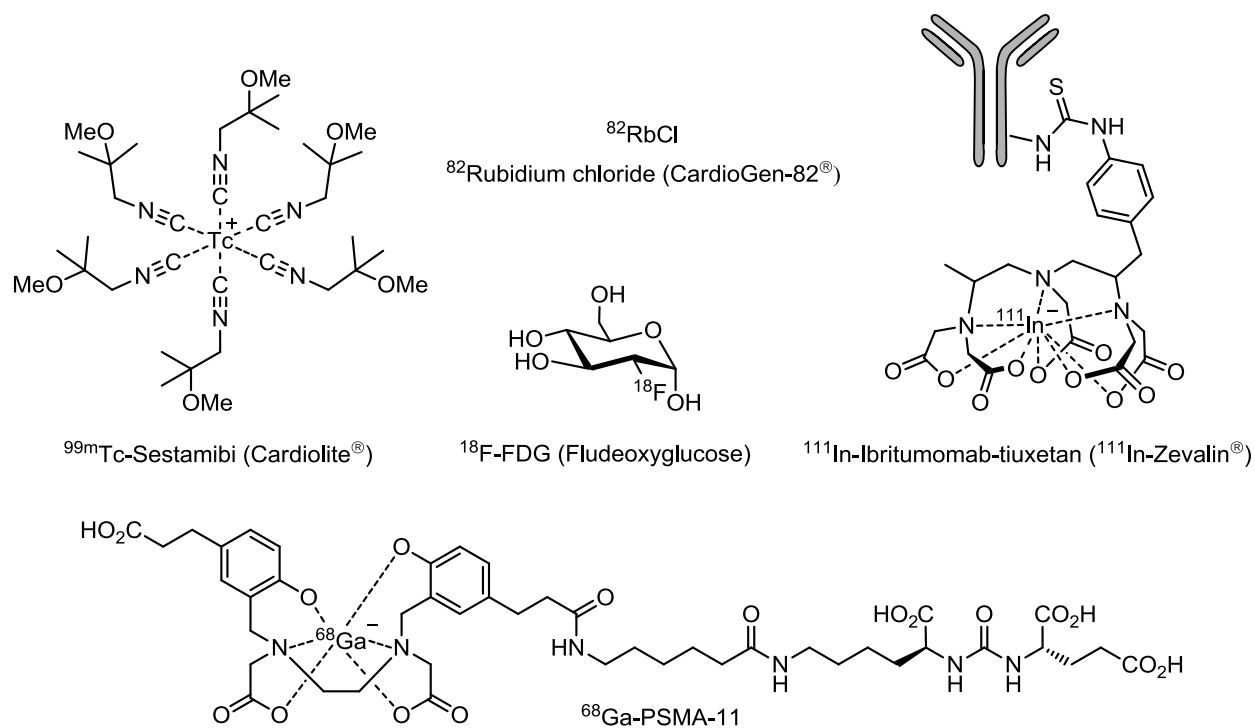
A considerable number of radionuclides can be used for SPECT or PET, respectively. While some are already in widespread clinical use, others have only recently emerged and are still being investigated for new applications. Table 1.1 gives an overview of the decay characteristics of some of the most popular clinical and preclinical imaging nuclides used in SPECT or PET, respectively.

**Table 1.1.** Properties of radionuclides used for nuclear imaging by SPECT or PET, respectively. From refs.<sup>7, 9-12</sup>

<b>SPECT nuclide</b>	<b>Half-life</b>	$E_\gamma$ [keV] (% $I_\gamma$ )	<b>Production</b>
$^{67}\text{Ga}$	78.3 h	93.3 (38.8) 184.6 (21.4) 300.2 (16.6)	Cyclotron $^{\text{nat}}\text{Zn}(p,x)^{67}\text{Ga}$ $^{68}\text{Zn}(p,2n)^{67}\text{Ga}$
$^{99\text{m}}\text{Tc}$	6.01 h	140.5 (89)	$^{99}\text{Mo}/^{99\text{m}}\text{Tc}$ Generator
$^{111}\text{In}$	67.4 h	245.4 (94.1) 171.3 (90.6)	Cyclotron $^{111}\text{Cd}(p,n)^{111\text{m,g}}\text{In}$ $^{112}\text{Cd}(p,2n)^{111\text{m,g}}\text{In}$
$^{123}\text{I}$	13.2 h	159.0 (83.3)	Cyclotron $^{124}\text{Xe}(p,2n)^{123}\text{Cs}/^{123}\text{Xe}/^{123}\text{I}$ $^{124}\text{Xe}(p,pn)^{123}\text{Xe}/^{123}\text{I}$
$^{131}\text{I}$	8.03 d	364.5 (81.5) 80.2 (2.6)	Reactor $^{131}\text{Te}(n,\gamma)^{131}\text{I}$
$^{133}\text{Xe}$	5.25 d	81.0 (36.9)	Fission $^{235}\text{U}(n,f)^{133}\text{Xe}$
$^{201}\text{Tl}$	73.1 h	167.4 (10.0) 135.3 (2.6)	Cyclotron $^{203}\text{Tl}(p,3n)^{201}\text{Pb}/^{201}\text{Tl}$

<b>PET nuclide</b>	<b>Half-life</b>	$E_{\beta^+ \text{ mean}}$ [keV] (% $I_{\beta^+}$ )	<b>Production</b>
$^{11}\text{C}$	20.4 min	385.7 (99.8)	Cyclotron $^{14}\text{N}(p,\alpha)^{11}\text{C}$
$^{13}\text{N}$	9.96 min	491.8 (99.8)	Cyclotron $^{16}\text{O}(p,\alpha)^{13}\text{N}$
$^{15}\text{O}$	122 s	735.3 (99.9)	Cyclotron $^{15}\text{N}(p,n)^{15}\text{O}$ $^{14}\text{N}(d,n)^{15}\text{O}$
$^{18}\text{F}$	110 min	249.8 (96.7)	Cyclotron $^{18}\text{O}(p,n)^{18}\text{F}$ $^{20}\text{Ne}(d,\alpha)^{18}\text{F}$
$^{68}\text{Ga}$	67.7 min	836.0 (87.7)	$^{68}\text{Ge}/^{68}\text{Ga}$ Generator
$^{82}\text{Rb}$	1.27 min	1167.6 (13.1) 1534.6 (81.8)	$^{82}\text{Sr}/^{82}\text{Rb}$ Generator
$^{89}\text{Zr}$	78.4 h	395.5 (22.7)	Cyclotron $^{89}\text{Y}(p,n)^{89}\text{Zr}$



**Figure 1.3.** A selection of diagnostic imaging agents clinically used for PET or SPECT.

Five examples of diagnostic imaging agents that are used clinically for PET or SPECT are shown in Figure 1.3. The cationic technetium-99m sestamibi complex and rubidium-82 chloride are both used for myocardial perfusion imaging by SPECT or PET, respectively.<sup>4</sup> The fluorine-18 labeled glucose analog fludeoxyglucose (FDG) is a PET tracer to image glucose metabolism and is widely applied for many conditions including diagnosis and management of cancer.<sup>4</sup> The murine anti-CD20 monoclonal antibody ibritumomab-tiuxetan (Zevalin<sup>®</sup>) can be radiolabeled with indium-111 for SPECT of non-Hodgkin's B-cell lymphoma. The antibody is modified with the DTPA chelator analog tiuxetan, which, alternatively, can be radiolabeled with the  $\beta^-$  emitter yttrium-90, which turns it into the approved radioimmunotherapy (RIT) agent for the same disease.<sup>13</sup> Currently in clinical trials, the gallium-68 PET tracer  $^{68}\text{Ga}$ -PSMA-11 has attracted much recent attention for diagnosis and therapy monitoring of recurrent prostate

cancer. The urea-based peptidomimetic is an inhibitor of prostate-specific membrane antigen (PSMA) and employs the acyclic HBED-CC chelator to coordinate radiogallium(III).<sup>14-18</sup>

## 1.2 Radiopharmaceuticals for Therapy

In contrast to diagnostic radiopharmaceuticals, which rely on nuclides that emit penetrating radiation, therapeutic radiopharmaceuticals use particulate radiation in the form of  $\alpha$ ,  $\beta^-$ , or Auger electron emission. These cytotoxic emissions greatly differ in their energies, range, and biological effects. Alpha particle emissions possess a large amount of energy, which they deposit over a very short distance of  $\sim 50\text{--}100\ \mu\text{m}$  and are therefore designated to have a high linear energy transfer (LET). Due to the short range of  $\alpha$  particles, only a few cell diameters are being passed, where the radiation induces highly cytotoxic DNA double-strand breaks (Figure 1.4). Since  $\alpha$  particles directly affect DNA, their cytotoxic effect is independent of oxygenation or active cell proliferation. This gives them a high relative biologic effectiveness (RBE) and renders them particularly promising to treat disseminated disease and micrometastases.<sup>19, 20</sup> Beta emitters deposit their energy over a relatively long range in tissue and therefore have a relatively low LET (Figure 1.4). The range of their  $\beta^-$  emission is dependent on the  $\beta^-$  energy and the cytotoxic effect is mostly achieved indirectly by generating reactive oxygen species (ROS) which damage DNA. To achieve its best effect,  $\beta^-$  emitters should concentrate inside or near a solid tumour so that crossfire and bystander effects can play together to damage surrounding malignant cells. Auger emitters have medium energy but a very low range and have therefore an intermediate LET (Figure 1.4). In order to be effective, Auger emitters have to localize in close proximity to radiosensitive cell components, such as the nucleus, or to cell membranes, which are less radiosensitive. Due to these stringent targeting requirements, only limited studies have been carried out with Auger emitters and they have not

been translated to the clinical setting yet. Still, they hold considerable therapeutic potential for specialized applications, too.<sup>21-25</sup>

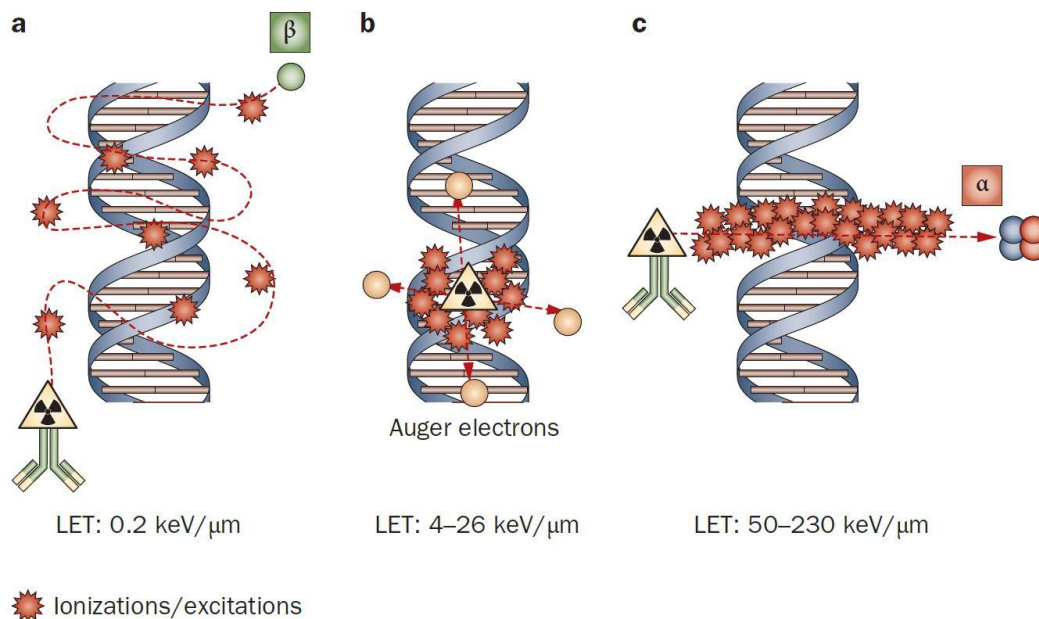


**Figure 1.4.** Comparison of ionization effects to DNA and linear energy transfer between a)  $\beta^-$  emission, b) Auger electron emission, and c)  $\alpha$  emission. Reproduced with permission from ref.<sup>26</sup> © 2011 Springer Nature.

Table 1.2 presents some radionuclides that can be used for targeted radionuclide therapy. To date, a number of radiopharmaceuticals based on  $\beta^-$  emitters gained regulatory approval but only one  $\alpha$  therapy, based on the  $\alpha$  emitter radium-223 (Xofigo<sup>®</sup>), is approved. This is bound to change in the near future as many new radiotherapeutic compounds are currently investigated in clinical trials. With new, highly specific targeting vectors becoming available and with increasing accessibility of more exotic therapeutic radionuclides, in particular the potent, underemployed  $\alpha$  particle emitters, the nuclear medicine community sees itself at the brink of an exciting new therapeutic era.<sup>20, 27-29</sup>

**Table 1.2.** Properties of selected radionuclides appropriate for radionuclide therapy. Compiled with refs.<sup>11, 22, 25,</sup>  
29-31

**$\alpha$  Emitters**

Nuclide	Half-life	Avg. $\alpha$ energy (MeV)	Avg. $\alpha$ range ( $\mu\text{m}$ )	Production
<sup>211</sup> At	7.2 h	6.79	60	Cyclotron
<sup>213</sup> Bi	45.6 min	8.32	84	Generator
<sup>223</sup> Ra	11.4 days	6.79	45	Cyclotron
<sup>225</sup> Ac	9.9 days	6.83	61	Generator
<sup>227</sup> Th	18.7 days	5.9	~60	Generator

**$\beta^-$  Emitters**

Nuclide	Half-life	Max. $\beta^-$ energy (keV)	Max. $\beta^-$ range (mm)	Production
<sup>67</sup> Cu	61.9 h	575	2.1	Cyclotron
<sup>89</sup> Sr	50.5 days	1,491	7.0	Reactor
<sup>90</sup> Y	64.1 h	2,284	11.3	Generator
<sup>131</sup> I	8.0 days	606	2.3	Reactor
<sup>153</sup> Sm	46.3 h	803	8.7	Cyclotron
<sup>166</sup> Ho	28.8 h	1,854	9.0	Reactor
<sup>177</sup> Lu	6.6 days	497	1.8	Reactor
<sup>186</sup> Re	3.7 days	1,077	4.8	Reactor
<sup>188</sup> Re	17.0 h	2,120	10.4	Generator

**Auger electron (AE) emitters**

Nuclide	Half-life	AE energy/decay (keV)	AE range	Production	# of AE/decay
<sup>67</sup> Ga	3.3 days	6.3	0.1 nm–2.7 $\mu\text{m}$	Cyclotron	4.7
<sup>111</sup> In	2.8 days	6.8	0.3 nm–14 $\mu\text{m}$	Cyclotron	14.7
<sup>125</sup> I	59.4 days	12.2	1.5 nm–14 $\mu\text{m}$	Reactor	24.9
<sup>201</sup> Tl	3.0 days	15.3	3 nm–40 $\mu\text{m}$	Cyclotron	36.9

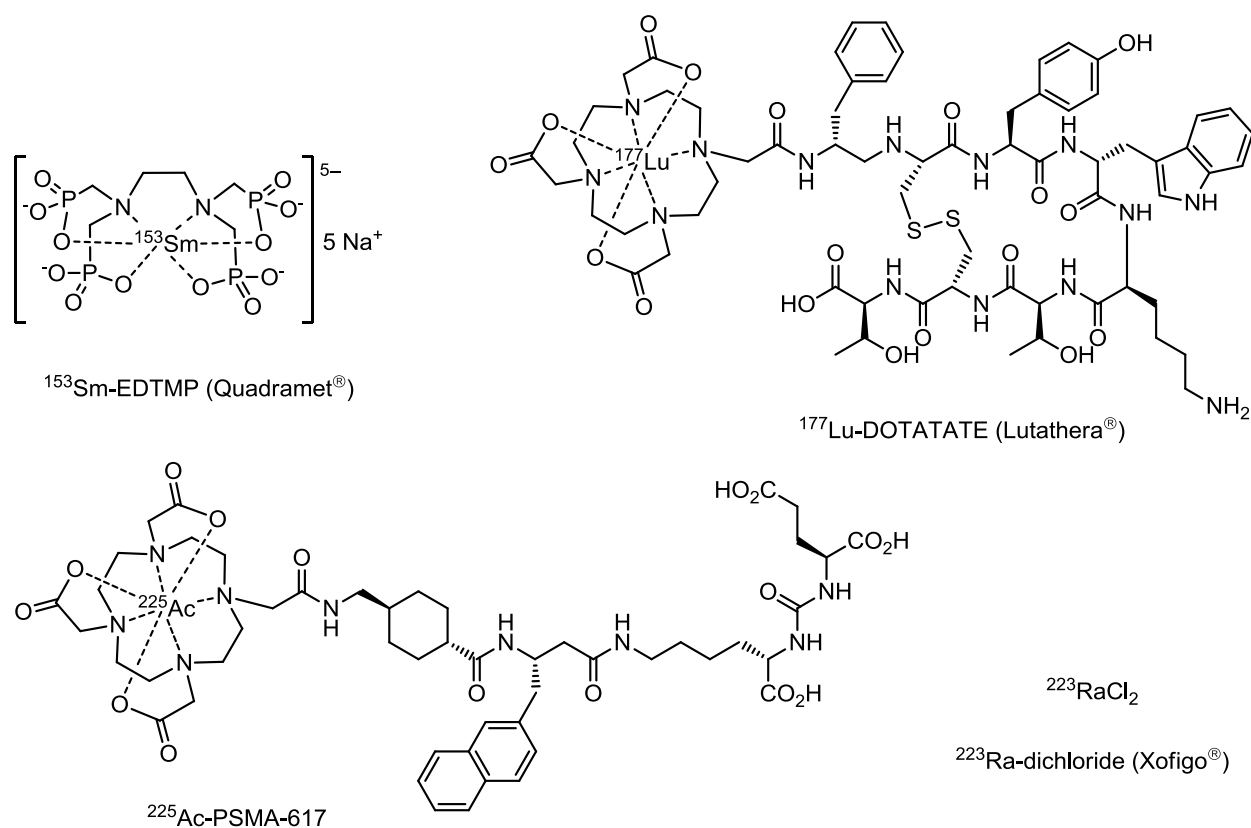


**Figure 1.5.** A selection of therapeutic radiopharmaceuticals.

Figure 1.5 shows four examples of therapeutic radiopharmaceuticals. As mentioned above, the only  $\alpha$  emitting radiopharmaceutical approved to date is based on radium-223 in form of its dichloride salt.  $^{223}\text{RaCl}_2$  (Xofigo<sup>®</sup>) is used to treat bone metastases in metastatic castration-resistant prostate cancer.<sup>20, 32</sup> The other approved therapeutic radiopharmaceuticals are all  $\beta^-$  emitters and are also employed for internal radiation therapy in oncology. Just as  $^{223}\text{RaCl}_2$ , the samarium-153 lexitronam (EDTMP) radiocomplex has bone-seeking properties and is used in palliative care of bone metastases.<sup>33</sup> Lutetium-177 labeled peptide octreotate ( $^{177}\text{Lu-DOTATATE}$ , Lutathera<sup>®</sup>) acts as somatostatin analog and was recently approved (EMA: 2017, FDA: 2018) for the treatment of neuroendocrine tumours (NETs). The peptide is closely related to octreotide, which was previously investigated for radionuclide therapy with the

higher energetic  $\beta^-$  emitter yttrium-90 ( $^{90}\text{Y}$ -DOTATOC).<sup>34-36</sup> The investigational drug  $^{225}\text{Ac}$ -PSMA-617 is an  $\alpha$ -emitting compound that is currently in clinical trials and shows very impressive results for salvage therapy of metastatic prostate cancer (*cf.*, Figure 1.6). PSMA-617 is a urea-based antagonist of prostate-specific membrane antigen (PSMA). The attached DOTA chelator was radiolabeled with the  $\alpha$  emitter actinium-225 or with the  $\beta^-$  emitter lutetium-177 and both radiotherapeutics are currently being investigated clinically.<sup>37-42</sup>

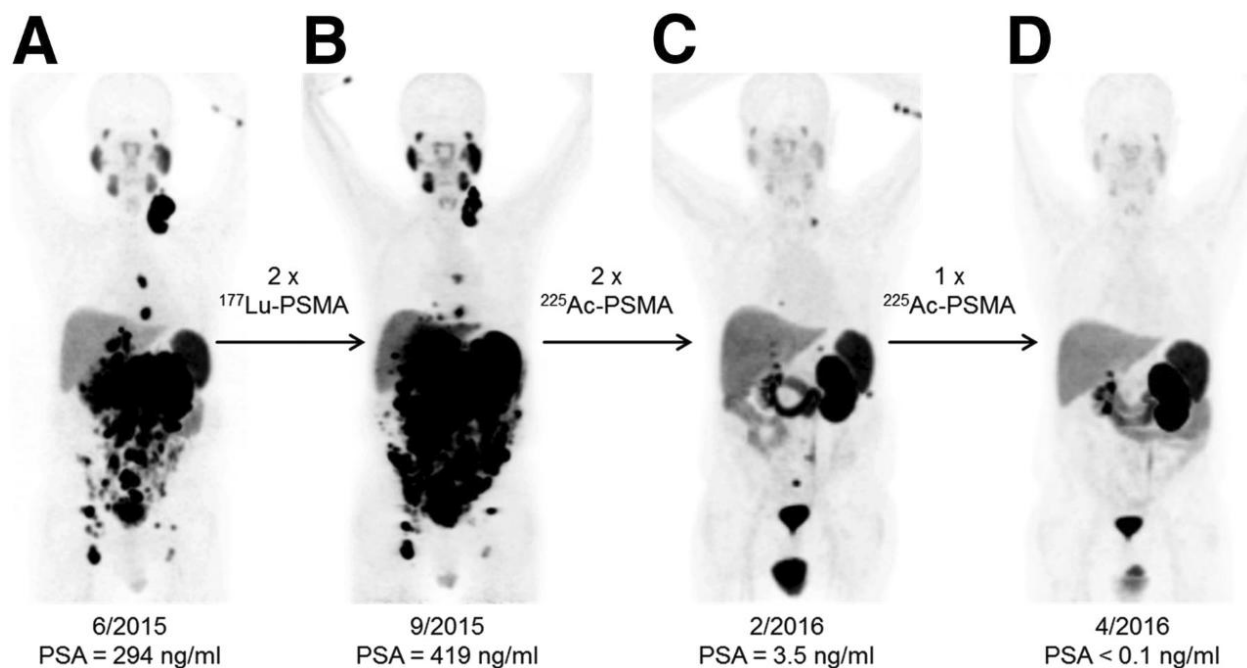


**Figure 1.6.** A clinical example demonstrating the huge potential of radiopharmaceuticals for therapy and diagnostic treatment monitoring. A) Baseline PET scan with the radiotracer  $^{68}\text{Ga}$ -PSMA-11 (*vide supra*) before targeted radionuclide therapy shows a very high disease burden with a lot of distant metastases; B) After two cycles of  $\beta^-$  therapy with  $^{177}\text{Lu}$ -PSMA-617, restaging of the same patient showed disease progression; C and D) Switching to  $\alpha$  therapy with the  $^{225}\text{Ac}$  analog  $^{225}\text{Ac}$ -PSMA-617 led to an impressive treatment response. After three cycles of  $\alpha$  therapy, levels of the biomarker prostate-specific antigen (PSA) dropped below the measurable level, corroborating the therapeutic response. PET images are shown as maximum intensity projections (MIPs). Reproduced with permission from ref.<sup>41</sup> © 2016 SNMMI.

### 1.3 Design of Metal-based Radiopharmaceuticals

When contemplating the development of a new radiopharmaceutical, a suitable radionuclide must be selected to meet the demands of the given application. Important selection criteria are decay properties such as half-life, and type and energy of emissions. Availability, the radiochemistry of a nuclide, cost, and specific activity are additional central factors to be considered.<sup>1</sup> The majority of the periodic table and of the chart of nuclides is made up of metals, thus it is not surprising that a large number of nuclides with feasible properties for nuclear medicine applications are radiometals (Figure 1.7).<sup>10, 43-46</sup>

H		■ Imaging ■ Therapy ■ Imaging & Therapy																He
Li	Be											B	C	N	O	F	Ne	
Na	Mg											Al	Si	P	S	Cl	Ar	
K	Ca	Sc	Ti	V	Cr	Mn	Fe	Co	Ni	Cu	Zn	Ga	Ge	As	Se	Br	Kr	
Rb	Sr	Y	Zr	Nb	Mo	Tc	Ru	Rh	Pd	Ag	Cd	In	Sn	Sb	Te	I	Xe	
Cs	Ba		Hf	Ta	W	Re	Os	Ir	Pt	Au	Hg	Tl	Pb	Bi	Po	At	Rn	
Fr	Ra																	
La	Ce	Pr	Nd	Pm	Sm	Eu	Gd	Tb	Dy	Ho	Er	Tm	Yb	Lu				
Ac	Th	Pa	U	Np	Pu	Am	Cm	Bk	Cf	Es	Fm	Md	No	Lr				

**Figure 1.7.** A large number of elements possess useful radioisotopes for applications in nuclear medicine. Elements with radioisotopes suitable for diagnostic imaging are shaded ochre in this periodic table, elements with therapeutic radioisotopes are shaded red, and elements that possess diagnostic and therapeutic isotopes are shaded blue. Many of the highlighted elements are metallic elements that require chelation for their use in radiopharmaceuticals. Compiled with refs.<sup>26, 47, 48</sup>

Radiometals typically require stable sequestration by a chelating agent (a chelator), with only few exceptions where the metal can simply be used as salt or colloid (*e.g.*, <sup>223</sup>RaCl<sub>2</sub> and

$^{99m}\text{Tc}$ -colloids). Robust complexation of a radiometal ion by a chelator is critical in modifying its biodistribution profile and avoiding undesired off-target distribution of the radionuclide. By means of a bifunctional chelator (BFC), a radiometal complex can be covalently tethered to carrier entities that can act as targeting vectors. Targeting vectors are often biomolecules such as antibodies, antibody-fragments, peptides, or nucleic acid oligomers. They are selected for their high affinity and specificity for features of the target site, such as overexpressed receptors on target cell surfaces. Using a bifunctional chelate approach, target-specific metallo-radiopharmaceuticals should therefore include the following components (Figure 1.8):

- (1) Radiometal nuclide: possesses desired decay properties
- (2) Bifunctional chelator: sequesters the radiometal ion by matching its coordination chemistry and provides functionality for covalent attachment to targeting vector
- (3) Linker: provides spacing between chelator and targeting vector and may tune overall polarity
- (4) Targeting vector: provides specificity and affinity for target tissue

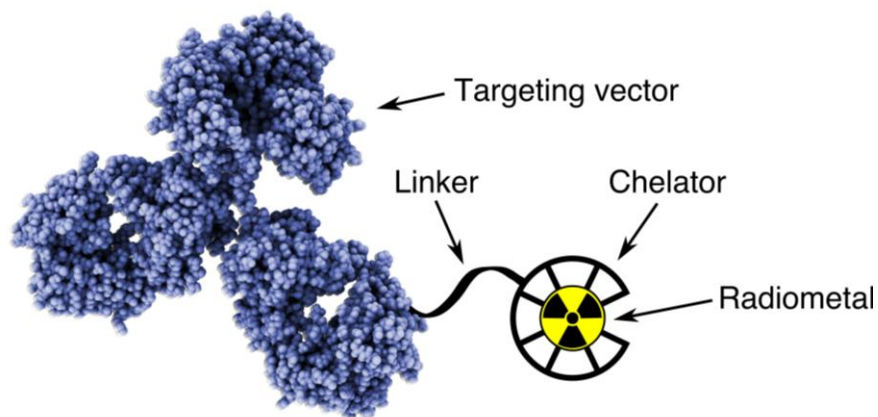


**Figure 1.8.** Schematic overview of the components of metal-based radiopharmaceuticals using a bifunctional chelate approach. (Targeting vector structure generated with QuteMol<sup>49</sup> from protein databank entry 1igy<sup>50</sup>).

The thermodynamic stability and kinetic inertness of the radiometal complex is critical for the physiologic stability of metal-based radiopharmaceuticals.<sup>1, 10, 46, 51, 52</sup> The chelator must strongly coordinate the radiometal ion to prevent chemical and/or recoil dissociation from the radiopharmaceutical. Released radionuclides would distribute away from the targeting vector and accumulate in non-target tissues. This would result in an increase in undesired background signal for imaging, and in detrimental long-term exposure of healthy tissues to radiation. The chelator must therefore be carefully crafted to best match the coordination chemistry of the radiometal ion for maximal physiologic and metabolic stability.

In the design of new chelates, the metal's chemical properties need to be taken into account. Consideration should be given to the metal's preference in valence and electronics, coordination number, relative hardness, Lewis basicity, and coordination geometry.<sup>45, 46, 51, 53</sup> The overall charge should also be taken into account as it can affect the biodistribution of metallo-radiopharmaceuticals.<sup>11</sup> To attain high thermodynamic stability, a coordinating ligand should provide donor groups that offer the metal ion its preferred coordination environment. The metal ion's coordination sphere should be fully saturated and the metal core shielded from solvent access. Increased denticity of the ligand can thermodynamically stabilize the coordination complex further by virtue of the chelate effect. Hence, it is desirable to use a polydentate ligand that ideally matches in denticity with the metal ion's maximal coordination number.<sup>54</sup> Macrocyclic chelators typically tend to provide higher kinetic inertness than acyclic chelators since they provide a higher degree of preorganization. A higher kinetic inertness is critical to prevent the coordination complex from transchelation and transmetallation under the competitive dilute conditions encountered in biological systems. Compared to acyclic chelators, this preorganization reduces the entropic penalty paid upon metal ion coordination. This so-called macrocycle effect explains for example why, even though they have comparable

thermodynamic stabilities, macrocyclic  $^{90}\text{Y}$ -DOTA is kinetically more inert and physiologically stable, than the acyclic  $^{90}\text{Y}$ -DTPA chelate.<sup>51, 52, 55</sup> On the contrary, macrocycles often require elevated reaction temperatures or prolonged reaction times to achieve radiometal chelation.<sup>56</sup> These can be important limitations in the radiolabeling of heat-sensitive targeting vectors (*e.g.*, proteins), or when working with short-lived radionuclides that mandate short reaction times.

A large number of chelators have been developed and studied with a broad range of metal ions. Figure 1.9 shows some of the most widely applied chelators with bifunctional derivatives. For certain radiometal ions these chelators have established themselves as gold-standards and are routinely used in clinical practice. For other metals ions, however, less than optimal complex stabilities are achieved and new ligands that better match the metal's coordination preference are sought. A number of excellent reviews thoroughly discuss benefits and drawbacks of pertinent chelators and provide rankings with regards to different metal ions.<sup>11, 45, 56</sup>

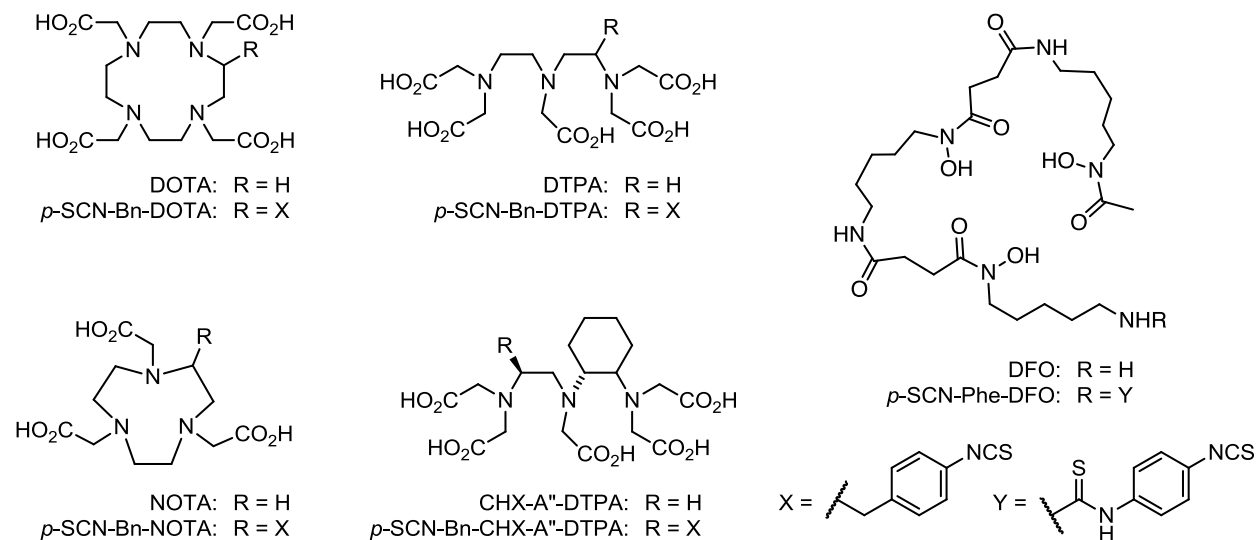


**Figure 1.9.** Gold-standard chelators and their bifunctional isothiocyanate derivatives that are commonly used with a range of radiometal nuclides.

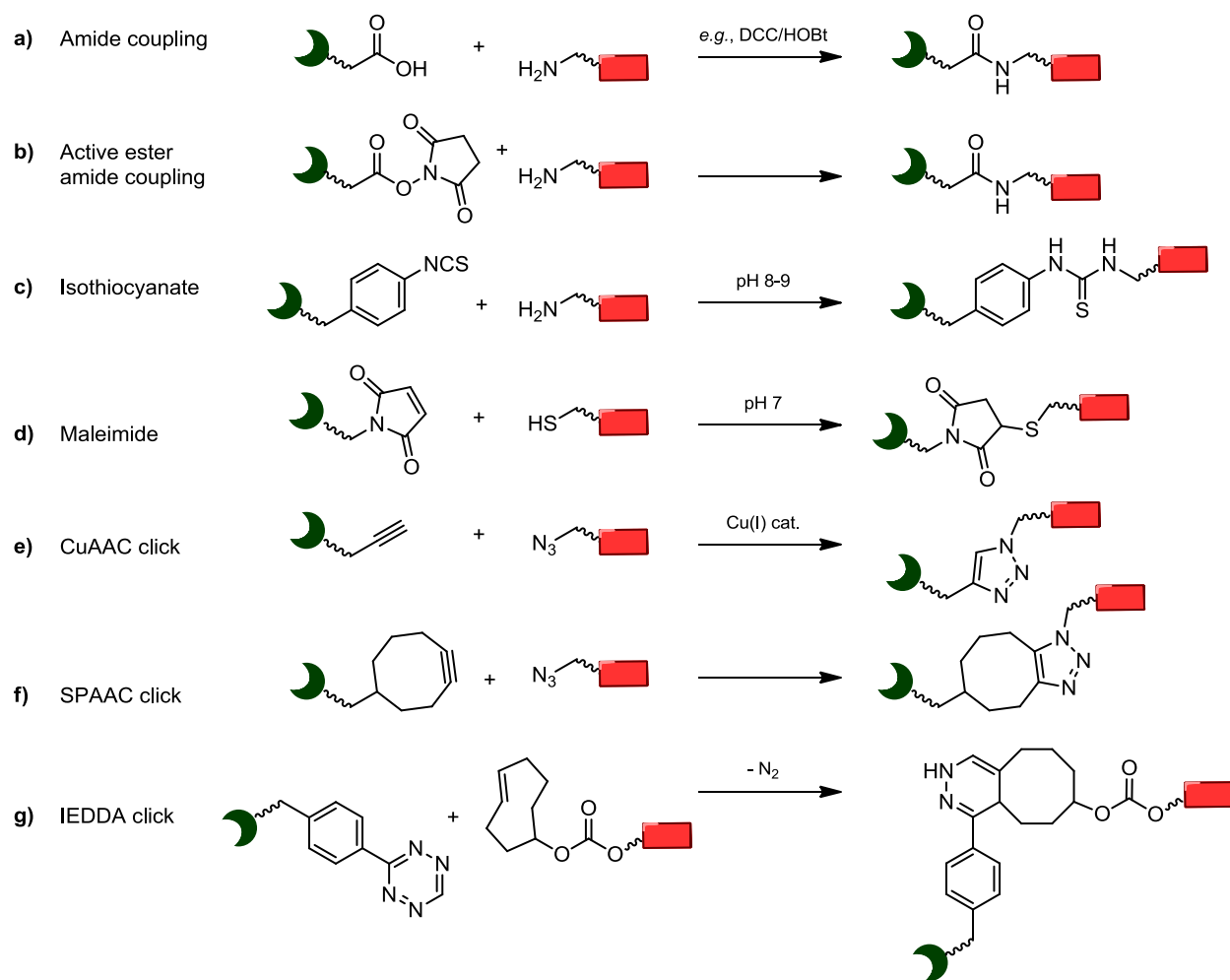


**Figure 1.10.** A selection of conjugation strategies commonly used for the attachment of chelates (dark-green) to targeting vectors (red): a) Amide coupling between a carboxylic acid and an amine with coupling reagents; b) amide coupling between an active ester and an amine; c) thiourea formation between an isothiocyanate and an amine; d) thioether formation between a maleimide and a thiol; e) copper-catalyzed azide-alkyne [3+2] cycloaddition (CuAAC) between an alkyne and an azide; f) strain-promoted azide-alkyne [3+2] cycloaddition (SPAAC) between a strained alkyne and an azide; g) inverse electron demand Diels-Alder [4+2] cycloaddition (IEDDA) between a 1,2,4,5-tetrazine (Tz) and a *trans*-cyclooctene (TCO).<sup>11, 56, 57</sup>

In order to allow covalent attachment of chelates to targeting vectors, chelators can be functionalized by introducing a reactive conjugation group.<sup>56, 57</sup> Such a chelator is then termed a bifunctional chelator (BFC) since it serves two functions: first, to stably coordinate the metal ion, and secondly, to provide a point for covalent conjugation to a targeting entity. Several different

strategies can be employed to (bio)conjugate BFCs to targeting entities, each coming with their individual requirements for reaction conditions. Figure 1.10 gives an overview of some of the most commonly used conjugation strategies that can be readily used with sensitive biomolecules.

Of particular importance in the design of new chelators is the choice of the binding units that provide the donor atoms to coordinate the metal ion. The relative hardness and basicity of the donor groups should match the electronic requirements of the metal ion. A range of binding units have been employed in the design of polydentate chelators. Some common motifs include hydroxamic acids, catechols, picolinic acids, 8-hydroxyquinolines, 2-hydroxyisophthalamides, 2,3-dihydroxyterephthalamides, hydroxypyrones, and hydroxypyridinones (Figure 1.11). With the exception of 2-hydroxyisophthalamides, these bidentate compounds all form five-membered chelate rings with metal ions. For larger metal ions, such five-membered chelate rings are generally favourable over six-membered rings.<sup>58</sup> In the following we will focus on hydroxypyridinones and hydroxypyrones, since key compounds in this work are based on these structures.

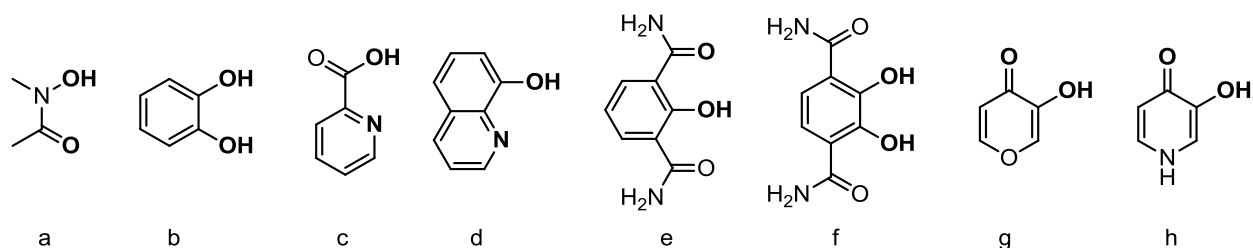


**Figure 1.11.** Chemical structures of selected bidentate binding units: (a) hydroxamic acid, (b) catechol, (c) picolinic acid, (d) 8-hydroxyquinoline, (e) 2-hydroxyisophthalamide, (f) 2,3-dihydroxyterephthalamide, (g) hydroxypyrene, and (h) hydroxypyridinone (HOPO). Donor groups are highlighted in boldface.

## 1.4 Hydroxypyridinones and Hydroxypyrones as Metal Binding Units

Hydroxypyridinones and hydroxypyrones are two classes of *N*- and *O*-heterocycles, respectively, that feature a keto- and a hydroxy-group in *ortho*-position relative to each other (Figure 1.11g, h).<sup>59</sup> Hydroxypyrones have been studied extensively and have been found to be effective chelators for various metal ions such as Al<sup>III</sup>, Fe<sup>III</sup>, V<sup>III/IV</sup>, Zn<sup>II</sup>, Ga<sup>III</sup>, and In<sup>III</sup>.<sup>59-63</sup> This compound class is considered to possess a very favourable toxicity profile as is evidenced by the two hydroxypyrones maltol and ethylmaltol (Figure 1.12) being approved as food flavouring additives.<sup>64</sup>

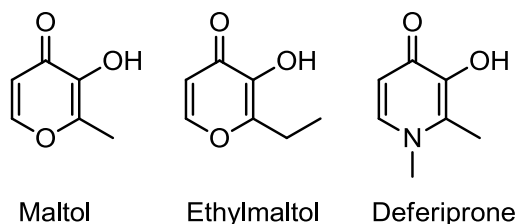


**Figure 1.12.** Chemical structures of the two hydroxypyrones maltol and ethylmaltol, which are approved food additives, and of the 3,4-HOPO deferiprone, which is an approved medication for iron chelation therapy.

Hydroxypyridinones (HOPOs) are closely related structures, which are typically synthesized from the corresponding hydroxypyrones. Depending on the position of the ring nitrogen, three forms of HOPOs can be distinguished, which are the 1-hydroxy-2-pyridinone (1,2-HOPO), the 3-hydroxy-2-pyridinone (3,2-HOPO), and the 3-hydroxy-4-pyridinone (3,4-HOPO) form (Figure 1.13). Like hydroxypyrones, HOPOs possess a partially aromatic character, which becomes evident from their zwitterionic resonance structures (Figure 1.13).

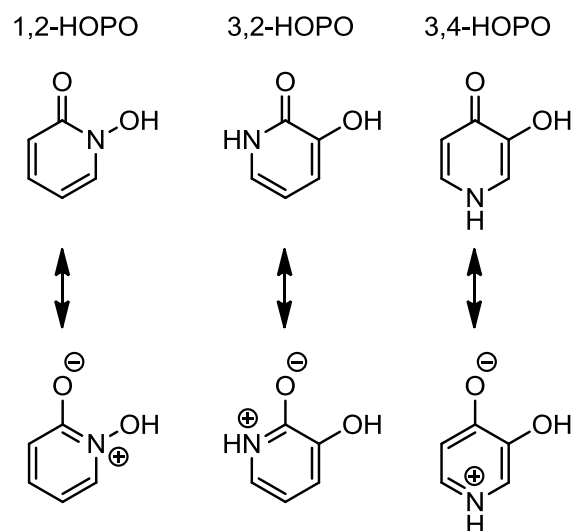


**Figure 1.13.** Three forms of hydroxypyridinones in their neutral and zwitterionic aromatic resonance forms.

HOPOs typically form even stronger metal complexes than their hydroxypyrene congeners and have therefore gained considerable attention as metal chelators.<sup>59, 65, 66</sup> The 3,4-HOPO deferiprone (Ferriprox<sup>®</sup>, Figure 1.12) is an approved treatment for iron overload from thalassemia. Mono- and poly-HOPO ligands have been studied extensively since the late 1980s and have been investigated as metal chelators for a variety of metal ions including Fe<sup>III</sup>, Al<sup>III</sup>, Ga<sup>III</sup>, Pu<sup>IV</sup>, Zr<sup>IV</sup>, Gd<sup>III</sup>, and Eu<sup>III</sup>.<sup>31, 36-44</sup> The intended medical applications of these HOPO ligands include as scavengers for chelation therapy of iron- and aluminium-overload, as actinide decorporation agents, as magnetic resonance contrast agents, as antimicrobials (by depriving microbes of Fe<sup>III</sup>), and for radiopharmaceutical applications.<sup>59, 63, 67-74</sup>

## 1.5 Zirconium-89 for PET Imaging

Among the many radionuclides that can be used for molecular imaging, zirconium-89 (<sup>89</sup>Zr) is a particularly interesting positron-emitter for PET imaging of antibodies and other long-circulating targeting vectors. Antibodies are immunoglobulin proteins with exquisite specificity and affinity for their target antigens. Besides acting as formidable targeting vectors that can

differentiate otherwise untargeted disease, many monoclonal antibodies (mAbs) are used therapeutically to trigger an immune response or to deliver cytotoxic cargo in antibody-drug conjugates (ADCs). Since such immunologic treatments are not equally effective in all patients and can lead to serious adverse effects (besides being very costly), having a non-invasive diagnostic tool available to assess whether a given patient would benefit from such an intervention is very valuable to personalize care. Antibody-based PET (immunoPET) has therefore gained much recent attention and  $^{89}\text{Zr}$  is a promising radionuclide to achieve immunoPET.<sup>75-78</sup>  $^{89}\text{Zr}$  decays with a half-life of 78.4 h by electron capture (EC, 76.2%) and positron decay (22.7%,  $E_{\beta^+ \text{ mean}}$  395.5 keV) to metastable yttrium-89m.<sup>7</sup> This short-lived nuclide ( $t_{1/2}$  15.7 s) subsequently undergoes quantitative isomeric transition (IT) to give stable  $^{89}\text{Y}$ , under emission of a 909.0 keV photon ( $I_{\gamma}$  99.2%) (Figure 1.14).<sup>7</sup> The emissions of this gamma ray, as well as conversion and Auger electrons that accompany the electron capture event do not interfere with PET imaging.<sup>54</sup>

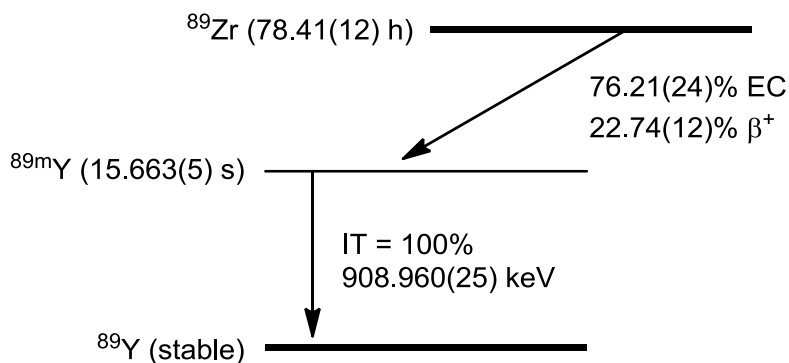


**Figure 1.14.** A simplified nuclear decay scheme for  $^{89}\text{Zr}$ . Values taken from ref.<sup>7</sup>

The relatively long half-life of  $^{89}\text{Zr}$  of over three days matches the slow pharmacokinetics of targeting vectors such as mAbs that have a long biological half-life. In addition to the matched half-life,  $^{89}\text{Zr}$ 's emitted positron is of relatively low energy compared to other long-lived radionuclides (e.g.,  $^{124}\text{I}$ ,  $t_{1/2}$  4.18 days,  $E_{\beta^+ \text{ mean}}$  687.0 keV (11.7%), 974.7 keV

(10.7%)). This low positron energy translates into favourably high PET image resolution and renders  $^{89}\text{Zr}$  a suitable radionuclide for immunoPET applications.<sup>79</sup>

$^{89}\text{Zr}$  can be readily produced in a cyclotron in a  $^{89}\text{Y}(p,n)^{89}\text{Zr}$  transmutation reaction or, less frequently, in a  $^{89}\text{Y}(d,2n)^{89}\text{Zr}$  reaction from a solid or liquid  $^{89}\text{Y}$  target, which has a 100% natural abundance.<sup>79-82</sup> Purification of the produced  $^{89}\text{Zr}$  is then most commonly achieved by weak cation exchange chromatography over a hydroxamate-functionalized resin and is eluted with 1 M oxalic acid as  $[\text{}^{89}\text{Zr}(\text{oxalate})_4]^{4-}$  in high specific activity and radionuclidic and radiochemical purity.<sup>79, 80</sup>

The +IV oxidation state dominates zirconium's aqueous chemistry, with the reduction potential to  $\text{Zr}^{\text{III}}$  being too high to be biologically relevant ( $-1.4$ – $1.5$  V *vs.* standard hydrogen electrode).<sup>54</sup>  $\text{Zr}^{\text{IV}}$  is a hard Lewis acid that prefers hard donor atoms such as oxygen donors and has a strong preference for high coordination numbers of 8–9. Its ionic radius is 84 and 89 pm when 8- and 9-coordinated, respectively.<sup>54, 56, 83</sup> Experiments in mice showed that 'free'  $^{89}\text{Zr}^{\text{IV}}$  accumulates in bone where it deposits into the hydroxyapatite matrix.<sup>84</sup> Surprisingly, in humans, bone uptake of  $^{89}\text{Zr}^{\text{IV}}$  appears to be much less pronounced; when administered as citrate the radionuclide was found to be mostly associated with blood serum proteins with a plasma half-life of around 1–2 days.<sup>83, 85</sup>

## 1.6 Reported Zirconium-89 Chelates

In order to prevent loss of the radionuclide from  $^{89}\text{Zr}$ -targeting vector conjugates, it is of great importance that the radionuclide be stably complexed and remains chelated under physiologic conditions. Among the different chelators that have been studied for  $^{89}\text{Zr}$  complexation, the bacterial siderophore desferrioxamine B (DFO, Figure 1.9) is by far the most widely employed chelator. Besides its widespread use in preclinical studies, it has also been

studied in the clinical setting. To date, no  $^{89}\text{Zr}$ -based radiopharmaceutical has gained regulatory approval, but around 22 clinical trials are currently either underway or have already been completed.<sup>78</sup> Among these clinical studies the vast majority investigate  $^{89}\text{Zr}$ -immunoconjugates that are radiolabeled with bifunctional versions of DFO. In spite of its popularity, preclinical results in mice consistently show considerable bone uptake, which suggests that  $^{89}\text{Zr}$ -DFO is not sufficiently stable *in vivo* and releases osteophilic  $^{89}\text{Zr}^{\text{IV}}$ .<sup>79, 86-92</sup> This is generally attributed to DFO's hexadentate chelation, which cannot fully saturate  $\text{Zr}^{\text{IV}}$ 's octadentate coordination preference. Computational studies by Holland *et al.*<sup>86</sup> suggest that in aqueous medium  $\text{Zr}^{\text{IV}}$ 's coordination sphere is complemented by two aquo ligands. While this octadentate complex was calculated to be thermodynamically stable, the two aquo ligands are likely kinetically labile, which may render the metal ion exposed to solvent exchange. These stability concerns have recently spurred a quest for alternative chelators that may provide improved *in vivo* stability.

Over the last around six years, a range of new chelators have been developed and investigated with  $^{89}\text{Zr}^{\text{IV}}$  and the state of the art is the subject of several recent reviews.<sup>54, 84, 93</sup> Figure 1.15 presents a selection of zirconium(IV) chelators. A coloured-coded ranking serves as an approximate indicator of chelate stability.

Drawing from DFO's success, many new ligands were designed based on similar scaffolds relying on bidentate hydroxamate functionalities. Decristoforo and co-workers<sup>94, 95</sup> reported on fusarinine C (FSC), a hexadentate macrocyclic siderophore based on three hydroxamate groups, while Boros *et al.*<sup>96</sup> studied a small library of macrocyclic ligands with three to four pendant hydroxamate groups. Rousseau *et al.*<sup>97, 98</sup> and Guérard *et al.*<sup>99</sup> developed several acyclic and macrocyclic tetrahydroxamic acid chelators. As a rational extension of DFO, Gasser, Mindt, and co-workers<sup>100</sup> elongated the siderophore ligand by an additional hydroxamate group to make the octadentate congener DFO\*, which shows particularly

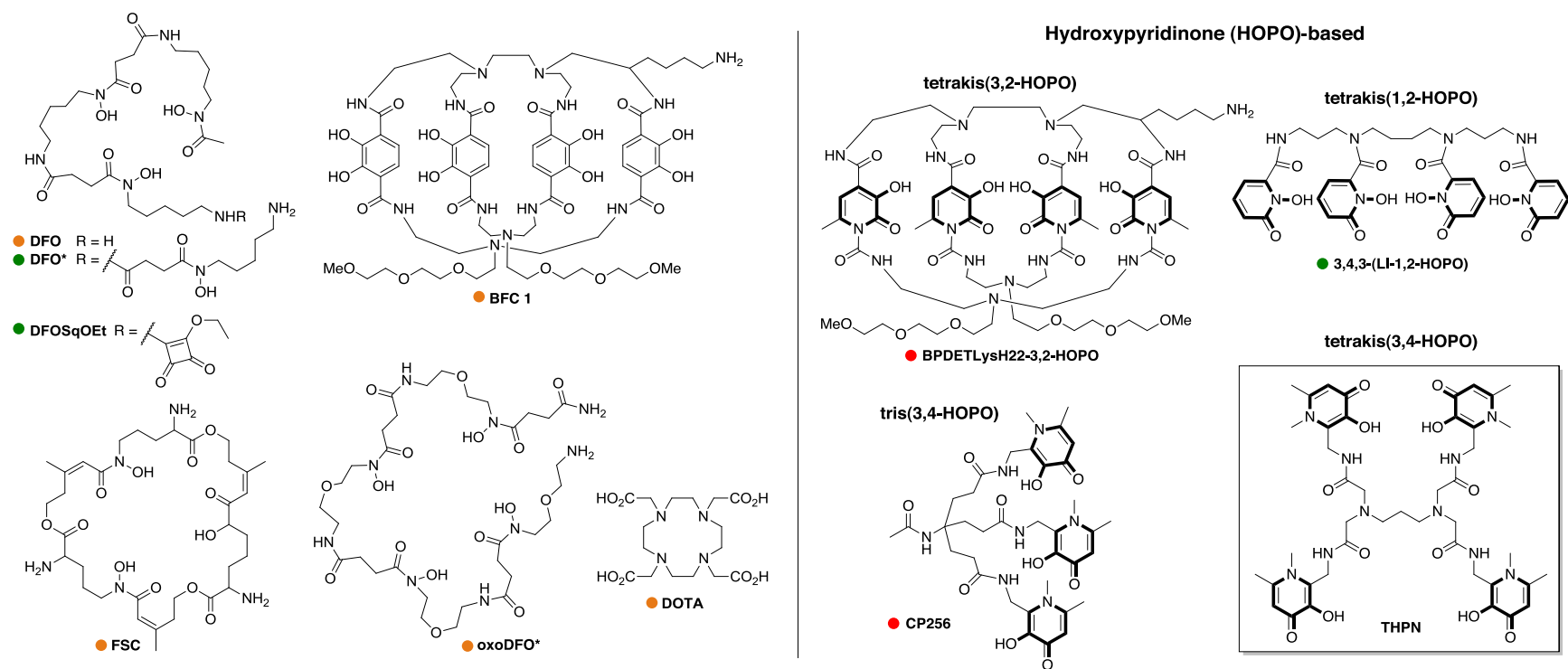


**Figure 1.15.** A selection of reported  $Zr^{IV}$ -chelators. Colour-coding indicates long-term chelate stability: green: favourable long-term stability, superior to DFO; orange: intermediate stability or unexplored long-term stability; red: poor stability.

promising stability over DFO.<sup>100, 101</sup> The same team recently improved the limited water solubility of DFO\* by introducing oxygen atoms to the backbone to produce the chelator oxoDFO\*.<sup>102</sup> Rudd *et al.*<sup>103</sup> reported on the squaramide ethyl ester derivative DFOSqOEt as a modified DFO ligand, while Allott *et al.*<sup>104</sup> extended DFO by a 1,2-HOPO group. Pandya *et al.*<sup>105</sup> have recently examined three tetraazamacrocycles as <sup>89</sup>Zr-chelators and found the widely used ligand 1,4,7,10-tetraazacyclododecane-1,4,7,10-tetraacetic acid (DOTA) to form a particularly stable <sup>89</sup>Zr-complex. Others have studied systems based on picolinic acid,<sup>106</sup> hydroxyisophthalamide,<sup>107</sup> 2,3-dihydroxyterephthalamide (TAM),<sup>108</sup> or, perhaps most relevant here, hydroxypyridinone (HOPO) groups as alternative <sup>89</sup>Zr-chelators.

The HOPO chelators that have been investigated with <sup>89</sup>Zr are based on three to four HOPO units (of either the 1,2-, the 3,2-, or the 3,4-HOPO positional isomers). Guérard *et al.*<sup>109</sup> compared Zr(HOPO)<sub>4</sub> complexes of individual HOPO ligands of either the 1,2-, the 3,2-, or the 3,4-HOPO isomers in terms of geometry, stability, and inertness. Deri *et al.*<sup>110, 111</sup> studied <sup>89</sup>Zr-complexation with the previously reported linear tetrakis(1,2-HOPO) ligand 3,4,3-(LI-1,2-HOPO), and Tinianow *et al.*<sup>112</sup> reported on the di-macrocyclic ligand BPDETLysH22-3,2-HOPO, which is based on four 3,2-HOPO units. Ma *et al.*<sup>113</sup> investigated the previously reported tripodal Ga<sup>III</sup>-ligand CP256 (and its bifunctional derivative YM103) with <sup>89</sup>Zr as an example of a poly(3,4-HOPO) ligand. In contrast to the octadentate 1,2-HOPO and 3,2-HOPO ligands, which provided promising <sup>89</sup>Zr complexes stability, <sup>89</sup>Zr-CP256 showed insufficient *in vivo* stability. This finding was attributed to the three 3,4-HOPO units, which only provide hexadentate coordination and do not satisfy the octadentate coordination preference by Zr<sup>IV</sup>.<sup>63, 113</sup> As a result of the work presented in this dissertation, we reported on the first octadentate tetrakis(3,4-HOPO) chelator THPN, which we investigated with <sup>89</sup>Zr.<sup>114</sup>

## 1.7 Dissertation Overview and Research Objectives

A range of bifunctional chelators are available for radiopharmaceutical development, however the coordination chemistry of several radionuclides is still not ideally matched or the required radiolabeling conditions are problematic with certain targeting vectors. In this work we aimed to develop alternative bifunctional chelators to expand the repertoire of chelating agents for the complexation of medically relevant metal ions, with a particular focus on new zirconium-89 chelators.

The underlying research hypothesis was therefore formulated as follows:

Bifunctional tetrapodal, octadentate ligands are suitable chelators to provide fast and stable complexation of radiometal ions and to allow their conjugation to targeting vectors for applications in nuclear medicine.

The specific research objectives were:

- (1) Synthesize and characterize a tetrapodal, octadentate ligand system and study (radio)complex formation and stability with radiopharmaceutically relevant metal ions
- (2) Develop a bifunctional derivative and investigate conjugation of the chelate to delivery vehicles
- (3) Evaluate the stability of the such formed radioconjugates both *in vitro* and *in vivo*

# Chapter 2: Efforts Towards an Octadentate Hydroxypyryone-Based Ligand System

## 2.1 Introduction

In our design of an octadentate ligand to chelate large metal ions we set out to produce a ligand based on a branched tetrapodal backbone bearing binding units on each of its four pendant arms. As binding units, we opted for bidentate 3-hydroxy-4-pyrone (discussed here) or 3,4-HOPO units (discussed in subsequent chapters) based on their favourable binding properties discussed above. Since the pyrone starting material was available earlier, we commenced with this binding unit.

## 2.2 Results and Discussion

### 2.2.1 Synthesis and Characterization

We set out to directly develop a bifunctional chelator that would bear a pendant *para*-isothiocyanatobenzyl linker group on the backbone to allow covalent attachment to amino groups of carrier molecules (*e.g.*, from lysine residues). Figure 2.1 shows the envisioned bifunctional tetrakis(3-hydroxy-4-pyrone) chelator, abbreviated as *p*-SCN-Bn-THPO. From our retrosynthetic analysis we devised a synthetic plan to produce *p*-SCN-Bn-THPO from four starting materials in seven steps. Scheme 2.1 depicts the synthetic strategy we pursued.

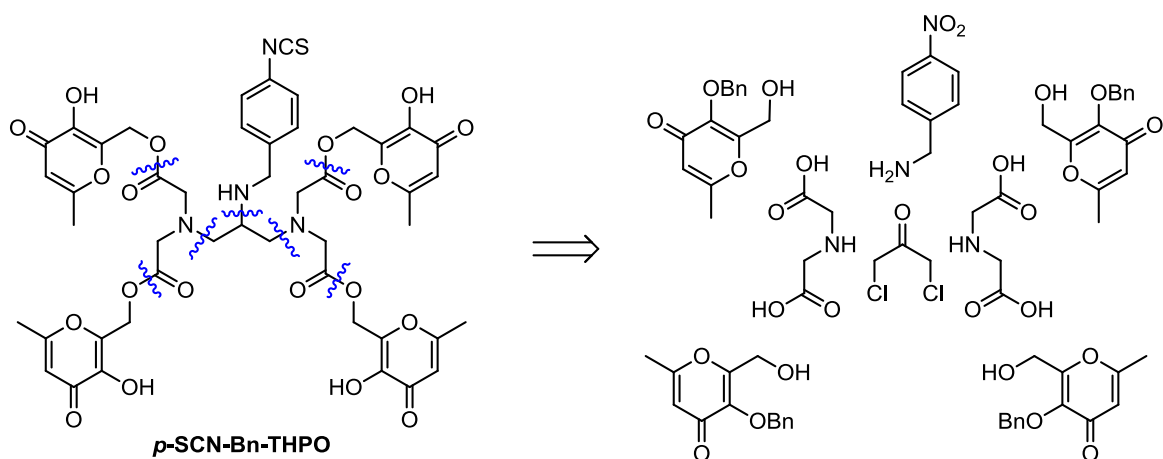
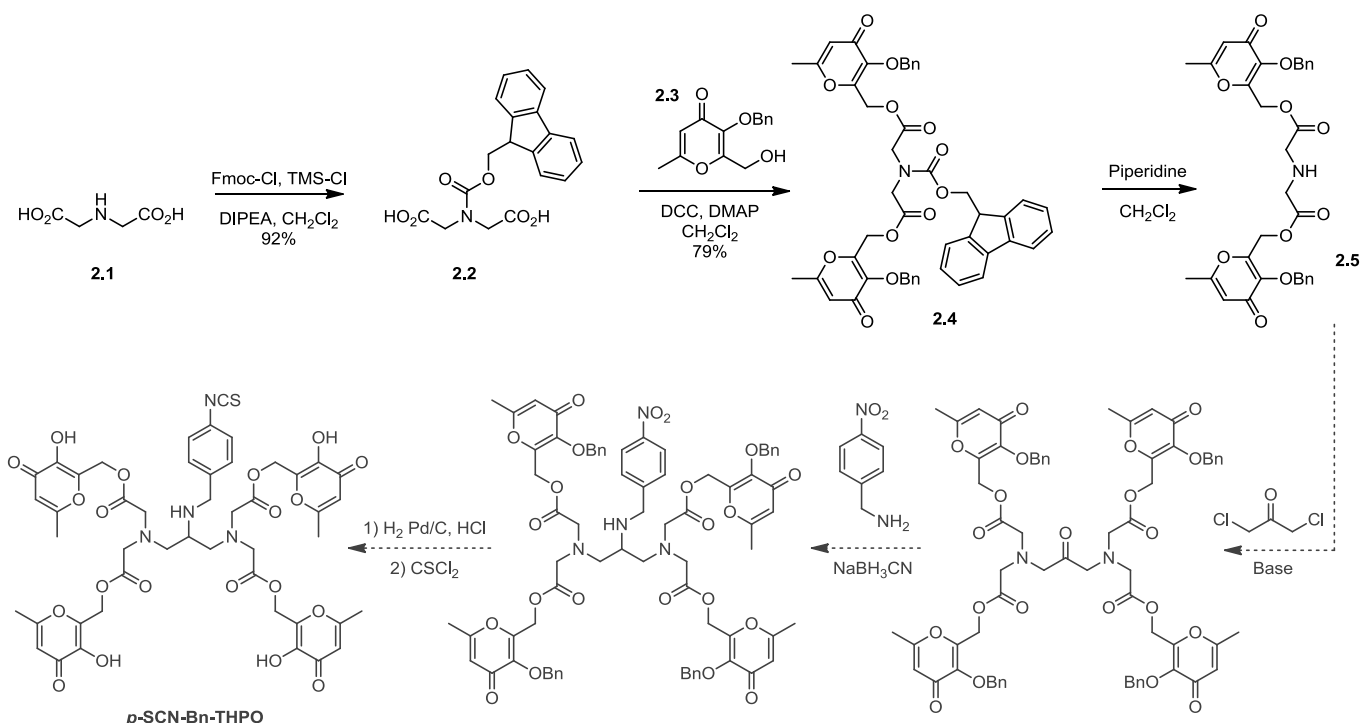


**Figure 2.1.** Retrosynthetic analysis of the intended tetrakis(hydroxypyrrone) chelator *p*-SCN-Bn-THPO reveals the building blocks from which the chelator may be assembled.



**Scheme 2.1.** Synthetic route towards the intended tetrakis(hydroxypyrrone) chelator *p*-SCN-Bn-THPO.

Starting from commercially available iminodiacetic acid (**2.1**), the secondary amine should first be Fmoc-protected before a Steglich esterification<sup>115</sup> would couple two equivalents of the benzyl-protected pyrone-alcohol **2.3**. After deprotecting the amino group, two of such obtained equivalents (**2.5**) should be amine alkylated by nucleophilic substitution to 1,3-

dichloroacetone. In the next step, the conjugation handle should be installed by reductive amination with 4-nitrobenzylamine. The last steps would involve hydrogenolysis of the benzyl protecting groups to produce the 3-hydroxy-4-pyrone moieties, as well as transformation of the nitrobenzyl to an aniline group and subsequent conversion to an activated isothiocyanatobenzyl functionality.

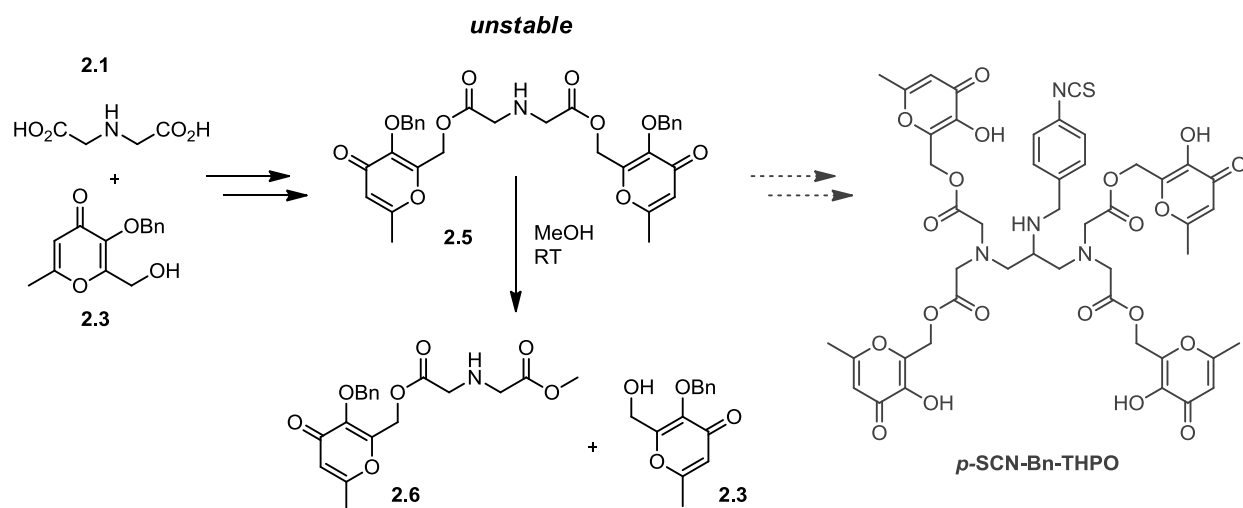
The first reaction step was reproduced from a reported procedure<sup>116</sup> and produced the Fmoc-protected intermediate **2.2** in excellent yield of 92%. The following ester coupling was relatively efficient and although two chromatographic separations were required to remove all coupling reagent residues, intermediate **2.4** could still be obtained in a yield of 79% and was fully characterized. The subsequent step involved the cleavage of the Fmoc protecting group with piperidine, which proceeded fairly quickly, as observed by HPLC. While intermediate **2.5** could be characterized, we observed that the compound was degrading during and after purification.

Acidic aqueous workup compromised product stability considerably and led to very poor isolated yields. When this workup procedure was avoided and the product was instead isolated by column chromatography, decomposition could be minimized and better yields were achieved. However, also in this case, the product was found to already having partially degraded during purification.

### **2.2.2 Ester Bond Instability**

In order to better understand this degradation behaviour, we incubated a small amount of purified intermediate **2.5** (which already contained some degradation products) in methanol and analyzed aliquots over time by HPLC (Figure 2.2). After four days at ambient temperature, the HPLC peak for compound **2.5** ( $t_R$  14.2 min) had disappeared almost completely

and two new species had emerged at earlier retention times ( $t_R$  12.5 min and 13.4 min). We separated and isolated the two degradation products by column chromatography and analyzed them by  $^1\text{H}$  NMR spectroscopy and mass spectrometry. The two isolated degradation products were identified as the pyrone alcohol **2.3** and a methyl ester **2.6**, suggesting that intermediate **2.5** underwent transesterification with methanol (Scheme 2.2).



**Scheme 2.2.** The two degradation products **2.3** and **2.6** formed by transesterification of intermediate **2.5**.

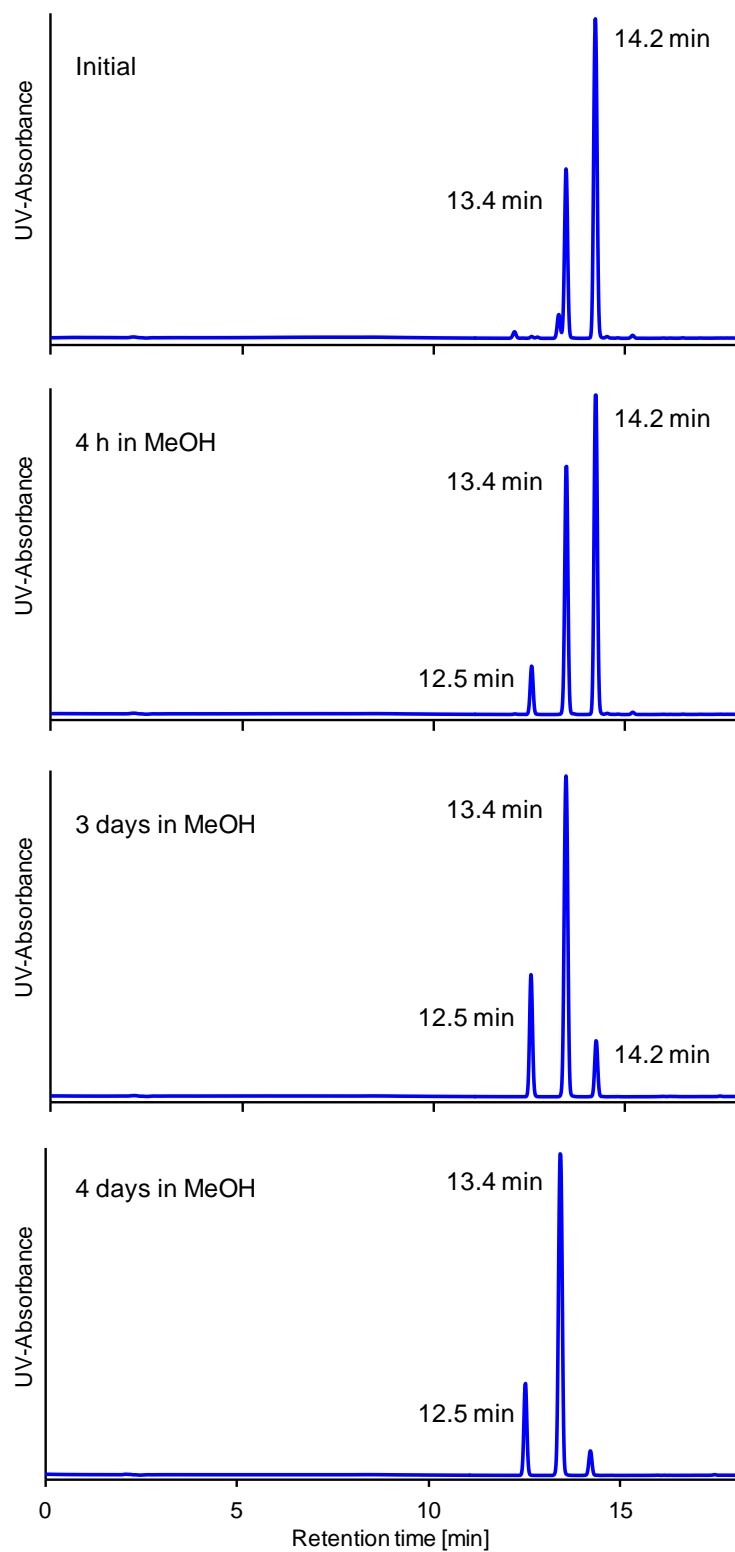
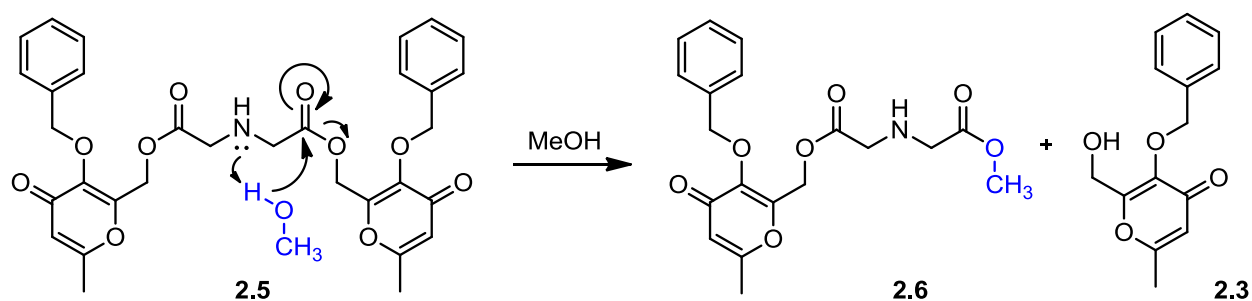


**Figure 2.2.** HPLC analysis over 4 days showed decomposition of compound 2.5 ( $t_R$  14.2 min, which already partially degraded at the beginning of the experiment) into two fragments ( $t_R$  12.5 and 13.4 min) that could be identified as compounds 2.6 and 2.3, respectively.

Although ester bonds are known to be prone to transesterification and hydrolysis, these reactions usually require the presence of catalytic amounts of acid or base in order for the reaction to proceed at a noticeable rate. A possible explanation for the accelerated reaction rate could be the presence of the free amino group after deprotection. The secondary amine could act as a Lewis base and polarize a solvent molecule (methanol) to facilitate its nucleophilic attack at the nearby ester carbonyl centre. Due to the proximity of the basic amine to the ester groups it could likely act as an intramolecular catalyst in this transesterification reaction (Scheme 2.3).



**Scheme 2.3.** Proposed mechanism of ester degradation by transesterification with methanol yielding the observed fragments **2.3** and **2.6**.

Avoiding protic solvents during purification could alleviate this problem and we indeed found the compound to remain stable for several hours when dissolved in aprotic solvents such as acetonitrile, acetone, and ethyl acetate. From a synthetic perspective it should therefore be possible to overcome this limitation by conducting subsequent synthetic steps in aprotic solvents and using anhydrous techniques. However, considering the aqueous environment in the intended biological applications, the observed instability would arguably result in a major stability liability for the target chelator. We therefore deemed it sensible to adapt our synthetic strategy and revisit our ligand design.

One potential alternative to overcome the instability of ester bonds would be to construct the chelator using amides instead. Amide bonds are known to be much more resistant to cleavage than ester bonds. We therefore chose to base our subsequent ligand design on amide bonds to provide superior stability for the binding unit-backbone linkages.

In addition to this change, we also opted to switch the 3-hydroxy-4-pyrone binding units for 3-hydroxy-4-pyridinone groups instead. The pyridinone binding units generally provide stronger metal ion complexation than the pyrone analogs do.

## 2.3 Conclusions

Our synthetic efforts towards a bifunctional tetrakis(3-hydroxy-4-pyrone) chelator based on four ester linkages (*p*-SCN-Bn-THPO) were abandoned after instability of a synthetic intermediate was observed. The ester bonds of intermediate **2.5** were found to be unstable in protic solvents. Analysis of the degradation products suggested that the compound was susceptible to transesterification reaction with methanol and hydrolysis in aqueous media. The intermediate was stable in aprotic solvents, thus the synthetic strategy could in theory still be pursued employing aprotic reaction and purification conditions. However, in view of the intended application of the target chelator in an aqueous, biologic environment, this ester bond instability was deemed a potential liability of the ligand system. This warranted the reconsideration of our ligand and synthesis design. Amide bonds were identified as potential solutions to this instability. An alternative ligand synthesis was therefore pursued which was to be designed based on amide linkages to connect the binding units to the ligand backbone. Besides this modification, 3-hydroxy-4-pyridinone groups were chosen as binding units instead of 3-hydroxy-4-pyrone groups since they generally form stronger metal complexes. The design,

synthesis, and evaluation of this modified chelator system are discussed in the following chapters.

## 2.4 Experimental

### 2.4.1 Materials and Methods

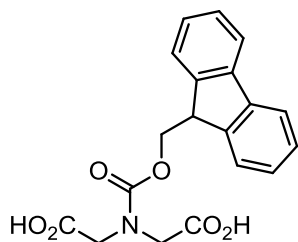
All chemicals were used as received without further purification. Building block **2.2** (2-(hydroxymethyl)-6-methyl-3-(phenylmethoxy)-4(1*H*)-pyranone) was prepared by Drs. Stoyan Karagiozov and Katayoun Saatchi according to a published procedure<sup>117</sup> with minor adjustments. Iminodiacetic acid was purchased from TCI. *N,N'*-Dicyclohexylcarbodiimide (DCC) was obtained from Acros. All other chemicals and solvents were purchased from Sigma-Aldrich. All water used was ultrapure (18.2 M $\Omega$ ·cm) and was purified with a Millipore Milli-Q Integral-10 water purification system. Parsability of chemical nomenclature was confirmed with OPSIN.<sup>118, 119</sup> NMR spectra were recorded on a Bruker Ascend 400 spectrometer (400.13 MHz for <sup>1</sup>H; 100.62 MHz for <sup>13</sup>C) at 297.16 K. Chemical shifts ( $\delta$  relative to residual solvent peak) are reported as parts per million (ppm) and coupling constants (*J*) in hertz (Hz). ESI-MS spectra were recorded on an AB Sciex QTrap 5500 mass spectrometer. High-resolution mass spectrometry (HR-MS) analysis was acquired on a Thermo Scientific Q Exactive mass spectrometer. IR spectra were recorded on a PerkinElmer Frontier FT-IR spectrometer equipped with an attenuated total reflectance (ATR) crystal. HPLC was performed on a Waters Alliance e2695 separations module coupled to a Waters 2489 UV/Vis-detector. The column was a reversed phase C18 Waters Atlantis T3, 100 Å, 5  $\mu$ m particle size (4.6  $\times$  150 mm), supported by a C18 guard cartridge and was operated in an oven (40 °C). The column was eluted with following gradient (method A): A = 0.1% trifluoroacetic acid (TFA) in water; B = methanol; flow

rate = 1 mL/min; 0–5 min 90% A; 5–15 min 10–100% B; 15–18 min 100% B. Flash chromatography was performed on a Biotage Isolera One system using Biotage SNAP KP-Sil or ZIP silica gel cartridges. Analytical thin layer chromatography (TLC) was performed using silica gel 60 F<sub>254</sub> plates with aluminium backing obtained from Merck Millipore. Silica gel for gravity column chromatography was from SiliCycle.

## 2.4.2 Syntheses

### 2.4.2.1 *N*-(9-Fluorenylmethoxycarbonyl)iminodiacetic acid (**2.2**)

This synthesis was adapted from a literature procedure.<sup>116</sup> In a dry round-bottom flask TMS-Cl (trimethylchlorosilane, 406.1  $\mu$ L, 3.2 mmol) was dropwise added to a suspension of iminodiacetic acid (**2.1**, 133.0 mg, 1 mmol) in anhydrous CH<sub>2</sub>Cl<sub>2</sub> (4 mL) and it was heated at reflux for 3.5 h. The mixture was cooled in an ice bath and DIPEA (*N,N*-diisopropylethylamine, 522.5  $\mu$ L, 3 mmol) was added dropwise, followed by addition of Fmoc-Cl (9-fluorenylmethoxycarbonyl chloride, 310.4 mg, 1.2 mmol) as a powder. The reaction was stirred for one hour at 0 °C and then overnight at ambient temperature. The reaction mixture was evaporated under reduced pressure and the residue was washed with Et<sub>2</sub>O and extracted with 10% Na<sub>2</sub>CO<sub>3</sub> (3  $\times$  20 mL). The combined aqueous phases were washed one more time with Et<sub>2</sub>O (20 mL) and then precipitated by addition of concentrated HCl at 0 °C. The precipitate was collected on paper by filtration and was dried in a desiccator to give compound **2.2** as a white powder in 92% yield (328 mg, 0.92 mmol).

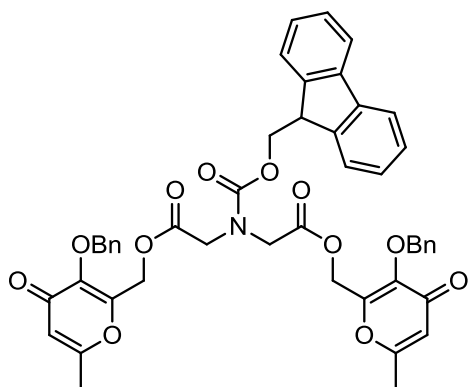


<sup>1</sup>H NMR (400 MHz, CD<sub>3</sub>OD):  $\delta$  4.11 (s, 4H, NCH<sub>2</sub>), 4.25 (t,  $J$  = 6.8 Hz, 1H, CHCH<sub>2</sub>), 4.36 (d,  $J$  = 6.8 Hz, 2H, OCH<sub>2</sub>), 7.31 (t,  $J$  = 7.4 Hz, 2H, arom.), 7.39 (t,  $J$  = 7.5 Hz, 2H, arom.), 7.61 (d,  $J$  = 7.4 Hz, 2H, arom.), 7.80 (d,  $J$  = 7.5 Hz, 2H, arom.); <sup>13</sup>C NMR (100 MHz, CD<sub>3</sub>OD):  $\delta$  173.0 (COOH),

158.0 (COON), 145.1 (arom. C), 142.6 (arom. C), 128.9 (arom. CH), 128.2 (arom. CH), 126.1 (arom. CH), 121.0 (arom. CH), 69.6 (OCH<sub>2</sub>), 50.5 (NCH<sub>2</sub>), 50.2 (NCH<sub>2</sub>), 48.2 (CH<sub>2</sub>C=CH); FT-IR (neat, ATR):  $\nu_{\max}/\text{cm}^{-1}$  1724 (s), 1696s, 1446m, 1417m, 1364s, 1266s, 1250s, 1135s, 972m; HR-ESI-MS: calcd. ( $m/z$ ) for C<sub>19</sub>H<sub>16</sub>NO<sub>6</sub><sup>-</sup> [M-H]<sup>-</sup>: 354.09831; found: 354.09851; ESI-MS ( $m/z$ ) 353.7 [M-H]<sup>-</sup>; HPLC:  $t_R$  = 15.3 min (method A).

#### 2.4.2.2 Bis((3-(benzyloxy)-6-methyl-4-oxo-4H-pyran-2-yl)methyl) 2,2' N-(9-fluorenyl methoxycarbonyl)iminodiacetate (2.4)

*N*-(9-Fluorenylmethoxycarbonyl)iminodiacetic acid (**2.2**, 177.7 mg, 0.50 mmol) and 2-(hydroxymethyl)-6-methyl-3-(phenylmethoxy)-4(1*H*)pyranone (**2.3**, 258.6 mg, 1.05 mmol) were



suspended in anhydrous CH<sub>2</sub>Cl<sub>2</sub> (3 mL) and DMAP (4-dimethylaminopyridine, 12.2 mg, 0.1 mmol) was added.

In an ice bath, DCC (*N,N'*-dicyclohexylcarbodiimide, 206.3 mg, 1.0 mmol) was added as a solid and the mixture was stirred overnight at ambient temperature.

After HPLC analysis indicated complete consumption of the starting material, the reaction mixture was filtered, rinsed with DCM, and the filtrate was washed with 0.5 M HCl (2 × 20 mL) and saturated NaHCO<sub>3</sub> (2 × 20 mL). The organic phase was dried over MgSO<sub>4</sub>, filtered, and evaporated. The resulting oil was purified by two consecutive flash chromatographic separations over silica (0–8% MeOH/DCM) and product fractions were pooled and evaporated to give the title compound **2.4** as a transparent oil in 79% yield (321 mg, 0.40 mmol).

<sup>1</sup>H NMR (400 MHz, CDCl<sub>3</sub>):  $\delta$  7.71 (d,  $J$  = 7.2 Hz, 2H, arom.), 7.47 (d,  $J$  = 7.6 Hz, 2H, arom.), 7.22–7.36 (m, 14H, arom.), 6.15 (d,  $J$  = 4.4 Hz, 2H, CHCO), 5.19 (s, 4H, OCH<sub>2</sub>Ph), 4.85 (d,  $J$

= 6.8 Hz, 4H, OCH<sub>2</sub>CO), 4.37 (d, *J* = 6.8 Hz, 2H, Fmoc-CH<sub>2</sub>), 4.18 (t, *J* = 6.6 Hz, 1H, Fmoc-CH), 4.09 (s, 2H, NCH<sub>2</sub>), 4.02 (s, 2H, NCH<sub>2</sub>), 2.17 (s, 3H, CH<sub>3</sub>), 2.09 (s, 3H, CH<sub>3</sub>). <sup>13</sup>C NMR (100 MHz, CDCl<sub>3</sub>): δ 175.4 and 175.3 (CH<sub>2</sub>C=O), 168.4 and 168.2 (C=CH<sub>2</sub>N), 164.7 and 164.6 (C=CH<sub>3</sub>), 155.4 (NOCO), 152.7 and 152.6 (OCH<sub>2</sub>C=O), 143.7 and 143.6 (COBn), 143.3 (Fmoc-C), 141.0 (Fmoc-C), 136.0 (CH<sub>2</sub>C=CH), 128.9 and 128.8 (arom. CH), 128.3 and 128.3 (arom. CH), 127.6 (arom. CH), 126.9 (arom. CH), 124.6 (arom. CH), 119.8 (arom. CH), 114.9 and 114.9 (CHCO), 73.6 and 73.6 (OCH<sub>2</sub>Ph), 68.1 (Fmoc-CH<sub>2</sub>), 58.3 and 58.2 (OCH<sub>2</sub>CO), 48.7 and 48.4 (NCH<sub>2</sub>), 46.7 (Fmoc-CH), 19.3 and 19.3 (CH<sub>3</sub>). HR-ESI-MS: calcd. (*m/z*) for C<sub>47</sub>H<sub>42</sub>NO<sub>12</sub><sup>+</sup> [M+H]<sup>+</sup>: 812.27015; found: 812.26989, calcd. (*m/z*) for C<sub>47</sub>H<sub>41</sub>NNaO<sub>12</sub><sup>+</sup> [M+Na]<sup>+</sup>: 834.25210; found: 834.25084; ESI-MS (*m/z*) 812.5 [M+H]<sup>+</sup>, 834.5 [M+Na]<sup>+</sup>; HPLC: *t*<sub>R</sub> = 17.4 min (method A).

#### 2.4.2.3 Bis((3-(benzyloxy)-6-methyl-4-oxo-4*H*-pyran-2-yl)methyl) 2,2'-iminodiacetate (2.5)

Compound 2.4 (~92 mg, 0.11 mmol) was dissolved in DCM (1 mL) and piperidine (33.6 μL, 0.34 mmol) was added at 0 °C. After stirring for 1.5 h the reaction mixture was evaporated, the residue was taken up in an EtOAc/hexane mixture and loaded on a short silica column. Impurities were washed off with EtOAc/hexane (1:1) before eluting the product with MeOH/DCM (10%). The eluate was evaporated and analyzed. Although degradation products were observed after purification, the identity and predominance of the intended product, title compound 2.5, could be confirmed.

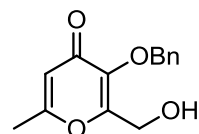
<sup>1</sup>H NMR (400 MHz, CDCl<sub>3</sub>): δ 7.34 (m, 10H, arom.), 6.19 (s, 2H, CH), 5.19 (s, 4H, CH<sub>2</sub>Ph), 4.86 (s, 4H, OCH<sub>2</sub>-pyr), 3.45 (s, 2H, NCH<sub>2</sub>), 3.41 (s, 2H, NCH<sub>2</sub>), 2.22 (s, 6H, CH<sub>3</sub>). HR-ESI-MS: calcd. (*m/z*) for C<sub>32</sub>H<sub>32</sub>NO<sub>10</sub><sup>+</sup> [M+H]<sup>+</sup>: 590.20207; found: 590.20374, calcd. (*m/z*) for

$C_{32}H_{31}NNaO_{10}^+$   $[M+Na]^+$ : 612.18402; found: 612.18384; ESI-MS ( $m/z$ ) 590.3  $[M+H]^+$ , 612.2  $[M+Na]^+$ ;  
HPLC:  $t_R$  = 14.2 min (method A).

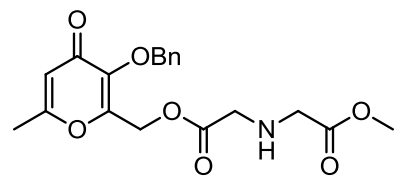
### 2.4.3 Decomposition Study

In an HPLC autosampler vial, a small amount of compound **2.5** was dissolved in MeOH (2 mL). The solution was kept at ambient temperature and the transesterification reaction was monitored over 4 days by regular HPLC injections, at which point HPLC indicated nearly all starting material had been consumed. The solution was evaporated and separated with EtOAc over a small silica gel column. Two fractions were isolated, pooled, evaporated, and analyzed.

*Fraction 1* was identified as compound **2.3** (2-(hydroxymethyl)-6-methyl-3-(phenylmethoxy)-4(1*H*)pyranone): <sup>1</sup>H NMR (400 MHz, CDCl<sub>3</sub>):  $\delta$  7.38 (s, 5H, arom.), 6.19 (s, 1H, CH), 5.22 (s, 2H, CH<sub>2</sub>Ph), 4.28 (d,  $J$  = 6.8 Hz, 2H, OCH<sub>2</sub>-pyr), 2.26 (s, 3H, CH<sub>3</sub>). ESI-MS ( $m/z$ ) 268.6  $[M+Na]^+$  (calcd. 269.1); HPLC:  $t_R$  = 13.4 min (method A).



*Fraction 2* was identified as compound **2.6** ((3-(benzyloxy)-6-methyl-4-oxo-4*H*-pyran-2-yl)methyl 2-((2-methoxy-2-oxoethyl)amino)acetate): <sup>1</sup>H NMR (400 MHz, CDCl<sub>3</sub>):  $\delta$  7.40-7.31 (m, 5H, arom.), 6.21 (s, 1H, CH), 5.22 (s, 2H, CH<sub>2</sub>Ph), 4.89 (s, 2H, OCH<sub>2</sub>-pyr), 3.74 (s, 3H, OCH<sub>3</sub>), 3.51-3.42 (m, 2H, NCH<sub>2</sub>COOMe), 3.51-3.42 (m, 2H, NCH<sub>2</sub>COOR), 2.26 (s, 3H, CCH<sub>3</sub>); ESI-MS ( $m/z$ ) 398.3  $[M+Na]^+$  (calcd. 398.1); HPLC:  $t_R$  = 12.5 min (method A).



# Chapter 3: The Octadentate Tetrakis(3-Hydroxy-4-Pyridinone) Chelator THPN for Zirconium(IV) Complexation

This chapter is, in part, an adaptation of published work, reproduced with permission from The Royal Society of Chemistry (C. Buchwalder, C. Rodríguez-Rodríguez, P. Schaffer, S. K. Karagiozov, K. Saatchi and U. O. Häfeli; *A new tetrapodal 3-hydroxy-4-pyridinone ligand for complexation of <sup>89</sup>zirconium for positron emission tomography (PET) imaging*, Dalton Transactions, **2017**, 46, 9654-9663).

## 3.1 Introduction

Zirconium-89 is an appealing radionuclide for PET with long-circulating targeting vectors (*cf.*, Section 1.5). The most widely employed chelator to complex <sup>89</sup>Zr<sup>IV</sup> is the linear hexadentate tris(hydroxamic acid) ligand desferrioxamine B (DFO). However, DFO is deemed not a perfect chelator for zirconium(IV) and alternative ligands that could provide improved *in vivo* complex stability are needed. We sought to develop a tetrapodal octadentate ligand for Zr<sup>IV</sup> complexation to potentially overcome DFO's limitations.

After the encountered stability issues in our initial synthetic efforts towards a tetrapodal 3-hydroxy-4-pyrone chelator (Chapter 2), the ligand design was revisited. In addition to replacing the ester bonds (which were prone to cleavage) by amide bonds, we took the opportunity to also exchange the four 3-hydroxy-4-pyrone groups for four 3,4-HOPO binding units. Hydroxypyridinones generally form stronger metal complexes than their hydroxypyrene analogs and we therefore selected 3,4-HOPO groups to coordinate the hard Zr<sup>IV</sup> metal ion.

Several hexadentate 3,4-HOPO ligands have been reported in the literature and have been mainly studied with iron(III) or gallium(III).<sup>63, 67, 120</sup> Only one of those tris(3,4-HOPO) chelators, CP256 (and its bifunctional derivative YM103), has also been studied with Zr<sup>IV</sup> by Blower and co-workers.<sup>113</sup> However, the hexadentate <sup>89</sup>Zr-CP256 complex suffered from considerable *in vivo* instability and readily decomposed. We were hopeful that (as also speculated by Blower *et al.*) an octadentate 3,4-HOPO chelator could provide more robust complexation of <sup>89</sup>Zr by satisfying Zr<sup>IV</sup>'s coordination preference for eight donor atoms.

The only octadentate HOPO ligands reported prior to our work were based on either four 1,2- or 3,2-HOPO groups (*cf.*, Chapter 1) and to the best of our knowledge, no octadentate 3,4-HOPO chelator had yet been reported. Before tackling the direct synthesis of a bifunctional chelator, we therefore set out to develop an octadentate 3,4-HOPO chelator. After successful synthesis and characterization of the tetrakis(3,4-HOPO) chelator we named THPN, we investigated the potential of this new chelator in depth with zirconium(IV). Contingent on strong metal ion complexation, a bifunctional derivative was synthesized (Chapter 4).

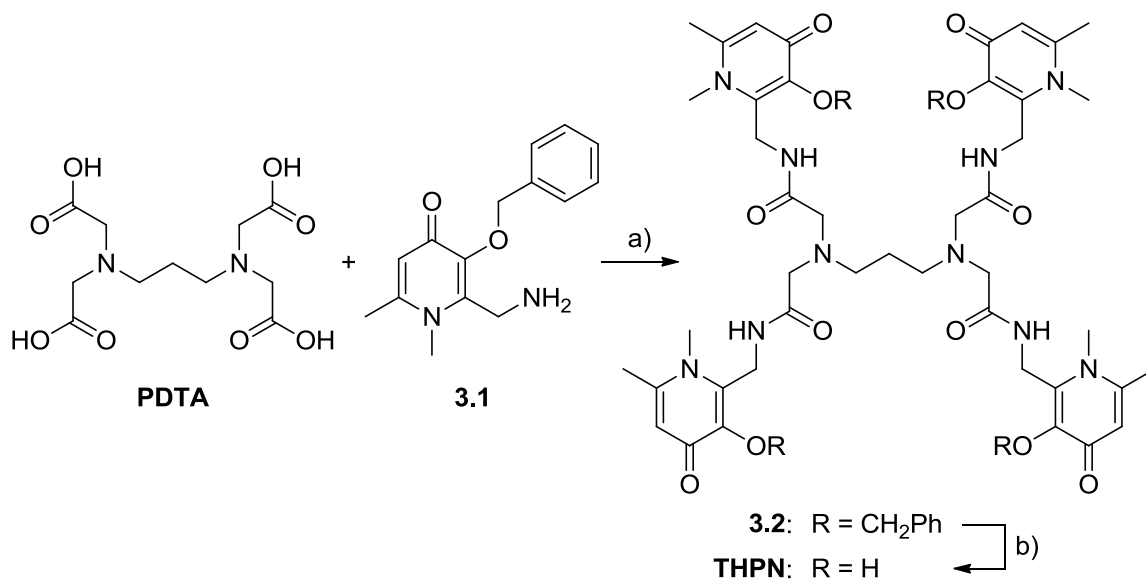
In this chapter, the synthesis and characterization of the tetrapodal ligand THPN and its Zr-THPN complex is presented along with the measurements of thermodynamic stability, radiolabeling of THPN with <sup>89</sup>Zr, and the *in vitro* stability and *in vivo* biodistribution of the <sup>89</sup>Zr-THPN complex in mice.

## 3.2 Results and Discussion

### 3.2.1 Synthesis and Characterization of THPN and Zr-THPN

The octadentate chelator THPN was designed to contain four pendant arms with 3,4-HOPO coordinating groups. The length and positioning of the linker arms *ortho* and *meta* to the

coordination groups were chosen to facilitate a monometallic coordination behaviour.<sup>121</sup> THPN was synthesized in two steps from the previously reported<sup>117</sup> building block **3.1** (2-(aminomethyl)-1,6-dimethyl-3-(phenylmethoxy)-4(1*H*)-pyridinone, Scheme 3.1). Four equivalents of this benzyl-protected 3,4-HOPO amine were conjugated to 1,3-propanediamine-*N,N,N',N'*-tetraacetic acid (PDTA) using DCC/HOBt. The coupling reaction was monitored by HPLC and reached completion after six days at ambient temperature. Inspired by a published report,<sup>122</sup> we also performed the coupling in a microwave (MW) reactor at 55 °C, which decreased the reaction time considerably and led to completion after six hours of irradiation. Subsequently, hydrogenolysis of the benzyl groups gave the unprotected tetrakis(3,4-HOPO) ligand THPN, which was purified by reversed phase chromatography and recrystallization. Using microwave conditions for the first reaction also increased the cumulative yield from ~51% to ~64% over two steps.



**Scheme 3.1.** Two-step synthesis of the tetrakis(3,4-HOPO) ligand THPN. a) DCC, HOBt, DMF, RT or MW 55 °C; b) H<sub>2</sub>, Pd/C, MeOH, RT.

Next, we produced the non-radioactive Zr-THPN complex by adding an equimolar amount of a ZrCl<sub>4</sub> solution to THPN. Formation of the monometallic complex was demonstrated by MALDI-TOF mass spectrometry, which confirmed a 1:1 metal-to-ligand ratio with characteristic Zr-isotope pattern (Appendix A, Figure A.1). Using HPLC, formation of the Zr-THPN complex was observed by a single peak, which eluted with a slight delay in retention time (34 s) compared to the ligand THPN. Notable changes were also observed in the IR spectrum, where frequencies of the HOPO groups shifted upon complexation (Appendix A, Figure A.2). <sup>1</sup>H NMR spectroscopy of the Zr-THPN complex gave broad and complex signals that were difficult to analyze. However, upon complexation signal splitting was observed for the HOPO ring protons suggesting an asymmetric constitution. This is in agreement with the slightly distorted DFT-optimized structure (*vide infra*).

### 3.2.2 Computational Studies

Since crystals suitable for X-ray diffraction analysis could unfortunately not be obtained, we conducted *ab initio* density functional theory (DFT) calculations of the Zr-THPN complex to simulate the coordination geometry around the Zr<sup>IV</sup> centre. Calculations were carried out using the Gaussian 09 suite<sup>123</sup> with the B3LYP functional<sup>124-126</sup> and two different basis sets. First, we used the LanL2DZ basis set<sup>127-130</sup> with B3LYP as these are among the most common parameters used for Zr-chelates.<sup>96, 100, 131</sup> Since Holland *et al.*<sup>131</sup> reported that for their Zr-systems the computationally more demanding basis set DGDZVP<sup>132, 133</sup> provided slightly more accurate results, we repeated our calculations using this DGDZVP/B3LYP methodology as well.

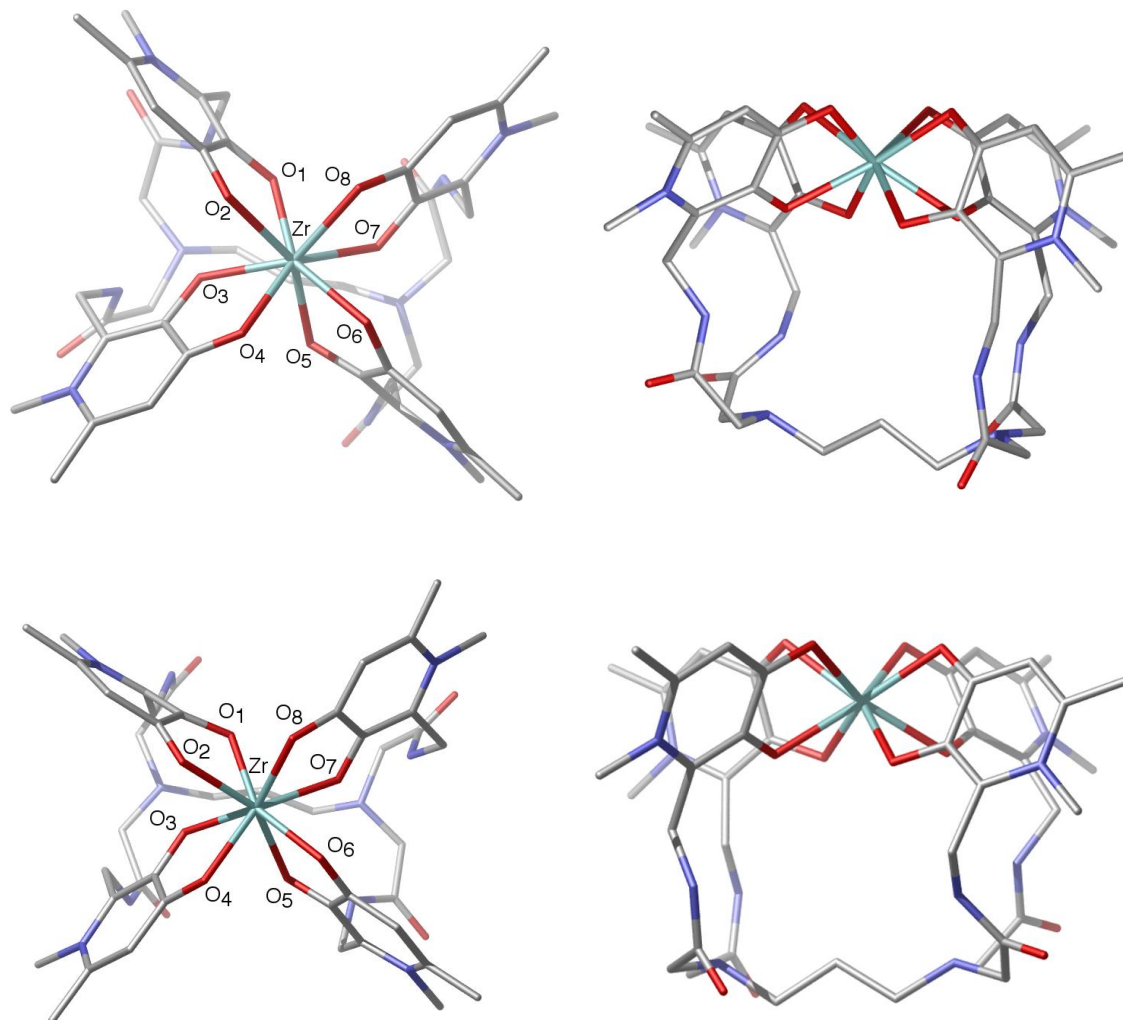


**Figure 3.1.** DFT-optimized Zr-THPN complex structures in top-down (left) and side views (right). While the structures on top were calculated with LanL2DZ/B3LYP, the bottom structures were generated using the DGDZVP/B3LYP methodology. Images were rendered in CYLview<sup>134</sup> and hydrogen atoms were omitted for clarity.

The DFT-optimized Zr-THPN structure (Figure 3.1) shows a saturated coordination sphere around the  $Zr^{4+}$  ion by the octadentate THPN ligand. The complex looks fairly symmetric and displays a square antiprismatic geometry with a slight distortion of the HOPO groups. The structures obtained with the two different DFT basis sets differ only marginally from each other (Figure 3.1). The calculated Zr–O bond lengths range between 2.18–2.29 Å using the LanL2DZ and 2.20–2.30 Å using the DGDZVP basis set. These values are comparable

to Zr–O bond lengths reported for the crystal structure of Zr-(3,4,3-(LI-1,2-HOPO)),<sup>110</sup> or the DFT-optimized structure of Zr-DFO<sup>86</sup> (Table 3.1). With both basis sets, the Zr–O bond lengths of the hydroxylic oxygen atoms (O<sub>1</sub>, O<sub>3</sub>, O<sub>5</sub>, O<sub>7</sub>) were calculated to be slightly shorter than those of the ketonic HOPO oxygen atoms. Table 3.2 compares the O–Zr–O bond angles around the Zr<sup>IV</sup> centre, which ranged between 69.8°–81.4° (LanL2DZ) and 70.2°–82.7° (DGDZVP) for Zr-THPN.

**Table 3.1.** Comparison of Zr–O bond lengths for different Zr-complexes.<sup>a</sup>

Bond	[Zr-THPN] <sup>b,c</sup>	[Zr-THPN] <sup>b,d</sup>	[Zr-DFO- <i>cis</i> (OH <sub>2</sub> ) <sub>2</sub> ] <sup>+b,e</sup>	[Zr-(3,4,3-(LI-1,2-HOPO))] <sup>f,g</sup>
Zr–O <sub>1</sub>	2.183	2.205	2.26	2.1929
Zr–O <sub>2</sub>	2.267	2.304	2.12	2.1957
Zr–O <sub>3</sub>	2.219	2.246	2.19	2.1821
Zr–O <sub>4</sub>	2.249	2.295	2.11	2.1838
Zr–O <sub>5</sub>	2.188	2.203	2.25	2.2432
Zr–O <sub>6</sub>	2.291	2.277	2.20	2.1721
Zr–O <sub>7</sub>	2.234	2.231	2.33 <sup>h</sup>	2.1981
Zr–O <sub>8</sub>	2.286	2.268	2.47 <sup>i</sup>	2.2036

<sup>a</sup> All bond lengths are given in Å; <sup>b</sup> by DFT calculations; <sup>c</sup> using basis set LanL2DZ; <sup>d</sup> using basis set DGDZVP; <sup>e</sup> from ref.<sup>86</sup>; <sup>f</sup> by X-ray crystallography; <sup>g</sup> from ref.<sup>110</sup>; <sup>h</sup> axial, and <sup>i</sup> equatorial water ligands coordinating to Zr<sup>IV</sup>.

**Table 3.2.** O–Zr–O bond angles for DFT-optimized Zr-THPN structure calculated with different DFT basis sets.

Bond angle	[Zr-THPN] <sup>a</sup>	[Zr-THPN] <sup>b</sup>	Bond angle	[Zr-THPN] <sup>a</sup>	[Zr-THPN] <sup>b</sup>
O <sub>1</sub> –Zr–O <sub>2</sub>	72.9°	72.2°	O <sub>8</sub> –Zr–O <sub>2</sub>	74.9°	70.4°
O <sub>2</sub> –Zr–O <sub>3</sub>	76.1°	80.6°	O <sub>8</sub> –Zr–O <sub>1</sub>	80.7°	82.7°
O <sub>3</sub> –Zr–O <sub>4</sub>	71.9°	70.8°	O <sub>1</sub> –Zr–O <sub>3</sub>	73.5°	70.2°
O <sub>4</sub> –Zr–O <sub>5</sub>	81.4°	82.1°	O <sub>3</sub> –Zr–O <sub>5</sub>	78.1°	74.1°
O <sub>5</sub> –Zr–O <sub>6</sub>	72.6°	72.7°	O <sub>5</sub> –Zr–O <sub>7</sub>	69.8°	73.8°
O <sub>6</sub> –Zr–O <sub>7</sub>	78.7°	77.9°	O <sub>7</sub> –Zr–O <sub>1</sub>	74.2°	77.8°
O <sub>7</sub> –Zr–O <sub>8</sub>	70.8°	71.7°	O <sub>2</sub> –Zr–O <sub>4</sub>	79.1°	75.2°
O <sub>6</sub> –Zr–O <sub>8</sub>	76.1°	77.9°	O <sub>4</sub> –Zr–O <sub>6</sub>	71.1°	74.5°

<sup>a</sup> Calculated using LanL2DZ/B3LYP; <sup>b</sup> calculated using DGDZVP/B3LYP methodology

### 3.2.3 Thermodynamic Solution Studies

In order to quantify the thermodynamic stability of the Zr-THPN complex, we investigated the THPN ligand and its Zr-complex formation in several thermodynamic solution studies.

#### 3.2.3.1 THPN Ligand Protonation Constants

Since the Zr<sup>IV</sup>-affinity of the THPN ligand, and in particular of the HOPO groups, depends on the acid-base properties, the protonation equilibria of the THPN ligand were first determined by combined spectrophotometric-potentiometric titrations in aqueous solution. The UV-potentiometric titrations of an acidic THPN solution ( $8.47 \times 10^{-5}$  M) were carried out in the pH range 1.6–11.5 by addition of standardized NaOH and measured at 25 °C,  $I = 0.16$  M NaCl. Analysis of the combined potentiometric-spectrophotometric data with the software HypSpec2014<sup>135</sup> allowed us to determine all ten protonation constants of THPN (Table 3.3) and generate the corresponding speciation plot (Figure 3.2d).

**Table 3.3.** Protonation constants of THPN.<sup>a</sup>

<b>Equilibrium reaction</b>	<b>log <math>\beta</math></b>	<b>log <math>K</math></b>
L + H <sup>+</sup> $\rightleftharpoons$ HL	10.28(2)	10.28
HL + H <sup>+</sup> $\rightleftharpoons$ H <sub>2</sub> L	20.11(2)	9.83
H <sub>2</sub> L + H <sup>+</sup> $\rightleftharpoons$ H <sub>3</sub> L	29.41(2)	9.30
H <sub>3</sub> L + H <sup>+</sup> $\rightleftharpoons$ H <sub>4</sub> L	38.12(2)	8.71
H <sub>4</sub> L + H <sup>+</sup> $\rightleftharpoons$ H <sub>5</sub> L	42.43(3)	4.31
H <sub>5</sub> L + H <sup>+</sup> $\rightleftharpoons$ H <sub>6</sub> L	46.14(3)	3.71
H <sub>6</sub> L + H <sup>+</sup> $\rightleftharpoons$ H <sub>7</sub> L	49.35(2)	3.21
H <sub>7</sub> L + H <sup>+</sup> $\rightleftharpoons$ H <sub>8</sub> L	52.49(2)	3.14
H <sub>8</sub> L + H <sup>+</sup> $\rightleftharpoons$ H <sub>9</sub> L	54.97(1)	2.48
H <sub>9</sub> L + H <sup>+</sup> $\rightleftharpoons$ H <sub>10</sub> L	56.77(2)	1.80

<sup>a</sup> Determined by simultaneous UV-potentiometric titrations at 25 °C,  $I = 0.16$  M NaCl. Charges are omitted for clarity.

The speciation plot shows that at a physiologic pH of 7.4, THPN predominantly exists in its neutral form  $H_4$ THPN. From the analysis of the spectra, two different buffer regions could be distinguished between pH 1.6–6 and pH 6–11, which are characterized by spectral evolutions marked by the appearance of different isosbestic points. Six protonation constants could be calculated from spectra in the pH range 1.6–6 (Figure 3.2a-b). Comparison with similar spectroscopic features of reported HOPO analogues<sup>136-140</sup> allowed to attribute these constants to the protonations of the 4-oxo groups in the HOPO rings and to the protonations of the tertiary amines of the backbone. The highest protonation value in this buffer region ( $\log K = 4.31(3)$ ), could be attributed to one of the tertiary amines, while the other tertiary amine was assigned the most acidic protonation constant,  $\log K = 1.80(2)$ . This difference in acidity between the two amines can be explained by electronic repulsion between the two protonated amines as well as the possibility for stabilization of the protonated amine by hydrogen bonding with a neighbouring amide carbonyl. The remaining four protonation constants in this region ( $\log K = 2.48, 3.14, 3.21, 3.71$ ) were assigned to the protonations of the 4-oxo groups of the four HOPO moieties.

In the first dissociation equilibrium, there are two bands present at  $\lambda_{\max} = 247$  and 282 nm, and two isosbestic points at 221 and 240 nm (Figure 3.2a). The spectroscopic features for the five successive equilibria are characterized by a decrease of the band at 247 nm, the increase of the band at 282 nm, and the appearance of a new band at 225 nm, as well as three new isosbestic points at 219, 236, and 255 nm, respectively (Figure 3.2b). The second buffer region between pH 6–11 (Figure 3.2c), presents the spectroscopic evolutions for the four equilibria involving the hydroxy functionalities in the HOPO units. The spectrum at pH 5.60 presents two maxima at 221 and 282 nm (Figure 3.2c). Upon increasing the pH, these bands shift to higher wavelengths and new bands appear at 230 and 312 nm with the occurrence of three

new isosbestic points at 225, 250, and 295 nm, confirming the presence of different species in this pH interval.

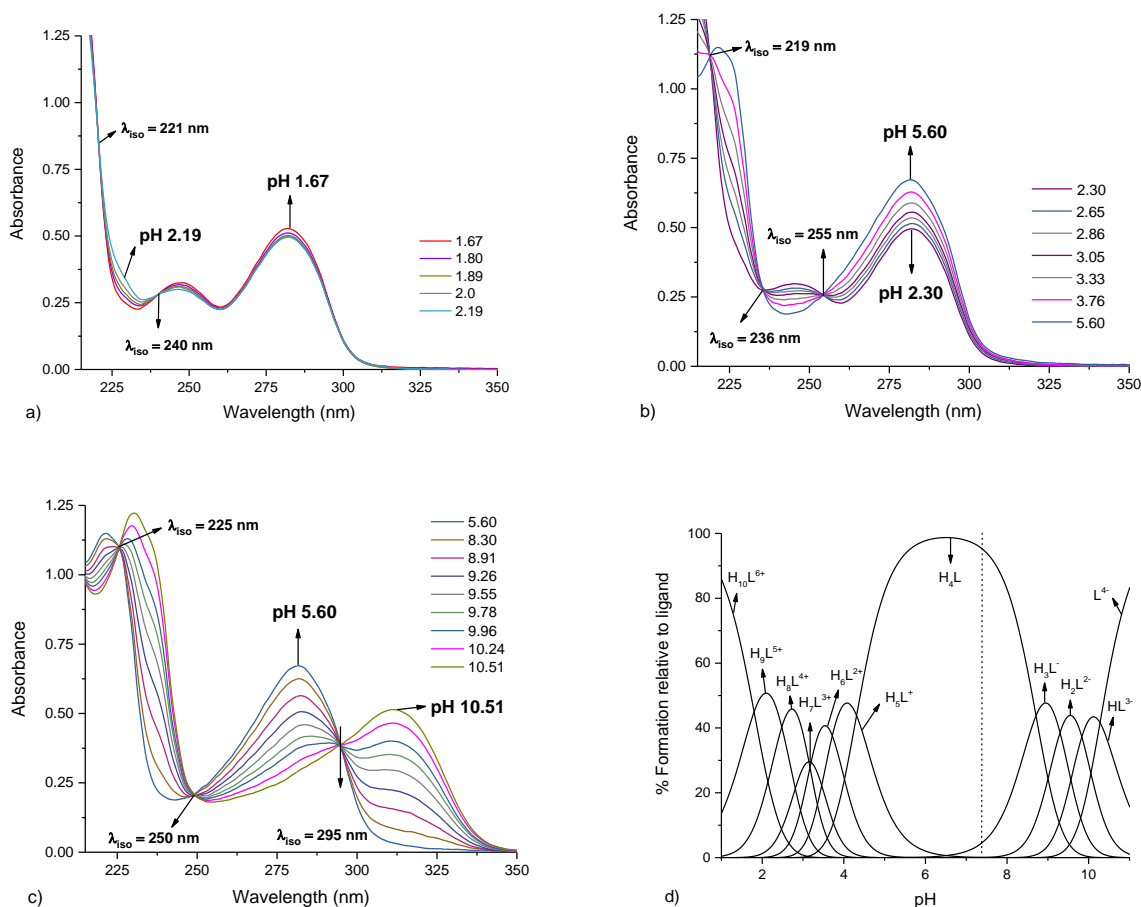


**Figure 3.2.** a-c) Representative spectra of the UV-potentiometric titration of an  $8.47 \times 10^{-5}$  M solution of THPN at different pH (at 25 °C, 0.16 M NaCl,  $l = 0.2$  cm); d) Speciation plot for the THPN ligand calculated with protonation constants in Table 3.3,  $[THPN] = 8.47 \times 10^{-5}$  M; dashed line represents pH = 7.4.

### 3.2.3.2 Complex Formation Equilibria with $Fe^{3+}$ and $Zr^{4+}$

The strength of the metal complexes formed between THPN and  $Zr^{4+}$  made it necessary to employ a combination of different methods. Attempts to directly determine the  $Zr^{IV}$ -THPN stability constants by proton competition experiments were not conclusive by

themselves as Zr<sup>IV</sup>-complexation was completed immediately after addition of the Zr<sup>4+</sup> solution and the complex formation could not be reversed even at the most acidic pH studied. As an alternative, we therefore first determined the stability constants of the Fe<sup>III</sup>-THPN system and then conducted an Fe<sup>III</sup>-Zr<sup>IV</sup> metal-metal competition experiment. From combining these results the Zr<sup>IV</sup>-THPN stability constants could then be determined indirectly.

The Fe<sup>III</sup>-THPN formation constants were determined by direct UV-Vis batch proton competitions, as well as by direct simultaneous potentiometric-spectrophotometric titrations. Figure 3.3 shows representative spectra from the batch titration of the Fe<sup>III</sup>-THPN system as the pH was raised. From pH 0.16–1.47 a new band emerges centered at 510 nm (Figure 3.3b), which is characteristic of red coloured Fe<sup>III</sup>-HOPO complexes and indicates the formation of the [Fe<sup>III</sup>(H<sub>2</sub>THPN)]<sup>+</sup> complex from the colourless [Fe<sup>III</sup>(OH<sub>2</sub>)<sub>6</sub>]<sup>3+</sup> in solution. In the pH range 1.47–3.26, a new band appears at 458 nm and two isosbestic points are observed at 360 and 503 nm, which indicate two species in equilibrium (Figure 3.3a,c). This is attributed to the deprotonation of a hydroxy group from one HOPO unit (pK<sub>a</sub> = 2.01), which leads to the formation of the fully coordinated Fe<sup>III</sup>-complex [Fe<sup>III</sup>(H<sub>3</sub>THPN)]. In fact, the last hydroxy substituent deprotonates with pK<sub>a</sub> = 8.23 to form the negatively charged [Fe(THPN)]<sup>-</sup> species, for which the spectrum remains unchanged because the last HOPO unit is not involved in the coordination sphere (Appendix C, Figure C.1). The Fe<sup>III</sup>-complex formation by THPN is further confirmed by a red shift of the free protonated ligand from 282 nm to 290 nm as the pH is raised from 0.16 to 3.26 (Figure 3.3d). The spectroscopic features in the formation of the Fe<sup>III</sup>-THPN complexes evolve similarly to those of the clinically used iron chelator deferiprone and other reported deferiprone analogs in the formation of their 1:1, 1:2, and 1:3 metal-to-ligand complexes.<sup>138-140</sup> Table 3.4 presents the stability constants determined for the Fe<sup>III</sup>-THPN

complexes by refinement of the spectroscopic data with the HypSpec2014 software.<sup>135</sup> The corresponding speciation plot is shown in Figure 3.5a.

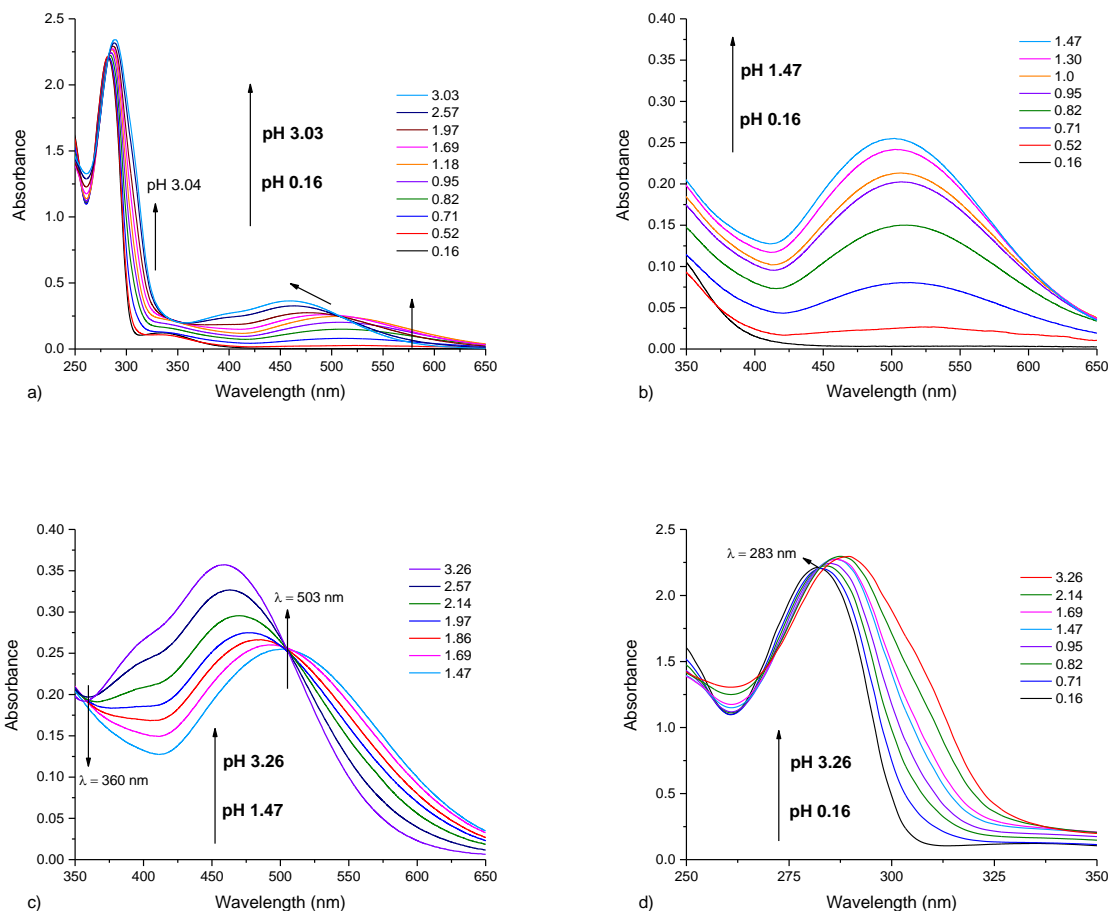


**Figure 3.3.** Representative spectra of the UV-Vis titrations of the Fe<sup>III</sup>-THPN system at increasing pH values : a) from 250 to 650 nm and pH range 0.16–3.03; b) from 350 to 650 nm and pH range 0.16–1.47; c) from 350 to 650 nm and pH range 1.47–3.26; d) from 250 to 350 nm and pH range 0.16–3.26. [THPN] = [Fe<sup>3+</sup>] = 7.16 × 10<sup>-5</sup> M, 25 °C, I = 0.16 M NaCl, l = 1 cm.

Next, an indirect metal-metal competition UV-Vis titration was performed to determine the stability constants of the Zr<sup>IV</sup>-THPN complexes, as the stability constants were too high to be determined by direct methods. This method exploited the fact that, other than the Fe<sup>III</sup>-THPN complexes, the Zr<sup>IV</sup>-THPN complexes are spectroscopically silent in the visible

range. The competition between the Fe<sup>III</sup>- and the Zr<sup>IV</sup>-complexes can therefore be observed by the disappearance of the red ligand-to-metal charge transfer (LMCT) band of the [Fe(H<sub>2</sub>THPN)]<sup>+</sup> and [Fe(HTHPN)] complexes upon addition of Zr<sup>4+</sup> equivalents (Figure 3.4 and Appendix C, Figure C.2). In addition, we observed a slight red shift of the UV band centered at 290 to 295 nm upon Zr<sup>IV</sup>-transmetalation of the Fe<sup>III</sup>-THPN complexes (Figure 3.4 left inset, Appendix C, Figure C.2, and Figure C.3). The pH was held constant at pH 2 to avoid precipitation of iron hydroxides.

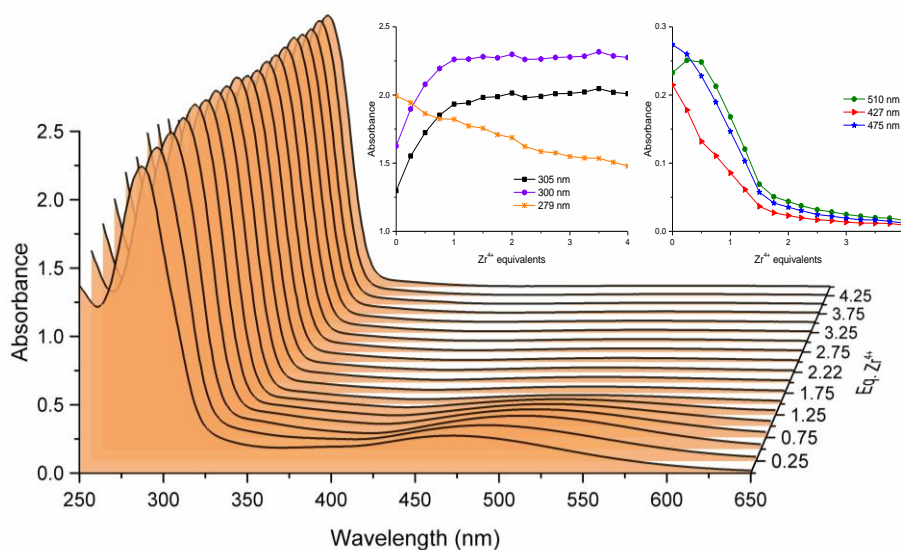


**Figure 3.4.** Metal-metal competition spectra of the Fe<sup>III</sup>-THPN system with increasing equivalents of Zr<sup>4+</sup>. [THPN] = [Fe<sup>3+</sup>] = 7.16 × 10<sup>-5</sup> M; [Zr<sup>4+</sup>]/[Fe<sup>3+</sup>] = 0–4.5; pH = 2, 25 °C, I = 0.16 M NaCl, l = 1 cm. The insets represent the change in absorbance with increasing equivalents of Zr<sup>4+</sup> at λ = 279, 300, or 305 nm (left) and at λ = 427, 475, or 510 nm (right), respectively.

The stability constant of the [Zr(H<sub>2</sub>THPN)]<sup>2+</sup> species could then be calculated from comparison with the spectra of the Fe<sup>III</sup>-THPN complexes present at pH 2 and are presented in Table 3.4. In additional direct UV-potentiometric titrations we found that [Zr(H<sub>2</sub>THPN)]<sup>2+</sup> deprotonates its two protons with dissociation constants of pK<sub>a</sub> = 3.32 and 3.85, respectively to yield the neutral [Zr(THPN)] complex. These deprotonations are accompanied by a shift of the

band at 295 nm to 305 nm and the occurrence of an isosbestic point at 298 nm (Appendix C, Figure C.3). At pH ~6.5 the neutral [Zr(THPN)] complex started to precipitate and the potentiometric data were therefore not included in the calculations. However, as shown by the UV spectra in Appendix C, Figure C.3, the [Zr(THPN)] complex does not exhibit further transformations and remains stable at higher pH. The distribution diagrams for the Zr<sup>IV</sup>-THPN complexes were calculated using the stability constants presented in Table 3.4 and are shown in Figure 3.5.

**Table 3.4.** Stability constants for the complexes formed by THPN with Fe<sup>3+</sup> and Zr<sup>4+</sup> ions, respectively at 25 °C, *I* = 0.16 M NaCl.

Model	Fe <sup>III</sup> -THPN		Zr <sup>IV</sup> -THPN	
	log $\beta$	p <i>K</i>	log $\beta$	p <i>K</i>
MH <sub>2</sub> L	54.95(1) <sup>a</sup>		57.51(5) <sup>c</sup>	
MHL	52.94(1) <sup>a</sup>	2.01	54.2(1) <sup>b</sup>	3.3
ML	44.71(7) <sup>b</sup>	8.23	50.3(1) <sup>b</sup>	3.9
<b>pM</b>	<b>38.0</b>		<b>42.8</b>	

<sup>a</sup> Determined by proton competition UV-Vis titrations; <sup>b</sup> determined by simultaneous UV-potentiometric titrations; <sup>c</sup> determined by metal-metal competition UV-Vis titrations. Charges are omitted for simplicity.

The stability constants of the [Zr(THPN)] and the [Fe(THPN)]<sup>-</sup> complexes are both very strong (log  $\beta_{110}$  = 50.3(2) and log  $\beta_{110}$  = 44.71(7), respectively), with the Zr<sup>IV</sup> complex stability exceeding that of the Fe<sup>III</sup> complex. This confirms that THPN is capable of forming a thermodynamically stable Zr<sup>IV</sup>-complex. To the best of our knowledge, the stability constant for the [Zr(THPN)] complex, is the highest reported stability constant for Zr<sup>IV</sup> complexes in aqueous solution thus far. The closest value reported is for the [Zr(3,4,3-LI(1,2-HOPO))] complex and is seven orders of magnitude lower (log  $\beta_{110}$  = 43.1(6)).<sup>141</sup>

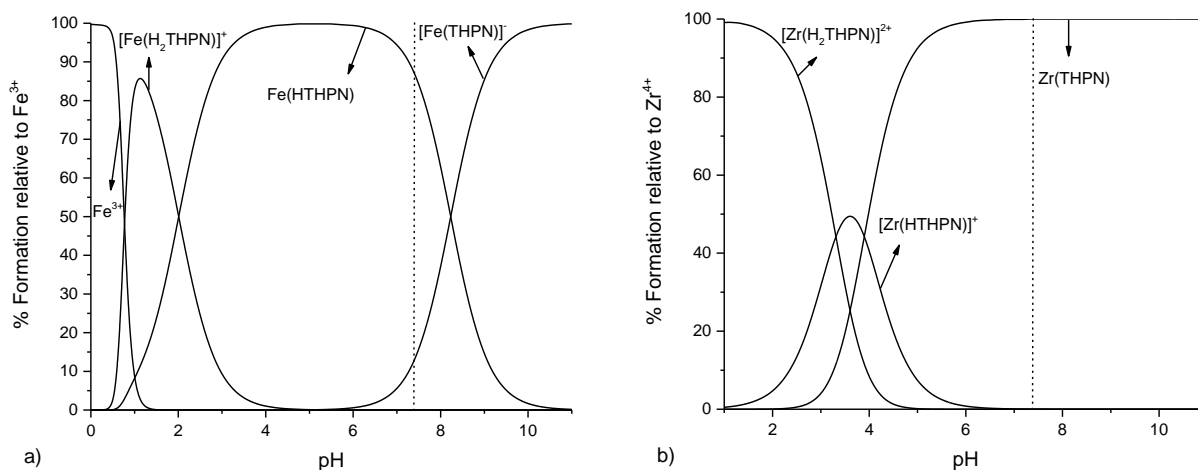


**Figure 3.5.** Speciation plots for a) Fe<sup>III</sup>-THPN complexes and b) Zr<sup>IV</sup>-THPN complexes calculated with stability constants from Table 3.4. [THPN] = [M<sup>n+</sup>] = 1.10 × 10<sup>-4</sup> M; dashed line indicates pH = 7.4.

While the stability constant is a good measure for the overall thermodynamic complex stability in solution, an even more effective way to compare different chelators for biological applications is by employing pM values. pM is linearly correlated to the stability constant of the metal complexes at physiologically relevant conditions, and is defined as  $pM = -\log [M^{n+}]_{\text{free}}$  at pH 7.4 with  $[M^{n+}] = 1 \mu\text{M}$  and  $[L^{x-}] = 10 \mu\text{M}$ .<sup>142, 143</sup> Besides the thermodynamic stability constant of the metal complexes, the pM value also takes ligand acid-base properties into account, allowing for the most suitable comparison of the ability of different ligands with diverse basicities and/or denticities and different metal-to-ligand stoichiometries.<sup>144, 145</sup> Even though the [Zr(THPN)] complex has the higher overall stability constant, the higher ligand basicity of THPN results in a 1.2 unit lower pM value for [Zr(THPN)] when compared to [Zr(3,4,3-LI(1,2-HOPO))] (Table 3.5). Still, both HOPO complexes exert impressively high thermodynamic stability. Surprisingly, the stability constants and pM values for Zr<sup>IV</sup>-complexes with DFO or the recently introduced DFO\* family of chelators have not been experimentally determined to date. Abergel and co-workers, however estimated the pM value for the Zr<sup>IV</sup>-

complex of DFO to be between 29 and 31.<sup>141, 146</sup> pM values based on computational approximations have also been reported for the Zr-complexes of DTPA and citrate<sup>141, 147</sup> and the values are included in the comparison in Table 3.5. Hence, from a thermodynamic stability point of view, both THPN and 3,4,3-LI(1,2-HOPO) appear to be much more effective in sequestering Zr<sup>4+</sup> and form much stronger Zr<sup>IV</sup>-complexes than DFO, DTPA, or citrate.<sup>147</sup>

**Table 3.5.** Comparison of pM values for Zr<sup>IV</sup>-complexes with THPN or literature chelators.

	THPN	3,4,3-LI(1,2-HOPO)	DTPA	DFO	Citrate
pM	42.8	44.0 <sup>a</sup>	~35.0 <sup>a,b</sup>	~29–31 <sup>c</sup>	~28.7 <sup>a,b</sup>

<sup>a</sup> From ref.<sup>141</sup>; <sup>b</sup> calculated, from ref.<sup>147</sup>; <sup>c</sup> estimated, from refs.<sup>141, 146</sup>

These results further indicate that THPN is also an excellent Fe<sup>III</sup>-chelator. The pM value for Fe<sup>III</sup>-THPN (pM 38.0) exceeds that of the iron(III) chelate with the siderophore enterobactin (pM 34.3),<sup>148, 149</sup> one of the strongest iron chelators. THPN may therefore hold therapeutic potential for treatment of iron overload disease.

### 3.2.4 Radiolabeling of THPN with <sup>89</sup>Zr<sup>IV</sup>

Next, the radiolabeling of THPN was investigated with positron-emitting zirconium-89. To this end, a neutralized <sup>89</sup>Zr-oxalate solution (1.1 MBq, 29 μCi, 72 μL, pH ~7.5) was added to a THPN solution (8 μL, 1 mM; final [THPN] = 100 μM in water). Within 10 min at ambient temperature this quantitatively produced the single radiochemical species <sup>89</sup>Zr-THPN, as determined by radio-HPLC. The radiocomplex eluted at a nearly identical retention time as the non-radioactive complex, with a minor difference (15 s) between the UV- and the gamma-traces due to the sequential arrangement of the detectors (Figure 3.6). In contrast, <sup>89</sup>Zr-oxalate alone eluted with the mobile phase front, confirming that THPN is in fact chelating <sup>89</sup>Zr<sup>4+</sup>. On instant

thin-layer chromatography (ITLC) strips the chelated  $^{89}\text{Zr}$ -THPN complex remained at the origin, whereas  $^{89}\text{Zr}$ -oxalate moved along with the mobile phase front (Appendix A, Figure A.3), further supporting the radio-HPLC results.

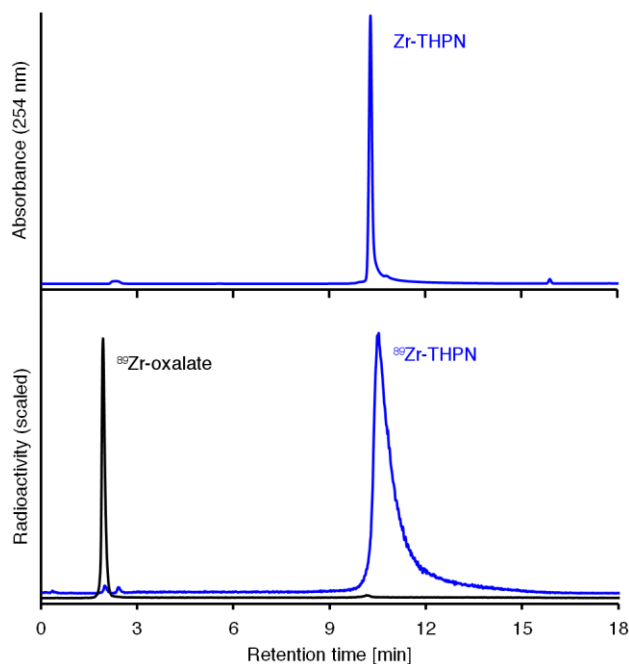


**Figure 3.6.** UV-HPLC trace of non-radioactive Zr-THPN (top) compared with radio-HPLC trace of  $^{89}\text{Zr}$ -THPN (bottom in blue).  $^{89}\text{Zr}$ -oxalate alone elutes with the mobile phase front (bottom in black). Radiotracers were normalized.

### 3.2.5 Concentration Dependence of Radiolabeling

The concentration dependence of the  $^{89}\text{Zr}$ -radiolabeling of THPN was studied and compared to DFO. Ligand solutions of four different concentrations (167  $\mu\text{M}$ , 16.7  $\mu\text{M}$ , 1.67  $\mu\text{M}$ , and 167 nM final concentration, respectively) were incubated with a neutralized solution of  $^{89}\text{Zr}$ -oxalate ( $\sim 0.37$  MBq, 10  $\mu\text{Ci}$ , pH  $\sim 7.0$ ) and left to react at ambient temperature. The radiochemical yield (RCY) of the labeling reactions was quantified by ITLC at 10 min, 30 min, 1 h, 2 h, and 24 h. The same was done with DFO chelator solutions of the same concentrations.

ITLC strips were developed and the peaks were integrated to quantify the RCY of chelated  $^{89}\text{Zr}$ . Figure 3.7 shows the RCY as a function of time with different concentrations of THPN or DFO, respectively.

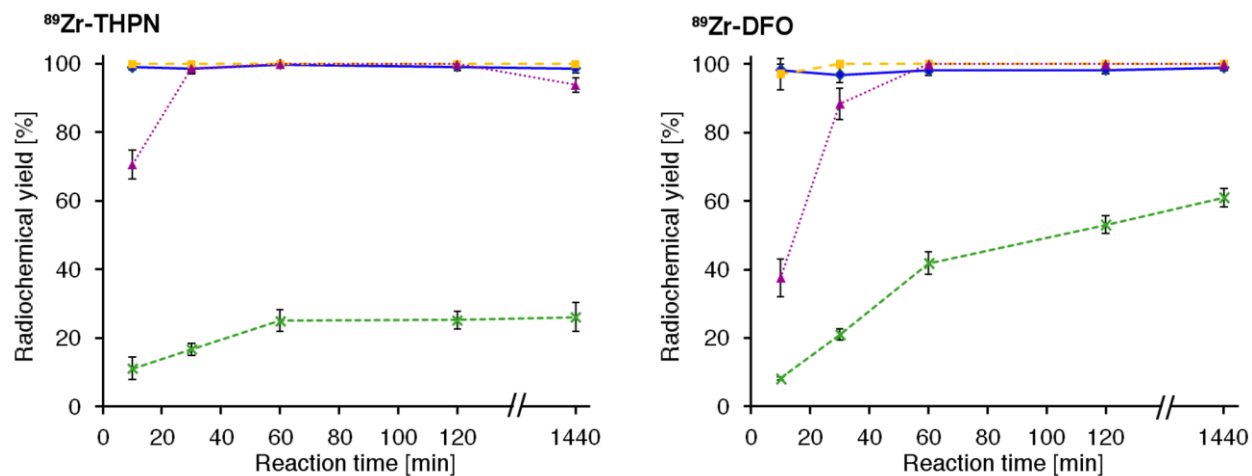


**Figure 3.7.** Radiochemical yield (RCY) of  $^{89}\text{Zr}$ -radiolabeling over time with THPN (left) or DFO ligand (right) at different ligand concentrations: 167  $\mu\text{M}$  ( $\blacklozenge$ ), 16.7  $\mu\text{M}$  ( $\blacklozenge$ ), 1.67  $\mu\text{M}$  ( $\blacktriangle$ ), and 167 nM ( $\blackcross$ ). Error bars indicate standard deviations.

At micromolar concentrations THPN provides faster radiolabeling kinetics than DFO. At a THPN concentration of 1.67  $\mu\text{M}$ , >95% RCY was achieved within 30 min, whereas DFO solutions of the same concentration took 1 h to reach a similar labeling yield. At ten- or one hundred-fold higher concentrations (16.7  $\mu\text{M}$  or 167  $\mu\text{M}$ ), both DFO and THPN achieve quantitative RCY within 10 min. At sub-micromolar concentrations (167 nM) both ligands lead to incomplete radiolabeling, with DFO ultimately achieving a higher (~61%) RCY by the end of the experiment. One data point from DFO's data set was excluded after a Grubbs test identified it as a statistical outlier.

The fast, quantitative radiolabeling provided by THPN is of importance to provide high specific activity under mild conditions (temperature, pH, solvent), which is crucial for the radiolabeling of sensitive antibodies or other biological targeting vectors.

### 3.2.6 Distribution Coefficients

As an estimate for lipophilicity, the distribution coefficients  $\log D_{7.4}$  for  $^{89}\text{Zr}$ -THPN and  $^{89}\text{Zr}$ -DFO were measured between *n*-octanol and phosphate-buffered saline (PBS) at pH 7.4 (Table 3.6). Both radiocomplexes demonstrated hydrophilic character, which can be attributed to their polar nature. Our data suggest  $^{89}\text{Zr}$ -THPN to be a factor of three times more hydrophilic than  $^{89}\text{Zr}$ -DFO. The  $\log D_{7.4}$  value we measured for  $^{89}\text{Zr}$ -DFO deviated by the same amount from previously reported data for the same complex ( $-3.1 \pm 0.1$ ),<sup>96</sup> which leads us to conclude the two radiocomplexes are similar in terms of their lipophilicity. A hydrophilic distribution coefficient of the radiocomplex could be advantageous for immunoPET applications as it should be less likely to drastically alter the solubility and biodistribution of antibodies.

**Table 3.6.** Distribution coefficients  $\log D_{7.4}$  measured for  $^{89}\text{Zr}$ -complexes.<sup>a</sup>

Complex	$\log D_{7.4}$
$^{89}\text{Zr}$ -THPN	$-3.1 \pm 0.2$ ( $n = 3$ )
$^{89}\text{Zr}$ -DFO	$-2.6 \pm 0.2$ ( $n = 4$ )

<sup>a</sup> Distribution coefficients between *n*-octanol and PBS at pH 7.4. Values are reported as average  $\pm$  standard deviation.

### 3.2.7 In Vitro Stability Experiments

Next, the *in vitro* stability of the  $^{89}\text{Zr}$ -THPN complex was assessed in a series of *in vitro* challenge studies and the results were compared against  $^{89}\text{Zr}$ -DFO.

### 3.2.7.1 Transchelation Competition Study

A direct transchelation competition study was performed between THPN and DFO. For this, increasing concentrations of the challenge ligand DFO were added to  $^{89}\text{Zr}$ -THPN in THPN solutions. Similarly, different concentrations of THPN as a challenge ligand were added to  $^{89}\text{Zr}$ -DFO in DFO solutions. The reactions were monitored by ITLC (Biodex (dark green), sodium citrate mobile phase, 100 mM, pH 5.5), where  $^{89}\text{Zr}$ -THPN remained at the origin as a single spot (Figure 3.8A), whereas any  $^{89}\text{Zr}$ -DFO present was evident by activity migration<sup>113</sup> (Figure 3.8B). Since the  $^{89}\text{Zr}$ -DFO migration was diffuse, and a small amount potentially remained at the baseline, integration to quantify the ratio between the two radiocomplexes was not possible, however the different appearances allowed the qualitative distinction of the predominating radiocomplex. Other ITLC conditions were also tried with different mobile (DTPA solution, 50 mM, pH 7.0) and stationary phases (Biodex (black), silica plates, or Whatman paper strips), but under these conditions the two radiocomplexes could not be distinguished from one another.

In the first three reactions, the  $^{89}\text{Zr}$ -THPN complex was first formed by adding  $^{89}\text{Zr}$ -oxalate (~0.37 MBq, 10  $\mu\text{Ci}$ , pH ~7) to a THPN solution (5  $\mu\text{L}$ ; 1 mM), which was confirmed by ITLC (Figure 3.8A). Aliquots of increasing concentration of DFO (5  $\mu\text{L}$ ; 100 mM, 10 mM, or 1 mM, respectively) were then added to these mixtures. Reactions were monitored by ITLC after 10 min, 30 min, 1 h, 2 h, and 73 h, which showed that  $^{89}\text{Zr}$ -THPN was stable to competition from free DFO ligand at all tested concentrations over the duration of the experiment (Figure 3.8C). Even when exposed to a one hundred-fold excess DFO compared to THPN, no transchelation was observed.

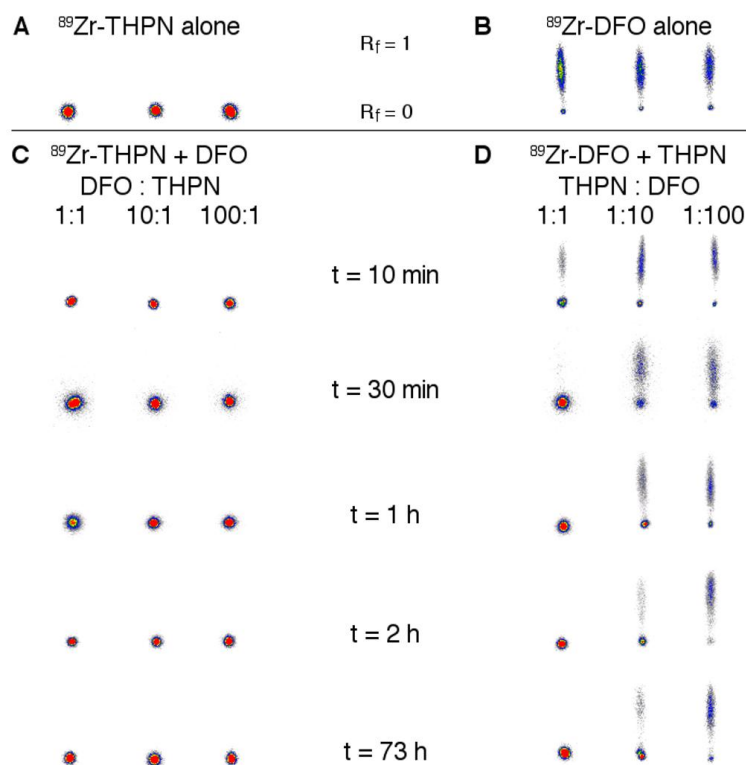


**Figure 3.8.** ITLC chromatograms of A)  $^{89}\text{Zr}$ -THPN complex alone; B)  $^{89}\text{Zr}$ -DFO complex alone; C) transchelation challenge of  $^{89}\text{Zr}$ -THPN incubated with different amounts of DFO over time; D) transchelation challenge of  $^{89}\text{Zr}$ -DFO incubated with different amounts of THPN over time. Whereas  $^{89}\text{Zr}$ -THPN resists transchelation,  $^{89}\text{Zr}$ -DFO loses  $^{89}\text{Zr}^{\text{IV}}$  to the THPN competition at a 1:1 ligand ratio within 30 min. ITLC strips were developed with sodium citrate solution (100 mM, pH 5.5).

Next, the reverse experiment was performed by challenging  $^{89}\text{Zr}$ -DFO with THPN.  $^{89}\text{Zr}$ -oxalate (~0.37 MBq, 10  $\mu\text{Ci}$ , pH ~7) was added to three vials containing DFO solutions (5  $\mu\text{L}$ ; 1 mM). Formation of the  $^{89}\text{Zr}$ -DFO complex was confirmed by ITLC (Figure 3.8B) and then aliquots of decreasing concentration of THPN (5  $\mu\text{L}$ ; 1 mM, 100  $\mu\text{M}$ , or 10  $\mu\text{M}$ , respectively) were added to the mixtures. This time we used lower concentrations of the challenge ligand such that the THPN to DFO ratio was 1:1, 1:10, or 1:100 in favor of DFO. Monitoring by ITLC showed that after 30 min  $^{89}\text{Zr}^{\text{IV}}$  transchelation took place from DFO to THPN in the 1:1 competition (Figure 3.8D). Even when only a tenth of THPN was present, some transchelation was evident after 1–2 h. Under conditions in which THPN:DFO was 1:100, no

transchelation was observed. All experiments were repeated for triplicates (Appendix A, Figure A.4).

These results show that when in direct competition, the new chelator THPN outperforms DFO in terms of its potential to bind  $^{89}\text{Zr}^{\text{IV}}$ . Whereas  $^{89}\text{Zr}$ -THPN appears resistant to transchelation even when exposed to a one hundred-fold excess of DFO, the  $^{89}\text{Zr}$ -DFO complex does not withstand a 1:1 challenge with THPN.

### 3.2.7.2 EDTA Challenge

In order to further examine the Zr-complex stability, we challenged aliquots of the  $^{89}\text{Zr}$ -THPN and  $^{89}\text{Zr}$ -DFO complexes with one hundred-fold excess of free EDTA. The mixtures were incubated at a range of pH values (pH 5.0–8.0) at 37 °C over a period of seven days and the quantity of intact radiocomplex was determined by ITLC (Table 3.7). Interestingly, we did not observe the extent of  $^{89}\text{Zr}$ -DFO instability reported by Deri *et al.*<sup>111</sup> Over a period of 7 days both,  $^{89}\text{Zr}$ -THPN and  $^{89}\text{Zr}$ -DFO, remained >99% intact at pH 6.0–8.0 and resisted transchelation. Transchelation to EDTA was only observed at pH 5.0. At this pH,  $^{89}\text{Zr}$ -DFO disintegrated completely and after one day only  $1.6 \pm 0.5\%$  remained intact.  $^{89}\text{Zr}$ -THPN was affected by transchelation at this pH, but exhibited much better stability than the DFO-complex. After seven days at pH 5.0,  $41.6 \pm 11.1\%$  of  $^{89}\text{Zr}$ -THPN remained intact.

In the physiologically more relevant pH range 6.0–8.0 the 100-fold excess EDTA did thus not impair  $^{89}\text{Zr}$ -THPN or  $^{89}\text{Zr}$ -DFO. Under the more extreme conditions at pH 5.0,  $^{89}\text{Zr}$ -THPN exhibited superior complex stability compared to  $^{89}\text{Zr}$ -DFO.

**Table 3.7.** EDTA challenge.<sup>a</sup>

Complex	pH	initial	1 h	1 d	3 d	5 d	7 d
<sup>89</sup> Zr-THPN	8.0	99.2 ± 0.6	>99.9	>99.9	>99.9	>99.9	>99.9
	7.0	99.2 ± 0.4	>99.9	>99.9	>99.9	>99.9	>99.9
	6.0	99.7 ± 0.3	99.9 ± 0.3	>99.9	>99.9	>99.9	>99.9
	5.0	99.1 ± 0.2	68.3 ± 5.1	62.1 ± 3.4	52.8 ± 13.3	40.5 ± 6.1	41.6 ± 11.1
<sup>89</sup> Zr-DFO	8.0	99.6 ± 0.3	99.7 ± 0.6	99.9 ± 0.2	99.7 ± 0.3	99.7 ± 0.3	99.5 ± 0.2
	7.0	99.5 ± 0.2	>99.9	99.9 ± 0.1	99.9 ± 0.1	99.9 ± 0.2	99.9 ± 0.2
	6.0	99.9 ± 0.2	99.7 ± 0.3	99.7 ± 0.3	99.5 ± 0.4	99.5 ± 0.4	99.6 ± 0.7
	5.0	99.5 ± 0.2	64.6 ± 3.1	1.6 ± 0.5	1.2 ± 0.6	1.1 ± 1.1	0.5 ± 0.1

<sup>a</sup> Values are reported as percentage of intact <sup>89</sup>Zr-complex (average ± standard deviation) after incubation with a 100-fold excess of EDTA at 37 °C. The experiments were performed in triplicate.

### 3.2.7.3 Serum Stability Study

Incubation of <sup>89</sup>Zr-THPN in human blood serum for seven days at 37 °C did not impair the complex stability considerably. ITLC analysis after incubation showed that 93 ± 2% of <sup>89</sup>Zr-THPN remained intact. This compares well to the <sup>89</sup>Zr-DFO complex, which remained 94 ± 8% intact.

### 3.2.8 In Vivo Behaviour

In order to investigate the *in vivo* biodistribution and clearance pathway of <sup>89</sup>Zr-THPN, the radiocomplex (5.22 ± 0.59 MBq, 141 ± 16 µCi) was injected intravenously into four healthy mice and imaged *via* PET/CT for 30 min post-injection. Within this short amount of time, most of the activity (~75 ± 13%) had already reached the urinary bladder and no other organ accumulation was detected (Appendix B, Figure B.1). After 27 h post-injection, the mice were sacrificed, the activity in the whole carcass was measured, and an *ex vivo* biodistribution

study was performed. After this time, only  $2.7 \pm 1.3\%$  of the injected dose (%ID) remained in the entire carcass as the rest was excreted during recovery from anesthesia. Biodistribution results are shown in Table 3.8.

**Table 3.8.** Biodistribution of  $^{89}\text{Zr}$ -THPN and  $^{89}\text{Zr}$ -DFO after 24 h post injection.<sup>a</sup>

<b>Organ</b>	<b><math>^{89}\text{Zr}</math>-THPN (<math>n = 4</math>)<sup>b</sup></b>	<b><math>^{89}\text{Zr}</math>-DFO (<math>n = 1</math>)</b>
Blood	$0.01 \pm 0.01$	0.07
Heart	$0.05 \pm 0.01$	0.03
Liver	$1.08 \pm 1.25$	0.58
Kidneys	$3.49 \pm 0.28$	4.81
Lungs	$0.24 \pm 0.31$	0.04
Small intestine	$0.08 \pm 0.04$	0.07
Bladder	$0.13 \pm 0.03$	0.08
Muscle	$0.02 \pm 0.01$	0.00
Spleen	$0.75 \pm 0.94$	2.37
Bone	$0.11 \pm 0.01$	0.12
Stomach	$0.06 \pm 0.02$	0.03
Pancreas	$0.02 \pm 0.01$	0.01
Feces	$0.70 \pm 0.47$ <sup>c</sup>	0.68
Urine	$0.21 \pm 0.05$	0.32

<sup>a</sup> Values are reported as percentage of injected dose per gram of tissue (%ID/g). Healthy female C57BL/6 mice were injected with either  $^{89}\text{Zr}$ -THPN ( $n = 4$ ), or  $^{89}\text{Zr}$ -DFO ( $n = 1$ ) *via* tail vein injection. The animals were sacrificed 27 h, or 25 h p.i., respectively; organs were harvested, weighed, and their activity was measured in a  $\gamma$  counter. <sup>b</sup> Average value from four animals  $\pm$  standard deviation. <sup>c</sup> One data point was excluded after a Grubbs test identified it as an outlier.

One mouse was injected with  $^{89}\text{Zr}$ -DFO (2.8 MBq, 77  $\mu\text{Ci}$ ) as control. Image quantification and subsequent biodistribution confirmed rapid renal excretion as well. Within

the first 30 min, ~43% of the injected activity reached the urinary bladder (Appendix B, Figure B.2) and 25 h post-injection only 2.4%ID remained in the entire mouse. Necropsy showed that this remaining activity was mainly associated with kidneys and spleen (Table 3.8). As the *in vivo* behaviour of  $^{89}\text{Zr}$ -DFO in murine models has been reported in many previous reports<sup>80, 86, 96, 111, 150</sup> we used a single animal in this study.

The fast blood clearance of the two radiocomplexes *via* the kidneys was expected due to their low molecular weights (<1 kDa) and was consistent with previous reports for  $^{89}\text{Zr}$ -DFO and other  $^{89}\text{Zr}$ -chelates.<sup>80, 86, 96, 111, 150</sup> The absence of significant residual organ uptake, in particular in the bones, indicates that the complexes were stable *in vivo* over the course of the experiment. The observed *in vivo* stability and the fast pharmacokinetic excretion of  $^{89}\text{Zr}$ -THPN were promising and encouraged us to further scrutinize its long-term *in vivo* stability. Due to the fast excretion of  $^{89}\text{Zr}$ -THPN, the radiochelate had to be conjugated to a long-circulating carrier molecule to allow a conclusive assessment of this long-term stability. For this, a bifunctional derivative of THPN had to be developed, which could then be conjugated to a carrier (Chapter 4).

### 3.3 Conclusions

The new octadentate tetrakis(3,4-HOPO) chelator THPN was synthesized, characterized, and studied as a Zr-chelator. The thermodynamic stability of THPN complexes with  $\text{Zr}^{\text{IV}}$ , as well as with  $\text{Fe}^{\text{III}}$ , were determined experimentally and found to be exceptionally high (Zr-THPN:  $\log \beta_{110}$  50.3; pM 42.8; Fe-THPN:  $\log \beta_{110}$  44.7; pM 38.0). The chelator was further investigated *in vitro* and *in vivo* with radioactive  $^{89}\text{Zr}^{\text{IV}}$  and quantitative radiolabeling was achieved with 16.7  $\mu\text{M}$  THPN concentrations within 10 min at ambient temperature. The radiocomplex was stable over a week in human blood serum and outperformed DFO in an

EDTA challenge, as well as a direct transchelation competition study. While  $^{89}\text{Zr}$ -THPN resisted a one hundred-fold excess of DFO, an equimolar amount of THPN induced transchelation of  $^{89}\text{Zr}^{\text{IV}}$  from DFO to THPN. The radiocomplex was stable *in vivo* and was excreted rapidly *via* the renal pathway. These results led us to conclude that the first octadentate 3,4-HOPO chelator THPN is a promising novel chelator for  $^{89}\text{Zr}$ -based PET tracers and we further examined this ligand system by developing a bifunctional derivative (Chapter 4).

## 3.4 Experimental

### 3.4.1 Materials and Methods

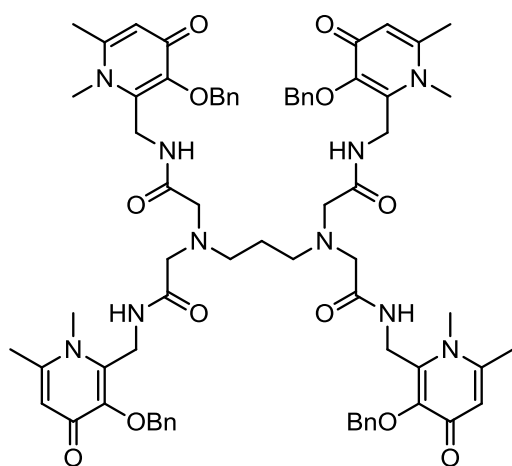
All chemicals were used as received without further purification and all water used was ultrapure (18.2 M $\Omega$ ·cm). Building block **3.1** (2-(aminomethyl)-1,6-dimethyl-3-(phenylmethoxy)-4(1*H*)-pyridinone) was prepared by Dr. Stoyan Karagiozov according to a published procedure<sup>117</sup> with minor adjustments or was purchased from Otava Ltd. 1,3-Propanediamine-*N,N,N',N'*-tetraacetic acid (PDTA) was purchased from TCI. 1-Hydroxybenzotriazole hydrate (HOBT·H<sub>2</sub>O) was purchased from AC PharmaChem. *N,N'*-Dicyclohexylcarbodiimide (DCC) and palladium on carbon (Pd/C) were purchased from Aldrich. Desferrioxamine (DFO, as mesylate salt), anhydrous *N,N*-dimethylformamide (DMF), acetonitrile, and methanol were purchased from Sigma-Aldrich. Zirconium(IV) chloride was purchased from Strem Chemicals. Celite 545 was purchased from Fisher Scientific. Parsability of chemical nomenclature was confirmed with OPSIN.<sup>118, 119</sup> NMR spectra were recorded on a Bruker Ascend 400 spectrometer (400.13 MHz for <sup>1</sup>H; 100.62 MHz for <sup>13</sup>C) at 297.16 K. Chemical shifts ( $\delta$  relative to residual solvent peak) are reported as parts per million (ppm) and coupling constants (*J*) in hertz (Hz). ESI-MS spectra were recorded on an AB Sciex QTrap 5500 mass

spectrometer. High-resolution mass spectrometry (HR-MS) analysis was acquired on a Thermo Scientific Q Exactive mass spectrometer. Matrix-assisted laser desorption/ionization time-of-flight (MALDI-TOF) mass spectrometry was performed on a Bruker autoflex by UBC Mass Spectrometry Centre. IR spectra were recorded on an Agilent Cary 660 FT-IR spectrometer equipped with an attenuated total reflectance (ATR) crystal. HPLC was performed on a Waters Alliance e2695 separations module coupled to a Waters 2489 UV/Vis-detector and, for radio-HPLC, a LabLogic Scan-RAM radio-detector. The column was a reversed phase C18 Waters Atlantis T3, 100 Å, 5 µm particle size (4.6 × 150 mm), supported by a C18 guard cartridge and was operated in an oven (40 °C). The column was eluted with following gradient: A = 0.1% trifluoroacetic acid (TFA) in water; B = methanol; flow rate = 1 mL/min; 0–5 min 90% A; 5–15 min 10–100% B; 15–18 min 100% B. Microwave reactions were conducted in a Biotage Initiator<sup>+</sup> microwave synthesizer. Flash chromatography was performed on a Biotage Isolera One system using a Biotage SNAP Ultra C18 reversed phase cartridge. <sup>89</sup>Zr was produced at TRIUMF on a TR13 cyclotron (Ebc Industries Ltd.) *via* the <sup>89</sup>Y(p,n)<sup>89</sup>Zr reaction from a Y(NO<sub>3</sub>)<sub>3</sub> solution target,<sup>82</sup> or at the BC Cancer Agency on a TR19 cyclotron (Advanced Cyclotron Systems Inc.) from a solid yttrium target (American Elements). <sup>89</sup>Zr was purified either following a procedure by Holland *et al.*<sup>80</sup> or using the commercially available ZR Resin (TrisKem International) and eluting with 0.05 M oxalic acid. <sup>89</sup>Zr-oxalate solutions were neutralized with Na<sub>2</sub>CO<sub>3</sub> solutions. Activities were measured using a Capintec CRC-55tR or a Biodex Atomlab 500 dose calibrator. Instant thin-layer chromatography (ITLC) was carried out using Biodex Tec-Control chromatography strips (black: #150-005, or dark green: #150-771), which were developed with an aqueous mobile phase of either DTPA solution (50 mM, pH 7.0) or sodium citrate solution (100 mM, pH 5.5)<sup>113</sup> and analyzed on a Packard Cyclone storage phosphor

screen imager. Biodistribution samples were counted on a calibrated Packard Cobra II gamma counter.

### 3.4.2 Syntheses

#### 3.4.2.1 2,2',2'',2'''-((Propane-1,3-diyl)bis(azanetriyl))tetrakis(N-((1,6-dimethyl-3-(phenylmethoxy)-4-oxo-1,4-dihydropyridin-2-yl)methyl)acetamide) (3.2)



(a) *Using standard conditions:* A mixture of PDTA (12.3 mg, 40.0  $\mu\text{mol}$ , 1 eq.), HOBt·H<sub>2</sub>O (29.4 mg, 192  $\mu\text{mol}$ , 4.8 eq.), and DCC (39.6 mg, 192  $\mu\text{mol}$ , 4.8 eq.) was suspended in anhydrous DMF (1 mL) and stirred at ambient temperature under N<sub>2</sub>. After 3 h, building block 3.1 (2-(aminomethyl)-1,6-dimethyl-3-(phenylmethoxy)-4(1H)-pyridinone, 49.6 mg,

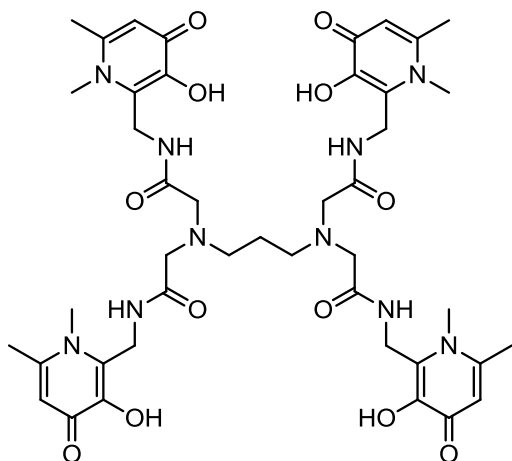
192  $\mu\text{mol}$ , 4.8 eq.) was added as a powder and the reaction mixture was stirred at ambient temperature under N<sub>2</sub> for 6 days until monitoring by HPLC showed complete consumption of the starting material 3.1. At this point the white slurry was filtered over fritted glass, rinsed with acetonitrile, evaporated, and purified by reversed phase flash chromatography (eluted with a gradient of 100% water with 0.1% formic acid to 100% methanol) to yield the title compound 3.2 as a colorless oil, containing some *N,N'*-dicyclohexylurea impurity that was removed in the subsequent reaction step.

(b) *Using microwave irradiation:* In a conical microwave reaction vial, a mixture of PDTA (50.5 mg, 165  $\mu\text{mol}$ , 1 eq.), HOBt·H<sub>2</sub>O (121.3 mg, 792  $\mu\text{mol}$ , 4.8 eq.), and DCC (163.4 mg, 792  $\mu\text{mol}$ , 4.8 eq.) was suspended in anhydrous DMF (10 mL) and crimp capped under N<sub>2</sub>. The mixture was stirred for 5 min at ambient temperature and then irradiated in a microwave

synthesizer in five intervals (2 h, 4 × 1 h) at 55 °C for a total of 6 h. Reaction progress was monitored by HPLC between MW intervals and once complete consumption of starting material **3.1** was achieved, the white slurry was filtered over fritted glass, rinsed with acetonitrile, evaporated, and purified by reversed phase flash chromatography (eluted with a gradient of 100% water with 0.1% formic acid to 100% methanol) to yield the title compound **3.2** as a colorless oil, containing some *N,N'*-dicyclohexylurea impurity that was removed in the subsequent reaction step.

### 3.4.2.2 2,2',2'',2'''-((Propane-1,3-diyl)bis(azanetriyl))tetrakis(*N*-((1,6-dimethyl-3-hydroxy-4-oxo-1,4-dihydropyridin-2-yl)methyl)acetamide) (THPN)

In a dry Schlenk flask under N<sub>2</sub>, Pd/C (10% w/w, 13.7 mg, 12.7 μmol Pd), was



suspended in MeOH (3 mL). To this was added a solution of compound **3.2** (39.6 mg, 31.2 μmol) in MeOH (3 mL) and it was rinsed with MeOH (7 mL). The reaction vessel was placed under a hydrogen atmosphere and stirred vigorously at ambient temperature. After 2.5 h, HPLC indicated completion of the reaction and the mixture was filtered through a

plug of Celite 545 and rinsed *ad libitum* with MeOH and water. The filtrate was concentrated *in vacuo* and purified by reversed phase chromatography (eluted with a gradient of 100% water to 100% methanol). The product fractions were pooled, evaporated, and recrystallized from MeOH/H<sub>2</sub>O (20:1) to give the title compound THPN as a white powder (~11.5 mg). Cumulative yield over two steps: 51% using standard method (a); 64% using microwave method (b).

$^1\text{H}$  NMR (400 MHz,  $\text{CD}_3\text{OD}$ ):  $\delta$  6.28 (s, 4H, CH), 4.60 (s, 8H,  $\text{OCNCH}_2$ ), 3.66 (s, 12H,  $\text{NCH}_3$ ), 3.21 (s, 8H,  $\text{OCCH}_2$ ), 2.51 (m, 4H,  $\text{NCH}_2\text{CC}$ ), 2.39 (s, 12H,  $\text{CCH}_3$ ), 1.51 (m, 2H,  $\text{CCH}_2\text{C}$ );  $^{13}\text{C}$  NMR (100 MHz,  $\text{CD}_3\text{OD}/\text{D}_2\text{O}$  (4:1)):  $\delta$  174.0, 171.0, 149.0, 147.1, 132.5, 114.9, 59.6, 54.7, 37.3, 35.9, 25.9, 21.1; FT-IR (ATR):  $\nu_{\text{max}}/\text{cm}^{-1}$  1654.5s, 1624.3s, 1576.7s, 1503.0vs, 1241.4vs; HR ESI-MS: calcd. ( $m/z$ ) for  $\text{C}_{43}\text{H}_{59}\text{N}_{10}\text{O}_{12}^+$   $[\text{M}+\text{H}]^+$ : 907.43084; found: 907.42932, (1.68 ppm); calcd. ( $m/z$ ) for  $\text{C}_{43}\text{H}_{57}\text{N}_{10}\text{O}_{12}^-$   $[\text{M}-\text{H}]^-$ : 905.41629; found: 905.41681, (0.57 ppm); ESI-MS ( $m/z$ ) 907.6  $[\text{M}+\text{H}]^+$ , 929.3  $[\text{M}+\text{Na}]^+$ , 905.4  $[\text{M}-\text{H}]^-$ ; elemental analysis (%) calcd. for  $\text{C}_{43}\text{H}_{58}\text{N}_{10}\text{O}_{12}\cdot 2(\text{CH}_3\text{OH})\cdot \text{H}_2\text{O}$ : C 54.65, H 6.93, N 14.16; found: C 54.85, H 6.81, N 14.31; HPLC:  $t_{\text{R}} = 9.7$  min.

### 3.4.2.3 Zr-THPN Complex

An aqueous solution of  $\text{ZrCl}_4$  (669  $\mu\text{L}$ , 10 mM, 6.69  $\mu\text{mol}$  1.05 eq.) was dropwise added to a stirring solution of THPN in 1:1 MeOH/water (637  $\mu\text{L}$ , 10 mM, 6.37  $\mu\text{mol}$ , 1.00 eq.), the pH was adjusted with 0.1 M  $\text{Na}_2\text{CO}_3$  (170  $\mu\text{L}$ ) to pH ~6–7 and the solution was stirred overnight at ambient temperature. The cloudy mixture was centrifuged (5 min at 13,000 rpm) and the supernatant was removed. The precipitate was characterized as the Zr-THPN complex by MALDI-TOF MS, HPLC, and FT-IR spectroscopy. FT-IR (ATR):  $\nu_{\text{max}}/\text{cm}^{-1}$  1647.2s, 1560.7s, 1509.5vs, 1476.6s, 1300.0s, 1259.3s; MALDI-TOF MS: calcd. ( $m/z$ ) for  $\text{C}_{43}\text{H}_{55}\text{N}_{10}\text{O}_{12}\text{Zr}^+$   $[\text{Zr-THPN}+\text{H}]^+$ : 993.3; found: 993.3; HPLC:  $t_{\text{R}} = 10.3$  min.

### 3.4.3 Computational Studies

Density functional theory (DFT) calculations were conducted as implemented in the Gaussian 09 revision E.01 suite of *ab initio* quantum chemistry programs.<sup>123</sup> Geometry optimizations were performed by using the B3LYP<sup>124-126</sup> functional in combination with

LanL2DZ<sup>127-130</sup> or DGDZVP<sup>132, 133</sup> basis sets, which were used for description of the valence electrons as well as the effective core potentials of the Zr<sup>IV</sup> ion. Normal self-consistent field (SCF) and geometry convergence criteria were employed and Zr-THPN was optimized in the gas phase without the use of symmetry constraints.

### 3.4.4 Thermodynamic Solution Studies

#### 3.4.4.1 Materials and Methods

Protonation constants and metal stability constants were obtained by combined potentiometric-spectrophotometric titrations as described before.<sup>151</sup> Measurements were conducted at 25 °C and an ionic strength of  $I = 0.16$  M NaCl, using a Metrohm Titrand 809 equipped with a Ross combined electrode, a Metrohm Dosino 800, and a Varian Cary 60 UV-Vis spectrophotometer (200–800 nm spectral range) connected to a 0.2 cm path length (l) optic dip probe immersed in the titration cell. Additional batch experiments to study proton competition or metal-metal competition were carried out in a 1 cm cuvette at 25 °C and 0.16 M NaCl ionic strength to determine the formation constants of the Fe<sup>III</sup>-THPN and Zr<sup>IV</sup>-THPN systems. Metal ion solutions were prepared from atomic absorption (AA) standard metal ion solutions. The exact amount of acid present in the iron and zirconium standards was determined by Gran's method,<sup>152</sup> titrating equimolar solutions of either metal ion and Na<sub>2</sub>H<sub>2</sub>EDTA. All potentiometric measurements were processed using the Hyperquad2013 software,<sup>153</sup> whereas spectrophotometric data were processed using the HypSpec2014 software.<sup>135</sup> Speciation plots for the ligand and metal complexes were calculated with HySS<sup>154</sup> using the constants in Table 3.3 and Table 3.4 and the metal hydrolysis equilibrium constants. The molar absorptivities of all protonated species of THPN were included in the metal stability calculations. Proton dissociation constants corresponding to hydrolysis of aqueous Fe<sup>3+</sup> and Zr<sup>4+</sup> ions included in the calculations were

taken from Baes and Mesmer.<sup>155</sup> The species formed in the studied systems were characterized by the general equilibrium:  $mM + lL + hH \rightleftharpoons M_mL_lH_h$  (charges omitted). For convention, a complex containing metal ion  $M$ , ligand  $L$ , and proton  $H$  has the general formula  $M_mL_lH_h$ . The stoichiometric index  $m$  might also be 0 in the case of protonation equilibria. Negative values for the index  $h$  refer to proton removal or hydroxide ion addition during formation of a  $M$ -OH complex. The overall equilibrium constant for the formation of the complex  $M_mL_lH_h$  from its components is designated as  $\log \beta$ . Stepwise equilibrium constants  $\log K$  correspond to the difference in log units between the overall constants of sequentially protonated (or hydroxide) species.  $pM$  is defined as  $-\log [M^{n+}]_{\text{free}}$  and is always calculated at  $[M^{n+}] = 1 \mu\text{M}$ ,  $[L^{x-}] = 10 \mu\text{M}$ ,  $\text{pH } 7.4$ , and  $25 \text{ }^\circ\text{C}$ .<sup>143</sup> To facilitate reading, ligand nomenclature is generally described using the neutral form THPN herein without reflecting its protonation state unless specific protonation of the ligand is being discussed.

#### 3.4.4.2 THPN Ligand Protonation Constants

Protonation equilibria of the ligand were studied by simultaneous potentiometric-spectrophotometric titrations of an acidic solution of THPN ( $8.47 \times 10^{-5} \text{ M}$ ) at  $25 \text{ }^\circ\text{C}$ ,  $l = 0.2 \text{ cm}$  and  $0.16 \text{ M NaCl}$  ionic strength. Electromotive force values and spectra were recorded after each addition of  $\text{NaOH}$  ( $0.1496 \text{ M}$ ) or  $\text{HCl}$  and both instruments were synchronized in order to have constant delays between each titrant addition and to allow enough time to reach equilibrium. The potentiometric and spectrophotometric data collected for at least three replicates were processed using the HypSpec2014 and Hyperquad2013 software suites.<sup>135, 153</sup> The respective molar absorptivities of the differently protonated species were also determined.

### 3.4.4.3 Metal Complex Formation Constants

The strength of the resulting metal complexes made it necessary to employ different methods to study the complexation of THPN with Fe<sup>III</sup> and Zr<sup>IV</sup>. UV-Vis experiments were conducted to determine the Fe<sup>III</sup>-THPN formation constants by direct proton competition and to study the Fe<sup>III</sup>/Zr<sup>IV</sup> competition. In addition to these experiments, direct simultaneous potentiometric-spectrophotometric titrations were carried out with both, the Fe<sup>III</sup>-THPN and the Zr<sup>IV</sup>-THPN systems, once their first formation constants were determined using the above methods.

Direct proton competition experiments were carried out by UV-potentiometric batch experiments (spectral range 200–800 nm, 25 °C, l = 1 cm) on a set of 22 solutions containing [THPN] = [Fe<sup>3+</sup>] = 7.16 × 10<sup>-5</sup> M with different amounts of standardized HCl to cover a pH range of 0.16–3.26. The ionic strength of each sample was adjusted to 0.16 M by addition of different amounts of NaCl.

To determine the formation constant of the [Zr(H<sub>2</sub>THPN)]<sup>2+</sup> complex, metal-metal competition UV-Vis titrations were carried out. A set of 20 solutions containing [THPN] = [Fe<sup>3+</sup>] = 7.16 × 10<sup>-5</sup> M with varying amounts of competing Zr<sup>4+</sup> ions were prepared with [Zr<sup>4+</sup>]:[Fe<sup>3+</sup>] molar ratios ranging from 0 to 4.5. The pH was adjusted with standardized HCl to pH 2 and the ionic strength of each sample was adjusted to 0.16 M by addition of different amounts of NaCl as supporting electrolyte. The samples were left up to 24 h in order to reach equilibrium before measurement of pH and UV-Vis spectra. UV-Vis measurements were carried out in a 1 cm cuvette at 25 °C and 250–700 nm spectral range.

Additional direct UV-potentiometric titrations were carried out for either the Fe<sup>III</sup>-THPN or the Zr<sup>IV</sup>-THPN system, by titrating equimolar solutions of THPN ligand and the metal ion with standardized NaOH ([THPN] = [M<sup>n+</sup>] ≈ 2.11 × 10<sup>-4</sup> M, 25 °C, 0.16 M NaCl, l = 0.2 cm).

### 3.4.5 Concentration Dependence of $^{89}\text{Zr}$ -Radiolabeling

Aliquots of a neutralized solution of  $^{89}\text{Zr}$ -oxalate (25  $\mu\text{L}$ ,  $\sim 0.37$  MBq, 10  $\mu\text{Ci}$ , pH  $\sim 7$ ) were added to aqueous THPN or DFO ligand solutions of different concentrations (5  $\mu\text{L}$ ; 1 mM, 100  $\mu\text{M}$ , 10  $\mu\text{M}$ , or 1  $\mu\text{M}$ ) and were left to react at ambient temperature. Each reaction mixture was analyzed by ITLC (black strips, DTPA mobile phase, 50 mM, pH 7.0) after 10 min, 30 min, 1 h, 2 h, and 24 h reaction time and the percentage of chelated  $^{89}\text{Zr}$  was determined by integration of the ITLC peaks. The experiments were performed in triplicate.

### 3.4.6 Human Serum Stability

A neutralized solution of  $^{89}\text{Zr}$ -oxalate (48  $\mu\text{L}$ ,  $\sim 0.85$  MBq, 23  $\mu\text{Ci}$ , pH  $\sim 7$ ) was added to aqueous ligand solutions of THPN or DFO, respectively (5.3  $\mu\text{L}$ , 1 mM) and quantitative radiocomplex formation was confirmed by ITLC. Human serum (500  $\mu\text{L}$  from a healthy male donor) was added to these mixtures and the vials were incubated for 7 days at 37  $^{\circ}\text{C}$  with agitation (500 rpm). Aliquots were analyzed by ITLC (black strips, DTPA mobile phase, 50 mM, pH 7.0) after 3, 5, and 7 days incubation and the percentage of chelated  $^{89}\text{Zr}$  was determined by integration. As a control,  $^{89}\text{Zr}$ -oxalate was incubated with human serum. The experiment was performed in duplicate.

### 3.4.7 Distribution Coefficients

A neutralized solution of  $^{89}\text{Zr}$ -oxalate (102  $\mu\text{L}$ ,  $\sim 0.81$  MBq, 22  $\mu\text{Ci}$ ) was added to aqueous ligand solutions of THPN or DFO, respectively (20  $\mu\text{L}$ , 1 mM) and quantitative radiocomplex formation was confirmed after 15 min at ambient temperature by ITLC (black

strips, DTPA mobile phase, 50 mM, pH 7.0). Aliquots of radiocomplex solutions in replicates (30  $\mu\text{L}$ ,  $\sim 6 \mu\text{Ci}$ , THPN:  $n = 3$ ; DFO:  $n = 4$ ) were diluted with PBS (470  $\mu\text{L}$ ), 1-octanol (500  $\mu\text{L}$ ) was added, and the mixtures were thoroughly vortexed for 1 min at 3,000 rpm. After centrifugation for 5 min at 14,000 rpm,  $\sim 200 \mu\text{L}$  of both the organic and of the aqueous phases were removed and counted separately in a gamma counter. Results were corrected for decay and the distribution coefficients at pH 7.4 of [ $^{89}\text{Zr}$ -THPN] and [ $^{89}\text{Zr}$ -DFO] were then calculated as  $\log D_{7.4} = \log_{10} ([^{89}\text{Zr}]_{\text{octanol}} / [^{89}\text{Zr}]_{\text{aqueous}})$ .

### 3.4.8 Transchelation Competition Study

Aliquots of a neutralized solution of  $^{89}\text{Zr}$ -oxalate (30  $\mu\text{L}$ ,  $\sim 0.37 \text{ MBq}$ , 10  $\mu\text{Ci}$ , pH  $\sim 7$ ) were added to solutions of THPN (5  $\mu\text{L}$ ; 1 mM) and left to react for 15 min and formation of  $^{89}\text{Zr}$ -THPN was verified by ITLC. After this, aliquots of DFO (5  $\mu\text{L}$ ; 100 mM, 10 mM, or 1 mM) were added to the mixtures. Each reaction mixture was analyzed by ITLC (dark green strips, sodium citrate mobile phase, 100 mM, pH 5.5) after 10 min, 30 min, 1 h, 2 h, and 73 h reaction time at ambient temperature. The experiments were performed in triplicate.

In a different set of experiments, aliquots of a neutralized solution of  $^{89}\text{Zr}$ -oxalate (30  $\mu\text{L}$ ,  $\sim 0.37 \text{ MBq}$ , 10  $\mu\text{Ci}$ , pH  $\sim 7$ ) were added to solutions of DFO (5  $\mu\text{L}$ ; 1 mM) and left to react for 15 min and formation of  $^{89}\text{Zr}$ -DFO was verified by ITLC. After this, aliquots of THPN (5  $\mu\text{L}$ ; 1 mM, 100  $\mu\text{M}$ , or 10  $\mu\text{M}$ ) were added to the mixtures. Each reaction mixture was analyzed by ITLC (dark green strips, sodium citrate mobile phase, 100 mM, pH 5.5) after 10 min, 30 min, 1 h, 2 h, and 73 h reaction time at ambient temperature. The experiments were performed in triplicate.

### 3.4.9 EDTA Competition Study

Aliquots of a neutralized solution of  $^{89}\text{Zr}$ -oxalate ( $\sim 0.67$  MBq,  $18\ \mu\text{Ci}$ ,  $35\ \mu\text{L}$ ,  $\text{pH} \sim 7.5$ ) were added to solutions of either THPN or DFO ( $0.1\ \text{mM}$ ,  $55\ \mu\text{L}$ ) and left to react for 15 min. Formation of  $^{89}\text{Zr}$ -THPN or  $^{89}\text{Zr}$ -DFO, respectively, was verified by ITLC. After this, EDTA solutions ( $5\ \text{mM}$ ,  $110\ \mu\text{L}$ ) of different pH values ( $\text{pH}\ 5.0$ ,  $6.0$ ,  $7.0$ , or  $8.0$ ) were added as well as sodium acetate solutions ( $0.5\ \text{M}$ ,  $50\ \mu\text{L}$ ) of the same pH value. The mixtures were incubated for 7 days at  $37\ ^\circ\text{C}$  with slight agitation ( $350\ \text{rpm}$ ) and samples were analyzed by ITLC (black strips, DTPA mobile phase,  $50\ \text{mM}$ ,  $\text{pH}\ 7.0$ ) after 1 h, 1 d, 3 d, 5 d, and 7 d. The percentage of intact radiocomplex was determined by integration. Whereas intact  $^{89}\text{Zr}$ -THPN and  $^{89}\text{Zr}$ -DFO remained at the ITLC baseline, transchelated  $^{89}\text{Zr}$ -EDTA moved with the eluent front. The experiments were performed in triplicate.

### 3.4.10 *In Vivo* Study of $^{89}\text{Zr}$ Complexes

This animal study was performed in accordance with the animal care committee (ACC) of the University of British Columbia under the approved protocol A12-0172. Two-month-old healthy female C57BL/6 mice (Charles River Laboratories) were anesthetized using isoflurane inhalation and received a subcutaneous injection of lactated Ringer's solution ( $0.5\ \text{mL}$ ) for hydration prior to the experiment. Sterile filtered ( $0.22\ \mu\text{m}$ ) solutions of  $^{89}\text{Zr}$ -THPN ( $5.22 \pm 0.59$  MBq,  $141 \pm 16\ \mu\text{Ci}$ ,  $n = 4$ ) or  $^{89}\text{Zr}$ -DFO ( $2.8$  MBq,  $77\ \mu\text{Ci}$ ,  $n = 1$ ) in PBS were intravenously administered *via* tail vein injection. Oxalate concentrations were minimized ( $<30\ \text{mM}$ ) to account for its toxicity. The animals were imaged on a PET/CT scanner during the first 30 min post-injection and recovered from anesthesia after the scan. After 27 h ( $^{89}\text{Zr}$ -THPN) or 25 h post-injection ( $^{89}\text{Zr}$ -DFO) the animals were sacrificed and the total body  $^{89}\text{Zr}$  activity was

measured in a dose calibrator. Then, organs were excised, weighed, and their activity was counted in a  $\gamma$  counter and decay corrected to conduct a biodistribution.

### 3.4.11 PET/CT Imaging

Animals were imaged on a dedicated small animal PET/SPECT/CT scanner (VECTor/CT, MILabs) equipped with a HEUHR high energy multipinhole collimator suitable for PET isotopes. Dynamic whole body scans were acquired in list-mode format over 30 min. Following each PET acquisition, a whole body CT scan was performed to obtain anatomical information and both images were registered. The photopeak energy window was centered at 511 keV with a 20% energy window width. Throughout the entire scanning procedure, mice were kept under isoflurane anesthesia and constant body temperature was maintained using a heating pad. For quantitative analysis, PET data were reconstructed with ordered subset expectation maximization logarithm (OS-EM) using ten iterations of 16 subsets and 0.4 mm<sup>3</sup> voxel size. The images were decay corrected and after CT registration, attenuation correction was applied using MILabs proprietary software. Volumes of interest were manually defined using the software AMIDE (v.1.0.4) to determine the time activity pattern per target organ. Thus, the delineated regions were urinary bladder and background. In order to relate the scanner units (counts/pixel) to radioactivity concentration (mCi/mL), a calibration factor was determined by scanning a 12 mL syringe with a known concentration of <sup>89</sup>Zr.

# Chapter 4: Bifunctionalization of THPN and Study of $^{89}\text{Zr}$ -THPN Conjugates

## 4.1 Introduction

After the study of THPN with zirconium(IV) identified the tetrakis(3,4-HOPO) ligand as a very promising  $\text{Zr}^{\text{IV}}$ -chelator (Chapter 3), we set out to investigate THPN in conjunction with delivery vehicles. For this, a bifunctional derivative of THPN was first developed to allow covalent attachment to carrier molecules. In a nine-step synthesis, we produced a bifunctional THPN derivative bearing an isothiocyanate group on the backbone. This functional group is reactive to amino groups and can thus be tethered to any amine-bearing delivery vehicle. Once a bifunctional THPN ligand was produced, we investigated its conjugation and  $^{89}\text{Zr}$ -radiolabeling with four different carrier molecules; the two monoclonal antibodies trastuzumab and anti-programmed death ligand-1 (anti-PD-L1), the protein mouse serum albumin, as well as polymeric nanoparticles based on hyperbranched polyglycerol (HPG).

The radiolabeling of HPG radioconjugates was found to be particularly robust and thus, HPG was chosen as carrier molecule to examine the long-term radiocomplex stability *in vivo*. The behaviour of  $^{89}\text{Zr}$ -THPN-HPG radioconjugates was investigated in healthy mice in an acute biodistribution and PET/CT imaging study and was compared against two radiolabeled HPG conjugates prepared with literature chelators,  $^{89}\text{Zr}$ -DFO-HPG and  $^{89}\text{Zr}$ -DFO\*-HPG.

## 4.2 Results and Discussion

### 4.2.1 Synthesis of Bifunctional THPN

In order to allow covalent conjugation of THPN to delivery vehicles, a bifunctional derivative of THPN had to be produced. The central carbon of THPN's propyl backbone was chosen as position to install a conjugation handle in the form of a *para*-isothiocyanatobenzyl group. This positioning should allow the conjugation group to point away from the metal coordination groups to minimize interference between conjugated targeting molecules and metal complexation. Furthermore, this is the only position that maintains the symmetry of the molecule and thereby avoids the creation of chiral centres. Figure 4.1 depicts the intended bifunctional THPN derivative *p*-SCN-Bn-THPN **4.10** and the building blocks it may be synthesized from.

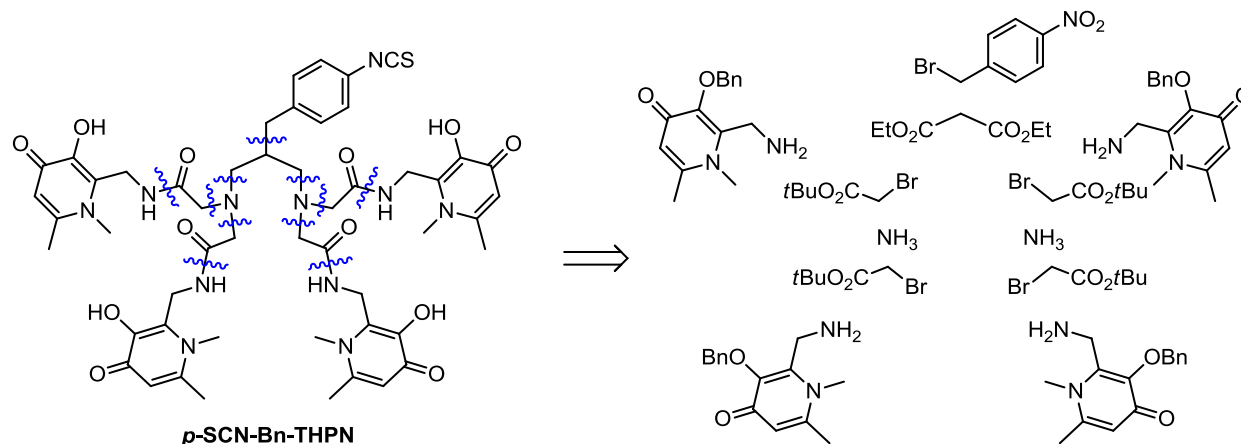
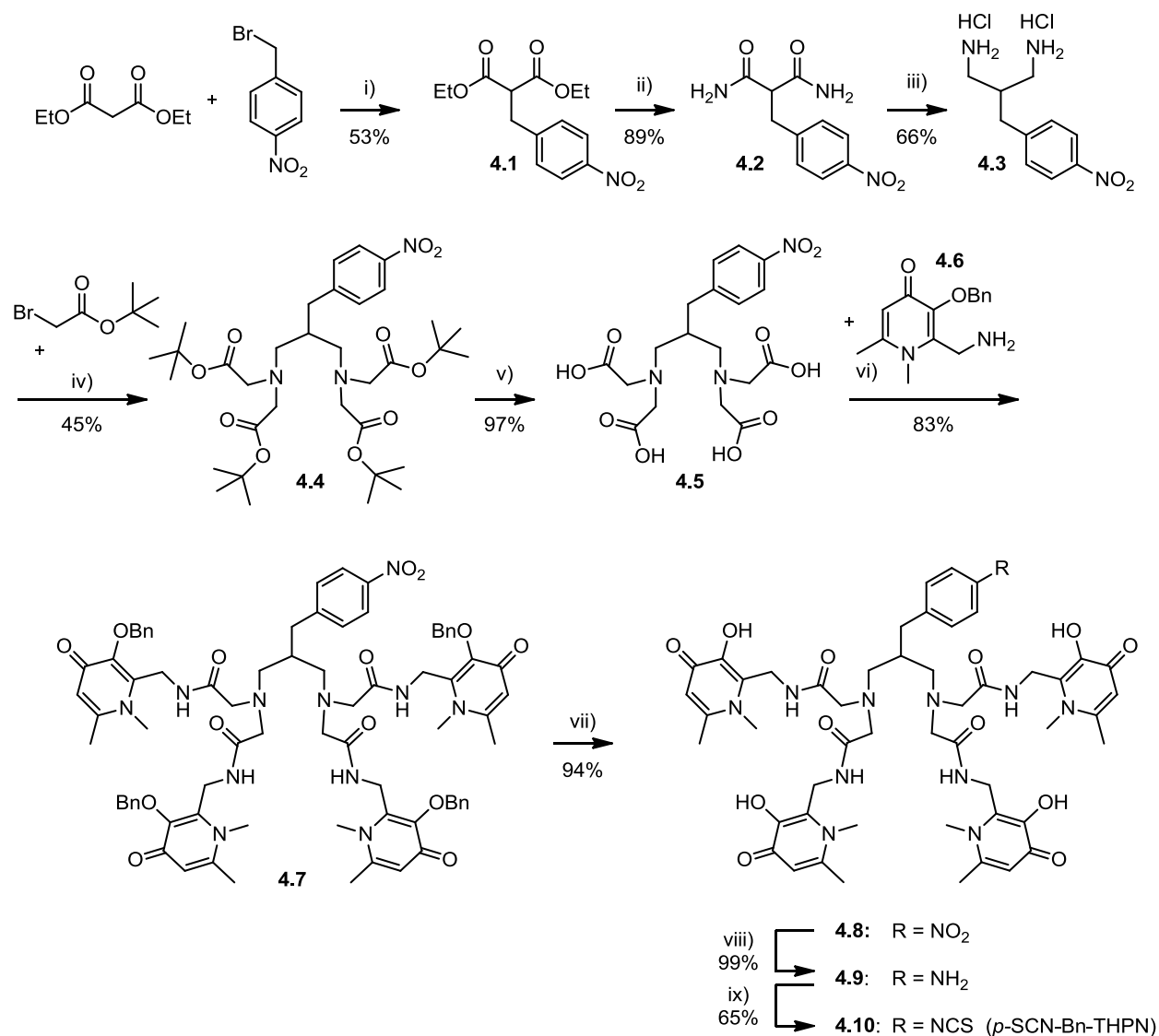


**Figure 4.1.** Retrosynthetic analysis of the intended bifunctional THPN derivative *p*-SCN-Bn-THPN reveals the building blocks from which the bifunctional chelator may be assembled.

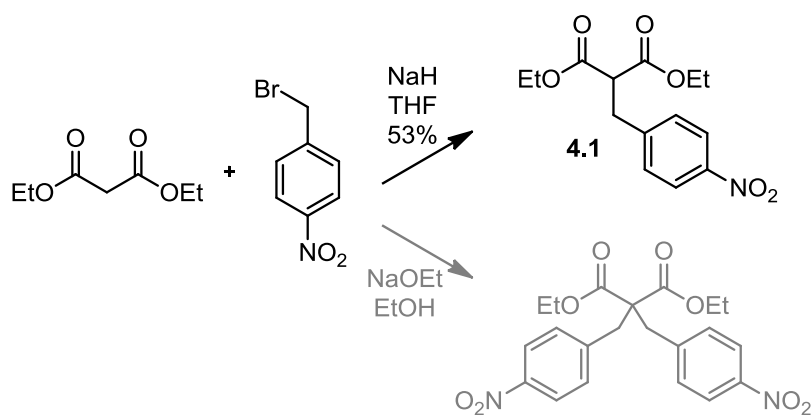


**Scheme 4.1.** Nine-step synthesis of the bifunctional ligand *p*-SCN-Bn-THPN, **4.10**. i) NaH, THF, 35 °C; ii) NH<sub>3</sub>, MeOH, RT; iii) BH<sub>3</sub>·THF, THF, RT; iv) Na<sub>2</sub>CO<sub>3</sub>, DMF, RT; v) H<sub>3</sub>PO<sub>4</sub>, MeCN, 45 °C; vi) DCC, HOBt, DMF, MW 55 °C; vii) AcOH/HCl (conc.), 50 °C; viii) H<sub>2</sub>, Pd/C, MeOH, RT; ix) CSCL<sub>2</sub>, CHCl<sub>3</sub>/H<sub>2</sub>O, RT. Cumulative yield over nine steps: ~7%.

The nine-step synthesis of the bifunctional chelator *p*-SCN-Bn-THPN **4.10** is presented in Scheme 4.1. The benzyl-protected HOPO-methylamine building block **4.6** is a relatively expensive starting material and was the limiting reagent in this synthesis. We therefore introduced the HOPO motif only at a late stage in the synthesis to reduce losses of this starting material. We chose to install the conjugation handle at the beginning of the synthesis, similarly

to a strategy pursued by Price *et al.*<sup>156</sup> The conjugation handle should be introduced in the form of a protected *para*-nitrobenzyl group which could be converted in the last reaction steps into a reactive *para*-isothiocyanatobenzyl group. After installation of the *para*-nitrobenzyl group, the four arms of the backbone should be assembled to allow subsequent coupling with four HOPO binding units. The final steps involved deprotections and activation of the conjugation handle as isothiocyanate group, which is reactive towards conjugation to amino group bearing delivery vehicles.

The first step of the reaction sequence involved the alkylation of the C3 building block diethyl malonate with 4-nitrobenzyl bromide (Scheme 4.2). Initially, we tried to reproduce a literature procedure<sup>156</sup> that uses sodium ethoxide as a base in ethanol. In our hands, this procedure, however, only led to the doubly alkylated product (Scheme 4.2). Variation of stoichiometry or temperature did not change this, but a workaround was found by changing the base and solvent. Following a different literature procedure,<sup>157</sup> we employed sodium hydride as base with the solvent tetrahydrofuran. This approach produced the intended mono-alkylated product **4.1** in 53% yield, similar to the literature protocol (52%).



**Scheme 4.2.** Alkylation of diethyl malonate greatly depends on reaction conditions leading to addition of either one or two equivalents of nitrobenzyl.

The next step involved the preparation of the diamide **4.2** by conversion of the two ethyl ester groups of **4.1** into amides. Following a reported procedure,<sup>156</sup> compound **4.1** was treated with methanolic ammonia to produce the diamide **4.2** in 89% yield (literature: 83%). Next, the amide groups were reduced to primary amines. Similarly to reported procedures,<sup>156, 158</sup> compound **4.2** was reacted with borane in THF to produce the diamine, which was isolated as dihydrochloride salt in 66% yield (literature: 60%). In order to introduce the four ligand arms, the two amino groups were then alkylated each with two equivalents of *tert*-butyl bromoacetate using sodium carbonate as a base. This produced the tetrakis(*tert*-butyl ester) **4.4** in ~46% yield. In the next step the *tert*-butyl ester protection groups were hydrolyzed to give the corresponding carboxylic acids. Attempts to saponify **4.4** using lithium hydroxide remained unsuccessful. This could, however, be overcome by employing aqueous *ortho*-phosphoric acid, which Li *et al.*<sup>159</sup> described as a mild deprotection reagent for *tert*-butyl esters. In this way, the deprotected tetraacid **4.5** was obtained in near-quantitative yield (97%).

Next, four equivalents of the benzyl-protected HOPO-methylamine **4.6** (2-(aminomethyl)-1,6-dimethyl-3-(phenylmethoxy)-4(1*H*)-pyridinone) were conjugated to the tetraacid **4.5**, similar to the amide couplings in the THPN synthesis (Chapter 3). The reaction was conducted in a microwave reactor with gentle heating and the coupling reagents DCC/HOBt were employed as before. The carbodiimide DCC is a reliable and widely used amide coupling reagent. It can, however, also lead to side reactions and forms different by-products that can be difficult to remove (Figure 4.2).

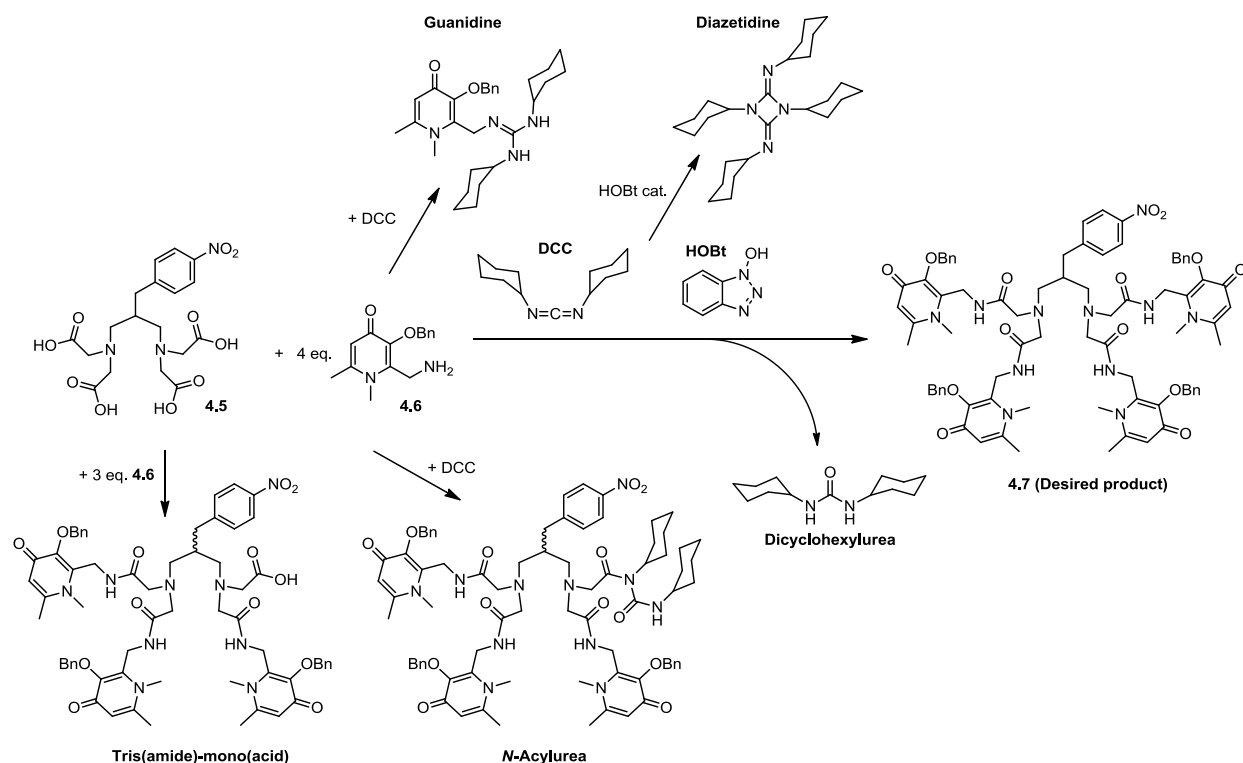


**Figure 4.2.** Possible side products and by-products that can form during the amide coupling reaction between compounds 4.5 and 4.6 in addition to the desired product 4.7.

Several steps were taken to minimize the formation of side products. The coupling mechanism of carbodiimide-mediated amide formation proceeds *via* an *O*-acylurea intermediate. This intermediate can either react with the amine to form the intended amide, or it can convert into an unreactive *N*-acylurea in an irreversible side reaction. In order to minimize this side reaction, HOBt was used as a coupling additive. HOBt is believed to react with the *O*-acylurea to form a more stable active ester intermediate, which can then react with the amine to produce the desired amide product.<sup>160-163</sup> Not only the acid, but also the amine 4.6 appears to react with DCC to irreversibly form a guanidine side product (Figure 4.2). To minimize this loss of valuable starting material, the tetraacid 4.5 was first reacted with DCC and HOBt alone for two hours to allow reaction time to form the active ester intermediate, before addition of the amine 4.6. The reaction was closely monitored by HPLC to follow the formation of product, as

well as side products. HPLC also proved very helpful in the optimization of the purification of the fairly complex reaction mixture. Filtration and purification by reversed phase flash chromatography was found to be an effective purification method. Elution with an acetonitrile gradient produced the tetraamide product **4.7** pure in ~83% yield. Using acetonitrile instead of methanol as organic component of the eluent was found to separate the product better from the coupling by-product *N,N'*-dicyclohexylurea (DCU), which is well soluble in MeOH but only sparingly soluble in MeCN.

The next two reactions involved the debenzoylation of the HOPO hydroxyls and the reduction of the *p*-nitrobenzyl group. Both of these conversions can be conducted in a single reaction step by acidic hydrogenation. Yet, we chose to perform the reactions in two separate steps, which allowed better control over the reaction and improved yield. First, the four debenzoylations were performed by heating overnight in a mixture of glacial acetic acid and concentrated hydrochloric acid. This gave the tetrakis(HOPO) compound **4.8** in excellent yield (94%). Next, the nitro group of **4.8** was reduced to its aniline analog by hydrogenation over a heterogeneous palladium catalyst to quantitatively produce compound **4.9**. It should be noted that the choice of the filter aid used during workup was found to be of importance. When the reaction mixture was passed through a filter plug of regular Celite® 545, a red-brown coloured filtrate was obtained and <sup>1</sup>H NMR peaks showed peak broadening. This may be the result of complexation of metal ion impurities (*e.g.*, Fe<sup>3+</sup>) that may be present in the filter material. This assumption is supported by the very similar colour of the Fe-THPN complex. When instead an acid-washed diatomaceous earth was used as filter aid, namely AW Standard Super-Cel®, the product was obtained colourlessly and NMR peaks were markedly sharper, suggesting no metal complexation.

Lastly, in order to activate the conjugation handle, the aniline group of **4.9** was converted into its isothiocyanate derivative by reaction with thiophosgene in a biphasic chloroform/water mixture. Purification in several batches by semi-preparative HPLC and reversed phase flash chromatography gave the activated bifunctional chelator *p*-SCN-Bn-THPN (**4.10**) in ~65% yield.

Cumulative yield over the entire nine-step synthesis was ~7%. It is worth mentioning that most of the lower yielding reactions occurred at the beginning of the multi-step synthesis where starting materials were inexpensive and readily available. The valuable HOPO-building block **4.6** was introduced at a later stage during the synthesis and the cumulative yield over the remaining four reaction steps of 50% was relatively high in comparison.

#### 4.2.2 <sup>89</sup>Zr-Trastuzumab Radioimmunoconjugates

Once the bifunctional derivative *p*-SCN-Bn-THPN was produced, its conjugation and <sup>89</sup>Zr-radiolabeling was investigated with several carrier molecules. First, the antibody trastuzumab was explored as a targeting vector. Trastuzumab is a humanized monoclonal antibody (mAb) that targets the human epidermal growth factor receptor 2 (HER2).<sup>164</sup> The transmembrane tyrosine kinase receptor HER2 is involved in the regulation of cell proliferation and survival. HER2 can be overexpressed in a variety of cancers and in particular in breast and stomach cancers, HER2 overexpression is associated with poor prognosis.<sup>165, 166</sup> Thus, the immunoglobulin G (IgG) trastuzumab (Herceptin<sup>®</sup>) is an approved treatment for HER2-positive breast and metastatic stomach cancers.

Conjugation and radiolabeling of trastuzumab with bifunctional THPN was explored pursuing either a postlabeling or a prelabeling strategy (Figure 4.3). In the postlabeling approach, the chelator is first tethered to the targeting vector and the resulting

immunoconjugate is radiolabeled in the second step. In contrast, in the prelabeling approach, the bifunctional chelator is first radiolabeled, following conjugation to the targeting vector.<sup>167</sup> The postlabeling approach is more commonly used for <sup>89</sup>Zr-radiolabeling as it allows for better control of the conjugation stoichiometry and for purification of the immunoconjugate from unreacted chelator. This often leads to higher radiochemical yields and specific activities (*i.e.*, [labeled mAb]/[unlabeled mAb]). A prelabeling strategy, on the other hand, also holds advantages. It can be particularly useful when only small amounts of targeting vector are available (such as expensive investigational mAbs) or when high toxicity is of concern as this approach reduces the number of handling steps.<sup>101</sup> Prelabeling is also an advantageous strategy if the radiolabeling requires harsh reaction conditions such as temperatures, solvents, or a pH that would compromise targeting vector integrity.<sup>167</sup>

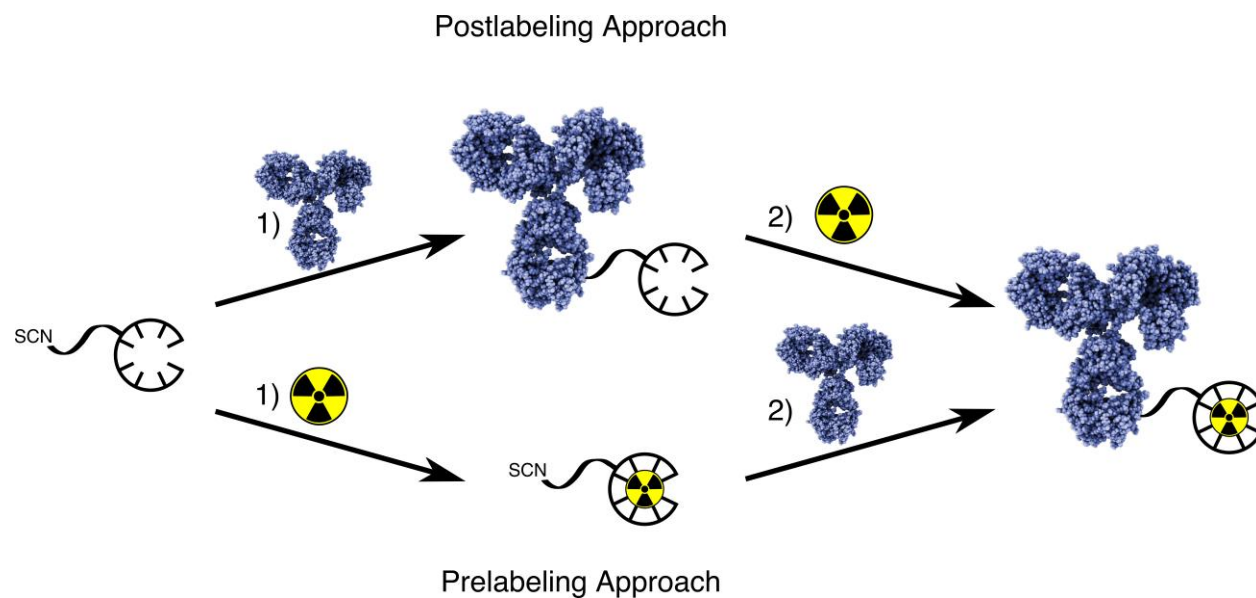
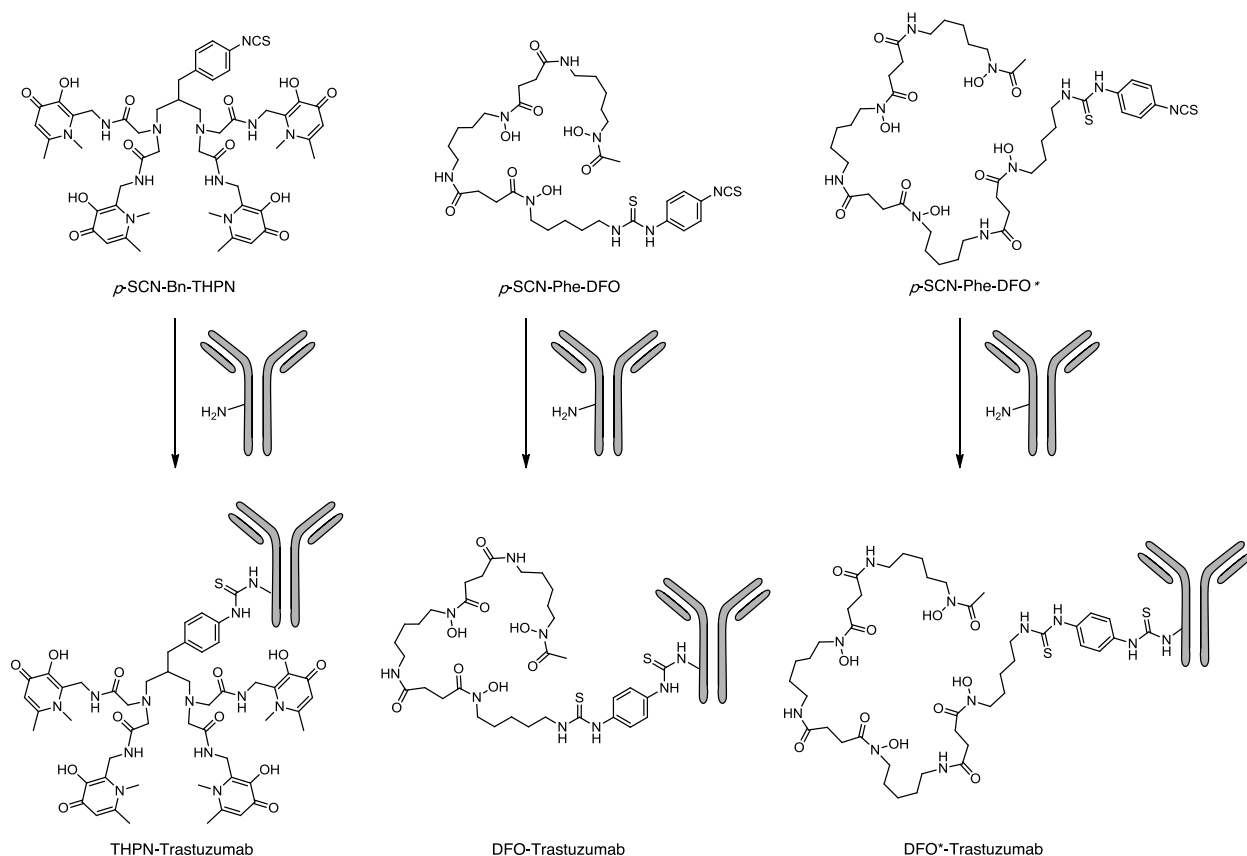


**Figure 4.3.** Two strategies can be pursued for the conjugation and radiolabeling of a bifunctional chelator. In the postlabeling approach (top), the chelator is first tethered to the targeting vector and the immunoconjugate is radiolabeled in the second step. In contrast, in the prelabeling approach (bottom), the bifunctional chelator is first radiolabeled and conjugated to the targeting vector in the second step. (mAb structure generated with QuteMol<sup>49</sup> from protein data bank entry 1igy<sup>50</sup>).

#### 4.2.2.1 $^{89}\text{Zr}$ -Labeling of Trastuzumab by Postlabeling

First, a postlabeling strategy was pursued since THPN exhibited fast radiolabeling kinetics with  $^{89}\text{Zr}$  at ambient temperature (Chapter 3). In analogy to a protocol by Vosjan *et al.*,<sup>168</sup> we modified trastuzumab with a five-fold molar excess of *p*-SCN-Bn-THPN by conjugation of the chelator's isothiocyanate group to amino groups of random mAb lysine residues (Scheme 4.3). The product was purified by size-exclusion chromatography (SEC) and/or ultrafiltration and the THPN-immunoconjugate was analyzed by SE-HPLC and by gel electrophoresis (SDS-PAGE) in which no changes were observed from unmodified trastuzumab. Analysis by MALDI-TOF mass spectrometry according to a published procedure<sup>169</sup> also confirmed a slight



**Scheme 4.3.** Modification of trastuzumab with the three chelators *p*-SCN-Bn-THPN, *p*-SCN-Phe-DFO, and *p*-SCN-Phe-DFO\*.

increase in average protein mass from 147.8 kDa to 148.5 kDa due to the conjugated chelator. Equivalent conjugations were also performed with the two literature chelators *p*-SCN-Phe-DFO and *p*-SCN-Phe-DFO\* as comparisons (Scheme 4.3). All three immunoconjugates showed no noticeable changes in their chromatograms on SE-HPLC.

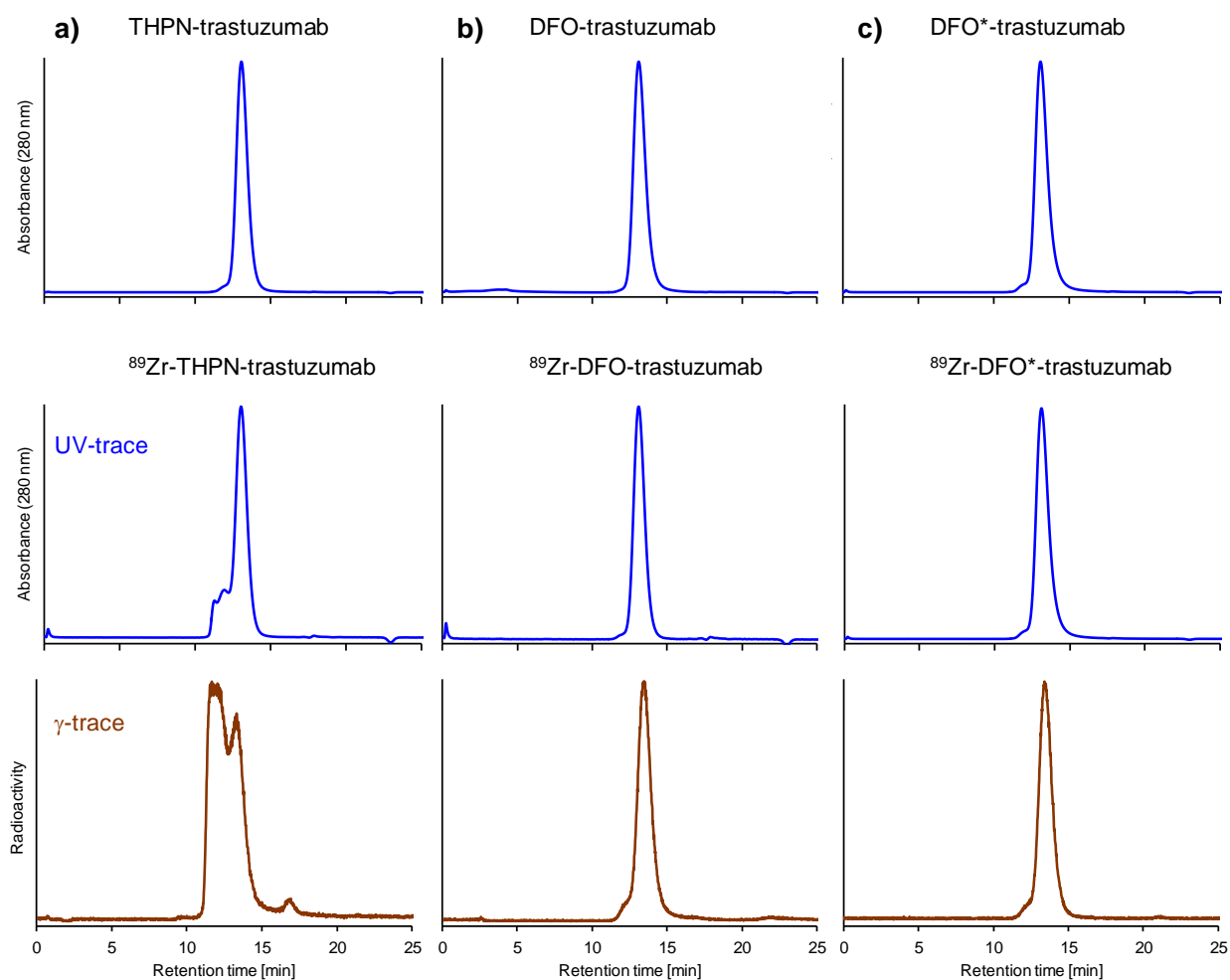


**Figure 4.4.** (Radio-)SE-HPLC chromatograms of a) THPN-, b) DFO-, and c) DFO\*-modified trastuzumab before (top) and after <sup>89</sup>Zr-radiolabeling by postlabeling (centre and bottom).

The three immunoconjugates were then radiolabeled with <sup>89</sup>Zr following the method by Vosjan *et al.*<sup>168</sup> and the reactions were monitored by ITLC (complexed <sup>89</sup>Zr-immunoconjugate:  $R_f \sim 0$ ; <sup>89</sup>Zr-oxalate:  $R_f \sim 1$ ). Once ITLC indicated satisfactory radiolabeling (typically near-

quantitative), the mixtures were purified by size-exclusion chromatography and/or ultrafiltration and were analyzed by radio-SE-HPLC (Figure 4.4).

The chromatograms of the DFO- and DFO\* radioimmunoconjugates looked as expected and showed a single major peak in the UV- and  $\gamma$ -traces that matched the unmodified and chelator-conjugated mAbs before labeling. Radiolabeling of the THPN-conjugate, on the other hand, led to multiple peaks in the radiochromatogram. While one peak matched the retention time of the intended radioimmunoconjugate, another large peak eluted at an earlier retention time, indicating the presence of species of larger molecular size. A small peak at a later retention time matched in retention time with  $^{89}\text{Zr}$ -oxalate and indicated presence of free  $^{89}\text{Zr}^{4+}$  or small sized  $^{89}\text{Zr}$  species. Moreover, this peak grew considerably after storage over three days at ambient temperature, suggesting a release of  $^{89}\text{Zr}$  from the larger species. We speculate that the large species are  $^{89}\text{Zr}$ -labeled antibody aggregates, such as antibody dimers or trimers, which is in line with analyses by gel electrophoresis (SDS-PAGE).

Various efforts were made to minimize the formation of aggregates and the radiolabeling was repeated with different batches of chelator and with modifications to a range of radiolabeling parameters. These modifications included: the THPN/mAb stoichiometry, the radiolabeling pH, the order of reagent addition, the concentration of immunoconjugate, the  $^{89}\text{Zr}$  activity concentration, the labeling buffer (PBS, HEPES, acetate), presence or absence of citrate as a transfer ligand, presence or absence of gentisic acid as protectant from radiolysis, the purification method (SEC *vs.* ultrafiltration), the form of  $^{89}\text{Zr}$  starting material ( $^{89}\text{Zr}$ -oxalate *vs.*  $^{89}\text{ZrCl}_4$ ), and the  $^{89}\text{Zr}$  sourcing and production method (solid *vs.* liquid  $^{89}\text{Y}$  target). Under certain conditions, the formation of aggregates could be reduced for small radiolabeling reactions (albeit with some inseparable free  $^{89}\text{Zr}$ ), yet when the reactions were scaled up to larger amounts of  $^{89}\text{Zr}$ , the aggregate formation increased again (Figure 4.5).

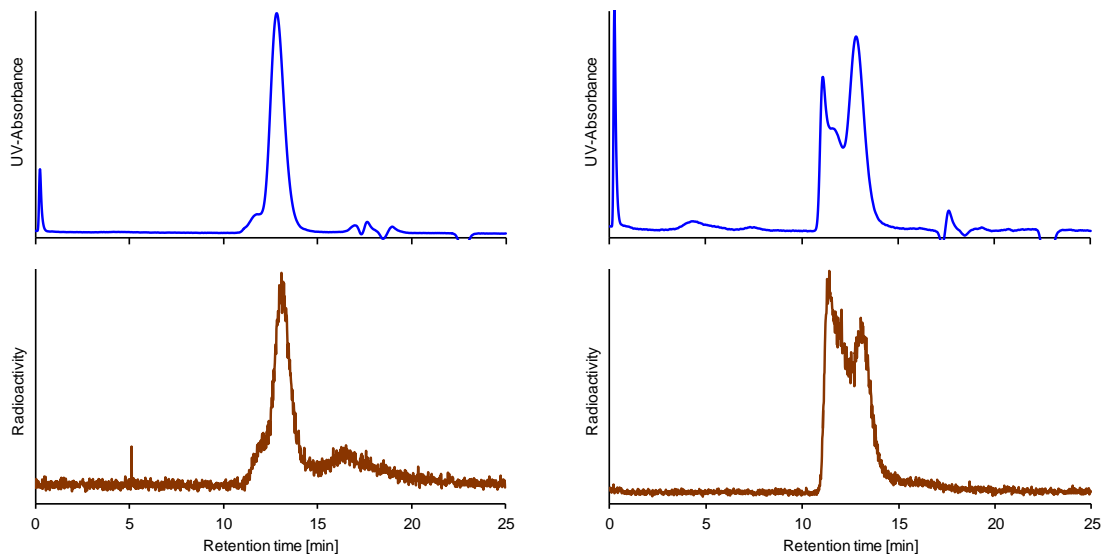


**Figure 4.5.** Radio-SE-HPLC chromatograms of  $^{89}\text{Zr}$ -THPN-trastuzumab using improved postlabeling conditions showed less aggregates on a small scale (left), but when repeated with more  $^{89}\text{Zr}$ , aggregate formation was again more pronounced (right).

To explore a different conjugation chemistry, a tetrazine-bearing THPN derivative (Tz-THPN) was produced. The 1,2,4,5-tetrazine group (Tz) can undergo an inverse electron demand [4 + 2] Diels-Alder (IEDDA) cycloaddition reaction with *trans*-cyclooctene (TCO). This conjugation reaction has recently been introduced as a bioorthogonal click reaction for pretargeting and *in vivo* click coupling.<sup>170-175</sup> To this end, we synthesized a PEG<sub>4</sub>-spaced THPN-tetrazine derivative **4.12** (Tz-THPN) by reacting *p*-SCN-Bn-THPN with a commercially available methyl-tetrazine amine (MeTz-PEG<sub>4</sub>-NH<sub>2</sub>) and purified it by reversed phase flash chromatography (Appendix D, Figure D.1). Meanwhile, trastuzumab was modified with TCO groups by reaction with a commercially available TCO active ester (TCO-NHS, Appendix D, Figure D.1). A colorimetric assay with a dye-tetrazine revealed an average presence of 1.8 reactive TCO groups per mAb when a 35 molar excess of TCO active ester was used.

Following this click conjugation strategy,  $^{89}\text{Zr}$ -radiolabeling was pursued both in a prelabeling and in a postlabeling approach (Appendix D, Figure D.1). Yet the results were not

satisfactory and the produced radioimmunoconjugates still showed aggregates as well as a tendency to stick to the HPLC tubing rendering such analyses difficult to interpret.

The limitations encountered with the postlabeling strategy and the persistent challenges with the Tz/TCO click conjugation approach motivated us to investigate radiolabeling of trastuzumab by a prelabeling approach.

#### 4.2.2.2 $^{89}\text{Zr}$ -Labeling of Trastuzumab by Prelabeling

With the aim of reducing the aggregate formation, a prelabeling approach was explored for the radiolabeling of THPN and trastuzumab. The bifunctional chelator (~51 nmol) was first complexed with a neutralized  $^{89}\text{Zr}^{4+}$  solution (~11 MBq, 300  $\mu\text{Ci}$ ) and analyzed after ten minutes by ITLC, which showed quantitative radiolabeling. At this point, unmodified trastuzumab (~1.5 mg) was added and the pH was raised to pH ~9 to allow thiourea bond formation between the radiocomplex and trastuzumab. After purification by size-exclusion chromatography,  $^{89}\text{Zr}$ -THPN-trastuzumab was isolated in 52% radiochemical yield and radio-SE-HPLC showed that the formation of aggregates could indeed be suppressed and the product was obtained in ~93% radiochemical purity (HPLC). The radioimmunoconjugate eluted as a single peak with only a very small shoulder (Figure 4.6A). The peak matched the retention time of unmodified trastuzumab and remained stable over three days when stored at 4 °C. Analysis by gel electrophoresis (SDS-PAGE, 7.5%) furthermore confirmed that trastuzumab was successfully radiolabeled and autoradiographic development clearly showed that the  $^{89}\text{Zr}$  activity was associated with the antibody band of around 146 kDa (Figure 4.6B). Only a very faint second band at around 250–300 kDa suggested minimal amount of presumably dimerized mAb, which is in line with the small shoulder observed in the radiochromatogram.

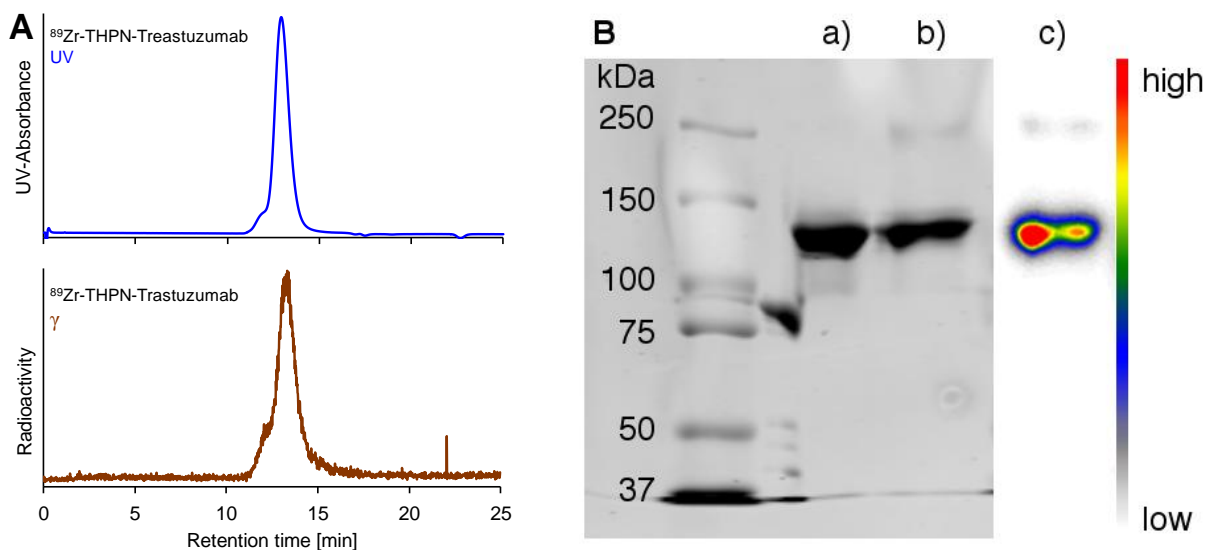


**Figure 4.6.** Analyses of  $^{89}\text{Zr}$ -THPN-trastuzumab produced by a prelabeling approach (A) by radio-SE-HPLC and (B) by gel electrophoresis. Coomassie blue staining of the SDS-PAGE (7.5%) gel shows a) unmodified trastuzumab (146 kDa) and b)  $^{89}\text{Zr}$ -THPN-trastuzumab of equivalent size. Autoradiography c) of lane b) shows clear association of  $^{89}\text{Zr}$  with the mAb band.

Scaling the radiolabeling up with more  $^{89}\text{Zr}$  (~47 MBq, 1.3 mCi) and less mAb was successful but remained challenging. Relatively large amounts of chelator (~17 nmol) were required to obtain sufficient radiolabeling and avoid presence of free  $^{89}\text{Zr}$ . This had to be pursued since the removal of unchelated  $^{89}\text{Zr}$  was found to be challenging and inefficient. A larger amount of chelator in turn required more antibody (~0.5 mg) to maintain a feasible conjugation ratio between mAb and radiochelate and therefore limited the attainable specific activity. Additionally, considerable amounts of activity were lost adhering to the reaction vial (~40%) or stuck to the size-exclusion column (~20%) during purification. Thus, the radioimmunoconjugate was isolated in ~22% radiochemical yield with a radiochemical purity of around 80% (radio-SE-HPLC). The specific activity was estimated as ~10 MBq/mg, 260  $\mu\text{Ci}/\text{mg}$ . The losses of  $^{89}\text{Zr}$  during the synthesis might be caused by hydrolysis of the isothiocyanate group, which at alkaline pH directly competes with the conjugation reaction to the antibody.

Additionally, the solubility of  $^{89}\text{Zr}$ -THPN-NCS appeared to be limited and could explain precipitation and adhesion of the radiocomplex to the reaction vial, rendering it unavailable for reaction with the mAb and, thus, lowering the yield.

The relatively low specific activity limited the possibility to perform a quantitative *in vivo* study by PET/CT imaging. Instead, an *in vitro* plasma stability study was conducted.

#### 4.2.2.3 *In Vitro* Plasma Stability Study

The stability of the  $^{89}\text{Zr}$ -THPN-trastuzumab radioimmunoconjugate was assessed in an *in vitro* plasma stability study. As a comparison, radioimmunoconjugates were also produced with the two literature chelators DFO and DFO\*. For consistency, these were also produced in a prelabeling strategy for this study. Vugts *et al.*<sup>101</sup> reported that the prelabeling approach was only successful with DFO\* and did not work with DFO. In our hands, however, both chelators could be prelabeled with  $^{89}\text{Zr}$  (5.4 MBq, 145  $\mu\text{Ci}$ ) and be conjugated to trastuzumab (~1.5 mg). The DFO- and DFO\*-radioimmunoconjugates were isolated in 58% and 55% radiochemical yield, respectively, and radiochemical purities of >99% (radio-SE-HPLC).

To conduct the *in vitro* plasma stability study the radioimmunoconjugates with either THPN, DFO, or DFO\* as chelator were diluted in mouse plasma and were incubated for seven days at 37 °C. The integrity of the radiocomplexes was assessed by analyzing aliquots by ITLC after 1, 3, 5, and 7 days of incubation. The experiment was conducted in duplicate and the results are presented in Table 4.1. As control, a freshly neutralized solution of  $^{89}\text{Zr}$ -oxalate was also incubated with mouse plasma and showed only very minor  $^{89}\text{Zr}$ -binding over seven days. The THPN and DFO radioimmunoconjugates remained largely intact and the DFO\* conjugate showed no signs of demetallation. Thus, all three radioimmunoconjugates remained over 95%

intact over seven days indicating reliable complex stability under these simulated physiologic conditions.

**Table 4.1.** Plasma stability of  $^{89}\text{Zr}$ -chelate-trastuzumab radioimmunoconjugates.<sup>a</sup>

<b>Radioimmunoconjugate</b>	<b>Day 0</b>	<b>Day 1</b>	<b>Day 3</b>	<b>Day 5</b>	<b>Day 7</b>
<b><math>^{89}\text{Zr}</math>-THPN-trastuzumab</b>	>99%	>99%	99%	99%	95%
<b><math>^{89}\text{Zr}</math>-DFO-trastuzumab</b>	99%	>99%	>99%	94%	99%
<b><math>^{89}\text{Zr}</math>-DFO*-trastuzumab</b>	>99%	>99%	>99%	>99%	>99%
<b><math>^{89}\text{Zr}</math>-oxalate (control)</b>	0%	0%	4%	6%	6%

<sup>a</sup> Stability over time is reported as percentage bound  $^{89}\text{Zr}$  after incubation in mouse plasma at 37 °C, 550 rpm. Radioimmunoconjugate experiments were performed in duplicate and are reported as mean, while the control experiment with  $^{89}\text{Zr}$ -oxalate was performed once.

### 4.2.3 $^{89}\text{Zr}$ -Anti-PD-L1 Radioimmunoconjugates

In order to explore whether the postlabeling approach for THPN could be more successful with another antibody instead of trastuzumab, a postlabeling strategy was investigated with a monoclonal anti-mouse antibody that targets programmed death ligand-1 (PD-L1). PD-L1 is a transmembrane protein that acts as a ligand for the immune checkpoint receptor programmed death-1 (PD-1). Inhibition of PD-1 or PD-L1 has recently gained attention as a promising target for cancer immunotherapy and new methods to monitor their expression levels are currently being sought.<sup>176-185</sup>

In analogy to the postlabeling method used with trastuzumab, anti-PD-L1 mAb was first modified according to the protocol by Vosjan *et al.*<sup>168</sup> by reacting it with a ten-fold molar excess of *p*-SCN-Bn-THPN. The antibody size was assessed by SE-HPLC, where no change was detected upon chelator conjugation (Figure 4.7). The immunoconjugate was then radiolabeled in HEPES buffer (0.5 M, pH 7.0) with neutralized  $^{89}\text{Zr}$ -oxalate. After purification by SEC and/or ultrafiltration, only small amounts of aggregates were detected. In a first batch, when ~100 μg

immunoconjugate was radiolabeled with 7.5 MBq, 202  $\mu\text{Ci}$   $^{89}\text{Zr}$ -oxalate, the purified product (recovered in 44%) showed three peaks on radio-SE-HPLC (Figure 4.7). The main peak (~64%) matched the retention time of the mAb and confirmed radiolabeling of the THPN-anti-PD-L1 immunoconjugate. A small shoulder peak (~10%) detected at an earlier retention time indicates presence of some larger molecular size compounds, presumably antibody aggregates. Another small peak (~10%) was detected at a later retention time and was attributed to small molecular size  $^{89}\text{Zr}$  species, such as free  $^{89}\text{Zr}^{\text{IV}}$  or  $^{89}\text{Zr}$ -EDTA (from quenching) that could not be removed during purification. The product was recovered in 44% radiochemical yield with a radiochemical purity of around 64% as indicated by radio-SE-HPLC

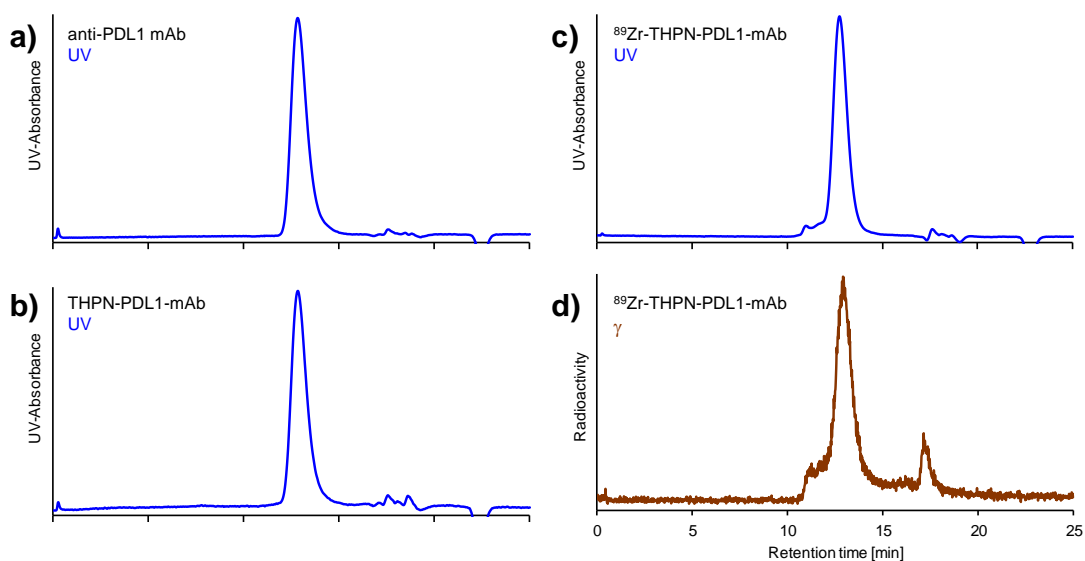


**Figure 4.7.** (Radio-)SE-HPLC chromatograms of a) unmodified anti-PD-L1 mAb, b) THPN-modified anti-PD-L1 mAb, and c & d)  $^{89}\text{Zr}$ -THPN-anti-PD-L1.

When in a different batch, larger amounts of both, immunoconjugate (~320  $\mu\text{g}$ ) and  $^{89}\text{Zr}$  activity (18 MBq, 476  $\mu\text{Ci}$ ) were used, the formation of aggregates was further reduced. However, a large second peak indicated more uncomplexed or free  $^{89}\text{Zr}$  species that could not be removed by SEC or ultrafiltration (Figure 4.8). It should be mentioned that a different SE-

HPLC column was used compared to the previous batch in an attempt to better separate the species, explaining the difference in retention times. The HPLC chromatogram further showed some streaking and adhesion of activity to the radiation detector, rendering this method not very conclusive (Figure 4.8). Analysis by SDS-PAGE, however, confirmed that the immunoconjugate was radiolabeled and only a small band at larger molecular size indicated the presence of larger sized aggregates (Figure 4.9). Small molecular sized activity may have been missed with this analytical method missed as it could have run off the gel and thus were excluded from autoradiographic exposure.

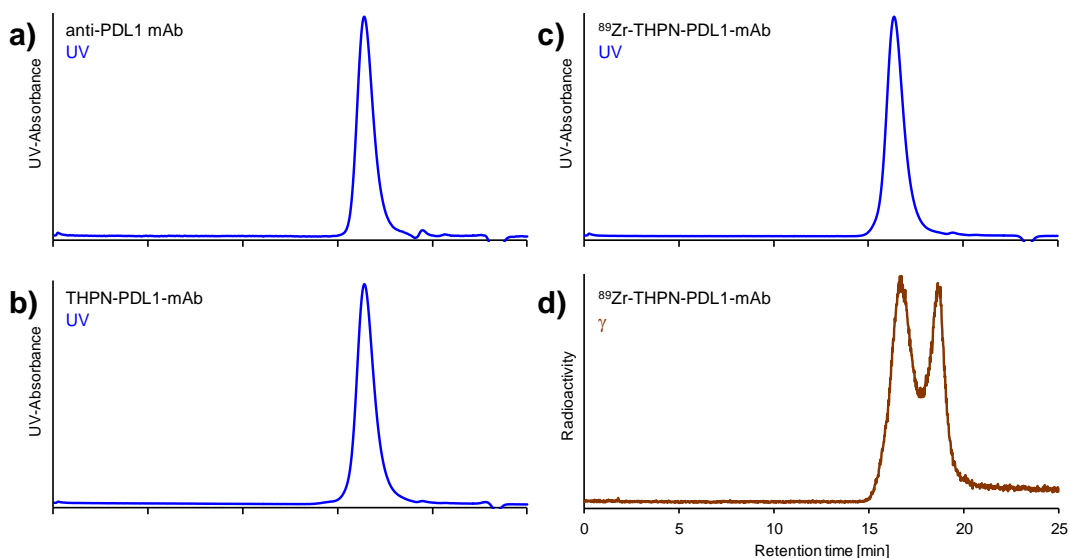


**Figure 4.8.** (Radio-)SE-HPLC chromatograms of a) unmodified anti-PD-L1 mAb, b) THPN-modified anti-PD-L1 mAb, c & d) <sup>89</sup>Zr-THPN-anti-PD-L1.

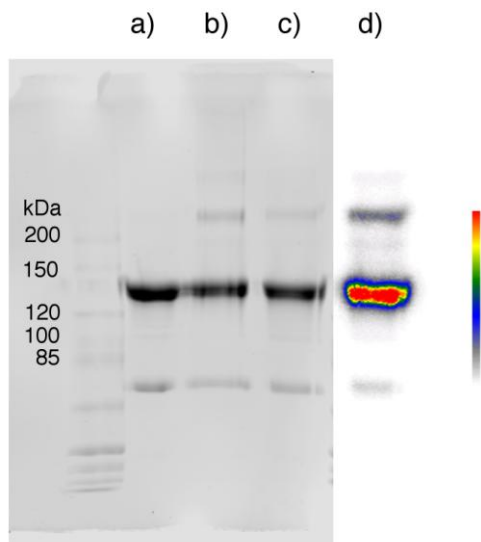


**Figure 4.9.** Analyses of anti-PD-L1 antibodies by SDS-PAGE (7.5%): a) unmodified anti-PD-L1 mAb, b) THPN-modified anti-PD-L1 mAb, c & d)  $^{89}\text{Zr}$ -THPN-anti-PD-L1; a-c) Coomassie blue stained, d) autoradiography of lane c).

These findings show that the radiolabeling of THPN-anti-PD-L1 by postlabeling remains challenging, but in contrast to trastuzumab, leads to considerably less antibody aggregation. The substantial aggregate formation observed for postlabeling of trastuzumab may therefore be the result of a particular incapability of trastuzumab's protein structure with the physicochemical properties of the  $^{89}\text{Zr}$ -THPN complex.

Proteins and antibodies in particular, are known to be susceptible to aggregation when modified with conjugates. This can be particularly often observed in the development of antibody drug conjugates (ADCs) with hydrophobic drugs, which induce a strong tendency to aggregate.<sup>186, 187</sup> Antibody aggregation was also reported as a potential pitfall for the production of radioimmunoconjugates.<sup>103, 187, 188</sup> The physicochemical properties of the attached chelates affect the native antibody structure and can lead to unfolding of subdomains or exposure of regions that can increase the tendency for aggregation.<sup>187</sup> Different antibodies that possess a

different amino acid sequence and tertiary structure may be more or less susceptible to a given modification.

#### 4.2.4 $^{89}\text{Zr}$ -Mouse Serum Albumin (MSA) Radioconjugates

To explore  $^{89}\text{Zr}$ -labeling of a different protein than an antibody with THPN, mouse serum albumin (MSA) was radiolabeled employing a postlabeling approach. MSA was modified with a tenfold molar excess of *p*-SCN-Bn-THPN and purified by size-exclusion chromatography. Analysis by SE-HPLC and gel electrophoresis indicated no noticeable changes upon modification. The THPN-MSA conjugate (~264  $\mu\text{g}$ ) was then radiolabeled in HEPES buffer (0.5 M, pH 7.0) with a neutralized solution of  $^{89}\text{Zr}$ -oxalate (5.0 MBq, 134  $\mu\text{Ci}$ ). After purification by size-exclusion chromatography, the product was obtained in an excellent radiochemical yield of 98% and in radiochemical purity of ~88% (HPLC) with a specific activity of ~15 kBq/ $\mu\text{g}$ ; 0.42  $\mu\text{Ci}/\mu\text{g}$ . Analysis by radio-SE-HPLC showed a matching retention time of the radiolabeled conjugate with unmodified and THPN-modified MSA (Figure 4.10). The only difference observed was some peak tailing upon radiolabeling, which might be due to a change in overall polarity that led to difference in the interaction with the column material. Analysis by SDS-PAGE also showed a consistent molecular size between the unmodified (66 kDa), THPN-modified, and radiolabeled MSA (Figure 4.11). Autoradiography clearly associated the large majority of activity with the MSA protein. Only a faint band was noticed at a larger molecular size. However, this larger band was also observed for the unmodified MSA and might be due to impurity of the starting material. Storage of the  $^{89}\text{Zr}$ -THPN-MSA radioconjugate for six days at ambient temperature or at 4 °C did not cause changes in radio-SE-HPLC indicating a good stability of the radioconjugate.

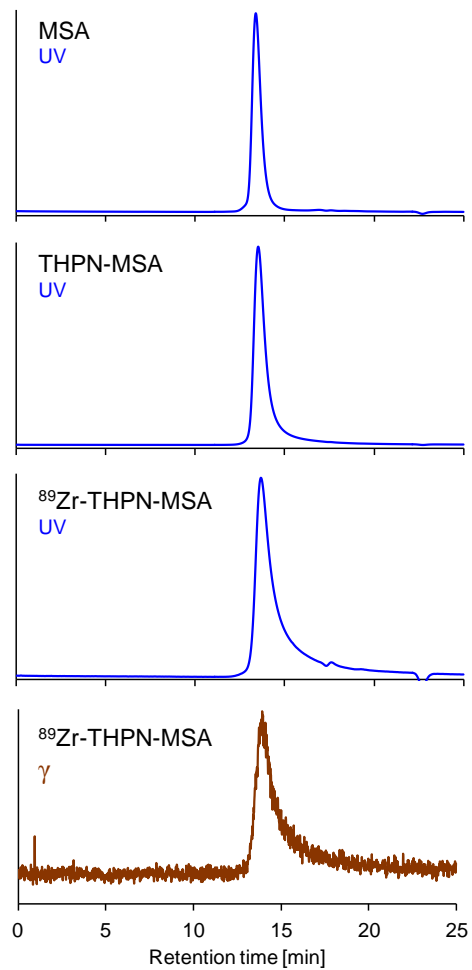


**Figure 4.10.** (Radio-)SE-HPLC chromatograms of unmodified MSA, THPN-modified MSA, and radiolabeled <sup>89</sup>Zr-THPN-MSA.

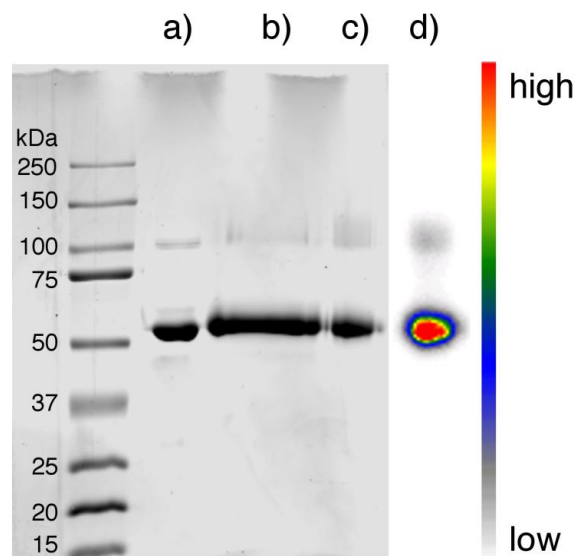


**Figure 4.11.** Analysis by SDS-PAGE (12%) of a) unmodified MSA (66 kDa), b) THPN-modified MSA, c & d) radiolabeled  $^{89}\text{Zr}$ -THPN-MSA; a-c) Coomassie blue stained, d) autoradiography of lane c) showing clear association of  $^{89}\text{Zr}$  with the MSA protein.

## 4.2.5 $^{89}\text{Zr}$ -Hyperbranched Polyglycerol (HPG) Radioconjugates

### 4.2.5.1 Chelator Conjugation and Radiolabeling

In order to evaluate the long-term stability of the  $^{89}\text{Zr}$ -THPN radiocomplex and compare it to the literature chelators DFO and DFO\*, polymeric nanoparticles based on hyperbranched polyglycerol (HPG) were selected as carrier molecules. HPG particles are highly biocompatible<sup>189-193</sup> and can be readily synthesized as globular macromolecules with narrow size distributions. They have been investigated as drug delivery vehicles,<sup>194</sup> as blood plasma expanders,<sup>195</sup> as cell surface protectants,<sup>196</sup> or as carrier molecules for imaging agents.<sup>193, 197, 198</sup> Owing to the long circulation half-life of large molecular weight HPG, these nanoparticles are suitable carriers to test the long-term stability of attached cargo molecules.

The three chelators *p*-SCN-Bn-THPN, *p*-SCN-Phe-DFO, and *p*-SCN-Phe-DFO\* were conjugated to amine-functionalized HPG particles by thiourea bond formation. After incubation overnight, the modified HPG particles were purified by SEC and ultrafiltration. Analysis by dynamic light scattering (DLS) indicated that chelator modifications did not significantly affect the particle size and size distribution, which was corroborated by indistinguishable SE-HPLC chromatograms (Figure 4.12).

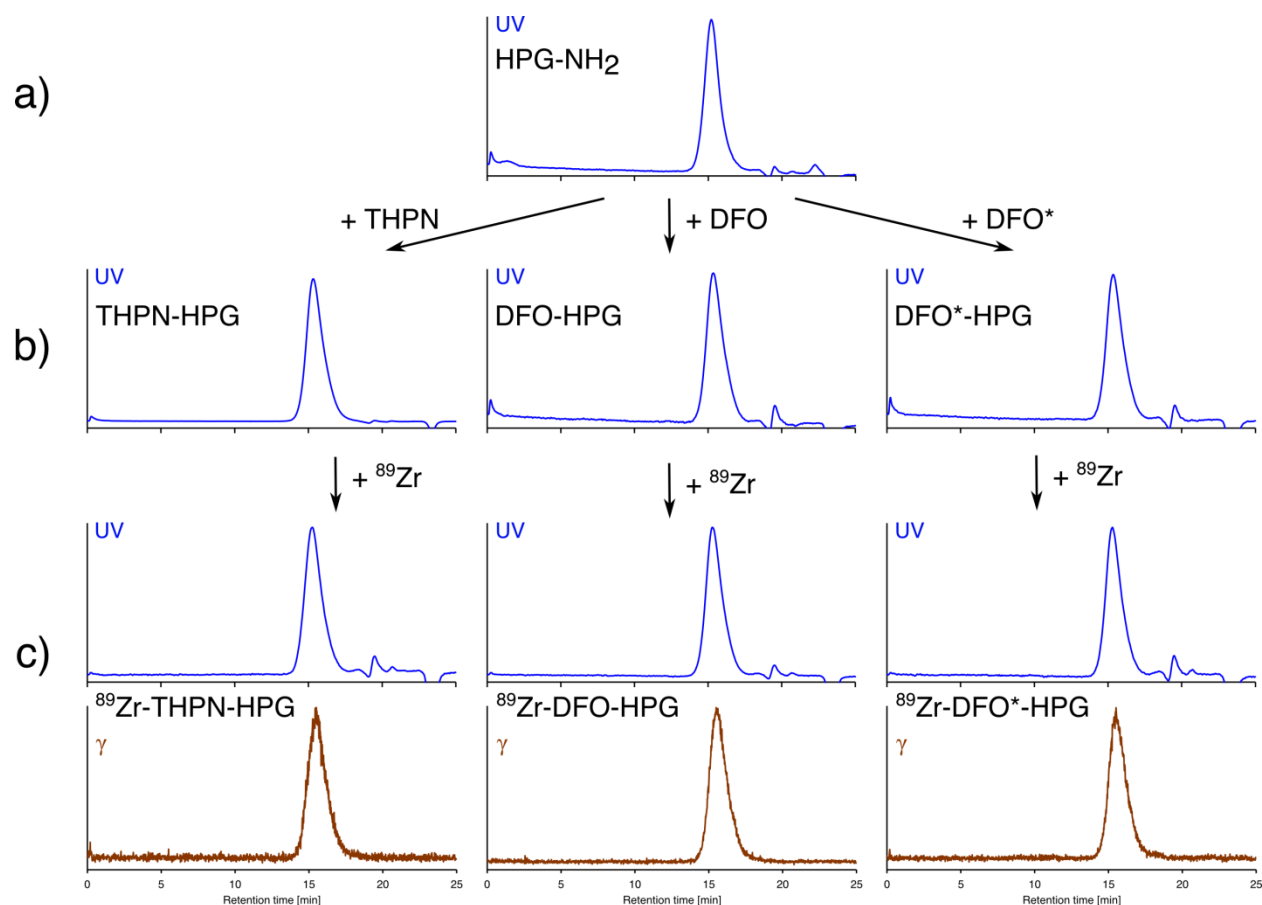


**Figure 4.12.** (Radio-)SE-HPLC chromatograms of a) unconjugated HPG-NH<sub>2</sub>, b) HPG-chelator conjugates, and c) radiolabeled <sup>89</sup>Zr-chelate-HPGs show no difference upon conjugation and radiolabeling.

The chelator-modified HPG nanoparticles were then radiolabeled at neutral pH with <sup>89</sup>Zr-oxalate solutions (~32 MBq, ~870 μCi). Once quantitative radiolabeling was reached, the reaction mixtures were purified by SEC and the radioconjugates were recovered in 97%

radiochemical yield for all three conjugates. The products were analyzed by ITLC and radio-SE-HPLC, which indicated >99% radiochemical purity and showed retention times and peak shapes that matched those of amino-HPG and chelator modified HPG particles (Figure 4.12). DLS analysis showed that the hydrodynamic diameter and polydispersity of the particles remained largely constant upon radiolabeling.

#### 4.2.5.2 *In Vitro* Plasma Stability of <sup>89</sup>Zr-HPG Conjugates

As a first indication of physiologic stability of the HPG radioconjugates, an *in vitro* plasma stability study was conducted. <sup>89</sup>Zr-HPG particles with either THPN, DFO, or DFO\* as chelator were diluted four-fold in human blood plasma and were incubated for five days at 37 °C. Aliquots were analyzed by ITLC after 1, 3, and 5 days. The fraction of intact radiocomplex was quantified by integration of the bound fraction of <sup>89</sup>Zr on ITLC plates, where complexed <sup>89</sup>Zr remained close to the baseline ( $R_f \sim 0$ ). The obtained results for the three radioconjugates are shown in Table 4.2. The DFO\* radioconjugate showed no signs of dissociation and also the other two radioconjugates remained largely intact and prevailed with >95% integrity after five days of exposure to plasma proteins.

**Table 4.2.** *In vitro* plasma stability of <sup>89</sup>Zr-chelate-HPG radioconjugates.<sup>a</sup>

Radioconjugate	initial	1 d	3 d	5 d
<sup>89</sup> Zr-THPN-HPG	>99%	97%	96%	96%
<sup>89</sup> Zr-DFO-HPG	>99%	>99%	>99%	97%
<sup>89</sup> Zr-DFO*-HPG	>99%	>99%	>99%	>99%

<sup>a</sup> Stability over time is reported as percentage of bound <sup>89</sup>Zr after incubation in human plasma at 37 °C, 550 rpm. Measurements were performed in triplicate and are reported as mean.

#### 4.2.5.3 *In Vivo* Stability of $^{89}\text{Zr}$ -HPG Conjugates

In order to investigate the long-term *in vivo* stability of the  $^{89}\text{Zr}$ -THPN radiocomplex and compare it against the radiocomplexes with DFO and DFO\*, healthy NSG mice were administered  $^{89}\text{Zr}$ -HPG nanoparticles with either of the chelates. For each radioconjugate, twelve mice were used for an acute biodistribution study and were sacrificed after either 1, 3, or 6 days post-injection ( $n = 4$  per group and time point). One animal per group received a larger dose of radioconjugate and was imaged by *in vivo* PET/CT after 1 h, 1, 3, and 6 days post-injection, before being also included in the biodistribution study.

PET images at 1 h and 1 day post-injection showed the majority of activity for all three radioconjugates to be associated with the blood circulation as hearts and carotid arteries were clearly distinguishable (Figure 4.15). After 3 and 6 days post-injection,  $^{89}\text{Zr}$  uptake in the joints and bones became particularly prominent in the mouse that received  $^{89}\text{Zr}$ -THPN-HPG conjugate. The other two mice showed much less bone uptake at these time points. All three mice also showed some activity uptake by liver and spleen.

The data from the acute biodistribution study confirmed these findings. For the mice that were administered the THPN-based radioconjugate,  $^{89}\text{Zr}$  sequestration to the bones increased over the six days and was significantly higher compared to the other two groups of mice (Figure 4.13). The full biodistribution data is presented in Table 4.3. Outliers were identified using a Grubbs test ( $p < 0.01$ ) using the software R<sup>199</sup> and were excluded from the reported results. Since released  $^{89}\text{Zr}$  tends to accumulate in bones, it is reasonable to regard bone uptake as a measure for the release of  $^{89}\text{Zr}$  from the complex. The *in vivo* data therefore suggest that the DFO- and DFO\*-radioconjugates possess superior *in vivo* stability over the THPN-radioconjugate.

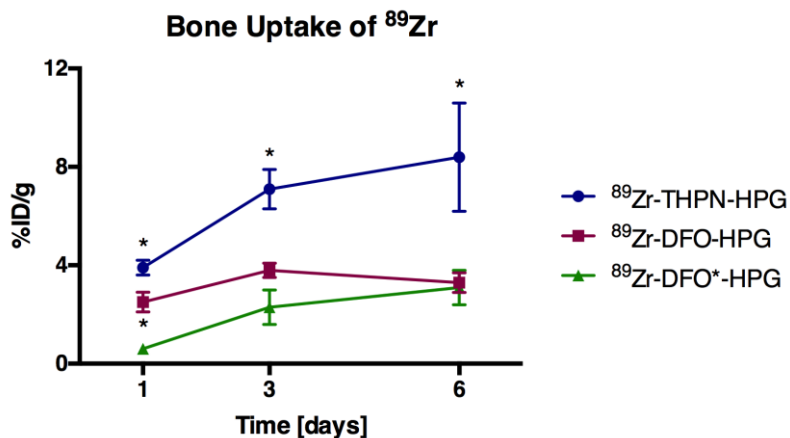


**Figure 4.13.** Bone uptake of <sup>89</sup>Zr for the three radioconjugates measured in biodistribution studies after 1, 3, or 6 days post-injection. Error bars indicate standard deviations.

We did not anticipate these findings since the thermodynamic stability of Zr-THPN was determined to be exceptionally high ( $\log \beta$  50.3, Chapter 3). It is, however, understood that the kinetic inertness can often have an even more profound effect on the *in vivo* stability of metallo-radiopharmaceuticals than the thermodynamic stability itself.<sup>1, 46, 48, 51, 56, 167, 200</sup> Diagnostic radiopharmaceuticals are administered in extremely low quantities which are further diluted as the compounds enter circulation. Under these highly dilute conditions, equilibrium conditions are no longer applicable and the rate of dissociation ( $k_{off}$ ) predominantly dictates *in vivo* stability (Figure 4.14).<sup>1, 48, 51, 167</sup> The radiometal complex, moreover, faces fierce competition from orders of magnitude higher concentrations of metal ions and native chelators for potential transmetallation or transchelation.

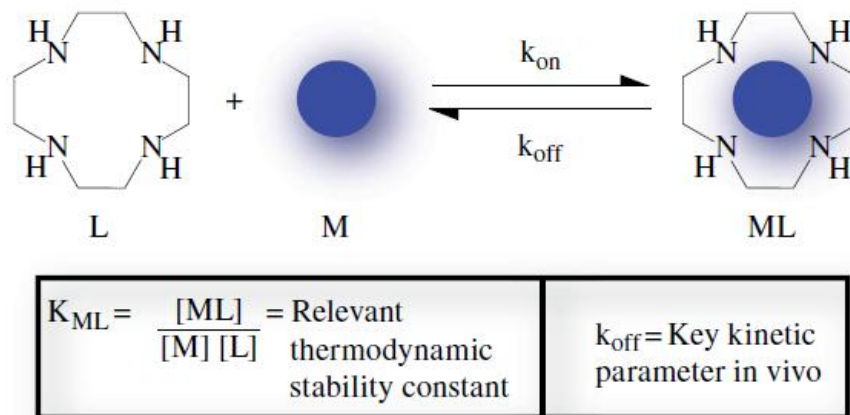


**Figure 4.14.** Schematic representation comparing thermodynamic and kinetic effects governing the stability of a radiometal complex *in vivo*, with the dissociation rate constant  $k_{\text{off}}$  being a critical factor. Reproduced with permission from ref.<sup>51</sup> © 2015 John Wiley & Sons.

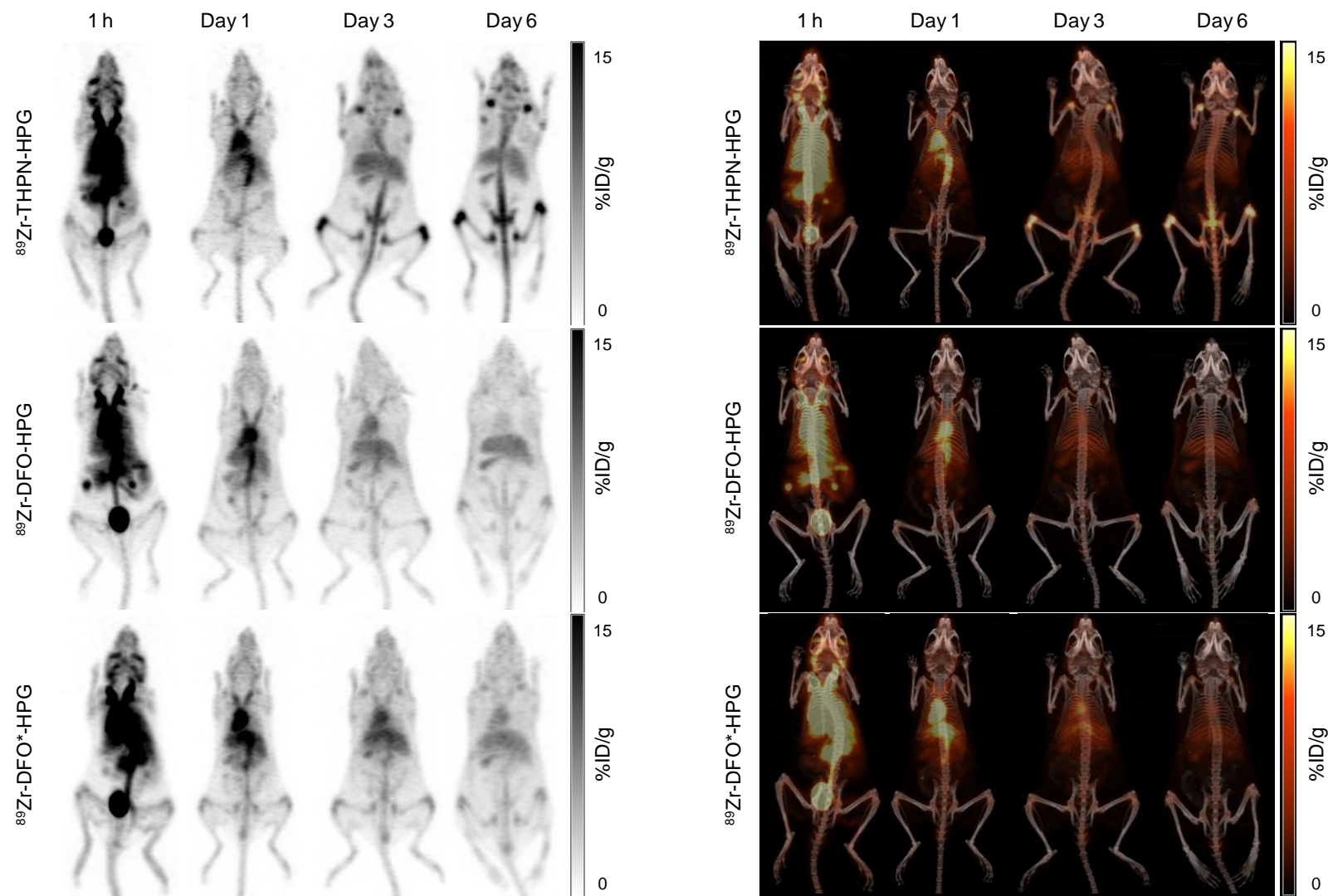


**Figure 4.15.** Maximum intensity projections of PET (left) and fused PET/CT images (right) over six days of three mice injected i.v. with either  $^{89}\text{Zr}$ -THPN-HPG (top),  $^{89}\text{Zr}$ -DFO-HPG (centre), or  $^{89}\text{Zr}$ -DFO\*-HPG (bottom).

**Table 4.3.** Acute biodistribution data for <sup>89</sup>Zr-HPG conjugates with values expressed as %ID/g.<sup>a</sup>

	Day 1			Day 3			Day 6		
	THPN	DFO	DFO*	THPN	DFO	DFO*	THPN	DFO	DFO*
<b>Blood</b>	20.0 ± 0.8	19.7 ± 1.3	5.8 ± 1.3	10.7 ± 1.3	9.0 ± 1.3	11.2 ± 2.3	2.9 ± 1.1	4.0 ± 1.3	6.4 ± 1.2
<b>Fat</b>	0.6 ± 0.1	0.7 ± 0.3	0.1 ± 0.0	0.6 ± 0.1	0.8 ± 0.2	0.6 ± 0.2	0.7 ± 0.2	0.6 ± 0.3	0.8 ± 0.0
<b>Uterus</b>	11.4 ± 4.4	7.1 ± 0.8	2.0 ± 0.3	11.1 ± 5.5	13.9 ± 4.4	8.2 ± 2.3	9.9 ± 1.9	7.8 ± 0.8	9.1 ± 0.3
<b>Ovaries</b>	8.9 ± 2.4	8.0 ± 1.1	2.2 ± 0.7	8.5 ± 2.7	12.8 ± 1.8	7.4 ± 2.0	8.4 ± 1.3	8.7 ± 1.1	18.1 ± 17.0
<b>Intestine</b>	1.8 ± 0.1	1.6 ± 0.2	0.5 ± 0.1	1.4 ± 0.1	1.2 ± 0.0	1.2 ± 0.3	0.8 ± 0.1	0.8 ± 0.2	1.1 ± 0.1
<b>Spleen</b>	8.3 ± 1.4	12.0 ± 3.2	3.4 ± 0.9	25.8 ± 16.8	18.6 ± 2.8	13.0 ± 5.8	21.8 ± 2.8	19.6 ± 3.2	22.7 ± 7.7
<b>Liver</b>	8.0 ± 0.6	3.9 ± 4.2	2.0 ± 0.5	9.5 ± 0.6	6.9 ± 0.9	6.4 ± 1.4	8.4 ± 0.7	5.9 ± 4.2	5.7 ± 0.6
<b>Pancreas</b>	1.6 ± 0.2	1.7 ± 0.6	0.4 ± 0.1	1.6 ± 0.3	1.8 ± 0.2	1.9 ± 0.4	1.7 ± 0.3	1.5 ± 0.6	1.7 ± 0.3
<b>Stomach</b>	2.2 ± 0.4	1.3 ± 0.9	0.6 ± 0.1	2.3 ± 0.2	2.0 ± 0.2	1.8 ± 0.6	1.4 ± 0.1	1.4 ± 0.9	1.8 ± 0.3
<b>Adrenal glands</b>	8.7 ± 2.6	10.5 ± 3.8	4.6 ± 4.1	13.6 ± 4.4	16.5 ± 13.1	9.3 ± 3.4	13.6 ± 4.7	13.7 ± 3.8	20.3 ± 10.0
<b>Kidney</b>	5.3 ± 1.0	4.3 ± 0.2	1.9 ± 0.4	3.9 ± 0.3	3.6 ± 0.2	3.7 ± 1.1	2.6 ± 0.4	2.0 ± 0.2	2.4 ± 0.3
<b>Lungs</b>	6.1 ± 0.8	5.9 ± 0.6	1.9 ± 0.5	5.0 ± 0.7	4.5 ± 0.8	4.4 ± 1.3	2.8 ± 0.3	2.6 ± 0.6	4.0 ± 1.2
<b>Heart</b>	4.0 ± 0.3	3.9 ± 0.5	1.2 ± 0.1	3.7 ± 0.5	3.3 ± 0.7	3.6 ± 1.0	2.6 ± 0.3	2.5 ± 0.5	3.1 ± 0.6
<b>Muscle</b>	1.0 ± 0.2	0.7 ± 0.1	0.3 ± 0.1	0.8 ± 0.1	1.2 ± 0.2	0.8 ± 0.1	1.0 ± 0.2	0.8 ± 0.1	0.9 ± 0.2
<b>Bone</b>	3.9 ± 0.3	2.5 ± 0.4	0.6 ± 0.2	7.1 ± 0.8	3.8 ± 0.3	2.3 ± 0.7	8.4 ± 2.2	3.3 ± 0.4	3.1 ± 0.7
<b>Brain</b>	0.3 ± 0.0	0.4 ± 0.1	0.1 ± 0.0	0.2 ± 0.0	0.2 ± 0.0	0.2 ± 0.1	0.1 ± 0.0	0.1 ± 0.1	0.2 ± 0.0
<b>Tail</b>	3.1 ± 0.4	2.4 ± 0.2	0.7 ± 0.1	4.0 ± 0.3	2.5 ± 0.0	2.2 ± 0.3	4.2 ± 0.4	1.7 ± 0.2	2.0 ± 0.2

<sup>a</sup> Studies were performed in healthy female NSG mice administered with <sup>89</sup>Zr-THPN-HPG, <sup>89</sup>Zr-DFO-HPG, or <sup>89</sup>Zr-DFO\*-HPG nanoparticles *via* i.v. tail vein injection (*n* = 4 per group). Results are reported as mean ± SD.

### 4.3 Conclusions

In order to study the Zr-THPN complex in combination with different carrier molecules, a bifunctional version of the chelator was produced. The novel isothiocyanate functionalized derivative *p*-SCN-Bn-THPN was synthesized in a nine step synthesis in ~7% cumulative yield and was, along with all synthetic intermediates, fully characterized. The isothiocyanate functionality enables covalent conjugation to amino group bearing carrier molecules by thiourea bond formation. The conjugation and <sup>89</sup>Zr-radiolabeling of *p*-SCN-Bn-THPN was then evaluated with four different carriers.

First, the anti-HER2 antibody trastuzumab was radiolabeled with THPN as chelator using either a post- or a prelabeling approach. The postlabeling strategy led to considerable antibody aggregation, which could not be avoided even by extensive optimization efforts. Instead, a prelabeling approach was more successful and trastuzumab could be <sup>89</sup>Zr-radiolabeled with THPN. Successful prelabeling with trastuzumab was achieved for the two literature chelators, DFO and DFO\*, even though other authors reported problems with DFO. The specific activities obtained for THPN using the prelabeling approach were too low for a meaningful *in vivo* imaging study. Instead, the three radioimmunoconjugates were examined in an *in vitro* mouse plasma stability study. All three radioimmunoconjugates remained 95% or more complexed over seven days at 37 °C. The DFO\* radioimmunoconjugate displayed the highest plasma stability as no transmetallation was observed.

Second, a monoclonal anti-mouse anti-PD-L1 antibody was <sup>89</sup>Zr-radiolabeled with THPN by a postlabeling approach. For this antibody, the postlabeling approach produced a much smaller amount of aggregates. Some aggregates and/or small molecular weight activity, however, remained problematic although these experiments showed that the extreme aggregation observed for trastuzumab does not apply to all antibodies.

Third, mouse serum albumin (MSA) was successfully  $^{89}\text{Zr}$ -radiolabeled with THPN by a postlabeling approach. No major aggregation products were detected and MSA thus constitutes a model protein for which the postlabeling approach leads to high radiochemical yield and purity.

Fourth, in order to evaluate the *in vivo* long-term stability of the  $^{89}\text{Zr}$ -THPN complex and compare it to the radiocomplexes with DFO and DFO\*, the three chelators were conjugated to hyperbranched polyglycerol (HPG) nanoparticles. These conjugates were successfully radiolabeled with radiochemical yields of 97% and radiochemical purities of >99%. Chelator conjugation and radiolabeling did not affect the HPG particle size or size distribution. In an *in vitro* human plasma stability study, all three radiochelate-HPGs retained >95% integrity after five days incubation at 37 °C, yet DFO\* appeared the most stable showing no signs of demetallation. The long-term *in vivo* stability of the three radiochelate-HPG conjugates was assessed over six days in healthy, immunocompromised mice by *in vivo* PET/CT imaging and an acute biodistribution study. PET images and the biodistribution results both revealed a significant  $^{89}\text{Zr}$  uptake by the bones for the  $^{89}\text{Zr}$ -THPN-HPG nanoparticles when compared to the DFO and DFO\* counterparts. This *in vivo* instability was not anticipated since the thermodynamic stability for Zr-THPN was experimentally determined to be exceptionally high. Yet, the *in vivo* stability is known to often be dominated by the kinetic inertness of a radiocomplex over its thermodynamic stability. Thus, these findings suggest that the kinetic stabilities of DFO and DFO\* exceed that of THPN and limit its biologic applicability. At the same time this reinforces the need to conduct such *in vivo* experiments to carefully evaluate physiologic stability of radiochelates over extended periods of time. For this purpose, we identified long-circulating HPG nanoparticles as a robust nanocarrier. Their high

biocompatibility, high solubility, and long circulation time render HPG nanoparticles a suitable investigative tool to assess the *in vivo* stability of radiochelates over several days.

## 4.4 Experimental

### 4.4.1 Materials and Methods

All reagents and solvents were purchased from commercial suppliers (Sigma-Aldrich, TCI, AC PharmaChem, Acros, Strem Chemicals, Fisher Scientific) and were used as received without further purification. All water used was ultrapure (18.2 M $\Omega$ -cm) and was purified with a Millipore Milli-Q Integral-10 water purification system. Building block **4.6** (2-(aminomethyl)-1,6-dimethyl-3-(phenylmethoxy)-4(1*H*)-pyridinone) was purchased from Otava Ltd or was prepared by Dr. Stoyan Karagiozov according to a published procedure<sup>117</sup> with minor adjustments. Trastuzumab (Herceptin) was generously supplied by BC Cancer Agency and was purified by ultrafiltration (Amicon Ultra 100K). Anti-PD-L1 mAb was purchased from Bio X Cell as *InVivo*MAB anti-mouse PD-L1 (B7-H1) solution (5.5 g/L in PBS, pH 6.5). Mouse serum albumin (MSA) was purchased from Innovative Research, Inc. as lyophilized powder and was reconstituted with water. Hyperbranched polyglycerol (HPG) was synthesized and amino-functionalized by Dr. Katayoun Saatchi according to published procedures.<sup>193, 197, 201</sup> In brief, HPG of approximately 800 kDa was synthesized by ring-opening multi-branching polymerization of glycidol. Hydroxyl groups were oxidized with NaIO<sub>4</sub>, followed by reductive amination with 1,10-diaza-4,7-dioxadecane and NaCNBH<sub>3</sub>. *p*-SCN-Phe-DFO (*p*-SCN-Bn-Deferoxamine) was purchased from Macrocyclics and *p*-SCN-Phe-DFO\* (*N*<sup>1</sup>-(8,19-dihydroxy-1-((4-isothiocyanato-phenyl)amino)-9,12,20,23-tetraoxo-1-thioxo-2,8,13,19,24-pentaazanonacosan-29-yl)-*N*<sup>1</sup>-hydroxy-*N*<sup>4</sup>-(5-(*N*-hydroxyacetamido)pentyl)succinamide) was produced by Pharma

Inventor Inc. and was generously supplied by Dr. François Bénard's lab (BC Cancer Agency). Methyltetrazine-PEG<sub>4</sub>-amine (**4.11**, 2-[2-[2-[2-[4-(6-methyl-1,2,4,5-tetrazin-3-yl)phenoxy]ethoxy]ethoxy]ethoxy]-ethanamine), TCO-NHS (succinimidyl (*E*)-cyclooct-4-en-1-yl carbonate), and sulfo-Cy3-methyltetrazine (2-[3-[1,3-dihydro-3,3-dimethyl-5-sulfo-1-(3-sulfopropyl)-2*H*-indol-2-ylidene]-1-propen-1-yl] 3,3-dimethyl-1-[6-[[[4-(6-methyl-1,2,4,5-tetrazin-3-yl)phenyl]methyl]amino]-6-oxohexyl]-5-sulfo-3*H*-indolium) were purchased from Broadpharm. Parsability of chemical nomenclature was confirmed with OPSIN.<sup>118, 119</sup>

NMR spectra were recorded on a Bruker Ascend 400 spectrometer (400.13 MHz for <sup>1</sup>H; 100.62 MHz for <sup>13</sup>C) at 297.16 K. Chemical shifts ( $\delta$  relative to residual solvent peak) are reported as parts per million (ppm) and coupling constants (*J*) in hertz (Hz). ESI-MS spectra were recorded on an AB Sciex QTrap 5500 mass spectrometer. High-resolution mass spectrometry (HR-MS) analyses were acquired by UBC Mass Spectrometry Centre on a Bruker HTCultra PTM Discovery mass spectrometry system. IR spectra were recorded on an Agilent Cary 660 FT-IR spectrometer equipped with an attenuated total reflectance (ATR) crystal. Microwave reactions were conducted in a Biotage Initiator<sup>+</sup> microwave synthesizer. Hydrodynamic diameter measurements were carried out by dynamic light scattering (DLS) on a Malvern Zetasizer Nano ZS. Measurements were performed in triplicate in water at 25 °C using a 173° backscatter angle and the material refractive index of polystyrene latex (1.590). Particle size diameters are reported as Z-average (Z-avg. (d)). Data were analyzed using the software Malvern Zetasizer (v. 7.12). Protein concentrations were quantified either by measuring absorbance at 280 nm on a Thermo Scientific NanoDrop 2000 spectrophotometer, or by Bradford assay measured at 595 nm on a BioTek SynergyMx 96-well plate reader and comparing against a bovine serum albumin calibration curve. HPLC was performed on a Waters Alliance e2695 separations module coupled to a Waters 2489 UV/Vis-detector and, for

radio-HPLC, a LabLogic Scan-RAM radio-detector. For reversed phase HPLC, the column was a C18 Waters Atlantis T3, 100 Å, 5 µm particle size (4.6 × 150 mm), supported by a C18 guard cartridge and was operated in an oven (40 °C). Method A used the following gradient: A = 0.1% trifluoroacetic acid (TFA) in water; B = methanol; flow rate = 1 mL/min; 0–5 min 90% A; 5–15 min 10–100% B; 15–18 min 100% B. Method B used the following gradient: A = 0.1% trifluoroacetic acid (TFA) in water; B = acetonitrile; flow rate = 1 mL/min; 0–5 min 90% A; 5–15 min 10–100% B; 15–18 min 100% B. Method C used the following gradient: A = 10 mM (NH<sub>4</sub>)HCO<sub>3</sub> in water; B = 10 mM (NH<sub>4</sub>)HCO<sub>3</sub> in 2:1 methanol/water; flow rate = 1 mL/min; 0–13 min 14–100% B; 13–18 min 100% B. Size-exclusion HPLC (SE-HPLC) was performed at ambient temperature on the same radio-HPLC system but using either a Waters Ultrahydrogel Linear column (method D, 10 µm, 7.8 × 300 mm) or a Waters Ultrahydrogel 250 column (method E, 250 Å, 6 µm, 7.8 × 300 mm). The mobile phase for methods D and E was an isocratic gradient consisting of a filtered aqueous phosphate buffer (50 mM NaH<sub>2</sub>PO<sub>4</sub>, 50 mM Na<sub>2</sub>HPO<sub>4</sub>, 150 mM NaCl, 10 mM NaN<sub>3</sub>, pH 6.2–7.0) and flow rate was 0.5 mL/min. Semi-preparative HPLC was performed on a Phenomenex Synergi Hydro-RP column (80 Å, 21.1 × 250 mm) connected to a Waters 600 controller and a Waters 2487 dual wavelength absorbance detector using the following gradient: A = 0.1% TFA in water; B = methanol; flow rate = 10 mL/min; 5–100% B over 25 min. Flash chromatography was performed on a Biotage Isolera One system using Biotage SNAP KP-Sil or ZIP silica gel cartridges (normal phase) or Biotage SNAP Ultra C18 cartridges (reversed phase). Solid phase extraction cartridges (Chromafix C18-ec) were obtained from Machery-Nagel. Analytical thin layer chromatography (TLC) was performed using silica gel 60 F<sub>254</sub> plates with aluminium backing obtained from Merck Millipore. AW Standard Super-Cel filter aid was purchased from Sigma-Aldrich. Semi-preparative size-exclusion chromatography was performed on PD-10 or PD MiniTrap G-25 desalting columns

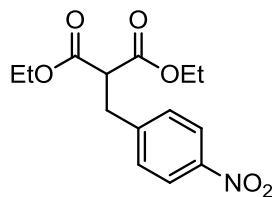
(Sephadex G-25, GE Healthcare). Ultrafiltration was performed using Amicon Ultra centrifugal filters of 30 kDa, 50 kDa, or 100 kDa NMWL of 0.5 mL or 2 mL volume (EMD Millipore).

$^{89}\text{Zr}$  was obtained either from TRIUMF, BC Cancer Agency, Sherbrooke University, or PerkinElmer Health Sciences Canada, Inc. and was produced *via* the  $^{89}\text{Y}(p,n)^{89}\text{Zr}$  reaction.  $^{89}\text{Zr}$  was either received already purified in 1 M oxalic acid or was purified either following a reported procedure<sup>80</sup> or using commercially available ZR Resin (TrisKem International) and eluted with 0.05 M oxalic acid.  $^{89}\text{Zr}$ -oxalate solutions were neutralized with  $\text{Na}_2\text{CO}_3$  solutions. Activities were measured using a Capintec CRC-55tR or a Capintec CRC-25R/W dose calibrator. Instant thin-layer chromatography (ITLC) was carried out using Biodex Tec-Control chromatography strips (#150-005, black). Unless otherwise mentioned, ITLC strips were developed using an aqueous DTPA solution as mobile phase (50 mM, pH 7.0). ITLC strips were analyzed on a Packard Cyclone storage phosphor screen imager with the OptiQuant software. Biodistribution samples were counted on a calibrated PerkinElmer 2480 Wizard<sup>2</sup> automated gamma counter. NSG mice (NOD.Cg-Prkdc<sup>scid</sup>Il2rg<sup>tm1Wjl</sup>/SzJ) were obtained through an in-house breeding program at the Animal Research Centre, BC Cancer Research Centre. PET/CT images were acquired on a Siemens Medical Solutions Inveon PET/CT small animal scanner.

## 4.4.2 Syntheses

### 4.4.2.1 Diethyl-2-(4-nitrobenzyl)malonate (4.1)

This synthesis was adapted from a literature procedure.<sup>157</sup> Diethyl malonate (3.20 g, 20.0 mmol) was dropwise added to a suspension of sodium hydride (60% in oil, 545 mg, 13.6 mmol) in anhydrous THF (7.5 mL) and was stirred 1 h at ambient temperature under argon. A solution of 4-nitrobenzyl bromide (2.55 g, 11.8 mmol) in THF (7.5 mL) was dropwise added while cooling in



an ice bath. After complete addition, the mixture was heated for 1.5 h at 35 °C. Once TLC indicated completion of the reaction, the mixture was evaporated, taken up in diethyl ether (20 mL) and washed with water (2 x 20 mL). The organic phase was dried with MgSO<sub>4</sub>, filtered, and evaporated. Recrystallization from 1:1 Et<sub>2</sub>O/hexane gave the title compound **4.1** as yellow needles in 53% yield (1.84 g, 6.24 mmol).

<sup>1</sup>H NMR (400 MHz, CDCl<sub>3</sub>): δ = 8.14 (d, *J* = 8.8 Hz, 2H, -Ph-H), 7.39 (d, *J* = 8.8 Hz, 2H, -Ph-H), 4.23–4.10 (m, 4H, -O-CH<sub>2</sub>-), 3.66 (t, *J* = 7.8 Hz, 1H, -CH-), 3.31 (d, *J* = 7.6 Hz, 2H, -CH<sub>2</sub>-Ph), 1.21 (t, *J* = 7.2 Hz, 6H, -CH<sub>3</sub>). <sup>13</sup>C NMR (100 MHz, CDCl<sub>3</sub>): δ = 168.2, 146.9, 145.6, 129.8, 123.7, 61.8, 53.1, 34.3, 14.0. HPLC (method A): *t<sub>R</sub>* = 15.9 min. ESI-MS: *m/z* 318.2 [M+Na]<sup>+</sup>; 294.2 [M-H]<sup>-</sup>.

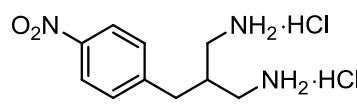
#### 4.4.2.2 2-(4-Nitrobenzyl)propanediamide (4.2)

This synthesis was adapted from a literature procedure.<sup>156</sup> Compound **4.1** (1.64 g, 5.56 mmol) was suspended in methanol (10 mL) and was placed in an ice bath. An ammonia solution (30 mL, 7 N in methanol) was dropwise added to this. The mixture was allowed to warm to ambient temperature and was stirred overnight. HPLC indicated consumption of the starting material but the presence of an intermediary product, which converted to the product after stirring for another night at ambient temperature as observed by HPLC. At this point, the suspension was filtered over fritted glass and washed with methanol and boiling acetonitrile. Drying *in vacuo* gave the title compound **4.2** as a white powder in 89% yield (1.18 g, 4.97 mmol).



<sup>1</sup>H NMR (400 MHz, DMSO-*d*<sub>6</sub>): δ = 8.14 (d, *J* = 8.8 Hz, 2H, -Ph-H), 7.48 (d, *J* = 8.8 Hz, 2H, -Ph-H), 7.29 (s, 2H, -NH<sub>2</sub>), 7.09 (s, 2H, -NH<sub>2</sub>), 3.38 (t, *J* = 7.6 Hz, 1H, -CH-), 3.10 (d, *J* = 7.6 Hz, 2H, -CH<sub>2</sub>-). <sup>13</sup>C NMR (100 MHz, DMSO-*d*<sub>6</sub>): δ = 170.2, 148.0, 146.1, 130.2, 123.3, 54.0, 34.5. HPLC (method A): *t<sub>R</sub>* = 11.46 min. ESI-MS: *m/z* 260.0 [M+Na]<sup>+</sup>.

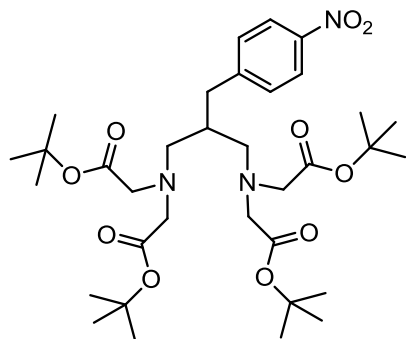
#### 4.4.2.3 1,3-Diamino-2-(4-nitrobenzyl)propane dihydrochloride (4.3)

This synthesis was adapted from reported procedures.<sup>156, 158</sup> A dry round-bottom flask was charged with compound **4.2** (129 mg, 542  $\mu\text{mol}$ ) and was placed under nitrogen. To this  was slowly added a solution of borane stabilized in THF ( $\text{BH}_3\cdot\text{THF}$ , 1 M in THF, 1.2 mL, 1.2 mmol) and it was stirred 45 min at ambient temperature. Some more anhydrous THF (5 mL) was added and it was heated at reflux overnight. The reaction progress was monitored by HPLC and another aliquot of borane solution (0.2 mL) was added to the mixture. It was heated for another night at reflux after which the reaction was quenched by dropwise addition of concentrated HCl (2 mL). The mixture was heated for an hour at reflux and volatiles were evaporated *in vacuo*. The yellow milky residue was taken up in water (3 mL) and at 0 °C, NaOH (6 M, 2.7 mL) was added using a dropping funnel. The mixture was extracted with DCM (5×15 mL), the organic phases were combined, dried over  $\text{MgSO}_4$ , and evaporated. The resulting yellow oil was suspended in ethanol (3 mL), a drop of concentrated HCl was added, and the mixture was left to precipitate over 3 days at -20 °C. The supernatant was removed and the precipitate was triturated with diethyl ether and then dried *in vacuo* to give the title compound **4.3** as a light yellow powder in 66% yield (101 mg, 357  $\mu\text{mol}$ ).

$^1\text{H}$  NMR (400 MHz,  $\text{D}_2\text{O}$ ):  $\delta$  = 8.23 (d,  $J$  = 8.8 Hz, 2H, -Ph-H), 7.50 (d,  $J$  = 8.8 Hz, 2H, -Ph-H), 3.15 (dd,  $J$  = 13.6 Hz, 6.7 Hz, 2H, -N- $\text{CH}_2$ -), 3.02 (dd,  $J$  = 13.6 Hz, 6.5 Hz, 2H, -N- $\text{CH}_2$ -), 2.95 (d,  $J$  = 7.6 Hz, 2H, - $\text{CH}_2$ -), 2.57-2.46 (m, 1H, -CH-).  $^{13}\text{C}$  NMR (100 MHz,  $\text{D}_2\text{O}$ ):  $\delta$  = 146.7, 145.2, 130.0, 124.0, 39.9, 36.6, 34.7. HPLC (method A):  $t_{\text{R}}$  = 6.64 min. ESI-MS:  $m/z$  210.0  $[\text{M}+\text{H}]^+$ .

#### 4.4.2.4 Tetra-*tert*-butyl 2,2',2'',2'''-((2-(4-nitrobenzyl)propane-1,3-diyl)bis(azanetriyl))-tetraacetate (4.4)

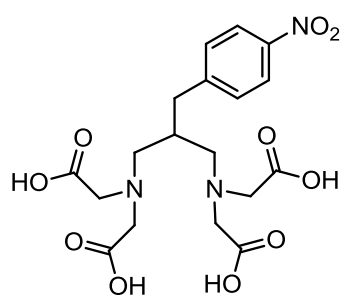
Compound 4.3 (56 mg, 0.20 mmol) was dissolved in anhydrous DMF (4 mL) and placed under N<sub>2</sub>. To this was added *tert*-butyl bromoacetate (129 μL, 0.87 μmol) and sodium carbonate (~0.39 g) and it was stirred overnight at ambient temperature. HPLC indicated completion of the reaction and the mixture was filtered and rinsed *ad libitum* with acetone. The filtrate was evaporated and purified by flash chromatography over silica with 0–20% ethyl acetate/hexane to give the title compound 4.4 as a yellow oil in 46% yield (60 mg, 90 μmol).



<sup>1</sup>H NMR (400 MHz, CDCl<sub>3</sub>): δ = 8.10 (d, *J* = 8.8 Hz, 2H, -Ph-H), 7.41 (d, *J* = 7.6 Hz, 2H, -Ph-H), 3.35 (s, 8H, -N-CH<sub>2</sub>-CO-), 2.88 (d, *J* = 6.0 Hz, 2H, -CH<sub>2</sub>-Ph-), 2.74 (m, 2H, -N-CH<sub>2</sub>-CH-), 2.47 (m, 2H, -N-CH<sub>2</sub>-CH-), 1.96 (m, 1H, -CH-), 1.43 (s, 36H, -CH<sub>3</sub>). <sup>13</sup>C NMR (100 MHz, CDCl<sub>3</sub>): δ = 170.6, 149.6, 146.1, 130.2, 123.3, 80.9, 56.6, 56.4, 38.3, 36.6, 28.1. HPLC (method A): *t<sub>R</sub>* = 16.57 min. *R<sub>f</sub>* = 0.37 (20% EtOAc/hexane). ESI-MS: *m/z* 666.1 [M+H]<sup>+</sup>, 688.1 [M+Na]<sup>+</sup>.

#### 4.4.2.5 2,2',2'',2'''-(2-(4-Nitrobenzyl)propane-1,3-diyl-bis(azanetriyl))-tetraacetic acid (4.5)

Compound 4.4 (249 mg, 374 μmol) was dissolved in 4.5 mL acetonitrile and *ortho*-phosphoric acid (~1.5 mL, 85 wt%) was dropwise added. This mixture was stirred one night at ambient temperature and then heated another night at 45 °C. Once HPLC indicated complete conversion, 3 mL water were added and the mixture was concentrated *in vacuo*. The residual oil was taken up in (NH<sub>4</sub>)HCO<sub>3</sub> (15 mL, 0.1 M), washed with ethyl acetate (10 mL) and extracted with another 3 × 10 mL

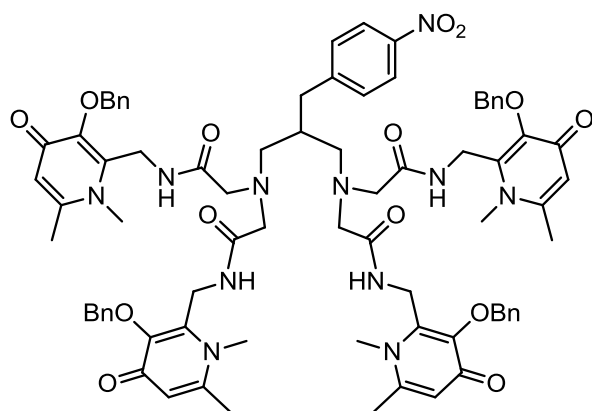


(NH<sub>4</sub>)HCO<sub>3</sub> solution. The combined aqueous layer was concentrated *in vacuo* and purified by reversed phase chromatography (eluted with a gradient of 100% water with 0.1% formic acid to 100% methanol). Fractions were pooled and evaporated to give the title compound **4.5** as a fluffy white powder in 97% yield (173 mg, 364 μmol).

<sup>1</sup>H NMR (400 MHz, CD<sub>3</sub>OD): δ = 8.17 (d, *J* = 8.8 Hz, 2H, -Ph-H), 7.51 (d, *J* = 8.8 Hz, 2H, -Ph-H), 3.81 (d, *J* = 16.8 Hz, 4H, -N-CH<sub>2</sub>-CO-), 3.68 (d, *J* = 16.8 Hz, 4H, -N-CH<sub>2</sub>-CO-), 3.48 (dd, *J* = 13.2, 3.6 Hz, 2H, -N-CH<sub>2</sub>-CH-), 3.09-3.03 (m, 2H, -N-CH<sub>2</sub>-CH-), 2.75 (d, *J* = 7.2 Hz, 2H, -CH<sub>2</sub>-Ph-), 2.7-2.6 (m, 1H, -CH-). <sup>13</sup>C NMR (100 MHz, CD<sub>3</sub>OD): δ = 172.8, 148.2, 148.0, 131.3, 124.7, 59.6, 56.8, 37.6, 33.4. HPLC: *t*<sub>R</sub> = 11.76 min. ESI-MS: *m/z* 442.1 [M+H]<sup>+</sup>, 464.2 [M+Na]<sup>+</sup>. Elemental analysis (%) calcd. for C<sub>18</sub>H<sub>23</sub>N<sub>3</sub>O<sub>10</sub>·H<sub>2</sub>O·½(CH<sub>3</sub>OH): C 46.77, H 5.72, N 8.84; found: C 46.97, H 5.77, N 9.01.

#### 4.4.2.6 2,2',2'',2'''-((2-(4-Nitrobenzyl)propane-1,3-diyl)bis(azanetriyl))tetrakis(N-((1,6-dimethyl-3-(phenylmethoxy)-4-oxo-1,4-dihydropyridin-2-yl)methyl)acetamide) (4.7)

A microwave vial was charged with compound **4.5** (108 mg, 226 μmol), which was suspended in anhydrous DMF (4 mL). To this was added HOBT·H<sub>2</sub>O (173 mg, 1.13 mmol, 5.0 eq.) and a solution of DCC (233 mg, 1.13 mmol, 5.0 eq.) in DMF (4.5 mL). The mixture was stirred for 2 h at ambient temperature under N<sub>2</sub>. At this point, 2-(aminomethyl)-1,6-dimethyl-3-(phenylmethoxy)-4(1*H*)-pyridinone (**4.6**, 292 mg, 1.13 mmol, 5.0 eq.) was added, it was rinsed with another 2 mL DMF and the vial was crimp capped under N<sub>2</sub>. The mixture was heated in a microwave reactor for 4 h at 55 °C and then stirred at ambient

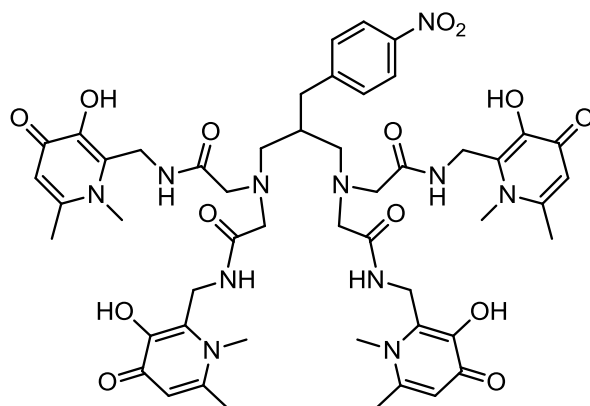


suspended in anhydrous DMF (4 mL). To this was added HOBT·H<sub>2</sub>O (173 mg, 1.13 mmol, 5.0 eq.) and a solution of DCC (233 mg, 1.13 mmol, 5.0 eq.) in DMF (4.5 mL). The mixture was stirred for 2 h at ambient temperature under N<sub>2</sub>. At this point, 2-

temperature overnight. The mixture was heated another 2 h at 55 °C in the microwave reactor and then stirred a second night at ambient temperature. At this point, HPLC indicated complete conversion and the mixture was filtered over a cotton plug, rinsed with acetonitrile, evaporated, and purified by reversed phase flash chromatography (eluted with a gradient of 100% water with 0.1% formic acid to 40% acetonitrile). Product fractions were pooled and concentrated *in vacuo* to give the title compound **4.7** as a yellow oil in ~83% yield (262 mg, 187  $\mu$ mol).

$^1\text{H}$  NMR (400 MHz,  $\text{CD}_3\text{OD}$ ):  $\delta$  = 8.01 (d,  $J$  = 8.4 Hz, 2H,  $\text{NO}_2\text{-Ph-H}$ ), 7.41-7.39 (m, 8H, Bn-H), 7.29-7.26 (m, 12H, Bn-H), 7.16 (d,  $J$  = 8.8 Hz, 2H,  $\text{NO}_2\text{-Ph-H}$ ), 6.40 (s, 4H,  $-\text{CO-CH-}$ ), 5.14 (s, 8H,  $-\text{O-CH}_2\text{-Ph}$ ), 4.42 (s, 8H,  $-\text{CO-N-CH}_2\text{-}$ ), 3.53 (s, 12H,  $-\text{N-CH}_3$ ), 3.02 (s, 8H,  $-\text{N-CH}_2\text{-CO-}$ ), 2.54 (d,  $J$  = 6.4 Hz, 2H,  $-\text{CH}_2\text{-Ph-NO}_2$ ), 2.47-2.43 (m, 2H,  $-\text{N-CH}_2\text{-CH-}$ ), 2.33 (s, 12H,  $-\text{C-CH}_3$ ), 2.21-2.16 (m, 2H,  $-\text{N-CH}_2\text{-CH-}$ ), 1.64-1.57 (m, 1H,  $-\text{CH-CH}_2\text{-N-}$ ).  $^{13}\text{C}$  NMR (100 MHz,  $\text{CD}_3\text{OD}$ ):  $\delta$  = 174.7, 173.4, 150.9, 149.9, 147.7, 147.3, 143.5, 138.4, 131.0, 130.0, 129.5, 129.4, 124.6, 119.2, 74.6, 60.5, 60.4, 39.5, 37.9, 37.5, 36.2, 20.9. HPLC (method B):  $t_{\text{R}}$  = 11.52 min. ESI-MS:  $m/z$  1402.8  $[\text{M}+\text{H}]^+$ , 1424.7  $[\text{M}+\text{Na}]^+$ ; 1400.8  $[\text{M}-\text{H}]^-$ . HR ESI-MS: calcd. ( $m/z$ ) for  $\text{C}_{78}\text{H}_{88}\text{N}_{11}\text{O}_{14}^+$   $[\text{M}+\text{H}]^+$ : 1402.6512; found: 1402.6532, (1.4 ppm).

#### 4.4.2.7 2,2',2'',2'''-((2-(4-Nitrobenzyl)propane-1,3-diyl)bis(azanetriyl))tetrakis(N-((1,6-dimethyl-3-hydroxy-4-oxo-1,4-dihydropyridin-2-yl)methyl)acetamide) (**4.8**).

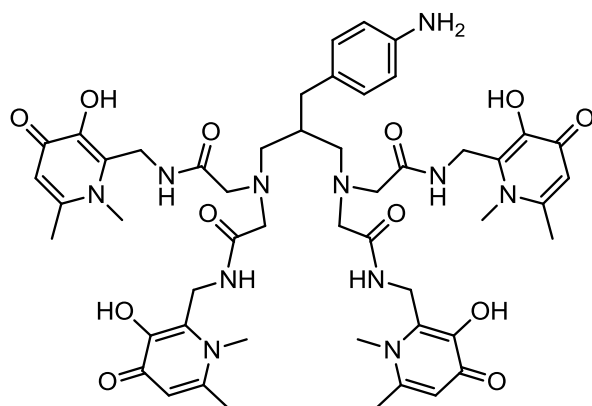


Compound **4.7** (262 mg, 187  $\mu$ mol) was dissolved in glacial acetic acid (2.5 mL) and concentrated HCl (2.5 mL) and was stirred 24 h at 50 °C. The solution was removed from heat and a stream of nitrogen was blown over it

overnight before evaporating the residue *in vacuo*. The residue was taken up in a small amount of methanol (~3.5 mL), precipitated by dropwise addition to diethyl ether (~40 mL), and placed in a freezer at -20 °C for 20 min. The supernatant was removed and the precipitate was dried *in vacuo* to give the title compound **4.8** as white hydrochloride salt in ~94% yield (243 mg, ~176 μmol).

<sup>1</sup>H NMR (400 MHz, CD<sub>3</sub>OD): δ = 8.19 (d, *J* = 8.0 Hz, 2H, NO<sub>2</sub>-Ph-H), 7.65 (d, *J* = 7.6 Hz, 2H, NO<sub>2</sub>-Ph-H), 7.18 (s, 4H, -CO-CH-), 4.81 (s, 8H, -CO-N-CH<sub>2</sub>-), 4.11 (sb, 8H, -N-CH<sub>2</sub>-CO-), 4.05 (s, 12H, -N-CH<sub>3</sub>), 3.44-3.32 (sb, 4H, -N-CH<sub>2</sub>-CH-), 3.04-2.94 (m, 1H, -CH-CH<sub>2</sub>-N-), 2.90-2.81 (m, 2H, -CH<sub>2</sub>-Ph-NO<sub>2</sub>), 2.68 (s, 12H, -C-CH<sub>3</sub>). <sup>13</sup>C NMR (100 MHz, CD<sub>3</sub>OD): δ = 168.6, 160.5, 150.7, 148.2, 147.2, 144.8, 140.3, 131.8, 124.8, 114.1, 61.1, 57.3, 40.5, 37.3, 36.1, 33.3, 21.4. HPLC (method A): *t<sub>R</sub>* = 11.07 min. ESI-MS: *m/z* 521.8 [M+2H]<sup>2+</sup>, 1042.4 [M+H]<sup>+</sup>, 1064.4 [M+Na]<sup>+</sup>. HR ESI-MS: calcd.(*m/z*) for C<sub>50</sub>H<sub>64</sub>N<sub>11</sub>O<sub>14</sub><sup>+</sup> [M+H]<sup>+</sup>: 1042.4634; found: 1042.4619, (1.4 ppm). Elemental analysis (%) calcd. for C<sub>50</sub>H<sub>63</sub>N<sub>11</sub>O<sub>14</sub>·7.4(HCl)·2.15(CH<sub>3</sub>OH): C 45.36, H 5.77, N 11.16; found: C 45.55, H 5.54, N 10.94.

#### 4.4.2.8 2,2',2'',2'''-((2-(4-Aminobenzyl)propane-1,3-diyl)bis(azanetriyl))tetrakis(N-((1,6-dimethyl-3-hydroxy-4-oxo-1,4-dihydropyridin-2-yl)methyl)acetamide) (4.9)

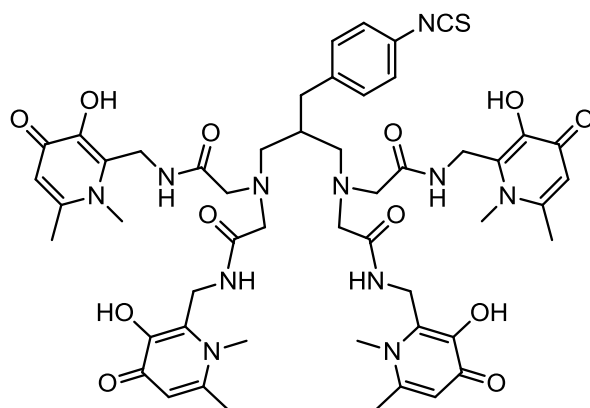


dissolved in methanol (~20 mL) and Pd/C was added (10% w/w, 19.6 mg, 18.4 μmol). The reaction vessel was sealed, placed under a hydrogen atmosphere (balloon), and the mixture was stirred vigorously at ambient

temperature. After 2.5 h, the reaction mixture was vented to nitrogen, filtered through a plug of filter aid, and generously rinsed with methanol. The filtrate was purified by reversed phase flash chromatography (eluting with 0–100% methanol/water with 0.1% formic acid). Product fractions were pooled, evaporated, and dried *in vacuo* to give the title compound **4.9** in its formic acid salt as an off-white solid in ~99% yield (~188 mg, ~173  $\mu\text{mol}$ ). (Molecular weight estimated from NMR integrals).

$^1\text{H}$  NMR (400 MHz,  $\text{CD}_3\text{OD}$ ):  $\delta$  = 6.75 (d,  $J$  = 8.4 Hz, 2H, -Ph-H), 6.64 (d,  $J$  = 8.0 Hz, 2H, -Ph-H), 6.35 (s, 4H, -CO-CH-), 4.61 (s, 8H, -CO-N-CH<sub>2</sub>-), 3.66 (s, 12H, -N-CH<sub>3</sub>), 3.19 (s, 8H, -N-CH<sub>2</sub>-CO-), 2.53-2.48 (m, 2H, -N-CH<sub>2</sub>-CH-), 2.36 (s, 12H, -C-CH<sub>3</sub>), 2.40-2.31 (m, 2H, -N-CH<sub>2</sub>-CH-), 2.40-2.31 (m, 2H, -CH<sub>2</sub>-Ph-), 1.64-1.59 (m, 1H, -CH-CH<sub>2</sub>-N-).  $^{13}\text{C}$  NMR (100 MHz,  $\text{CD}_3\text{OD}$ ):  $\delta$  = 173.7, 170.6, 148.8, 147.3, 144.2, 132.7, 132.4, 130.7, 117.9, 114.8, 61.0, 60.5, 39.6, 37.4, 37.4, 35.8, 21.0. HPLC (method A):  $t_R$  = 9.79 min. ESI-MS:  $m/z$  1012.5  $[\text{M}+\text{H}]^+$ , 1034.5  $[\text{M}+\text{Na}]^+$ . HR ESI-MS: calcd. ( $m/z$ ) for  $\text{C}_{50}\text{H}_{66}\text{N}_{11}\text{O}_{12}^+$   $[\text{M}+\text{H}]^+$ : 1012.4892; found: 1012.4908, (1.6 ppm).

#### 4.4.2.9 2,2',2'',2'''-((2-(4-Isothiocyanatobenzyl)propane-1,3-diy)bis(azanetriyl))tetrakis(N-((1,6-dimethyl-3-hydroxy-4-oxo-1,4-dihydropyridin-2-yl)methyl)acetamide) (*p*-SCN-Bn-THPN, **4.10**)



A solution of **4.9** (~116 mg, ~115  $\mu\text{mol}$ ) in water (~10 mL) was added to a solution of

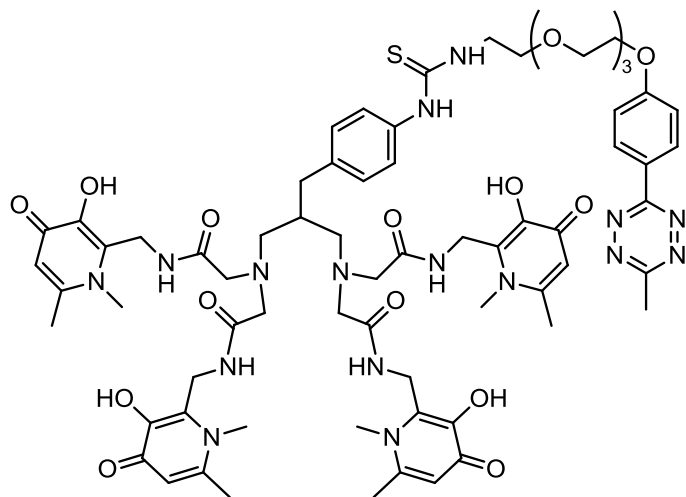
thiophosgene (131.8  $\mu\text{L}$ , 1.719 mmol, 15 eq.) in  $\text{CHCl}_3$  (1.5 mL) [note: thiophosgene is highly toxic and care must be exercised in its handling]. The reaction mixture was stirred vigorously overnight at ambient temperature. The mixture was transferred with water (5 mL) to a conical

centrifuge tube and was washed with CHCl<sub>3</sub> (4 × 1 mL) by biphasic stirring using a vortex and removing the organic layers with a pipette. The aqueous layer was diluted with H<sub>2</sub>O to ~25 mL and was purified in separate batches either by semi-preparative HPLC as described above or by reversed phase flash chromatography (eluted with a gradient of 5–70% methanol with 0.1% TFA/water with 0.1% TFA). Product fractions were pooled, concentrated by rotary evaporation, and dried overnight by lyophilization to yield the title compound **4.10** (*p*-SCN-THPN) as a white powder in ~65% yield (~79 mg, ~75 μmol).

<sup>1</sup>H NMR (400 MHz, CD<sub>3</sub>CN/D<sub>2</sub>O, 11:1 v/v): δ = 7.22 (d, *J* = 8.4 Hz, 2H, -Ph-H), 7.16 (d, *J* = 8.4 Hz, 2H, -Ph-H), 7.00 (s, 4H, -CO-CH-), 4.61-4.52 (m, 8H, -CO-N-CH<sub>2</sub>-), 3.79 (s, 12H, -N-CH<sub>3</sub>), 3.69-3.59 (m, 8H, -N-CH<sub>2</sub>-CO-), 3.01-2.97 (m, 2H, -N-CH<sub>2</sub>-CH-), 2.85-2.79 (m, 2H, -N-CH<sub>2</sub>-CH-), 2.48 (s, 12H, -C-CH<sub>3</sub>), 2.46-2.43 (m, 2H, -CH<sub>2</sub>-Ph-), 2.32-2.27 (m, 1H, -CH-CH<sub>2</sub>-Ph-). <sup>13</sup>C NMR (100 MHz, CD<sub>3</sub>CN/D<sub>2</sub>O, 11:1 v/v): δ = 170.3, 161.9, 150.4, 144.4, 139.5, 138.9, 131.3, 130.0, 126.8, 116.1, 114.3, 60.8, 57.1, 39.6, 36.6, 36.0, 33.8, 21.4. HPLC (method C): *t*<sub>R</sub> = 13.15 min. ESI-MS: *m/z* 527.8 [M+2H]<sup>2+</sup>, 1054.4 [M+H]<sup>+</sup>, 1076.4 [M+Na]<sup>+</sup>. HR ESI-MS: calcd. (*m/z*) for C<sub>51</sub>H<sub>64</sub>N<sub>11</sub>O<sub>12</sub>S<sup>+</sup> [M+H]<sup>+</sup>: 1054.4457; found: 1054.4493.

**4.4.2.10 2,2',2'',2'''-((2-(4-(3-(2-(2-(2-(2-(4-(6-methyl-1,2,4,5-tetrazin-3-yl)phenoxy)ethoxy)ethoxy)ethoxy)ethyl)thioureido)benzyl)propane-1,3-diy)bis(azanetriyl))-tetrakis(N-((1,6-dimethyl-3-hydroxy-4-oxo-1,4-dihydropyridin-2-yl)methyl)-acetamide) (Tz-THPN, 4.12)**

To a solution of *p*-SCN-Bn-THPN (~12.4 mg, ~11.8 μmol) in anhydrous DMSO (~0.4 mL) was added a solution of methyltetrazine-PEG<sub>4</sub>-amine·TFA (**4.11**, 2-[2-[2-[2-[4-(6-methyl-1,2,4,5-tetrazin-3-ylphenoxy)ethoxy] ethoxy] ethoxy]-ethanamine tetrafluoroacetate) in anhydrous DMSO (123.4 μL, 12.9 μL, 1.1 eq., 50 mg/mL). The pH was raised to pH ~9 by



addition of Et<sub>3</sub>N and the reaction mixture was incubated for 2 h at ambient temperature with agitation (650 rpm). Although HPLC indicated some remaining starting material, it was decided to proceed with work up since the tetrazine moiety is too sensitive towards alkaline conditions. The

reaction mixture was diluted with water, loaded on a small C18-ec solid-phase extraction cartridge, and purified by reversed phase flash chromatography using a gradient of 0–100% MeOH/water. Product fractions were pooled, evaporated, and dried *in vacuo* to give the title compound **4.12** as a pink solid with minor impurities (~2.3 mg, ~1.6 μmol, ~14%).

<sup>1</sup>H NMR (400 MHz, CD<sub>3</sub>OD): δ = 8.44 (d, *J* = 8.8 Hz, 2H, arom.), 7.29 (d, *J* = 8.0 Hz, 2H, arom.), 7.13 (d, *J* = 8.8 Hz, 2H, arom.), 7.03 (d, *J* = 8.0 Hz, 2H, arom.), 6.78 (s, 4H, HOPO-C5-H), 4.68 (s, 8H, HOPO-CH<sub>2</sub>-), 4.24 (m, 2H, terminal PEG), 3.90-3.87 (m, 2H, PEG), 3.85 (s, 12H, -N-CH<sub>3</sub>), 3.76-3.70 (m, 4H, PEG), 3.70-3.63 (m, 8H, 4 PEG), 3.55-3.46 (m, 8H, -N-CH<sub>2</sub>-CON-), 3.00 (s, 3H, -tetrazine-CH<sub>3</sub>), 2.80-2.72 (m, 4H, -N-CH<sub>2</sub>-CH), 2.51 (s, 12H, HOPO C6-CH<sub>3</sub>), 2.47-2.43 (m, 2H, -CH<sub>2</sub>-Ph-), 2.04 (m, 1H, -CH). HPLC (method A): *t<sub>R</sub>* = 13.7 min. ESI-MS: *m/z* 709.4 [M+2H]<sup>2+</sup>, 720.5 [M+H+Na]<sup>2+</sup>.

### 4.4.3 <sup>89</sup>Zr-Trastuzumab Radioimmunoconjugates

#### 4.4.3.1 Postlabeling Strategy

*Chelator-modifications of trastuzumab.* In analogy to a reported method by Vosjan *et al.*,<sup>168</sup> purified trastuzumab (~2 mg) was modified at pH ~9 and 37 °C with a five-fold molar

excess of either *p*-SCN-Bn-THPN, *p*-SCN-Phe-DFO, or *p*-SCN-Phe-DFO\* as bifunctional chelator. The immunoconjugates were purified by ultrafiltration and/or size-exclusion chromatography and concentrations were measured by absorbance at 280 nm or by Bradford assay. The purified immunoconjugates were analyzed by SE-HPLC (method E): *THPN-trastuzumab*:  $t_R = 13.1$  min; *DFO-trastuzumab*:  $t_R = 13.1$  min; *DFO\*-trastuzumab*:  $t_R = 13.2$  min; *unmodified trastuzumab*:  $t_R = 13.0$  min.

*Radiolabeling of chelator-trastuzumab immunoconjugates.* In three separate microcentrifuge tubes, a solution of  $^{89}\text{Zr}$ -oxalate (~78 MBq, ~2.1 mCi) in 0.05 M oxalic acid was neutralized with 0.1 M  $\text{Na}_2\text{CO}_3$  to pH ~7–7.5. To this was added either of the immunoconjugates, *i.e.*, THPN-, DFO-, or DFO\*-trastuzumab (~500  $\mu\text{g}$ , ~3.4 nmol). The mixtures were diluted with PBS to a total volume of 1 mL and incubated for one hour at ambient temperature with gentle agitation (300 rpm). At this point, an aliquot was removed and analyzed by ITLC to measure the radiolabeling yield. If the yield was not high enough, more immunoconjugate was added and the reaction was given another incubation period. Once ITLC indicated satisfactory radiolabeling, the mixtures were purified by size-exclusion chromatography and/or ultrafiltration. The purified radioimmunoconjugates were analyzed by ITLC and radio-SE-HPLC (method E):  $^{89}\text{Zr}$ -THPN-trastuzumab:  $t_R = 13.2$  min, aggregates:  $t_R \approx 11.8$  min, small/free  $^{89}\text{Zr}$ -species:  $t_R \approx 16.8$  min;  $^{89}\text{Zr}$ -DFO-trastuzumab:  $t_R = 13.4$  min;  $^{89}\text{Zr}$ -DFO\*-trastuzumab:  $t_R = 13.4$  min;  $^{89}\text{Zr}$ -oxalate (negative control):  $t_R = 17.1$  min.

#### 4.4.3.2 Prelabeling Strategy

A  $^{89}\text{Zr}$ -oxalate solution in 1 M oxalic acid was neutralized with 2 M  $\text{Na}_2\text{CO}_3$  to pH ~6.5, diluted with 0.9% saline (376  $\mu\text{L}$ ), and mixed to dissolve precipitated sodium oxalate. A

solution of *p*-SCN-Bn-THPN (10.2  $\mu$ L,  $\sim$ 51 nmol, 5 mM in anhydrous DMSO) was added to the  $^{89}\text{Zr}$  solution (11 MBq, 297  $\mu$ Ci) in portions with mixing in between additions. The mixture was incubated at ambient temperature with agitation (550 rpm). After 10 min, the reaction was analyzed by ITLC, which indicated quantitative radiolabeling. Trastuzumab (38.7  $\mu$ L, 38.7 g/L,  $\sim$ 1.5 mg,  $\sim$ 10 nmol) was added with mixing and the pH was raised to pH  $\sim$ 9 with 0.1 M  $\text{Na}_2\text{CO}_3$  ( $\sim$ 18  $\mu$ L). The mixture was incubated for 1 h at 37  $^\circ\text{C}$  with agitation (550 rpm) before purification by size-exclusion chromatography (PD MiniTrap G-25) eluted with sterile 0.9% saline (1 mL). The product fraction was recovered in 52% radiochemical yield and was analyzed by SDS-PAGE (7.5%), ITLC, and radio-SE-HPLC (method E,  $t_R = 13.3$  min). Radiochemical purity was determined as  $\sim$ 93% by HPLC ( $\sim$ 99% by ITLC).

#### 4.4.3.3 *In Vitro* Plasma Stability Study

The stability of radioimmunoconjugates with either THPN, DFO, or DFO\* as chelator was assessed in an *in vitro* plasma stability study. The three radioimmunoconjugates were prepared following a prelabeling approach. DFO- and DFO\*-radioimmunoconjugates were prepared by prelabeling similarly to the prelabeling method reported for THPN. In short, a neutralized  $^{89}\text{Zr}$  solution (5.4 MBq, 145  $\mu$ Ci) was diluted with 0.9% saline (375  $\mu$ L) and a solution of either *p*-SCN-Phe-DFO or *p*-SCN-Phe-DFO\* (10.3  $\mu$ L,  $\sim$ 52 nmol, 5 mM in DMSO) was added. The mixture was incubated at ambient temperature with agitation (550 rpm). After 15 min, ITLC indicated  $>$ 97% radiolabeling and trastuzumab (38.7  $\mu$ L, 38.7 g/L,  $\sim$ 1.5 mg,  $\sim$ 10 nmol) was added. The pH was raised to pH  $\sim$ 9 with  $\text{Na}_2\text{CO}_3$  and the mixture was incubated for 1 h at 37  $^\circ\text{C}$  with agitation (550 rpm). The products were purified by size-exclusion chromatography (PD MiniTrap G-25) with sterile 0.9% saline (1 mL) to give the DFO and DFO\*

radioimmuno-conjugates in 58% and 54% radiochemical yield, respectively, and radiochemical purities of >99% (radio-SE-HPLC).

The three radioimmunoconjugates with THPN, DFO, or DFO\* chelates were diluted (1:4 v/v) with mouse plasma. The mixtures were incubated for seven days at 37 °C and aliquots were analyzed by ITLC (mobile phase: EDTA, 50 mM, pH 5.0) at the start and after 1, 3, 5, and 7 days of incubation. The experiment was conducted in duplicate. As a control, <sup>89</sup>Zr-oxalate was incubated in mouse plasma.

#### 4.4.3.4 *Trans*-Cyclooctene (TCO) Modification of Trastuzumab

Trastuzumab was modified with TCO groups similarly to published procedures.<sup>172, 202-204</sup> A solution of freshly purified trastuzumab (210 µL, 2.80 mg, 19.2 nmol) was diluted with PBS (413 µL) that was adjusted to pH 8.8 with 0.1 M NaHCO<sub>3</sub>. To this was added a solution of TCO-NHS (succinimidyl (*E*)-cyclooct-4-en-1-yl carbonate) in anhydrous DMSO (7.2 µL, 25 g/L, 673 nmol) to give a 35:1 molar ratio of TCO:mAb, while keeping the total DMSO concentration below 2%. The mixture was briefly vortexed and then incubated in the dark for 1 h at 21 °C with agitation (500 rpm). The TCO-mAb conjugate was purified by size-exclusion chromatography (PD-10), which was eluted in fractions with PBS (pH 7.4) and antibody concentrations were determined spectrophotometrically. The most concentrated fraction was analyzed for its number of reactive TCO groups/mAb, which was determined as 1.8. It was further analyzed by SE-HPLC (method E): *t<sub>R</sub>* = 13.0 min; (*unmodified mAb*: *t<sub>R</sub>* = 12.8 min).

#### 4.4.3.5 Determination of Number of Reactive TCO Groups per mAb

This experiment was inspired by a procedure reported elsewhere.<sup>204</sup> An aliquot of TCO-modified trastuzumab (28.7  $\mu\text{L}$ ,  $\sim 50 \mu\text{g}$ ) was diluted in PBS (pH 7.4, 271  $\mu\text{L}$ ). To this was added a large excess of sulfo-Cy3-methyltetrazine (99 eq., 3.0  $\mu\text{L}$ , 11.0 mM in anhydrous DMSO, sulfo-Cy3 dye:  $\epsilon_{\lambda = 555 \text{ nm}} = 150,000 \text{ L}\cdot\text{mol}^{-1}\cdot\text{cm}^{-1}$ ). The mixture was briefly vortexed and incubated in the dark for 20 min at 21  $^{\circ}\text{C}$  with agitation (500 rpm). The solution was submitted to size-exclusion chromatography (PD MiniTrap G-25) and it was eluted with 2 x 0.5 mL PBS, pH 7.4. The eluted fractions were further purified by ultrafiltration on an Amicon Ultra centrifugal filter (100 kDa NMWL) and washed with PBS (0.5 mL, pH 7.4). The recovered sulfo-Cy3-mAb conjugate was analyzed by SE-HPLC (method E):  $t_{\text{R}} = 13.1 \text{ min}$ . Using the Proteins and Labels function of a Thermo Scientific NanoDrop 2000 spectrophotometer, the antibody concentration was measured as 4.5  $\mu\text{M}$  and sulfo-Cy3 dye concentration was measured as 8.3  $\mu\text{M}$ . Thus, the relative number of reactive TCO groups per mAb was determined as 1.8.

#### 4.4.3.6 Radiolabeling by Tetrazine/*Trans*-Cyclooctene Click Chemistry

*[A reaction scheme for orientation is provided in Appendix D, Figure D.1.]*

*Postlabeling approach.* To a solution of TCO-modified trastuzumab in PBS pH 7.4 (284  $\mu\text{L}$ ,  $\sim 500 \mu\text{g}$ ,  $\sim 3.33 \text{ nmol}$ ,  $\sim 1.8 \text{ TCO/mAb}$ ) was added in five portions a solution of Tz-THPN in DMSO (**4.12**, 4.1 nmol, 10  $\mu\text{L}$ , 10 mM) with immediate mixing between additions. The volume was adjusted with PBS, pH 7.4 to a total of 300  $\mu\text{L}$  and the reaction was incubated in the dark at ambient temperature with agitation (500 rpm). After 30 min, the mixture was purified by size-exclusion chromatography (PD MiniTrap G-25) eluting with PBS, pH 7.4, followed by ultrafiltration (100 kDa NMWL) and the centrifugal filter was rinsed once with PBS, pH 7.4. The recovered immunoconjugate was analyzed by SE-HPLC and its concentration was determined

by a Bradford assay. A solution of  $^{89}\text{Zr}$ -oxalate in 1 M oxalic acid was then neutralized with 2 M  $\text{Na}_2\text{CO}_3$  to pH 6.5–7.0, left to react for several minutes, and centrifuged. The supernatant (~60  $\mu\text{L}$ , 13.5 MBq, 365  $\mu\text{Ci}$ ) was transferred to a solution of the immunoconjugate in PBS, pH 7.4 (28.9  $\mu\text{L}$ , ~50  $\mu\text{g}$ , ~1.73 mg/mL), was immediately briefly vortexed, and was incubated at 21 °C with agitation (650 rpm). The radiolabeling yield was monitored by ITLC at several time intervals and two more aliquots of immunoconjugate were added for a total of ~100  $\mu\text{g}$  (57.8  $\mu\text{L}$ ) immunoconjugate until ITLC indicated 91% of bound  $^{89}\text{Zr}$ . After a total incubation period of 2 h 15 min, the reaction was quenched by addition of ~5  $\mu\text{L}$  50 mM EDTA, pH 7.0. The mixture was purified by size-exclusion chromatography (PD MiniTrap G-25) and the product was recovered in 74% radiochemical yield (10.0 MBq, 269  $\mu\text{Ci}$ ). Analyses by radio-SE-HPLC indicated the presence of radiolabeled mAb with some aggregates but were hampered by adhesion of activity to the detector tubing.

*Prelabeling approach.* A solution of  $^{89}\text{Zr}$ -oxalate in 1 M oxalic acid was neutralized with 2 M  $\text{Na}_2\text{CO}_3$  to pH ~7.5, was spun, and the supernatant (~56  $\mu\text{L}$ , 16.3 MBq, 441  $\mu\text{Ci}$ ) was transferred to a separate reaction vial. To this were added aliquots of Tz-THPN (**4.12**, total of 4.1 nmol, 8.22  $\mu\text{L}$  as 0.25 mM solution in 1:4 DMSO/HEPES (0.5 M, pH 7.0) and 2.06  $\mu\text{L}$  as 1 mM solution in DMSO) and the mixture was incubated in the dark at 21 °C with agitation (650 rpm). Small amounts of 1 M oxalic acid were added to adjust the reaction pH to 7.5–8. Radiolabeling yield was monitored by ITLC at several time intervals and aliquots of Tz-THPN were added until ITLC indicated 96% of bound  $^{89}\text{Zr}$ . Total reaction time was 2 h. This mixture was then added to a solution of TCO-modified trastuzumab in PBS, pH 7.4 (210  $\mu\text{L}$ , ~371  $\mu\text{g}$ , ~2.54 nmol, ~1.8 TCO/mAb) for an intended molar ratio of ~1.1 tetrazine groups per reactive TCO groups. However, ~58% of activity were lost to adhesion to the previous reaction vial, even after rinsing

with HEPES buffer (152  $\mu$ L, 0.5 M, pH 7.0), which was added to the reaction mixture. The reaction was incubated in the dark for 1 h at 21  $^{\circ}$ C with agitation (650 rpm) and was then purified by size-exclusion chromatography (PD MiniTrap G-25). The product was eluted with 1 mL HEPES buffer and was recovered in overall 20% radiochemical yield (3.23 MBq, 87.3  $\mu$ Ci). Analyses by radio-SE-HPLC indicated presence of radiolabeled mAb with a limited amount of aggregation but were hampered by adhesion of activity to the detector tubing.

#### 4.4.4 $^{89}\text{Zr}$ -Anti-PD-L1 Radioimmunoconjugates

##### 4.4.4.1 THPN-Modification of anti-PD-L1 mAb

A solution of anti-mouse PD-L1 mAb (45.4  $\mu$ L,  $\sim$ 250  $\mu$ g, 5.5 g/L in PBS pH 6.5) was diluted with  $\text{NaHCO}_3/\text{Na}_2\text{CO}_3$  buffer (50  $\mu$ L, 0.1 M, pH  $\sim$ 9) and a freshly prepared *p*-SCN-Bn-THPN solution (8.3  $\mu$ L,  $\sim$ 10 eq., 2 mM) in 10% DMSO was added. The solution was carefully mixed, the pH was adjusted to pH  $\sim$ 8.7–9.0 (0.1 M  $\text{Na}_2\text{CO}_3$ ) and the reaction was incubated for 2 h at 37  $^{\circ}$ C with gentle agitation (350 rpm). The mixture was purified by size-exclusion chromatography over a PD-10 desalting column and/or by ultrafiltration over an Amicon Ultra 100K centrifugal filter, rinsed twice, and recovered with HEPES buffer (0.5 M, pH 7.0). The immunoconjugate product was analyzed by SE-HPLC (method E):  $t_R = 12.8$  min (*unmodified anti-PD-L1 mAb*:  $t_R = 12.8$  min).

##### 4.4.4.2 $^{89}\text{Zr}$ -Labeling of THPN-anti-PD-L1 immunoconjugate

A stock solution of  $^{89}\text{Zr}$ -oxalate in 1 M oxalic acid was neutralized with 2 M  $\text{Na}_2\text{CO}_3$  to pH  $\sim$ 7 and the supernatant ( $\sim$ 36  $\mu$ L, 7.5 MBq, 202  $\mu$ Ci) was added to a solution of THPN-modified anti-PD-L1 mAb ( $\sim$ 50  $\mu$ g) in HEPES buffer (48.6  $\mu$ L, 0.5 M, pH 7.0). It was briefly

mixed and then incubated at 22 °C with gentle agitation (350 rpm). After 15 min, the reaction mixture was analyzed by ITLC and another aliquot of THPN-anti-PD-L1 (~50 µg, 16.4 µL) was added. After another 15 min, ITLC indicated a radiolabeling yield of 70%, at which point the reaction was quenched by adding EDTA (5 µL, 50 mM, pH 7.0). The mixture was purified by ultrafiltration (Amicon Ultra 100K centrifugal filter) and analyzed by radio-SE-HPLC (method E):  $t_R = 12.7$  min. Isolated radiochemical yield was 47% and radiochemical purity was ~64% (HPLC).

#### 4.4.5 <sup>89</sup>Zr-Mouse Serum Albumin (MSA) Radioconjugates

##### 4.4.5.1 THPN-Modification of MSA

A freshly prepared *p*-SCN-Bn-THPN solution in DMSO (11.4 µL, 20 mM, 10 eq.) was diluted with water (138.6 µL) and carbonate buffer (225 µL, pH ~8.7). To this, an aqueous solution of mouse serum albumin (MSA) was added (75 µL, 20 g/L, 1.5 mg). The pH of the mixture was adjusted to pH 8.3–8.5 (0.1 M Na<sub>2</sub>CO<sub>3</sub>) and the reaction was incubated overnight at 21 °C with gentle agitation (350 rpm). The mixture was purified by size-exclusion chromatography over a PD-10 desalting column, eluted with HEPES buffer (0.5 M, pH 7.0), and the product fraction was analyzed by SDS-PAGE (Figure 4.11) and SE-HPLC (method E):  $t_R = 13.5$  min (*unmodified MSA*:  $t_R = 13.3$  min).

##### 4.4.5.2 <sup>89</sup>Zr-Radiolabeling of THPN-MSA

To a freshly neutralized solution of <sup>89</sup>Zr-oxalate (5.0 MBq, 134 µCi) was added a solution of THPN-modified MSA (142 µL, ~264 µg, ~1.8 g/L) in HEPES buffer (0.5 M, pH 7.0). The mixture was very briefly vortexed and incubated at 21 °C with gentle agitation (350 rpm).

After 20 min, an aliquot was analyzed by ITLC, which indicated 99% radiolabeling yield. The reaction mixture was purified by size-exclusion chromatography over a PD-10 desalting column with HEPES buffer (25 mM, pH 7.0) as eluent. The product was isolated in 98% radiochemical yield and was analyzed by SDS-PAGE (Figure 4.11) and radio-SE-HPLC (method E):  $t_R = 13.6$  min. Radiochemical purity (HPLC) was ~88% and specific activity was determined as ~15 kBq/ $\mu$ g; 0.42  $\mu$ Ci/ $\mu$ g by measuring a known volume in a dose calibrator and determining the protein concentration in a Bradford assay.

#### 4.4.6 $^{89}\text{Zr}$ -HPG Radioconjugates

##### 4.4.6.1 Chelator Conjugation to HPG-Nanoparticles

*THPN-, DFO-, and DFO\*-HPG Conjugates.* In three separate reaction vials, aqueous solutions (100  $\mu$ L, 40 g/L, ~5 nmol) of amine-functionalized hyperbranched polyglycerol (HPG, ~800 kDa molecular weight) were diluted with sodium carbonate buffer (150  $\mu$ L, 0.1 M, pH 9) and ligand solutions of either *p*-SCN-Bn-THPN, *p*-SCN-Phe-DFO, or *p*-SCN-Phe-DFO\* were added (50  $\mu$ L, 0.5 M, ~5 eq.). DFO and DFO\* stock solutions were in anhydrous DMSO, while the THPN stock solution was in freshly diluted 5% DMSO (aq.). The pH of the reaction mixtures was adjusted to pH 8.5–9.0 with  $\text{Na}_2\text{CO}_3$  and the mixture was incubated overnight at 37 °C with gentle agitation (350 rpm). After 21 h, the mixture was loaded on a PD MiniTrap G-25 size-exclusion column, eluted with HEPES buffer (0.5 M, pH 7.0), and further purified by ultrafiltration over an Amicon Ultra 100K centrifugal filter (rinsed with 3  $\times$  0.4 mL HEPES buffer). The recovered HPG conjugates were analyzed by SE-HPLC and DLS.

*THPN-HPG Conjugate:* SE-HPLC (method D):  $t_R = 15.3$  min; DLS: Z-avg. (d)  $15.4 \pm 0.5$  nm; PDI:  $0.15 \pm 0.04$ . *DFO-HPG Conjugate:* SE-HPLC (method D):  $t_R = 15.4$  min; DLS: Z-avg. (d)  $19.2 \pm 0.6$  nm; PDI:  $0.32 \pm 0.05$ . *DFO\*-HPG Conjugate:* SE-HPLC (method D):  $t_R = 15.4$  min;

DLS: Z-avg. (d)  $16.9 \pm 0.4$  nm; PDI:  $0.23 \pm 0.02$ . *Unmodified HPG-NH<sub>2</sub> (control)*: SE-HPLC (method D):  $t_R = 15.2$  min; DLS: Z-avg. (d)  $16.7 \pm 0.2$  nm; PDI:  $0.23 \pm 0.01$ .

#### 4.4.6.2 <sup>89</sup>Zr-Radiolabeling of HPG-Chelator Conjugates

In three separate reaction vials, HPG-chelator solution (THPN, DFO, or DFO\*) was added to a neutralized <sup>89</sup>Zr-oxalate solution (~170  $\mu$ L, ~32 MBq, ~870  $\mu$ Ci, pH ~7), it was briefly vortexed and the mixtures were incubated at 21 °C with gentle agitation (350 rpm). Aliquots were analyzed by ITLC and more HPG-chelator solution was added in portions until quantitative radiolabeling was achieved. Added HPG-chelate volumes were 67.4, 75.6, and 66.6  $\mu$ L for the THPN, DFO, and DFO\* conjugates, respectively and total reaction volumes were ~250  $\mu$ L. After 3 h reaction time, the reactions were purified by size exclusion chromatography (PD MiniTrap G-25), and eluted with water in seven fractions. Isolated radiochemical yields for all three reactions were 97% and radiochemical purities were >99% (HPLC). The most active product fractions were pooled and analyzed by radio-SE-HPLC, ITLC, and DLS.

*<sup>89</sup>Zr-THPN-HPG Conjugate*: radio-SE-HPLC (method D):  $t_R = 15.3$  min; DLS: Z-avg. (d)  $16.2 \pm 1.0$  nm; PDI:  $0.25 \pm 0.02$ . *<sup>89</sup>Zr-DFO-HPG Conjugate*: radio-SE-HPLC (method D):  $t_R = 15.3$  min; DLS: Z-avg. (d)  $14.8 \pm 0.2$  nm; PDI:  $0.22 \pm 0.01$ . *<sup>89</sup>Zr-DFO\*-HPG Conjugate*: radio-SE-HPLC (method D):  $t_R = 15.3$  min; DLS: Z-avg. (d)  $18.3 \pm 0.7$  nm; PDI:  $0.29 \pm 0.03$ .

#### 4.4.6.3 *In Vitro* Plasma Stability of <sup>89</sup>Zr-HPG Conjugates

<sup>89</sup>Zr-chelate-HPG conjugates with THPN, DFO, or DFO\* prepared as described above were diluted 1:4 (v/v) with human blood plasma from a healthy donor. The mixtures were incubated for 5 days at 37 °C with gentle agitation (350 rpm). Aliquots were analyzed by ITLC

(black strips, DTPA mobile phase, 50 mM, pH 7.0) at the beginning of the experiment and after 1, 3, and 5 days incubation and the percentage of chelated  $^{89}\text{Zr}$  was determined by integration. Measurements were performed in triplicates.

#### 4.4.6.4 *In Vivo* Study of $^{89}\text{Zr}$ -HPG Conjugates

This animal study was performed in accordance with the animal care committee (ACC) of the University of British Columbia under the approved protocol A16-0104.  $^{89}\text{Zr}$ -chelate-HPG conjugates with THPN, DFO, or DFO\* chelators were prepared as described above on the day prior to the experiment and were stored overnight at 4 °C. On the day of administration, quality control of the radioconjugates was performed by radio-SE-HPLC and ITLC. Immediately before preparation of the injection doses, the aqueous radioconjugate stock solutions (~490  $\mu\text{L}$ ) were diluted with sterile-filtered (0.22  $\mu\text{m}$ ) concentrated PBS (10x, 54.4  $\mu\text{L}$ ). Eleven-week-old female, healthy, immunodeficient NSG mice (NOD.Cg-Prkdc<sup>scid</sup>Il2rg<sup>tm1Wjl</sup>/SzJ) were anesthetized using isoflurane inhalation (2% in O<sub>2</sub>) and were administered  $^{89}\text{Zr}$ -THPN-HPG,  $^{89}\text{Zr}$ -DFO-HPG, or  $^{89}\text{Zr}$ -DFO\*-HPG conjugate solutions *via* tail vein injection.

For biodistribution studies, each mouse was injected ~1.5 MBq (~40  $\mu\text{Ci}$ , median, ~40  $\mu\text{L}$ )  $^{89}\text{Zr}$ -chelate-HPG solution and mice were euthanized after 1, 3, or 6 days post-injection by CO<sub>2</sub> inhalation, followed by blood withdrawal by cardiac puncture ( $n = 4$  per group and time point). Tissues and organs were harvested, washed in Dulbecco's PBS, dried on paper, and weighed.  $^{89}\text{Zr}$  activities were measured using a calibrated  $\gamma$  counter. Data were decay corrected and compiled in Microsoft Excel and evaluated in GraphPad Prism and Excel. Statistical analysis of bone uptake was performed by multiple *t*-tests assuming equal variance with a significance level of  $\alpha = 0.05$ . Activity distributions are expressed as percentage of the injected dose per gram of tissue (%ID/g).

For PET/CT imaging, each mouse was injected ~5 MBq (~135  $\mu$ Ci, ~120  $\mu$ L) of  $^{89}\text{Zr}$ -chelate-HPG solution ( $n = 1$  per group). Prior to imaging, mice received a subcutaneous injection of 0.9% NaCl (0.2 mL) for hydration. Mice were imaged under isoflurane anesthesia with a CT scan followed by a 20 min PET acquisition at 1 h, 1 d, 3 d, and 6 d post-injection. After the last imaging time point, mice were euthanized by  $\text{CO}_2$  inhalation followed by blood withdrawal by cardiac puncture and were included in the respective biodistribution studies described above. Images were reconstructed using a three-dimensional ordered subsets expectation maximization (OSEM3D, 2 iterations), followed by a fast maximum a priori algorithm (FastMAP, 18 iterations) and attenuation correction was performed based on the CT image. Images were rendered using the Inveon Research Workplace software.

## Chapter 5: THPN with Other Medically Relevant Metal Ions

### 5.1 Introduction

To explore the potential of THPN as a chelator for metals other than Zr, THPN was screened with several medically interesting metal ions and the formation of monometallic complexes was investigated. The chelation potential of THPN for a few metal ions that have not been tested experimentally is also briefly discussed.

### 5.2 Results and Discussion

The two preceding chapters focused on the complexation of  $Zr^{4+}$  by THPN. As a preliminary assessment of the potential of THPN as a chelator for other metals and to provide a starting point for future development of this chelator, we explored the THPN complexation of eight other metal ions ( $Fe^{3+}$ ,  $Ga^{3+}$ ,  $Y^{3+}$ ,  $Sm^{3+}$ ,  $Gd^{3+}$ ,  $Tb^{3+}$ ,  $Lu^{3+}$ , and  $Bi^{3+}$ ) that are also of interest for applications in (nuclear) medicine.

Formation of the iron(III) complex was studied in the context of the thermodynamic stability study of Zr-THPN (Section 3.2.3.2). In that study, the formation constants of the Fe-THPN complex were determined and presented in Table 3.4 along with the speciation plot shown in Figure 3.5a. The thermodynamic complex stability of Fe-THPN was very high ( $\log \beta_{110}$  44.71,  $pM$  38.0) and THPN merits further exploration of its therapeutic potential to treat for example iron overload.

THPN also formed a monometallic complex with gallium(III), which shares a similar coordination chemistry with  $Fe^{III}$ . After incubation overnight at ambient temperature, electrospray ionization (ESI) mass spectrometry (MS) showed the formation of the

monometallic Ga-THPN complex. Signals at  $m/z$  973.3 and 995.3 Da featured Ga-distinctive isotope patterns and were assigned to the double-proton- and proton-sodium-adducts, respectively. Gallium complexes could be useful for PET with the  $\beta^+$ -emitting  $^{68}\text{Ga}$ , or for SPECT and Auger electron radionuclide therapy with  $^{67}\text{Ga}$ .

The group 3 transition metal ion yttrium(III) was complexed with THPN at ambient temperature and analyzed by mass spectrometry. In ESI-MS, the monometallic  $[\text{Y}(\text{H}_2\text{THPN})]^+$  complex<sup>†</sup> was detected in positive mode at  $m/z$  993.5 Da. Other signals also indicated the presence of a trinuclear  $[\text{Y}_3(\text{THPN})_2]^+$  species and two peaks at  $m/z$  1036.5 and 1047.5 Da were assigned to the doubly-charged proton and sodium adducts, respectively. Only the doubly-charged adducts could be detected since the singly-charged trinuclear complex exceeded the detection limit of the mass spectrometer of  $m/z$  1250 Da. Yttrium complexes with the high-energy  $\beta^-$  emitter  $^{90}\text{Y}$  are of interest to improve  $^{90}\text{Y}$ -microspheres for selective internal radiation therapy (SIRT) of solid tumours such as the radioembolization of hepatocellular carcinoma. The  $\beta^+$ -emitting  $^{86}\text{Y}$ , in turn, is a PET nuclide and can be employed as imaging surrogate for  $^{90}\text{Y}$  therapy.<sup>205</sup>

Complexation of the lanthanide ions samarium(III), gadolinium(III), terbium(III), and lutetium(III) with THPN also produced the monometallic  $[\text{Ln}(\text{H}_2\text{THPN})]^+$  complexes as indicated by ESI-MS. Yet all of these lanthanides also showed some—albeit sometimes small—peaks attributed to trinuclear  $\text{M}_3\text{L}_2$  species detected as  $[\text{Ln}_3(\text{THPN})_2\text{H}]^{2+}$ . The MS peaks of the Gd and Tb complexes also featured the characteristic isotopic patterns distinctive for these two lanthanides. Gadolinium complexes have desirable properties for contrast enhancement in magnetic resonance imaging (MRI).<sup>70</sup> Metal complexes with the  $\beta^-$ -emitters  $^{153}\text{Sm}$  and  $^{177}\text{Lu}$  are

---

<sup>†</sup> In this discussion of THPN metal complexes, THPN in complexes refers to the deprotonated ligand THPN<sup>4-</sup>.

feasible for targeted radionuclide therapy and each have one approved therapeutic radiocomplex ( $^{153}\text{Sm}$ -lexidronam and  $^{177}\text{Lu}$ -DOTATATE). Terbium complexes are compelling from a radiopharmaceutical perspective in that four Tb radionuclides cover all decay modes for nuclear medicine.  $^{155}\text{Tb}$  and  $^{152}\text{Tb}$  are suited for SPECT and PET, respectively, while the  $\beta^-$ - and Auger emitter  $^{161}\text{Tb}$  and the  $\alpha$ -emitter  $^{149}\text{Tb}$  have promising therapeutic emissions.<sup>206-208</sup>

In contrast to the metal ions discussed above, complexation of bismuth(III) appeared to form a binuclear  $\text{M}_2\text{L}$  species, which was detected as a major peak at  $m/z$  659.8 Da assigned to the doubly-charged bimetallic ion  $[\text{Bi}_2(\text{THPN})]^{2+}$ . Complexes with the potent bismuth nuclides  $^{213}\text{Bi}$  or  $^{212}\text{Bi}$  could be useful for targeted alpha therapy.<sup>20, 27, 209</sup>

With the exception of  $\text{Bi}^{\text{III}}$ , all other metal ions discussed above formed monometallic complexes with THPN at ambient temperature. This renders THPN a promising ligand to be further explored with these metals. With the exception of  $\text{Ga}^{\text{III}}$  complexation, no free THPN ligand was detected by ESI-MS, supporting THPN's expected preference for complexation of the metal ions. The small ligand peak observed for  $\text{Ga}^{\text{III}}$  complexation may be owed to an overestimation of the metal stock concentration since the number of crystallization water molecules in the metal salt was unknown. The observation of trinuclear species needs to be further investigated and complexation conditions may have to be optimized to avoid their formation. A possible explanation for their formation could be that even though an equimolar reaction stoichiometry was intended, inaccuracies in the preparation of THPN stock solutions due to the small scale of these experiments could have resulted in an excess of metal ions over ligand molecules.

In addition to iron, gallium, yttrium, and lanthanides, THPN may be an interesting ligand for the complexation of other metal ions such as actinides. The complexation of actinides has been explored with a number of other octadentate HOPO ligands by the groups of

Raymond, Abergel, and others.<sup>68, 141, 146, 210-215</sup> The recent development of a tetrapodal octadentate 3,2-HOPO ligand for chelation of the  $\alpha$  particle emitter  $^{227}\text{Th}^{\text{IV}}$  also looks promising and the resulting  $^{227}\text{Th}$  complex is believed to be investigated for radioimmunotherapy in a first-in-human clinical trial by the pharmaceutical company Bayer.<sup>214-216</sup> All octadentate HOPO chelators investigated with actinides are based on 1,2- or 3,2-HOPO groups, while THPN is thus far the only reported octadentate 3,4-HOPO chelator. Based on the promising results with those chelators, THPN is envisioned to also hold potential as an actinide chelator. Preliminary radiolabeling attempts with the  $\alpha$  particle emitter  $^{225}\text{Ac}^{\text{III}}$  were, unfortunately, not conclusive. The absence of a stable Ac isotope renders the exploration of its coordination chemistry particularly challenging and chelation was not further explored. But due to structural similarities to those literature chelators, and given THPN's octadentate  $\text{O}_8$  donor set, THPN may also be a feasible ligand to be explored with  $\text{Th}^{\text{IV}}$ , as well as other actinides. Such complexes would hold potential for targeted alpha particle therapy or for actinide decorporation.

### 5.3 Conclusions

To assess the potential of THPN as a chelator for medically relevant metals other than Zr, we studied the complex formation with eight additional metal ions ( $\text{Fe}^{3+}$ ,  $\text{Ga}^{3+}$ ,  $\text{Y}^{3+}$ ,  $\text{Sm}^{3+}$ ,  $\text{Gd}^{3+}$ ,  $\text{Tb}^{3+}$ ,  $\text{Lu}^{3+}$ , and  $\text{Bi}^{3+}$ ). The very high thermodynamic stability of the iron(III) complex suggests the exploration of THPN's therapeutic potential to treat iron overload or to deprive microorganisms of  $\text{Fe}^{3+}$  for antimicrobial applications. Monometallic complexes were also obtained with gallium(III), yttrium(III), and the lanthanides  $\text{Sm}^{\text{III}}$ ,  $\text{Gd}^{\text{III}}$ ,  $\text{Tb}^{\text{III}}$ , and  $\text{Lu}^{\text{III}}$  but complexation conditions need to be optimized to avoid formation of trinuclear species. From a radiopharmaceutical perspective, Ga and Tb complexes could be particularly interesting for

imaging and Y, Tb, and Lu complexes for targeted radionuclide therapy. Likewise, the potential for actinide chelation also merits exploration to further harness the therapeutic potency of actinide  $\alpha$  particle emitters.

## 5.4 Experimental

### 5.4.1 Materials and Methods

All chemicals were used as received without further purification. Metal salts were purchased from Strem Chemicals, Alfa Aesar, or Aldrich as  $\text{YCl}_3 \cdot 6\text{H}_2\text{O}$ ,  $\text{Ga}(\text{NO}_3)_3 \cdot x\text{H}_2\text{O}$ ,  $\text{SmCl}_3 \cdot 6\text{H}_2\text{O}$ ,  $\text{GdCl}_3 \cdot 6\text{H}_2\text{O}$ ,  $\text{TbCl}_3 \cdot 6\text{H}_2\text{O}$ ,  $\text{LuCl}_3 \cdot 6\text{H}_2\text{O}$ , and anhydrous  $\text{BiCl}_3$ . All water used was ultrapure (18.2 M $\Omega$ ·cm). ESI-MS spectra were recorded on an AB Sciex QTrap 5500 mass spectrometer in positive mode.

### 5.4.2 Syntheses

*Ga<sup>III</sup> complexation.* A solution of  $\text{Ga}(\text{NO}_3)_3$  (10.5  $\mu\text{L}$ , 0.5 M,  $\sim 5.3 \mu\text{mol}$ ) in 50% methanol/water was added to a solution of THPN in 5:1 methanol/water (600  $\mu\text{L}$ , 8 mM,  $\sim 4.8 \mu\text{mol}$ ). The mixture was briefly vortexed and left stirring overnight at ambient temperature. The solution was then precipitated by dropwise addition to THF ( $\sim 4 \text{ mL}$ ), centrifuged, and the supernatant was removed. The precipitate was air-dried, followed by freeze-drying, and the resulting white powder was analyzed by mass spectrometry. ESI-MS ( $m/z$ ) 973.3 [ $\text{ML}+2\text{H}$ ]<sup>+</sup> (calcd. 973.3); 995.3 [ $\text{ML}+\text{H}+\text{Na}$ ]<sup>+</sup> (calcd. 995.3).

*Y<sup>III</sup> complexation.* An aqueous solution of  $\text{YCl}_3$  (220  $\mu\text{L}$ , 5 mM,  $\sim 1.1 \mu\text{mol}$ ) was added to a solution of THPN in water (400  $\mu\text{L}$ , 2.8 mM,  $\sim 1.1 \mu\text{mol}$ ). The mixture was briefly vortexed and then incubated for 1.5 h at ambient temperature with agitation (700 rpm). At this point, an

aliquot was removed, diluted with methanol, and analyzed by mass spectrometry. ESI-MS ( $m/z$ ) 993.5 [ML+2H]<sup>+</sup> (calcd. 993.3); 1036.5 [M<sub>3</sub>L<sub>2</sub>+H]<sup>2+</sup> (calcd. 1036.2); 1047.5 [M<sub>3</sub>L<sub>2</sub>+Na]<sup>2+</sup> (calcd. 1047.2).

*Sm<sup>III</sup> complexation.* A solution of SmCl<sub>3</sub> in D<sub>2</sub>O (220 μL, 5 mM, ~1.1 μmol) was added to a solution of THPN in a D<sub>2</sub>O/H<sub>2</sub>O (4:1) mixture (250 μL, 4.4 mM, ~1.1 μmol). The mixture was incubated for 1 h at ambient temperature with agitation (700 rpm). An aliquot was removed, diluted with methanol, and analyzed by mass spectrometry. ESI-MS ( $m/z$ ) 1056.4 [ML+2H]<sup>+</sup> (calcd. 1056.3); 1129.9 [M<sub>3</sub>L<sub>2</sub>+H]<sup>2+</sup> (calcd. 1129.3).

*Gd<sup>III</sup> complexation.* A solution of GdCl<sub>3</sub> in water (276 μL, 4 mM, ~1.1 μmol) was added to a solution of THPN in D<sub>2</sub>O (100 μL, 11 mM, ~1.1 μmol). The mixture was incubated overnight at ambient temperature with agitation (700 rpm). An aliquot was removed, diluted with methanol, and analyzed by mass spectrometry. ESI-MS ( $m/z$ ) 1062.5 [ML+2H]<sup>+</sup> (calcd. 1062.3); 1140.5 [M<sub>3</sub>L<sub>2</sub>+H]<sup>2+</sup> (calcd. 1139.8).

*Tb<sup>III</sup> complexation.* A solution of TbCl<sub>3</sub> in D<sub>2</sub>O (220 μL, 5 mM, ~1.1 μmol) was dropwise added to a solution of THPN in D<sub>2</sub>O (250 μL, 4.4 mM, ~1.1 μmol). The mixture was incubated for 25 min at ambient temperature with agitation (700 rpm). A portion of the reaction mixture (200 μL) was removed, basified by addition of NaOH to pH ~8 (~20 μL, 0.1 M), and the mixture was incubated for another 25 min at ambient temperature with agitation. An aliquot was removed, diluted with methanol, and analyzed by mass spectrometry. ESI-MS ( $m/z$ ) 1063.5 [ML+2H]<sup>+</sup> (calcd. 1063.3); 1085.3 [ML+H+Na]<sup>+</sup> (calcd. 1085.3); 1141.4 [M<sub>3</sub>L<sub>2</sub>+H]<sup>2+</sup> (calcd. 1141.3); 1152.5 [M<sub>3</sub>L<sub>2</sub>+Na]<sup>2+</sup> (calcd. 1152.3).

*Lu<sup>III</sup> complexation.* THPN (5.3 mg, 5.4 μmol) was dissolved with heating in a mixture of methanol, water, and 0.1 M Na<sub>2</sub>CO<sub>3</sub> (20:5:1) and was allowed to cool to ambient temperature. To this ligand solution was dropwise added a solution of LuCl<sub>3</sub> in methanol (410 μL, 13.1 mM,

~5.4  $\mu\text{mol}$ ) and  $\text{Na}_2\text{CO}_3$  (6.8  $\mu\text{L}$ , 0.1 M) was added. The mixture was briefly vortexed and was then incubated overnight at ambient temperature with agitation (700 rpm). A solution of  $\text{Na}_2\text{CO}_3$  (80.4  $\mu\text{L}$ , 0.1 M) was added which caused turbidity and the mixture was mixed another night at ambient temperature. The slurry was then transferred to a microcentrifuge tube, centrifuged, the supernatant was removed, and the white precipitate was analyzed by mass spectrometry. ESI-MS ( $m/z$ ) 1079.4  $[\text{ML}+2\text{H}]^+$  (calcd. 1079.3); 1101.4  $[\text{ML}+\text{H}+\text{Na}]^+$  (calcd. 1101.3); 1176.9  $[\text{M}_3\text{L}_2+\text{Na}]^{2+}$  (calcd. 1176.3).

*Bi<sup>III</sup> complexation.* A freshly prepared solution of anhydrous  $\text{BiCl}_3$  in methanol (275  $\mu\text{L}$ , 4 mM, ~1.1  $\mu\text{mol}$ ) was dropwise added to a solution of THPN in methanol (300  $\mu\text{L}$ , 3.7 mM, ~1.1  $\mu\text{mol}$ ). The mixture was incubated for 1.5 h at ambient temperature with agitation (700 rpm). An aliquot was removed, diluted with methanol, and analyzed by mass spectrometry. ESI-MS ( $m/z$ ) 659.8  $[\text{M}_2\text{L}]^{2+}$  (calcd. 660.2).

## Chapter 6: Conclusions and Outlook

Metallic radiopharmaceuticals play a critical role in nuclear medicine and are desired for applications in imaging and therapy. To be utilized in most radiopharmaceutical compounds, radiometals need to be stably sequestered by chelating agents to avoid off-target distribution. The long-lived radionuclide zirconium-89 possesses compelling decay characteristics for antibody-targeted PET but is in need for alternative chelating agents. Through the work presented herein, a new class of octadentate chelators was introduced to expand the repertoire of available chelating agents and these chelators were investigated *in vitro* and *in vivo* with zirconium(IV).

Chapter 3 discussed the synthesis and characterization of the novel tetrapodal 3,4-HOPO ligand THPN and the examination of its complex with Zr<sup>IV</sup>. Using micromolar concentrations, the chelator rapidly forms a monometallic Zr-complex that is of exceptional thermodynamic stability. In challenge experiments, the new chelator outperformed the current literature standard and short-term *in vivo* stability showed promising rapid excretion of the <sup>89</sup>Zr-radiocomplex without signs of residual organ uptake.

In Chapter 4, this chelator was further functionalized in a multistep synthesis to introduce a reactive isothiocyanate handle to the backbone. This bifunctionalization then enabled (bio)conjugation to targeting entities. The bifunctional chelator was successfully conjugated to antibodies, a model protein, and polymeric nanoparticles and radiolabeling of these conjugates with <sup>89</sup>Zr was optimized. Subsequently, the stability of the radioconjugates was investigated *in vitro* and, if feasible, *in vivo* and was compared against two literature chelators. Polymeric hyperbranched polyglycerol nanoparticles were identified as a suitable platform to assess the physiologic stability of radiochelates. Their prolonged circulation time, robust chemistry, and innocuous toxicity profile render them suitable nanocarriers to evaluate the

long-term stability of conjugated radiocomplexes (or other cargo) in the blood stream over several half-lives. A six-day mouse study revealed inferior physiologic stability of  $^{89}\text{Zr}$ -THPN-nanoparticle conjugates compared to corresponding radiochelate-particles with two literature chelators. Since the thermodynamic stability of the radiocomplex was previously determined to be exceptionally high, the observed instability was attributed to suboptimal kinetic inertness, which is of particular importance for the *in vivo* stability of radiopharmaceuticals.

In order to improve this kinetic aspect, a more preorganized structure of the chelator may be beneficial. This could reduce the entropic penalty accrued upon metal ion complexation and should convey a higher kinetic inertness, as often seen for macrocycles.<sup>51</sup> Thus, a bi-macrocyclic cage or “clam-shell” like version of the ligand could be a rational extension of THPN. An imaginable strategy could be to connect the 3,4-HOPO groups not only at the C2 ring position, but also at the C5 position. Two potential ligand structures are suggested in Figure 6.1 and their Zr-complex geometries were simulated by DFT (Figure 6.2). Connecting the same linker as used for the THPN backbone at the C5 positions would give a bi-macrocyclic cage, while using two different linkers could give access to a “clam-shell” like bi-macrocycle, somewhat resembling a ligand reported by Tinianow *et al.*<sup>112</sup> Analogous to THPN, a conjugation handle could be introduced at the centre of one linking group. It should be taken into account, however, that the improved kinetic inertness of macrocycles commonly comes at the cost of more stringent reaction conditions for metal ion coordination. This aspect, together with synthetic feasibility, hydrophilicity, solubility, and geometric factors, therefore needs to be carefully considered when designing the next generation of this ligand system.

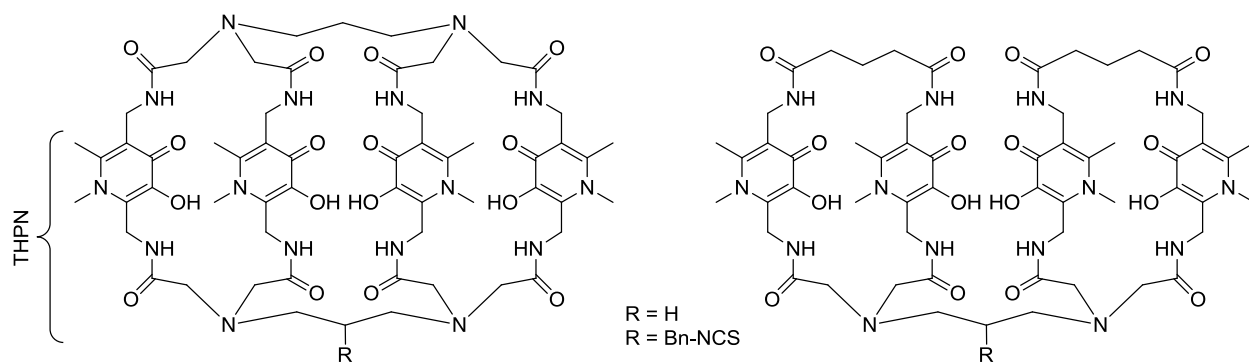


**Figure 6.1.** Suggested structures for a bi-macrocylic cage (left) or “clam-shell” like derivative (right) of THPN.

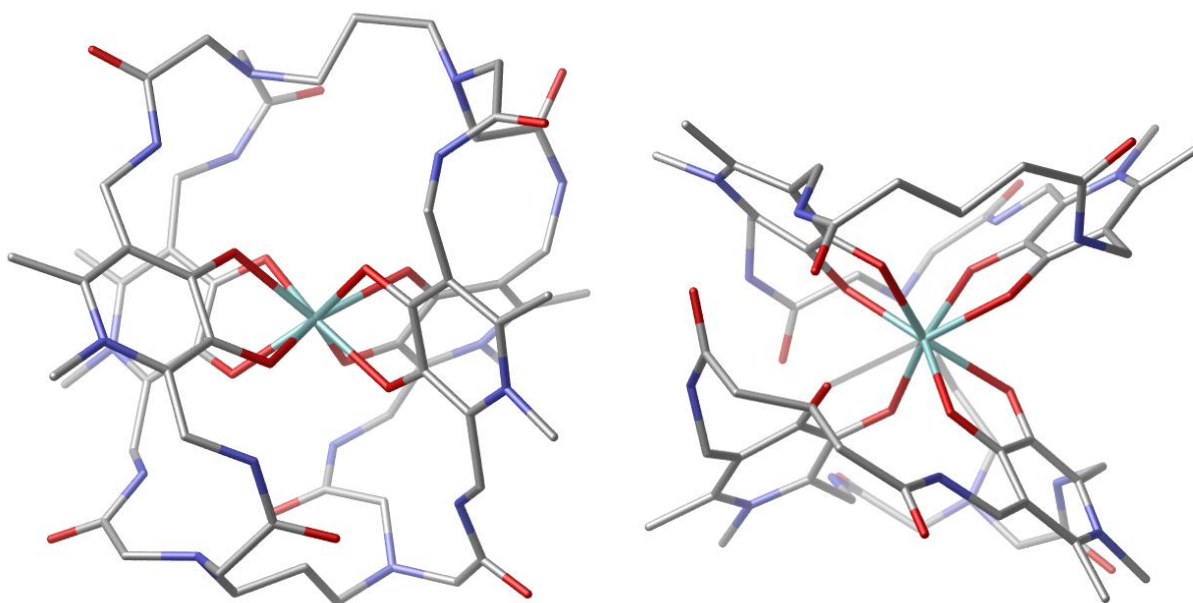


**Figure 6.2.** DFT-optimized structures of Zr-chelates with the proposed bi-macrocylic cage- (left) or “clam-shell”-like chelator (right). Calculations were performed with Gaussian 16<sup>123</sup> using B3LYP/LANL2DZ theory. Hydrogen atoms are omitted for clarity.

Apart from such ligand modifications, we believe that THPN itself holds the potential to form strong and inert complexes with a range of other metal ions. Our preliminary assessment discussed in Chapter 5 with a number of medically relevant metal ions confirmed the formation of monometallic complexes that merit further exploration. Now that the synthesis

of the chelator and a bifunctional derivative are established, exploring THPN with other radiometals and performing preclinical testing of bioconjugates should be straightforward and will hopefully yield promising radiopharmaceutical entities.

## References

1. V. Carroll, D. W. Demoin, T. J. Hoffman, and S. S. Jurisson, *Inorganic chemistry in nuclear imaging and radiotherapy: current and future directions*, *Radiochim. Acta*, **2012**, *100*, 653-667.
2. G. de Hevesy, *Nobel Lecture: Some Applications of Isotopic Indicators*, [https://www.nobelprize.org/nobel\\_prizes/chemistry/laureates/1943/hevesy-lecture.pdf](https://www.nobelprize.org/nobel_prizes/chemistry/laureates/1943/hevesy-lecture.pdf), (accessed Jun. 2, 2018).
3. W. G. Myers, *Georg Charles de Hevesy: The Father of Nuclear Medicine*, *J. Nucl. Med.*, **1979**, 590-594.
4. G. B. Saha, *Fundamentals of Nuclear Pharmacy*, Springer, New York, NY, USA, 6th edn., **2010**.
5. G. B. Saha, *Physics and Radiobiology of Nuclear Medicine*, Springer, New York, NY, USA, 4th edn., **2013**.
6. L. Jødal, C. L. Loirec, and C. Champion, *Positron range in PET imaging: an alternative approach for assessing and correcting the blurring*, *Phys. Med. Biol.*, **2012**, *57*, 3931-3943.
7. IAEA Nuclear Data Section, *Live Chart of Nuclides*, <https://www-nds.iaea.org/relnsd/vcharthtml/VChartHTML.html>, (accessed Aug 12, 2018).
8. M. Conti and L. Eriksson, *Physics of pure and non-pure positron emitters for PET: a review and a discussion*, *EJNMMI Physics*, **2016**, *3*, 8.
9. J. P. Holland, M. J. Williamson, and J. S. Lewis, *Unconventional Nuclides for Radiopharmaceuticals*, *Mol. Imaging*, **2010**, *9*, 1-20.
10. S. Bhattacharyya and M. Dixit, *Metallic radionuclides in the development of diagnostic and therapeutic radiopharmaceuticals*, *Dalton Trans.*, **2011**, *40*, 6112-6128.
11. C. F. Ramogida and C. Orvig, *Tumour targeting with radiometals for diagnosis and therapy*, *Chem. Commun.*, **2013**, *49*, 4720-4739.
12. C. A. Boswell and M. W. Brechbiel, *Development of radioimmunotherapeutic and diagnostic antibodies: an inside-out view*, *Nucl. Med. Biol.*, **2007**, *34*, 757-778.
13. Committee on State of the Science of Nuclear Medicine, National Research Council, and Institute of Medicine of the National Academies, *Advancing Nuclear Medicine Through Innovation*, National Academies Press, Washington, DC, USA, **2007**.
14. M. Eder, M. Schäfer, U. Bauder-Wüst, W.-E. Hull, C. Wängler, W. Mier, U. Haberkorn, and M. Eisenhut, *<sup>68</sup>Ga-Complex Lipophilicity and the Targeting Property of a Urea-Based PSMA Inhibitor for PET Imaging*, *Bioconjugate Chem.*, **2012**, *23*, 688-697.
15. A. Afshar-Oromieh, A. Malcher, M. Eder, M. Eisenhut, H. G. Linhart, B. A. Hadaschik, T. Holland-Letz, F. L. Giesel, C. Kratochwil, S. Haufe, U. Haberkorn, and C. M. Zechmann, *PET imaging with a [<sup>68</sup>Ga]gallium-labelled PSMA ligand for the diagnosis*

- of prostate cancer: biodistribution in humans and first evaluation of tumour lesions*, Eur. J. Nucl. Med. Mol. Imaging, **2013**, *40*, 486-495.
16. A. Afshar-Oromieh, E. Avtzi, F. L. Giesel, T. Holland-Letz, H. G. Linhart, M. Eder, M. Eisenhut, S. Boxler, B. A. Hadaschik, C. Kratochwil, W. Weichert, K. Kopka, J. Debus, and U. Haberkorn, *The diagnostic value of PET/CT imaging with the (68)Ga-labelled PSMA ligand HBED-CC in the diagnosis of recurrent prostate cancer*, Eur. J. Nucl. Med. Mol. Imaging, **2015**, *42*, 197-209.
  17. F. Sterzing, C. Kratochwil, H. Fiedler, S. Katayama, G. Habl, K. Kopka, A. Afshar-Oromieh, J. Debus, U. Haberkorn, and F. L. Giesel, *68Ga-PSMA-11 PET/CT: a new technique with high potential for the radiotherapeutic management of prostate cancer patients*, Eur. J. Nucl. Med. Mol. Imaging, **2016**, *43*, 34-41.
  18. A. Afshar-Oromieh, T. Holland-Letz, F. L. Giesel, C. Kratochwil, W. Mier, S. Haufe, N. Debus, M. Eder, M. Eisenhut, M. Schäfer, O. Neels, M. Hohenfellner, K. Kopka, H.-U. Kauczor, J. Debus, and U. Haberkorn, *Diagnostic performance of 68Ga-PSMA-11 (HBED-CC) PET/CT in patients with recurrent prostate cancer: evaluation in 1007 patients*, Eur. J. Nucl. Med. Mol. Imaging, **2017**, *44*, 1258-1268.
  19. J. Elgqvist, S. Frost, J. P. Pouget, and P. Albertsson, *The Potential and Hurdles of Targeted Alpha Therapy - Clinical Trials and Beyond*, Front. Oncol., **2014**, *3*, 324.
  20. M. Makvandi, E. Dupis, J. W. Engle, F. M. Nortier, M. E. Fassbender, S. Simon, E. R. Birnbaum, R. W. Atcher, K. D. John, O. Rixe, and J. P. Norenberg, *Alpha-Emitters and Targeted Alpha Therapy in Oncology: from Basic Science to Clinical Investigations*, Targ. Oncol., **2018**, *13*, 189-203.
  21. N. Falzone, B. Cornelissen, and K. A. Vallis, *Auger Emitting Radiopharmaceuticals for Cancer Therapy in Radiation Damage in Biomolecular Systems*, eds. G. García Gómez-Tejedor and M. C. Fuss, Springer, Dordrecht, Netherlands, **2012**, ch. 28, pp. 461-478.
  22. A. I. Kassis, *Therapeutic Radionuclides: Biophysical and Radiobiologic Principles*, Semin. Nucl. Med., **2008**, *38*, 358-366.
  23. A. I. Kassis, *Cancer Therapy with Auger Electrons: Are We Almost There?*, J. Nucl. Med., **2003**, *44*, 1479-1481.
  24. R. W. Howell, *Auger processes in the 21st century*, Int. J. Radiat. Biol., **2008**, *84*, 959-975.
  25. B. Cornelissen and K. A. Vallis, *Targeting the Nucleus: An Overview of Auger-Electron Radionuclide Therapy*, Curr. Drug Discov. Technol., **2010**, *7*, 263-279.
  26. J.-P. Pouget, I. Navarro-Teulon, M. Bardiès, N. Chouin, G. Cartron, A. Pèlerin, and D. Azria, *Clinical radioimmunotherapy—the role of radiobiology*, Nat. Rev. Clin. Oncol., **2011**, *8*, 720-734.
  27. J. Kozempel, O. Mokhodoeva, and M. Vlk, *Progress in Targeted Alpha-Particle Therapy. What We Learned about Recoils Release from In Vivo Generators*, Molecules, **2018**, *23*.

28. S. Aghevlian, A. J. Boyle, and R. M. Reilly, *Radioimmunotherapy of cancer with high linear energy transfer (LET) radiation delivered by radionuclides emitting  $\alpha$ -particles or Auger electrons*, *Adv. Drug Delivery Rev.*, **2017**, *109*, 102-118.
29. V. S. Gudkov, Y. N. Shilyagina, A. V. Vodeneev, and V. A. Zvyagin, *Targeted Radionuclide Therapy of Human Tumors*, *Int. J. Mol. Sci.*, **2016**, *17*.
30. F. C. Wong and E. E. Kim, *Therapeutic Applications of Radiopharmaceuticals in Handbook of Nuclear Medicine and Molecular Imaging*, eds. E. E. Kim, D.-S. Lee, U. Tateishi and R. P. Baum, World Scientific, Singapore, **2011**, pp. 401-434.
31. J. Dahle, J. Borrebæk, K. B. Melhus, Ø. S. Bruland, G. Salberg, D. R. Olsen, and R. H. Larsen, *Initial evaluation of  $^{227}\text{Th}$ -p-benzyl-DOTA-rituximab for low-dose rate  $\alpha$ -particle radioimmunotherapy*, *Nucl. Med. Biol.*, **2006**, *33*, 271-279.
32. L. Maffioli, L. Florimonte, D. C. Costa, J. Correia Castanheira, C. Grana, M. Luster, L. Bodei, and M. Chinol, *New radiopharmaceutical agents for the treatment of castration-resistant prostate cancer*, *Q. J. Nucl. Med. Mol. Imaging*, **2015**, *59*, 420-438.
33. M. J. Morris, N. Pandit-Taskar, J. Carrasquillo, C. R. Divgi, S. Slovin, W. K. Kelly, D. Rathkopf, G. A. Gignac, D. Solit, L. Schwartz, R. D. Stephenson, C. Hong, A. Delacruz, T. Curley, G. Heller, X. Jia, J. O'Donoghue, S. Larson, and H. I. Scher, *Phase I Study of Samarium-153 Lexidronam With Docetaxel in Castration-Resistant Metastatic Prostate Cancer*, *J. Clin. Oncol.*, **2009**, *27*, 2436-2442.
34. S. Severi, I. Grassi, S. Nicolini, M. Sansovini, A. Bongiovanni, and G. Paganelli, *Peptide receptor radionuclide therapy in the management of gastrointestinal neuroendocrine tumors: efficacy profile, safety, and quality of life*, *OncoTargets Ther.*, **2017**, *10*, 551-557.
35. J. Kunikowska, L. Królicki, A. Hubalewska-Dydejczyk, R. Mikołajczak, A. Sowa-Staszczak, and D. Pawlak, *Clinical results of radionuclide therapy of neuroendocrine tumours with  $^{90}\text{Y}$ -DOTATATE and tandem  $^{90}\text{Y}/^{177}\text{Lu}$ -DOTATATE: which is a better therapy option?*, *Eur. J. Nucl. Med. Mol. Imaging*, **2011**, *38*, 1788-1797.
36. F. Zoller, M. Eisenhut, U. Haberkorn, and W. Mier, *Endoradiotherapy in cancer treatment - Basic concepts and future trends*, *Eur. J. Pharmacol.*, **2009**, *625*, 55-62.
37. C. Kratochwil, F. Bruchertseifer, H. Rathke, M. Hohenfellner, F. L. Giesel, U. Haberkorn, and A. Morgenstern, *Targeted  $\alpha$ -Therapy of Metastatic Castration-Resistant Prostate Cancer with  $^{225}\text{Ac}$ -PSMA-617: Swimmer-Plot Analysis Suggests Efficacy Regarding Duration of Tumor Control*, *J. Nucl. Med.*, **2018**, *59*, 795-802.
38. A. Bräuer, L. S. Grubert, W. Roll, A. J. Schrader, M. Schäfers, M. Bögemann, and K. Rahbar,  *$^{177}\text{Lu}$ -PSMA-617 radioligand therapy and outcome in patients with metastasized castration-resistant prostate cancer*, *Eur. J. Nucl. Med. Mol. Imaging*, **2017**, *44*, 1663-1670.
39. M. S. Hofman, J. Violet, R. J. Hicks, J. Ferdinandus, S. P. Thang, T. Akhurst, A. Irvani, G. Kong, A. Ravi Kumar, D. G. Murphy, P. Eu, P. Jackson, M. Scalzo, S. G. Williams, and S. Sandhu,  *$^{177}\text{Lu}$ -PSMA-617 radionuclide treatment in patients with metastatic castration-resistant prostate cancer (LuPSMA trial): a single-centre, single-arm, phase 2 study*, *Lancet Oncol.*, **2018**, *19*, 825-833.

40. T. Das, M. Guleria, A. Parab, C. Kale, H. Shah, H. D. Sarma, V. R. Lele, and S. Banerjee, *Clinical translation of <sup>177</sup>Lu-labeled PSMA-617: Initial experience in prostate cancer patients*, Nucl. Med. Biol., **2016**, *43*, 296-302.
41. C. Kratochwil, F. Bruchertseifer, F. L. Giesel, M. Weis, F. A. Verburg, F. Mottaghy, K. Kopka, C. Apostolidis, U. Haberkorn, and A. Morgenstern, *<sup>225</sup>Ac-PSMA-617 for PSMA-Targeted  $\alpha$ -Radiation Therapy of Metastatic Castration-Resistant Prostate Cancer*, J. Nucl. Med., **2016**, *57*, 1941-1944.
42. M. Sathekge, F. Bruchertseifer, O. Knoesen, F. Reyneke, I. Lawal, T. Lengana, C. Davis, J. Mahapane, C. Corbett, M. Vorster, and A. Morgenstern, *<sup>225</sup>Ac-PSMA-617 in chemotherapy-naïve patients with advanced prostate cancer: a pilot study*, Eur. J. Nucl. Med. Mol. Imaging, **2019**, *46*, 129-138.
43. D. Brasse and A. Nonat, *Radiometals: towards a new success story in nuclear imaging?*, Dalton Trans., **2015**, *44*, 4845-4858.
44. B. M. Zeglis, J. L. Houghton, M. J. Evans, N. Viola-Villegas, and J. S. Lewis, *Underscoring the influence of inorganic chemistry on nuclear imaging with radiometals*, Inorg. Chem., **2014**, *53*, 1880-1899.
45. B. M. Zeglis and J. S. Lewis, *A practical guide to the construction of radiometallated bioconjugates for positron emission tomography*, Dalton Trans., **2011**, *40*, 6168-6195.
46. E. Boros, B. V. Marquez, O. F. Ikotun, S. E. Lapi, and C. L. Ferreira, *Coordination Chemistry and Ligand Design in the Development of Metal Based Radiopharmaceuticals in Ligand Design in Medicinal Inorganic Chemistry*, ed. T. Storr, John Wiley & Sons, Ltd., West Sussex, UK, **2014**.
47. P. J. Blower, *A nuclear chocolate box: the periodic table of nuclear medicine*, Dalton Trans., **2015**, *44*, 4819-4844.
48. S. Jurisson, C. Cutler, and S. V. Smith, *Radiometal complexes: characterization and relevant in vitro studies*, Q. J. Nucl. Med. Mol. Imaging, **2008**, *52*, 222-234.
49. M. Tarini, P. Cignoni, and C. Montani, *Ambient Occlusion and Edge Cueing for Enhancing Real Time Molecular Visualization*, IEEE Trans. Visual. Comput. Graphics, **2006**, *12*, 1237-1244.
50. L. J. Harris, E. Skaletsky, and A. McPherson, *Crystallographic structure of an intact IgG1 monoclonal antibody*, J. Mol. Biol., **1998**, *275*, 861-872.
51. E. W. Price and C. Orvig, *The Chemistry of Inorganic Nuclides (<sup>86</sup>Y, <sup>68</sup>Ga, <sup>64</sup>Cu, <sup>89</sup>Zr, <sup>124</sup>I) in The Chemistry of Molecular Imaging*, eds. N. Long and W.-T. Wong, John Wiley & Sons, Inc, Hoboken, NJ, USA, **2014**, ch. 5, pp. 105-135.
52. S. Liu, *Bifunctional coupling agents for radiolabeling of biomolecules and target-specific delivery of metallic radionuclides*, Adv. Drug Delivery Rev., **2008**, *60*, 1347-1370.
53. P. Comba, U. Jermilova, C. Orvig, B. O. Patrick, C. F. Ramogida, K. Rück, C. Schneider, and M. Starke, *Octadentate picolinic acid-based bispidine ligand for radiometal ions*, Chem. Eur. J., **2017**, *23*, 15945-15956.

54. J. R. Dilworth and S. I. Pascu, *The chemistry of PET imaging with zirconium-89*, Chem. Soc. Rev., **2018**, 47, 2554-2571.
55. D. K. Cabiness and D. W. Margerum, *Macrocyclic effect on the stability of copper(II) tetramine complexes*, J. Am. Chem. Soc., **1969**, 91, 6540-6541.
56. E. W. Price and C. Orvig, *Matching chelators to radiometals for radiopharmaceuticals*, Chem. Soc. Rev., **2014**, 43, 260-290.
57. G. T. Hermanson, *Bioconjugate Techniques*, Academic Press, San Diego, CA, USA, 3rd edn., **2013**.
58. R. D. Hancock, *Chelate ring size and metal ion selection. The basis of selectivity for metal ions in open-chain ligands and macrocycles*, J. Chem. Educ., **1992**, 69, 615-621.
59. K. H. Thompson, C. A. Barta, and C. Orvig, *Metal complexes of maltol and close analogues in medicinal inorganic chemistry*, Chem. Soc. Rev., **2006**, 35, 545-556.
60. V. M. Nurchi, G. Crisponi, J. I. Lachowicz, S. Murgia, T. Pivetta, M. Remelli, A. Rescigno, J. Niclós-Gutiérrez, J. M. González-Pérez, A. Domínguez-Martín, A. Castiñeiras, and Z. Szewczuk, *Iron(III) and aluminum(III) complexes with hydroxypyridone ligands aimed to design kojic acid derivatives with new perspectives*, J. Inorg. Biochem., **2010**, 104, 560-569.
61. R. D. Hancock and A. E. Martell, *Ligand design for selective complexation of metal ions in aqueous solution*, Chem. Rev., **1989**, 89, 1875-1914.
62. E. Kiss, I. Fábrián, and T. Kiss, *Kinetics of ligand substitution reactions in the oxovanadium(IV)-maltol system*, Inorg. Chim. Acta, **2002**, 340, 114-118.
63. R. Cusnir, C. Imberti, R. C. Hider, P. J. Blower, and M. T. Ma, *Hydroxypyridinone Chelators: From Iron Scavenging to Radiopharmaceuticals for PET Imaging with Gallium-68*, Int. J. Mol. Sci., **2017**, 18, 116.
64. U.S. Food and Drug Administration, *Part 172 - Food Additives Permitted for Direct Addition to Food for Human Consumption*, <https://www.ecfr.gov/cgi-bin/text-idx?SID=8716adb8ccb2f059e4272592f4783415&mc=true&node=pt21.3.172&rgn=div5>, (accessed Aug. 11, 2018).
65. C. A. Barta, K. Sachs-Barrable, J. Jia, K. H. Thompson, K. M. Wasan, and C. Orvig, *Lanthanide containing compounds for therapeutic care in bone resorption disorders*, Dalton Trans., **2007**, 5019-5030.
66. Z. D. Liu and R. C. Hider, *Design of clinically useful iron(III)-selective chelators*, Med. Res. Rev., **2002**, 22, 26-64.
67. A. Cilibrizzi, V. Abbate, Y.-L. Chen, Y. Ma, T. Zhou, and R. C. Hider, *Hydroxypyridinone Journey into Metal Chelation*, Chem. Rev., **2018**, 118, 7657-7701.
68. A. E. V. Gorden, J. Xu, K. N. Raymond, and P. Durbin, *Rational Design of Sequestering Agents for Plutonium and Other Actinides*, Chem. Rev., **2003**, 103, 4207-4282.
69. M. A. Santos, *Recent developments on 3-hydroxy-4-pyridinones with respect to their clinical applications: Mono and combined ligand approaches*, Coord. Chem. Rev., **2008**, 252, 1213-1224.

70. A. Datta and K. N. Raymond, *Gd-Hydroxypyridinone (HOPO)-Based High-Relaxivity Magnetic Resonance Imaging (MRI) Contrast Agents*, *Acc. Chem. Res.*, **2009**, *42*, 938-947.
71. M. A. Santos, S. M. Marques, and S. Chaves, *Hydroxypyridinones as “privileged” chelating structures for the design of medicinal drugs*, *Coord. Chem. Rev.*, **2012**, *256*, 240-259.
72. T. Zhou, H. Neubert, D. Y. Liu, Z. D. Liu, Y. M. Ma, X. L. Kong, W. Luo, S. Mark, and R. C. Hider, *Iron Binding Dendrimers: A Novel Approach for the Treatment of Haemochromatosis*, *J. Med. Chem.*, **2006**, *49*, 4171-4182.
73. M. A. Santos, *Hydroxypyridinone complexes with aluminium. In vitro/vivo studies and perspectives*, *Coord. Chem. Rev.*, **2002**, *228*, 187-203.
74. J. Burgess and M. Rangel, *Hydroxypyranones, hydroxypyridinones, and their complexes in Advances in Inorganic Chemistry*, ed. R. van Eldik, Academic Press, London, UK, **2008**, vol. 60, pp. 167-243.
75. Y. W. S. Jauw, C. W. Menke-van der Houwen van Oordt, O. S. Hoekstra, N. H. Hendrikse, D. J. Vugts, J. M. Zijlstra, M. C. Huisman, and G. A. M. S. van Dongen, *Immuno-Positron Emission Tomography with Zirconium-89-Labeled Monoclonal Antibodies in Oncology: What Can We Learn from Initial Clinical Trials?*, *Front. Pharmacol.*, **2016**, *7*, 131.
76. C. Bailly, P.-F. Cléry, A. Faivre-Chauvet, M. Bourgeois, F. Guérard, F. Haddad, J. Barbet, M. Chérel, F. Kraeber-Bodéré, T. Carlier, and C. Bodet-Milin, *Immuno-PET for Clinical Theranostic Approaches*, *Int. J. Mol. Sci.*, **2017**, *18*, 57.
77. L. E. Lamberts, S. P. Williams, A. G. T. Terwisscha van Scheltinga, M. N. Lub-de Hooge, C. P. Schröder, J. A. Gietema, A. H. Brouwers, and E. G. E. de Vries, *Antibody Positron Emission Tomography Imaging in Anticancer Drug Development*, *J. Clin. Oncol.*, **2015**, *33*, 1491-1504.
78. B. N. McKnight and N. T. Viola-Villegas, *<sup>89</sup>Zr-ImmunoPET Companion Diagnostics and their Impact in Clinical Drug Development*, *J. Labelled Compd. Radiopharm.*, **2018**, *61*, 727-738.
79. M. A. Deri, B. M. Zeglis, L. C. Francesconi, and J. S. Lewis, *PET imaging with <sup>89</sup>Zr: from radiochemistry to the clinic*, *Nucl. Med. Biol.*, **2013**, *40*, 3-14.
80. J. P. Holland, Y. Sheh, and J. S. Lewis, *Standardized methods for the production of high specific-activity zirconium-89*, *Nucl. Med. Biol.*, **2009**, *36*, 729-739.
81. G. M. Dias, C. F. Ramogida, J. Rousseau, N. A. Zacchia, C. Hoehr, P. Schaffer, K.-S. Lin, and F. Bénard, *<sup>89</sup>Zr for antibody labeling and in vivo studies - a comparison between liquid and solid target production*, *Nucl. Med. Biol.*, **2018**, *58*, 1-7.
82. E. Oehlke, C. Hoehr, X. Hou, V. Hanemaayer, S. Zeisler, M. J. Adam, T. J. Ruth, A. Celler, K. Buckley, F. Benard, and P. Schaffer, *Production of Y-86 and other radiometals for research purposes using a solution target system*, *Nucl. Med. Biol.*, **2015**, *42*, 842-849.

83. L. E. McInnes, S. E. Rudd, and P. S. Donnelly, *Copper, gallium and zirconium positron emission tomography imaging agents: The importance of metal ion speciation*, *Coord. Chem. Rev.*, **2017**, 352, 499-516.
84. B. N. Bhatt, N. D. Pandya, and J. T. Wadas, *Recent Advances in Zirconium-89 Chelator Development*, *Molecules*, **2018**, 23, 638.
85. J. Mealey Jr., *Turn-over of Carrier-free Zirconium-89 in Man*, *Nature*, **1957**, 179, 673.
86. J. P. Holland, V. Divilov, N. H. Bander, P. M. Smith-Jones, S. M. Larson, and J. S. Lewis, *<sup>89</sup>Zr-DFO-J591 for ImmunoPET of Prostate-Specific Membrane Antigen Expression In Vivo*, *J. Nucl. Med.*, **2010**, 51, 1293-1300.
87. T. K. Nayak, K. Garmestani, D. E. Milenic, and M. W. Brechbiel, *PET and MRI of Metastatic Peritoneal and Pulmonary Colorectal Cancer in Mice with Human Epidermal Growth Factor Receptor 1-Targeted <sup>89</sup>Zr-Labeled Panitumumab*, *J. Nucl. Med.*, **2012**, 53, 113-120.
88. D. S. Abou, T. Ku, and P. M. Smith-Jones, *In vivo biodistribution and accumulation of <sup>89</sup>Zr in mice*, *Nucl. Med. Biol.*, **2011**, 38, 675-681.
89. J. N. Tinianow, H. S. Gill, A. Ogasawara, J. E. Flores, A. N. Vanderbilt, E. Luis, R. Vandlen, M. Darwish, J. R. Junutula, S.-P. Williams, and J. Marik, *Site-specifically <sup>89</sup>Zr-labeled monoclonal antibodies for ImmunoPET*, *Nucl. Med. Biol.*, **2010**, 37, 289-297.
90. G. Fischer, U. Seibold, R. Schirmacher, B. Wängler, and C. Wängler, *<sup>89</sup>Zr, a Radiometal Nuclide with High Potential for Molecular Imaging with PET: Chemistry, Applications and Remaining Challenges*, *Molecules*, **2013**, 18, 6469-6490.
91. B. M. Zeglis, P. Mohindra, G. I. Weissmann, V. Divilov, S. A. Hilderbrand, R. Weissleder, and J. S. Lewis, *Modular Strategy for the Construction of Radiometalated Antibodies for Positron Emission Tomography Based on Inverse Electron Demand Diels-Alder Click Chemistry*, *Bioconjugate Chem.*, **2011**, 22, 2048-2059.
92. A. J. Chang, R. DeSilva, S. Jain, K. Lears, B. Rogers, and S. Lapi, *<sup>89</sup>Zr-Radiolabeled Trastuzumab Imaging in Orthotopic and Metastatic Breast Tumors*, *Pharmaceuticals*, **2012**, 5, 79-93.
93. S. Heskamp, R. Raavé, O. C. Boerman, M. Rijpkema, V. Goncalves, and F. Denat, *<sup>89</sup>Zr-Immuno-Positron Emission Tomography in Oncology: State-of-the-Art <sup>89</sup>Zr Radiochemistry*, *Bioconjugate Chem.*, **2017**, 28, 2211-2223.
94. C. Zhai, D. Summer, C. Rangger, G. M. Franssen, P. Laverman, H. Haas, M. Petrik, R. Haubner, and C. Decristoforo, *Novel Bifunctional Cyclic Chelator for <sup>89</sup>Zr Labeling-Radiolabeling and Targeting Properties of RGD Conjugates*, *Mol. Pharmaceutics*, **2015**, 12, 2142-2150.
95. D. Summer, J. Garousi, M. Oroujeni, B. Mitran, K. G. Andersson, A. Vorobyeva, J. Löfblom, A. Orlova, V. Tolmachev, and C. Decristoforo, *Cyclic versus Noncyclic Chelating Scaffold for <sup>89</sup>Zr-Labeled ZEGFR:2377 Affibody Bioconjugates Targeting Epidermal Growth Factor Receptor Overexpression*, *Mol. Pharmaceutics*, **2018**, 15, 175-185.

96. E. Boros, J. P. Holland, N. Kenton, N. Rotile, and P. Caravan, *Macrocyclic-Based Hydroxamate Ligands for Complexation and Immunoconjugation of <sup>89</sup>Zirconium for Positron Emission Tomography (PET) Imaging*, *ChemPlusChem*, **2016**, *81*, 274-281.
97. J. Rousseau, Z. Zhang, G. M. Dias, C. Zhang, N. Colpo, F. Bénard, and K.-S. Lin, *Design, synthesis and evaluation of novel bifunctional tetrahydroxamate chelators for PET imaging of <sup>89</sup>Zr-labeled antibodies*, *Bioorg. Med. Chem. Lett.*, **2017**, *27*, 708-712.
98. J. Rousseau, Z. Zhang, X. Wang, C. Zhang, J. Lau, E. Rousseau, M. Čolović, N. Hundal-Jabal, F. Bénard, and K.-S. Lin, *Synthesis and evaluation of bifunctional tetrahydroxamate chelators for labeling antibodies with <sup>89</sup>Zr for imaging with positron emission tomography*, *Bioorg. Med. Chem. Lett.*, **2018**, *28*, 899-905.
99. F. Guérard, Y.-S. Lee, and M. W. Brechbiel, *Rational Design, Synthesis, and Evaluation of Tetrahydroxamic Acid Chelators for Stable Complexation of Zirconium(IV)*, *Chem. Eur. J.*, **2014**, *20*, 5584-5591.
100. M. Patra, A. Bauman, C. Mari, C. A. Fischer, O. Blacque, D. Haussinger, G. Gasser, and T. L. Mindt, *An octadentate bifunctional chelating agent for the development of stable zirconium-89 based molecular imaging probes*, *Chem. Commun.*, **2014**, *50*, 11523-11525.
101. D. J. Vugts, C. Klaver, C. Sewing, A. J. Poot, K. Adamzek, S. Huegli, C. Mari, G. W. M. Visser, I. E. Valverde, G. Gasser, T. L. Mindt, and G. A. M. S. van Dongen, *Comparison of the octadentate bifunctional chelator DFO\*-pPhe-NCS and the clinically used hexadentate bifunctional chelator DFO-pPhe-NCS for <sup>89</sup>Zr-immuno-PET*, *Eur. J. Nucl. Med. Mol. Imaging*, **2017**, *44*, 286-295.
102. M. Briand, M. L. Aulsebrook, T. L. Mindt, and G. Gasser, *A solid phase-assisted approach for the facile synthesis of a highly water-soluble zirconium-89 chelator for radiopharmaceutical development*, *Dalton Trans.*, **2017**, *46*, 16387-16389.
103. S. E. Rudd, P. Roselt, C. Cullinane, R. J. Hicks, and P. S. Donnelly, *A desferrioxamine B squaramide ester for the incorporation of zirconium-89 into antibodies*, *Chem. Commun.*, **2016**, *52*, 11889-11892.
104. L. Allott, C. Da Pieve, J. Meyers, T. Spinks, D. M. Ciobota, G. Kramer-Marek, and G. Smith, *Evaluation of DFO-HOPO as an octadentate chelator for zirconium-89*, *Chem. Commun.*, **2017**, *53*, 8529-8532.
105. D. N. Pandya, N. Bhatt, H. Yuan, C. S. Day, B. M. Ehrmann, M. Wright, U. Bierbach, and T. J. Wadas, *Zirconium tetraazamacrocyclic complexes display extraordinary stability and provide a new strategy for zirconium-89-based radiopharmaceutical development*, *Chem. Sci.*, **2017**, *8*, 2309-2314.
106. E. W. Price, B. M. Zeglis, J. S. Lewis, M. J. Adam, and C. Orvig, *H6phosphatrazastuzumab: bifunctional methylenephosphonate-based chelator with <sup>89</sup>Zr, <sup>111</sup>In and <sup>177</sup>Lu*, *Dalton Trans.*, **2014**, *43*, 119-131.
107. N. B. Bhatt, D. N. Pandya, J. Xu, D. Tatum, D. Magda, and T. J. Wadas, *Evaluation of macrocyclic hydroxyisophthalamide ligands as chelators for zirconium-89*, *PLoS ONE*, **2017**, *12*, e0178767.

108. D. N. Pandya, S. Pailloux, D. Tatum, D. Magda, and T. J. Wadas, *Di-macrocyclic terephthalamide ligands as chelators for the PET radionuclide zirconium-89*, Chem. Commun., **2015**, 51, 2301-2303.
109. F. Guérard, M. Beyler, Y. S. Lee, R. Tripier, J. F. Gestin, and M. W. Brechbiel, *Investigation of the complexation of natZr(IV) and 89Zr(IV) by hydroxypyridinones for the development of chelators for PET imaging applications*, Dalton Trans., **2017**, 46, 4749-4758.
110. M. A. Deri, S. Ponnala, P. Kozlowski, B. P. Burton-Pye, H. T. Cicek, C. Hu, J. S. Lewis, and L. C. Francesconi, *p-SCN-Bn-HOPO: A Superior Bifunctional Chelator for 89Zr ImmunoPET*, Bioconjugate Chem., **2015**, 26, 2579-2591.
111. M. A. Deri, S. Ponnala, B. M. Zeglis, G. Pohl, J. J. Dannenberg, J. S. Lewis, and L. C. Francesconi, *An Alternative Chelator for 89Zr Radiopharmaceuticals: Radiolabeling and Evaluation of 3,4,3-(LI-1,2-HOPO)*, J. Med. Chem., **2014**, 57, 4849-4860.
112. J. N. Tinianow, D. N. Pandya, S. L. Pailloux, A. Ogasawara, A. N. Vanderbilt, H. S. Gill, S.-P. Williams, T. J. Wadas, D. Magda, and J. Marik, *Evaluation of a 3-hydroxypyridin-2-one (2,3-HOPO) Based Macrocyclic Chelator for (89)Zr(4+) and Its Use for ImmunoPET Imaging of HER2 Positive Model of Ovarian Carcinoma in Mice*, Theranostics, **2016**, 6, 511-521.
113. M. T. Ma, L. K. Meszaros, B. M. Paterson, D. J. Berry, M. S. Cooper, Y. Ma, R. C. Hider, and P. J. Blower, *Tripodal tris(hydroxypyridinone) ligands for immunoconjugate PET imaging with (89)Zr(4+): comparison with desferrioxamine-B*, Dalton Trans., **2015**, 44, 4884-4900.
114. C. Buchwalder, C. Rodríguez-Rodríguez, P. Schaffer, S. K. Karagiozov, K. Saatchi, and U. O. Häfeli, *A new tetrapodal 3-hydroxy-4-pyridinone ligand for complexation of 89zirconium for positron emission tomography (PET) imaging*, Dalton Trans., **2017**, 46, 9654-9663.
115. B. Neises and W. Steglich, *Simple Method for the Esterification of Carboxylic Acids*, Angew. Chem. Int. Ed., **1978**, 17, 522-524.
116. S. N. Khattab, A. El-Faham, A. M. El-Massry, E. M. E. Mansour, and M. M. Abd El-Rahman, *Coupling of iminodiacetic acid with amino acid derivatives in solution and solid phase*, Lett. Pept. Sci., **2001**, 7, 331-345.
117. Z. D. Liu, R. Kayyali, R. C. Hider, J. B. Porter, and A. E. Theobald, *Design, Synthesis, and Evaluation of Novel 2-Substituted 3-Hydroxypyridin-4-ones: Structure–Activity Investigation of Metalloenzyme Inhibition by Iron Chelators*, J. Med. Chem., **2002**, 45, 631-639.
118. D. M. Lowe, P. T. Corbett, P. Murray-Rust, and R. C. Glen, *Chemical Name to Structure: OPSIN, an Open Source Solution*, J. Chem. Inf. Model., **2011**, 51, 739-753.
119. D. M. Lowe, *OPSIN: Open Parser for Systematic IUPAC nomenclature*, <https://opsin.ch.cam.ac.uk/>, (accessed Sep. 20, 2018).
120. M. A. Santos and S. Chaves, *3-hydroxypyridinone derivatives as metal-sequestering agents for therapeutic use*, Future Med. Chem., **2015**, 7, 383-410.

121. T. Zhou, R. C. Hider, and X. Kong, *Mode of iron(iii) chelation by hexadentate hydroxypyridinones*, Chem. Commun., **2015**, 51, 5614-5617.
122. A. M. G. Silva, A. Leite, M. Andrade, P. Gameiro, P. Brandão, V. Felix, B. de Castro, and M. Rangel, *Microwave-assisted synthesis of 3-hydroxy-4-pyridinone/naphthalene conjugates. Structural characterization and selection of a fluorescent ion sensor*, Tetrahedron, **2010**, 66, 8544-8550.
123. M. J. Frisch, G. W. Trucks, H. B. Schlegel, G. E. Scuseria, M. A. Robb, J. R. Cheeseman, G. Scalmani, V. Barone, B. Mennucci, G. A. Petersson, H. Nakatsuji, M. Caricato, X. Li, H. P. Hratchian, A. F. Izmaylov, J. Bloino, G. Zheng, J. L. Sonnenberg, M. Hada, M. Ehara, K. Toyota, R. Fukuda, J. Hasegawa, M. Ishida, T. Nakajima, Y. Honda, O. Kitao, H. Nakai, T. Vreven, J. A. Montgomery Jr., J. E. Peralta, F. Ogliaro, M. J. Bearpark, J. Heyd, E. N. Brothers, K. N. Kudin, V. N. Staroverov, R. Kobayashi, J. Normand, K. Raghavachari, A. P. Rendell, J. C. Burant, S. S. Iyengar, J. Tomasi, M. Cossi, N. Rega, N. J. Millam, M. Klene, J. E. Knox, J. B. Cross, V. Bakken, C. Adamo, J. Jaramillo, R. Gomperts, R. E. Stratmann, O. Yazyev, A. J. Austin, R. Cammi, C. Pomelli, J. W. Ochterski, R. L. Martin, K. Morokuma, V. G. Zakrzewski, G. A. Voth, P. Salvador, J. J. Dannenberg, S. Dapprich, A. D. Daniels, Ö. Farkas, J. B. Foresman, J. V. Ortiz, J. Cioslowski, and D. J. Fox, *Gaussian 09*, rev. E.01, Gaussian Inc., Wallingford, CT, **2013**.
124. C. Lee, W. Yang, and R. G. Parr, *Development of the Colle-Salvetti correlation-energy formula into a functional of the electron density*, Phys. Rev. B, **1988**, 37, 785-789.
125. A. D. Becke, *Density-functional exchange-energy approximation with correct asymptotic behavior*, Phys. Rev. A, **1988**, 38, 3098-3100.
126. P. J. Stephens, F. J. Devlin, C. F. Chabalowski, and M. J. Frisch, *Ab Initio Calculation of Vibrational Absorption and Circular Dichroism Spectra Using Density Functional Force Fields*, J. Phys. Chem., **1994**, 98, 11623-11627.
127. T. H. Dunning and P. J. Hay, *Gaussian Basis Sets for Molecular Calculations in Methods of Electronic Structure Theory*, ed. H. F. Schaefer III, Springer, New York, NY, USA, **1977**, pp. 1-27.
128. P. J. Hay and W. R. Wadt, *Ab initio effective core potentials for molecular calculations. Potentials for K to Au including the outermost core orbitals*, J. Chem. Phys., **1985**, 82, 299-310.
129. P. J. Hay and W. R. Wadt, *Ab initio effective core potentials for molecular calculations. Potentials for the transition metal atoms Sc to Hg*, J. Chem. Phys., **1985**, 82, 270-283.
130. W. R. Wadt and P. J. Hay, *Ab initio effective core potentials for molecular calculations. Potentials for main group elements Na to Bi*, J. Chem. Phys., **1985**, 82, 284-298.
131. J. P. Holland and N. Vasdev, *Charting the mechanism and reactivity of zirconium oxalate with hydroxamate ligands using density functional theory: implications in new chelate design*, Dalton Trans., **2014**, 43, 9872-9884.
132. N. Godbout, D. R. Salahub, J. Andzelm, and E. Wimmer, *Optimization of Gaussian-type basis sets for local spin density functional calculations. Part I. Boron through neon, optimization technique and validation*, Can. J. Chem., **1992**, 70, 560-571.

133. C. Sosa, J. Andzelm, B. C. Elkin, E. Wimmer, K. D. Dobbs, and D. A. Dixon, *A local density functional study of the structure and vibrational frequencies of molecular transition-metal compounds*, *J. Phys. Chem.*, **1992**, *96*, 6630-6636.
134. C. Y. Legault, *CYLview*, v. 1.0b, Université de Sherbrooke, **2009**.
135. J. A. Carrasquillo, J. D. White, C. H. Paik, A. Raubitschek, N. Le, M. Rotman, M. W. Brechbiel, O. A. Gansow, L. E. Top, P. Perentesis, J. C. Reynolds, D. L. Nelson, and T. A. Waldmann, *Similarities and differences in <sup>111</sup>In- and <sup>90</sup>Y-labeled 1B4M-DTPA antiTac monoclonal antibody distribution*, *J. Nucl. Med.*, **1999**, *40*, 268-276.
136. X. Kong, H. Neubert, T. Zhou, Z. D. Liu, and R. C. Hider, *MALDI mass spectrometric determination of dendritic iron chelation stoichiometries and conditional affinity constants*, *J. Mass Spectrom.*, **2008**, *43*, 617-622.
137. S. Piyamongkol, Y. M. Ma, X. L. Kong, Z. D. Liu, M. D. Aytemir, D. van der Helm, and R. C. Hider, *Amido-3-hydroxypyridin-4-ones as iron(III) ligands*, *Chem. Eur. J.*, **2010**, *16*, 6374-6381.
138. V. M. Nurchi, G. Crisponi, T. Pivetta, M. Donatoni, and M. Remelli, *Potentiometric, spectrophotometric and calorimetric study on iron(III) and copper(II) complexes with 1,2-dimethyl-3-hydroxy-4-pyridinone*, *J. Inorg. Biochem.*, **2008**, *102*, 684-692.
139. C. Cheng, Y.-L. Chen, Y. Cao, Y. Ma, and R. C. Hider, *Synthesis and characterization of methyl substituted 3-hydroxypyridin-4-ones and their complexes with iron(III)*, *Can. J. Chem.*, **2018**, *96*, 293-298.
140. J. I. Lachowicz, V. M. Nurchi, G. Crisponi, M. G. Jaraquemada-Pelaez, M. Arca, A. Pintus, M. A. Santos, C. Quintanova, L. Gano, Z. Szewczuk, M. A. Zoroddu, M. Peana, A. Dominguez-Martin, and D. Choquesillo-Lazarte, *Hydroxypyridinones with enhanced iron chelating properties. Synthesis, characterization and in vivo tests of 5-hydroxy-2-(hydroxymethyl)pyridine-4(1H)-one*, *Dalton Trans.*, **2016**, *45*, 6517-6528.
141. M. Sturzbecher-Hoehne, T. A. Choi, and R. J. Abergel, *Hydroxypyridinonate Complex Stability of Group (IV) Metals and Tetravalent f-Block Elements: The Key to the Next Generation of Chelating Agents for Radiopharmaceuticals*, *Inorg. Chem.*, **2015**, *54*, 3462-3468.
142. W. R. Harris, C. J. Carrano, and K. N. Raymond, *Spectrophotometric Determination of the Proton-Dependent Stability Constant of Ferric Enterobactin*, *J. Am. Chem. Soc.*, **1979**, *101*, 2213-2214.
143. K. N. Raymond, B. E. Allred, and A. K. Sia, *Coordination Chemistry of Microbial Iron Transport*, *Acc. Chem. Res.*, **2015**, *48*, 2496-2505.
144. G. Crisponi and V. M. Nurchi, *Chelating Agents as Therapeutic Compounds - Basic Principles in Chelation Therapy in the Treatment of Metal Intoxication*, eds. J. Aaseth, G. Crisponi and O. Andersen, Academic Press, Boston, MA, USA, **2016**, ch. 2, pp. 35-61.
145. M. Tabata, *Conditional Constants, The IUPAC Stability Constants Database*, Academic Software, **1993**.
146. G. J. P. Deblonde, M. Sturzbecher-Hoehne, and R. J. Abergel, *Solution Thermodynamic Stability of Complexes Formed with the Octadentate Hydroxypyridinonate Ligand 3,4,3-*

- LI(1,2-HOPO): A Critical Feature for Efficient Chelation of Lanthanide(IV) and Actinide(IV) Ions*, Inorg. Chem., **2013**, 52, 8805-8811.
147. A. E. Martell, R. M. Smith, and R. J. Motekaitis, *NIST Critically Selected Stability Constants of Metal Complexes Database*, 8.0, NIST, Gaithersburg, MD, USA, **2004**.
  148. L. D. Loomis and K. N. Raymond, *Solution equilibria of enterobactin and metal-enterobactin complexes*, Inorg. Chem., **1991**, 30, 906-911.
  149. R. J. Abergel, J. A. Warner, D. K. Shuh, and K. N. Raymond, *Enterobactin Protonation and Iron Release: Structural Characterization of the Salicylate Coordination Shift in Ferric EnterobactinI*, J. Am. Chem. Soc., **2006**, 128, 8920-8931.
  150. W. E. Meijs, H. J. Haisma, R. Van Der Schors, R. Wijbrandts, K. Van Den Oever, R. P. Klok, H. M. Pinedo, and J. D. M. Herscheid, *A facile method for the labeling of proteins with zirconium isotopes*, Nucl. Med. Biol., **1996**, 23, 439-448.
  151. M. G. Jaraquemada-Peláez, X. Wang, T. J. Clough, Y. Cao, N. Choudhary, K. Emler, B. O. Patrick, and C. Orvig, *H4octapa: synthesis, solution equilibria and complexes with useful radiopharmaceutical metal ions*, Dalton Trans., **2017**, 46, 14647-14658.
  152. G. Gran, *Determination of the equivalence point in potentiometric titrations. Part II*, Analyst, **1952**, 77, 661-671.
  153. P. Gans, A. Sabatini, and A. Vacca, *Investigation of equilibria in solution. Determination of equilibrium constants with the HYPERQUAD suite of programs*, Talanta, **1996**, 43, 1739-1753.
  154. L. Alderighi, P. Gans, A. Ienco, D. Peters, A. Sabatini, and A. Vacca, *Hyperquad simulation and speciation (HySS): a utility program for the investigation of equilibria involving soluble and partially soluble species*, Coord. Chem. Rev., **1999**, 184, 311-318.
  155. C. Baes and R. Mesmer, *The hydrolysis of cations in The Hydrolysis of Cations*, John Wiley & Sons, New York, NY, USA, **1976**.
  156. E. W. Price, B. M. Zeglis, J. F. Cawthray, J. S. Lewis, M. J. Adam, and C. Orvig, *What a Difference a Carbon Makes: H4octapa vs H4C3octapa, Ligands for In-111 and Lu-177 Radiochemistry*, Inorg. Chem., **2014**, 53, 10412-10431.
  157. E. Dulière and J. Marchand-Brynaert, *A Convenient Synthesis of p-Aminobenzyl-tris(hydroxymethyl)methane as Precursor of Solid-Supported Tripodal Ligands*, Synthesis, **2002**, 2002, 39-42.
  158. D. A. Tomalia, J. R. Baker, R. C. Cheng, A. U. Bielinska, M. J. Fazio, D. M. Hedstrand, J. A. Johnson, d. Donald A. Kaplan, S. L. Klakamp, and W. J. Kruper, *Bioactive and/or targeted dendrimer conjugates*, **1998**, Pat. US5714166 A.
  159. B. Li, M. Berliner, R. Buzon, C. K. F. Chiu, S. T. Colgan, T. Kaneko, N. Keene, W. Kissel, T. Le, K. R. Leeman, B. Marquez, R. Morris, L. Newell, S. Wunderwald, M. Witt, J. Weaver, Z. Zhang, and Z. Zhang, *Aqueous Phosphoric Acid as a Mild Reagent for Deprotection of tert-Butyl Carbamates, Esters, and Ethers*, J. Org. Chem., **2006**, 71, 9045-9050.

160. C. Nájera, *From  $\alpha$ -Amino Acids to Peptides: All You Need for the Journey*, Synlett, **2002**, 2002, 1388-1404.
161. M. M. Joullié and K. M. Lassen, *Evolution of amide bond formation*, Arkivoc, **2010**, viii, 189-250.
162. E. Valeur and M. Bradley, *Amide bond formation: beyond the myth of coupling reagents*, Chem. Soc. Rev., **2009**, 38, 606-631.
163. C. A. G. N. Montalbetti and V. Falque, *Amide bond formation and peptide coupling*, Tetrahedron, **2005**, 61, 10827-10852.
164. C. A. Hudis, *Trastuzumab — Mechanism of Action and Use in Clinical Practice*, New Engl. J. Med., **2007**, 357, 39-51.
165. S. Parakh, H. K. Gan, A. C. Parslow, I. J. G. Burvenich, A. W. Burgess, and A. M. Scott, *Evolution of anti-HER2 therapies for cancer treatment*, Cancer Treat. Rev., **2017**, 59, 1-21.
166. V. Tolmachev, *Imaging of HER-2 Overexpression in Tumors for Guiding Therapy*, Curr. Pharm. Des., **2008**, 14, 2999-3019.
167. S. Liu and D. S. Edwards, *Bifunctional Chelators for Therapeutic Lanthanide Radiopharmaceuticals*, Bioconjugate Chem., **2001**, 12, 7-34.
168. M. J. W. D. Vosjan, L. R. Perk, G. W. M. Visser, M. Budde, P. Jurek, G. E. Kiefer, and G. A. M. S. van Dongen, *Conjugation and radiolabeling of monoclonal antibodies with zirconium-89 for PET imaging using the bifunctional chelate p-isothiocyanatobenzyl-desferrioxamine*, Nat. Protoc., **2010**, 5, 739-743.
169. E. W. Price, K. J. Edwards, K. E. Carnazza, S. D. Carlin, B. M. Zeglis, M. J. Adam, C. Orvig, and J. S. Lewis, *A comparative evaluation of the chelators H<sub>4</sub>octapa and CHX-A"-DTPA with the therapeutic radiometal <sup>90</sup>Y*, Nucl. Med. Biol., **2016**, 43, 566-576.
170. H. L. Evans, Q.-D. Nguyen, L. S. Carroll, M. Kaliszczak, F. J. Twyman, A. C. Spivey, and E. O. Aboagye, *A bioorthogonal <sup>68</sup>Ga-labelling strategy for rapid in vivo imaging*, Chem. Commun., **2014**, 50, 9557-9560.
171. M. K. Rahim, R. Kota, and J. B. Haun, *Enhancing Reactivity for Bioorthogonal Pretargeting by Unmasking Antibody-Conjugated trans-Cyclooctenes*, Bioconjugate Chem., **2015**, 26, 352-360.
172. B. M. Zeglis, K. K. Sevak, T. Reiner, P. Mohindra, S. D. Carlin, P. Zanzonico, R. Weissleder, and J. S. Lewis, *A pretargeted PET imaging strategy based on bioorthogonal Diels-Alder click chemistry*, J. Nucl. Med., **2013**, 54, 1389-1396.
173. N. K. Devaraj and R. Weissleder, *Biomedical Applications of Tetrazine Cycloadditions*, Acc. Chem. Res., **2011**, 44, 816-827.
174. M. R. Karver, R. Weissleder, and S. A. Hilderbrand, *Synthesis and Evaluation of a Series of 1,2,4,5-Tetrazines for Bioorthogonal Conjugation*, Bioconjugate Chem., **2011**, 22, 2263-2270.
175. J.-P. Meyer, P. Adumeau, J. S. Lewis, and B. M. Zeglis, *Click Chemistry and Radiochemistry: The First 10 Years*, Bioconjugate Chem., **2016**, 27, 2791-2807.

176. O. Hamid and R. D. Carvajal, *Anti-programmed death-1 and anti-programmed death-ligand 1 antibodies in cancer therapy*, *Expert Opin. Biol. Ther.*, **2013**, *13*, 847-861.
177. J. R. Brahmer, S. S. Tykodi, L. Q. M. Chow, W.-J. Hwu, S. L. Topalian, P. Hwu, C. G. Drake, L. H. Camacho, J. Kauh, K. Odunsi, H. C. Pitot, O. Hamid, S. Bhatia, R. Martins, K. Eaton, S. Chen, T. M. Salay, S. Alaparthi, J. F. Grosso, A. J. Korman, S. M. Parker, S. Agrawal, S. M. Goldberg, D. M. Pardoll, A. Gupta, and J. M. Wigginton, *Safety and Activity of Anti-PD-L1 Antibody in Patients with Advanced Cancer*, *New Engl. J. Med.*, **2012**, *366*, 2455-2465.
178. S. L. Topalian, F. S. Hodi, J. R. Brahmer, S. N. Gettinger, D. C. Smith, D. F. McDermott, J. D. Powderly, R. D. Carvajal, J. A. Sosman, M. B. Atkins, P. D. Leming, D. R. Spigel, S. J. Antonia, L. Horn, C. G. Drake, D. M. Pardoll, L. Chen, W. H. Sharfman, R. A. Anders, J. M. Taube, T. L. McMiller, H. Xu, A. J. Korman, M. Jure-Kunkel, S. Agrawal, D. McDonald, G. D. Kollia, A. Gupta, J. M. Wigginton, and M. Sznol, *Safety, Activity, and Immune Correlates of Anti-PD-1 Antibody in Cancer*, *New Engl. J. Med.*, **2012**, *366*, 2443-2454.
179. E. J. Lipson, W. H. Sharfman, C. G. Drake, I. Wollner, J. M. Taube, R. A. Anders, H. Xu, S. Yao, A. Pons, L. Chen, D. M. Pardoll, J. R. Brahmer, and S. L. Topalian, *Durable Cancer Regression Off-Treatment and Effective Reinduction Therapy with an Anti-PD-1 Antibody*, *Clin. Cancer Res.*, **2013**, *19*, 462.
180. O. Hamid, C. Robert, A. Daud, F. S. Hodi, W.-J. Hwu, R. Kefford, J. D. Wolchok, P. Hersey, R. W. Joseph, J. S. Weber, R. Dronca, T. C. Gangadhar, A. Patnaik, H. Zarour, A. M. Joshua, K. Gergich, J. Elassaiss-Schaap, A. Algazi, C. Mateus, P. Boasberg, P. C. Tumeh, B. Chmielowski, S. W. Ebbinghaus, X. N. Li, S. P. Kang, and A. Ribas, *Safety and Tumor Responses with Lambrolizumab (Anti-PD-1) in Melanoma*, *New Engl. J. Med.*, **2013**, *369*, 134-144.
181. C. Robert, A. Ribas, J. D. Wolchok, F. S. Hodi, O. Hamid, R. Kefford, J. S. Weber, A. M. Joshua, W.-J. Hwu, T. C. Gangadhar, A. Patnaik, R. Dronca, H. Zarour, R. W. Joseph, P. Boasberg, B. Chmielowski, C. Mateus, M. A. Postow, K. Gergich, J. Elassaiss-Schaap, X. N. Li, R. Iannone, S. W. Ebbinghaus, S. P. Kang, and A. Daud, *Anti-programmed-death-receptor-1 treatment with pembrolizumab in ipilimumab-refractory advanced melanoma: a randomised dose-comparison cohort of a phase 1 trial*, *Lancet*, **2014**, *384*, 1109-1117.
182. S. L. Topalian, M. Sznol, D. F. McDermott, H. M. Kluger, R. D. Carvajal, W. H. Sharfman, J. R. Brahmer, D. P. Lawrence, M. B. Atkins, J. D. Powderly, P. D. Leming, E. J. Lipson, I. Puzanov, D. C. Smith, J. M. Taube, J. M. Wigginton, G. D. Kollia, A. Gupta, D. M. Pardoll, J. A. Sosman, and F. S. Hodi, *Survival, Durable Tumor Remission, and Long-Term Safety in Patients With Advanced Melanoma Receiving Nivolumab*, *J. Clin. Oncol.*, **2014**, *32*, 1020-1030.
183. M. Konstantinidou, T. Zarganes-Tzitzikas, K. Magiera-Mularz, T. A. Holak, and A. Dömling, *Immune Checkpoint PD-1/PD-L1: Is There Life Beyond Antibodies?*, *Angew. Chem. Int. Ed.*, **2018**, *57*, 4840-4848.
184. C. Truillet, H. L. J. Oh, S. P. Yeo, C.-Y. Lee, L. T. Huynh, J. Wei, M. F. L. Parker, C. Blakely, N. Sevillano, Y.-H. Wang, Y. S. Shen, V. Olivás, K. M. Jami, A. Moroz, B.

- Jego, E. Jaumain, L. Fong, C. S. Craik, A. J. Chang, T. G. Bivona, C.-I. Wang, and M. J. Evans, *Imaging PD-L1 Expression with ImmunoPET*, *Bioconjugate Chem.*, **2018**, *29*, 96-103.
185. S. Heskamp, W. Hobo, J. D. M. Molkenboer-Kuenen, D. Olive, W. J. G. Oyen, H. Dolstra, and O. C. Boerman, *Noninvasive Imaging of Tumor PD-L1 Expression Using Radiolabeled Anti-PD-L1 Antibodies*, *Cancer Res.*, **2015**, *75*, 2928.
  186. W. Li, P. Prabakaran, W. Chen, Z. Zhu, Y. Feng, and S. D. Dimitrov, *Antibody Aggregation: Insights from Sequence and Structure*, *Antibodies*, **2016**, *5*.
  187. D. Vivier, S. K. Sharma, and B. M. Zeglis, *Understanding the in vivo fate of radioimmunoconjugates for nuclear imaging*, *J. Labelled Compd. Radiopharm.*, **2018**, *61*, 672-692.
  188. M. N. Lub-de Hooge, J. G. W. Kosterink, P. J. Perik, H. Nijhuis, L. Tran, J. Bart, A. J. H. Suurmeijer, S. de Jong, P. L. Jager, and E. G. E. de Vries, *Preclinical characterisation of (111)In-DTPA-trastuzumab*, *Br. J. Pharmacol.*, **2004**, *143*, 99-106.
  189. R. K. Kainthan, S. R. Hester, E. Levin, D. V. Devine, and D. E. Brooks, *In vitro biological evaluation of high molecular weight hyperbranched polyglycerols*, *Biomaterials*, **2007**, *28*, 4581-4590.
  190. R. K. Kainthan and D. E. Brooks, *In vivo biological evaluation of high molecular weight hyperbranched polyglycerols*, *Biomaterials*, **2007**, *28*, 4779-4787.
  191. R. K. Kainthan and D. E. Brooks, *Unimolecular Micelles based on Hydrophobically Derivatized Hyperbranched Polyglycerols: Biodistribution Studies*, *Bioconjugate Chem.*, **2008**, *19*, 2231-2238.
  192. M. Imran ul-haq, B. F. L. Lai, R. Chapanian, and J. N. Kizhakkedathu, *Influence of architecture of high molecular weight linear and branched polyglycerols on their biocompatibility and biodistribution*, *Biomaterials*, **2012**, *33*, 9135-9147.
  193. K. Saatchi, N. Gelder, P. Gershkovich, O. Sivak, K. M. Wasan, R. K. Kainthan, D. E. Brooks, and U. O. Häfeli, *Long-circulating non-toxic blood pool imaging agent based on hyperbranched polyglycerols*, *Int. J. Pharm.*, **2012**, *422*, 418-427.
  194. R. K. Kainthan, C. Mugabe, H. M. Burt, and D. E. Brooks, *Unimolecular Micelles Based On Hydrophobically Derivatized Hyperbranched Polyglycerols: Ligand Binding Properties*, *Biomacromolecules*, **2008**, *9*, 886-895.
  195. R. K. Kainthan, J. Janzen, J. N. Kizhakkedathu, D. V. Devine, and D. E. Brooks, *Hydrophobically derivatized hyperbranched polyglycerol as a human serum albumin substitute*, *Biomaterials*, **2008**, *29*, 1693-1704.
  196. N. A. A. Rossi, I. Constantinescu, R. K. Kainthan, D. E. Brooks, M. D. Scott, and J. N. Kizhakkedathu, *Red blood cell membrane grafting of multi-functional hyperbranched polyglycerols*, *Biomaterials*, **2010**, *31*, 4167-4178.
  197. K. Saatchi, P. Soema, N. Gelder, R. Misri, K. McPhee, J. H. E. Baker, S. A. Reinsberg, D. E. Brooks, and U. O. Häfeli, *Hyperbranched Polyglycerols as Trimodal Imaging Agents: Design, Biocompatibility, and Tumor Uptake*, *Bioconjugate Chem.*, **2012**, *23*, 372-381.

198. V. Schmitt, C. Rodriguez-Rodriguez, J. L. Hamilton, R. A. Sheno, P. Schaffer, V. Sossi, J. N. Kizhakkedathu, K. Saatchi, and U. O. Hafeli, *Quantitative SPECT imaging and biodistribution point to molecular weight independent tumor uptake for some long-circulating polymer nanocarriers*, RSC Adv., **2018**, 8, 5586-5595.
199. R Core Team, *R: A Language and Environment for Statistical Computing*, v. 3.5.1, R Foundation for Statistical Computing, Vienna, Austria, **2013**.
200. E. Boros and J. P. Holland, *Chemical aspects of metal ion chelation in the synthesis and application antibody-based radiotracers*, J. Labelled Compd. Radiopharm., **2017**, 61, 652-671.
201. R. K. Kainthan, E. B. Muliawan, S. G. Hatzikiriakos, and D. E. Brooks, *Synthesis, Characterization, and Viscoelastic Properties of High Molecular Weight Hyperbranched Polyglycerols*, Macromolecules, **2006**, 39, 7708-7717.
202. J.-P. Meyer, K. M. Tully, J. Jackson, T. R. Dilling, T. Reiner, and J. S. Lewis, *Bioorthogonal Masking of Circulating Antibody-TCO Groups Using Tetrazine-Functionalized Dextran Polymers*, Bioconjugate Chem., **2018**, 29, 538-545.
203. O. Keinänen, K. Fung, J. Pourat, V. Jallinoja, D. Vivier, N. K. Pillarsetty, A. J. Airaksinen, J. S. Lewis, B. M. Zeglis, and M. Sarparanta, *Pretargeting of internalizing trastuzumab and cetuximab with a 18F-tetrazine tracer in xenograft models*, EJNMMI Research, **2017**, 7, 95.
204. J.-P. Meyer, P. Kozlowski, J. Jackson, K. M. Cunanan, P. Adumeau, T. R. Dilling, B. M. Zeglis, and J. S. Lewis, *Exploring Structural Parameters for Pretargeting Radioligand Optimization*, J. Med. Chem., **2017**, 60, 8201-8217.
205. T. J. Wadas, E. H. Wong, G. R. Weisman, and C. J. Anderson, *Coordinating Radiometals of Copper, Gallium, Indium, Yttrium, and Zirconium for PET and SPECT Imaging of Disease*, Chem. Rev., **2010**, 110, 2858-2902.
206. J. Notni and H.-J. Wester, *Re-thinking the role of radiometal isotopes: Towards a future concept for theranostic radiopharmaceuticals*, J. Labelled Compd. Radiopharm., **2018**, 61, 141-153.
207. C. Müller, K. Zhernosekov, U. Köster, K. Johnston, H. Dorrer, A. Hohn, N. T. van der Walt, A. Türler, and R. Schibli, *A Unique Matched Quadruplet of Terbium Radioisotopes for PET and SPECT and for  $\alpha$ - and  $\beta$ -Radionuclide Therapy: An In Vivo Proof-of-Concept Study with a New Receptor-Targeted Folate Derivative*, J. Nucl. Med., **2012**, 53, 1951-1959.
208. C. Müller, K. A. Domnanich, C. A. Umbricht, and N. P. van der Meulen, *Scandium and terbium radionuclides for radiotheranostics: current state of development towards clinical application*, Br. J. Radiol., **2018**, 20180074.
209. S. Hassfjell and M. W. Brechbiel, *The Development of the  $\alpha$ -Particle Emitting Radionuclides  $^{212}\text{Bi}$  and  $^{213}\text{Bi}$ , and Their Decay Chain Related Radionuclides, for Therapeutic Applications*, Chem. Rev., **2001**, 101, 2019-2036.
210. J. Xu, B. Kullgren, P. W. Durbin, and K. N. Raymond, *Specific Sequestering Agents for the Actinides. 28. Synthesis and Initial Evaluation of Multidentate 4-Carbamoyl-3-*

- hydroxy-1-methyl-2(1H)-pyridinone Ligands for in Vivo Plutonium(IV) Chelation*, J. Med. Chem., **1995**, 38, 2606-2614.
211. J. Xu, D. W. Whisenhunt, A. C. Veeck, L. C. Uhler, and K. N. Raymond, *Thorium(IV) Complexes of Bidentate Hydroxypyridinonates*, Inorg. Chem., **2003**, 42, 2665-2674.
212. M. P. Kelley, G. J. P. Deblonde, J. Su, C. H. Booth, R. J. Abergel, E. R. Batista, and P. Yang, *Bond Covalency and Oxidation State of Actinide Ions Complexed with Therapeutic Chelating Agent 3,4,3-LI(1,2-HOPO)*, Inorg. Chem., **2018**.
213. J. L. Hatcher, *Fundamental Chemistry Related to the Separations and Coordination of Actinium-225, Thorium-227, and Technetium-99*, Ph.D. Thesis, City University of New York, **2018**.
214. H. T. Bonge-Hansen and B. R. Olav, *Radio-Pharmaceutical Complexes*, **2013**, Pat. WO2013/167754 A1.
215. T. Ramdahl, H. T. Bonge-Hansen, O. B. Ryan, Å. Larsen, G. Herstad, M. Sandberg, R. M. Bjerke, D. Grant, E. M. Brevik, and A. S. Cuthbertson, *An efficient chelator for complexation of thorium-227*, Bioorg. Med. Chem. Lett., **2016**, 26, 4318-4321.
216. ClinicalTrials.gov, *First-in-human Study of BAY2287411 Injection, a Thorium-227 Labeled Antibody-chelator Conjugate, in Patients With Tumors Known to Express Mesothelin*, <https://clinicaltrials.gov/ct2/show/NCT03507452>, (accessed Sep. 17, 2018).

# Appendices

## Appendix A: Data for Zr-THPN and $^{89}\text{Zr}$ -Labeling

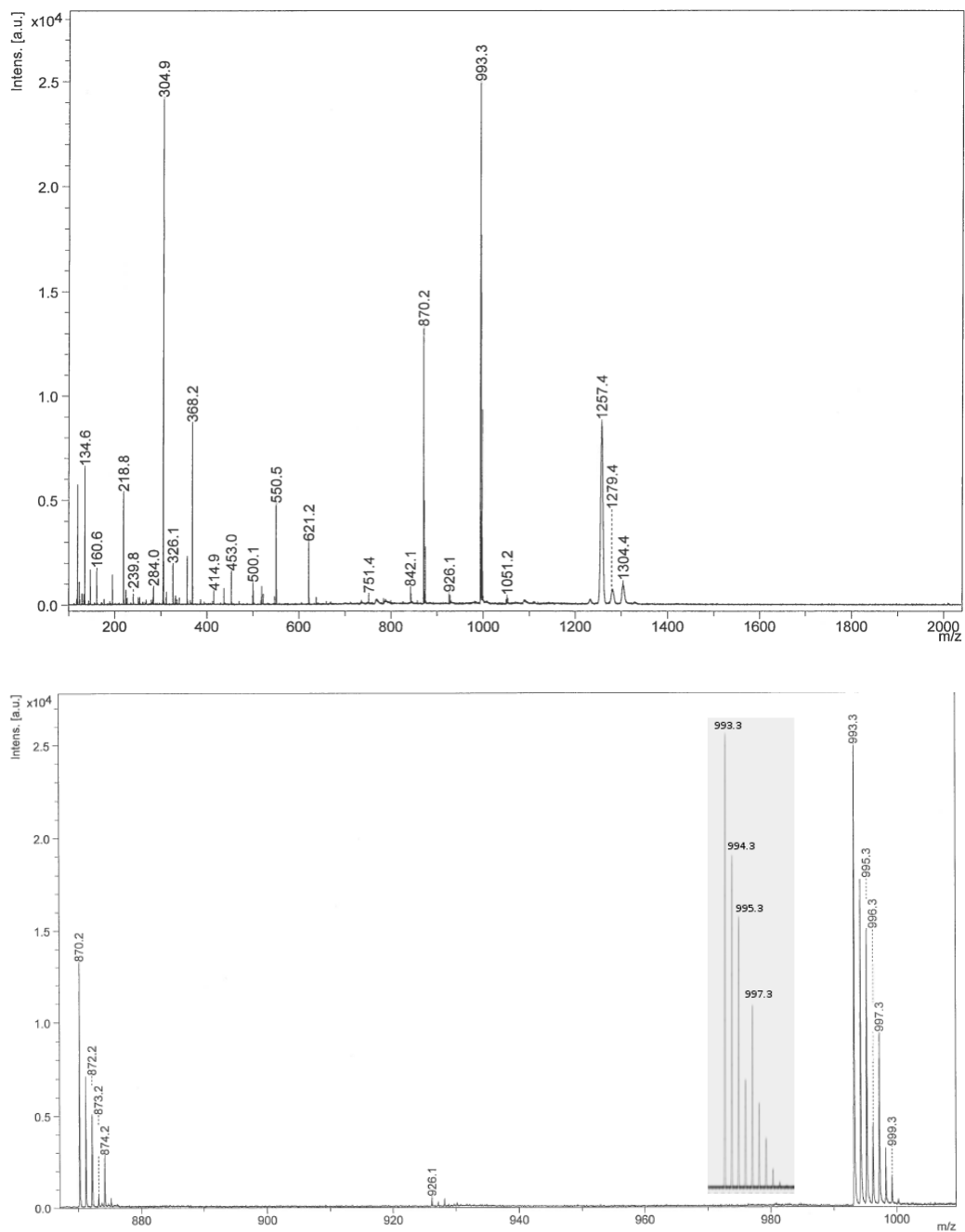


**Figure A.1.** MALDI-MS of Zr-THPN. The monometallic complex shows the expected  $[\text{M}+\text{H}]^+$  peak and isotope pattern at  $m/z$  993.3 that matches the predicted pattern (inset).



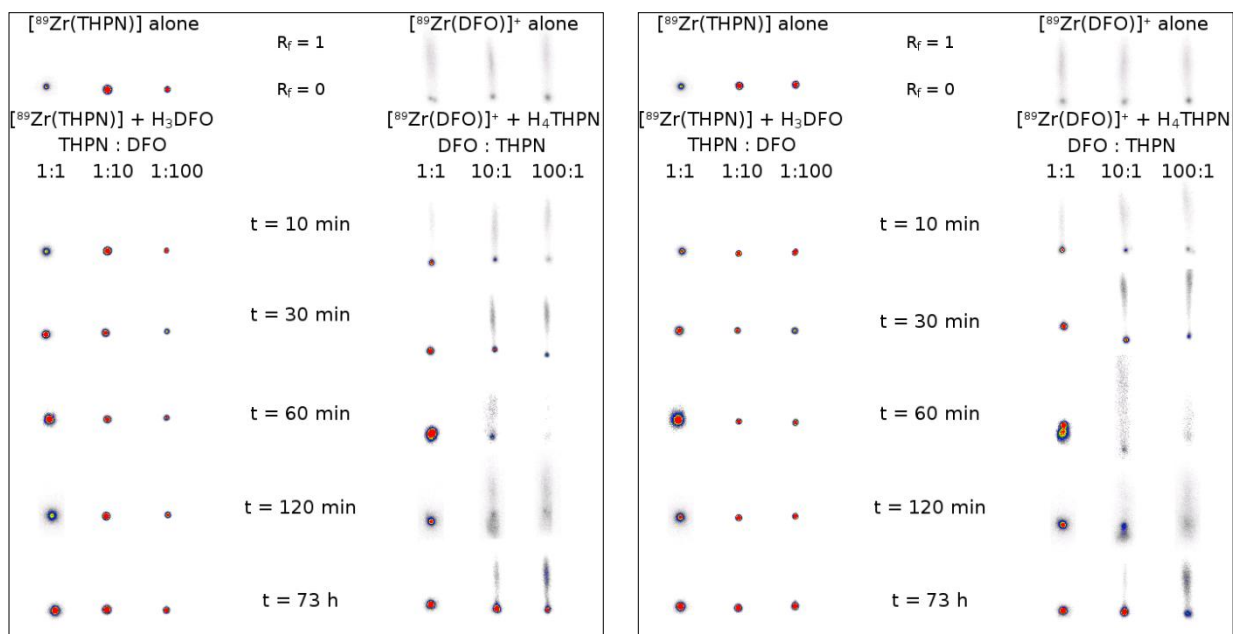


**Figure A.4.** ITLCs of transchelation competition (repetitions of Figure 3.8 for  $n = 3$ ). Biodex Tec-Control (dark green, #150-771) ITLC strips developed with aqueous sodium citrate solution (100 mM, pH 5.5).

Appendix B: PET/CT Images from *In Vivo* Study of  $^{89}\text{Zr}$ -Chelates

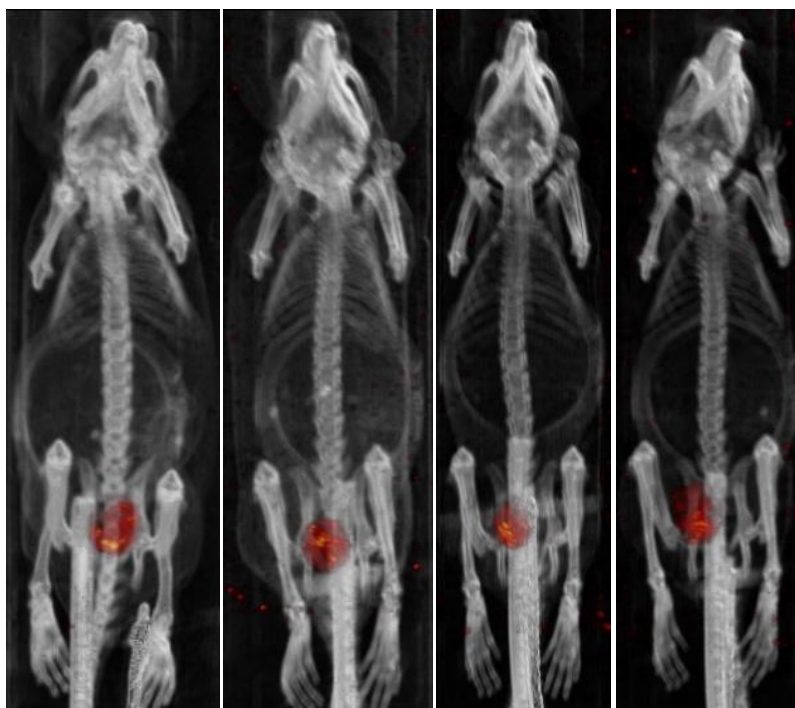


**Figure B.1.** Fused PET/CT images (MIP) of all four mice injected with  $^{89}\text{Zr}$ -THPN (0–30 min post injection).

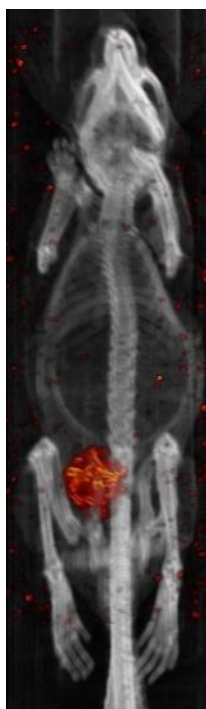


**Figure B.2.** Fused PET/CT image (MIP) of the mouse injected with  $^{89}\text{Zr}$ -DFO (0–30 min post injection).

## Appendix C: Spectra Pertaining to Thermodynamic Solution Studies

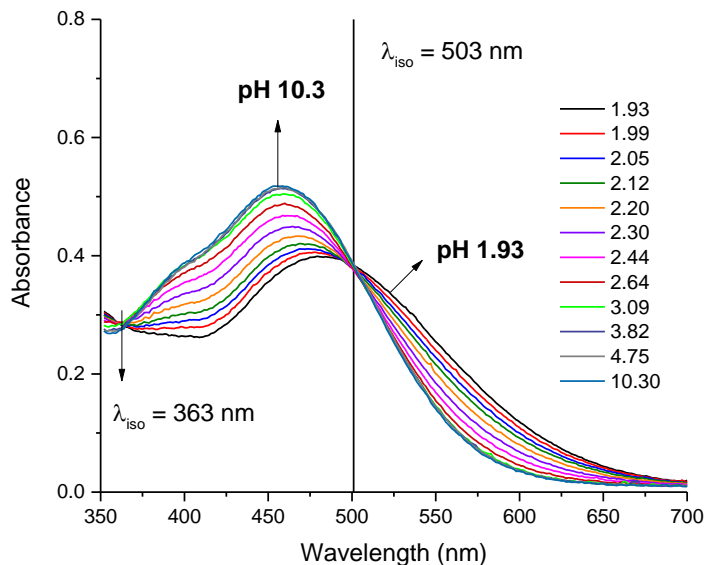


**Figure C.1.** Representative spectra of the direct UV-Vis potentiometric titration of the Fe<sup>III</sup>-THPN system ([THPN] = [Fe<sup>3+</sup>] =  $2.08 \times 10^{-4}$  M) as the pH is raised from 1.93 to 10.3, 25 °C, *I* = 0.16 M (NaCl), *l* = 0.5 cm.

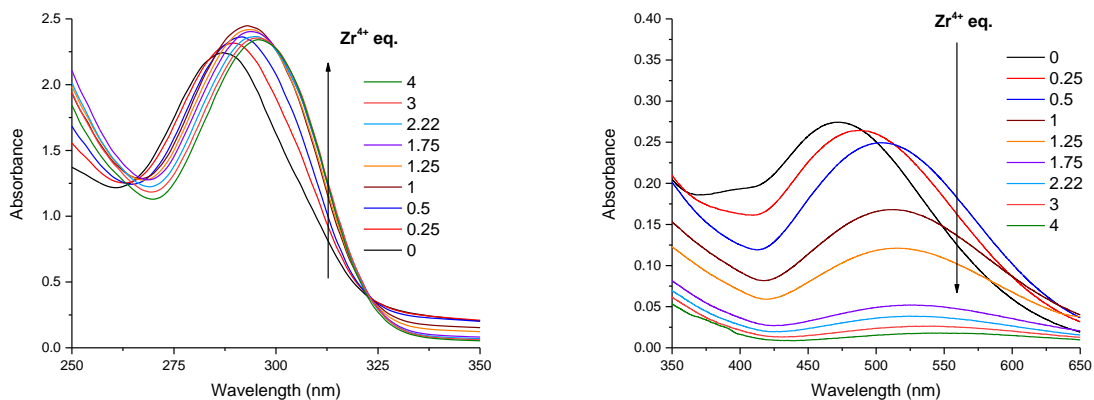


**Figure C.2.** Representative spectra of the metal-metal competition of the Fe<sup>III</sup>-THPN system by increasing the equivalents of Zr<sup>4+</sup>. [THPN] = [Fe<sup>3+</sup>] =  $7.16 \times 10^{-5}$  M, [Zr<sup>4+</sup>]/[Fe<sup>3+</sup>] = 0–4.5, pH = 2, 25 °C, *I* = 0.16 M (NaCl), *l* = 1 cm.

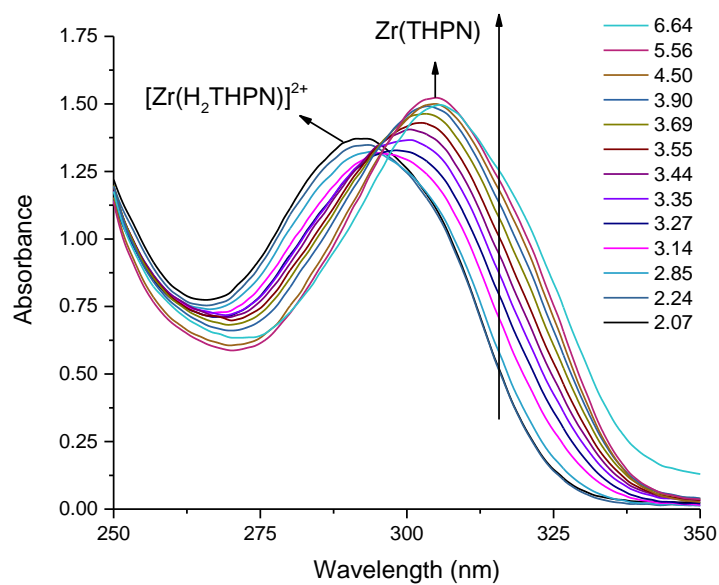


**Figure C.3.** Representative spectra of the combined UV-potentiometric titration of the  $Zr^{IV}$ -THPN system in the pH range 2.07–6.64.  $[THPN] = [Zr^{4+}] = 2.11 \times 10^{-4}$  M, at 25 °C,  $I = 0.16$  M (NaCl),  $l = 0.2$  cm.

## Appendix D: Inverse Electron Demand Diels-Alder Conjugation Conjugations

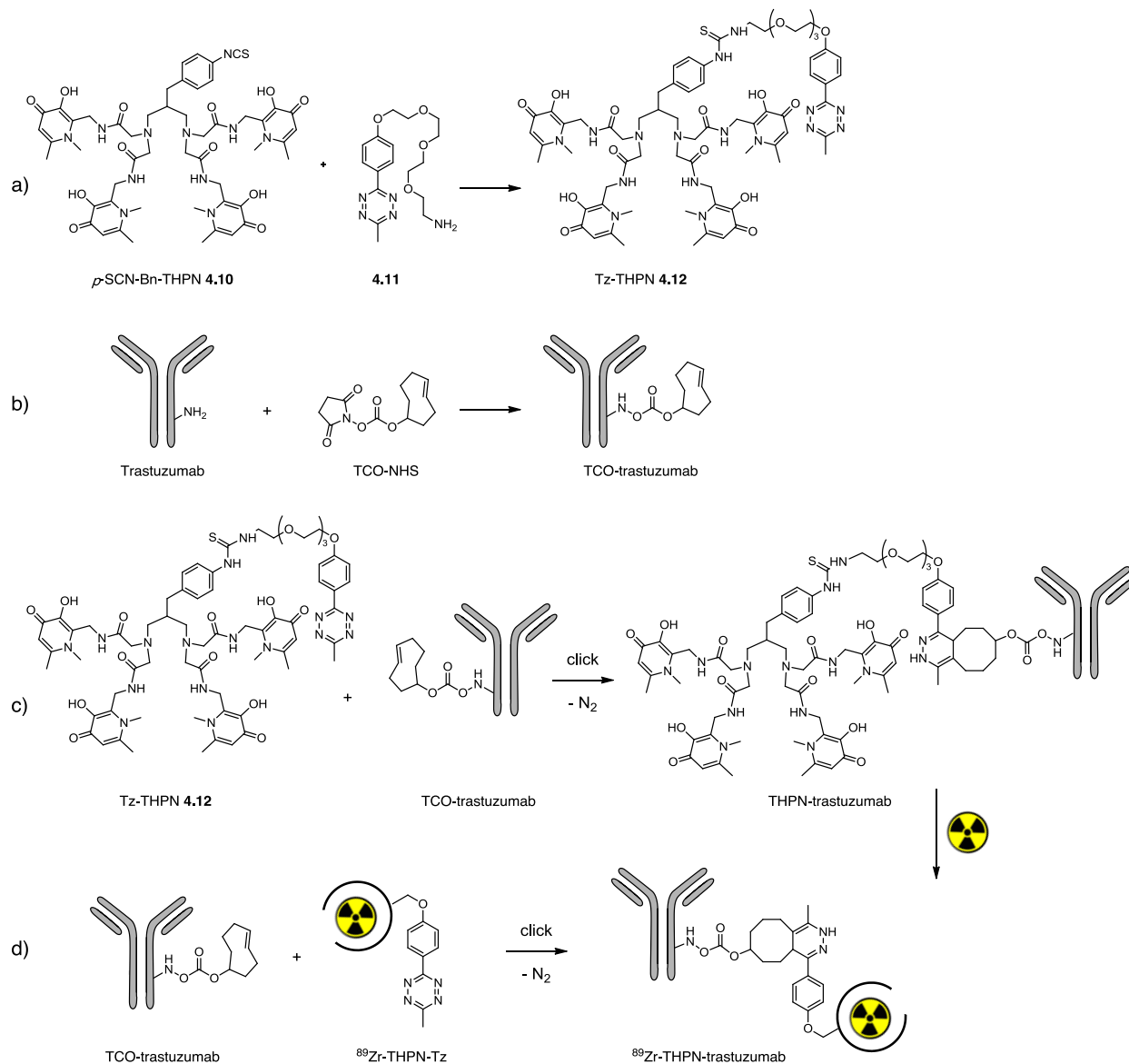


**Figure D.1.** Reaction sequences pursued for tetrazine/*trans*-cyclooctene conjugation strategies to radiolabel trastuzumab. a) Synthesis of tetrazine-THPN derivative **4.12**; b) TCO-modification of trastuzumab; c) postlabeling strategy by IEDDA cycloaddition between **4.12** and TCO-trastuzumab, followed by <sup>89</sup>Zr-labeling; d) prelabeling strategy by IEDDA cycloaddition between TCO-modified trastuzumab and radiolabeled <sup>89</sup>Zr-THPN-tetrazine (shown schematically).